THE UNIVERSITY
of EDINBURGH

PHOSPHO1: AN EXAMPLE OF THE INTERPLAY BETWEEN BONE MINERALISATION AND ENERGY METABOLISM

Karla Jade Oldknow

This thesis is presented for the degree of Doctor of Philosophy at The University of Edinburgh

2015

Declaration

I declare that this thesis has been composed entirely by the candidate, Karla Jade Oldknow. This work has not previously been submitted for a Doctor of Philosophy, a degree or any professional qualification. I have done all the work, unless acknowledged otherwise. All sources of information have been acknowledged.

Karla Jade Oldknow

Acknowledgements

I would firstly like to thank my supervisors Prof. Colin Farquharson and Dr. Vicky MacRae for their outstanding guidance and supervision throughout this work. Special thanks are due to my principle supervisor Prof. Colin Farquharson for his continuous confidence, encouragement and humour, resulting in a truly enjoyable 4 years. I would also like to express my gratitude to the BBSRC for funding this project.

Thanks must be paid to past and present members of the Bone Biology group who have helped me when in need of support and advice throughout my years at the Roslin Institute. In particular I would like to thank Dr. Ross Dobie, Dean Houston, Dr. Carmen Huesa, Elaine Seawright, Dr. Katherine Staines and Dr. Dongxing Zhu. I also wish to thank and acknowledge all the wonderful collaborators I have been fortunate to work with during this project who given me invaluable advice and technical guidance: Dr. Derek Ball, Dr. Lutz Bunger, Dr. Mathieu Ferron, Dr. Anyonya Guntur, Prof. Gerard Karsenty, Dr. Zohreh Khavandgar, Prof. José Luis Millán, Prof. Nik Morton, Dr. Monzur Murshed, Dr. Sophie Rajoanah, Prof. Clifford Rosen, Dr. Cal Vary, Dr. Tom Wishart and Dr. Manisha Yadav. I would like to pay a particular thanks to Prof. Lutz Bünger who has provided continued advice and support. In addition, appreciation is deserved for all the people within the Roslin Institute who have aided me in this project.

Finally, a special thank you has to be paid to my friends and family, particularly my parents and husband for their unconditional love, kind words, support and encouragement throughout this demanding period.

"Carefully watch your thoughts, for they become your words. Manage and watch your words, for they will become your actions. Consider and judge your actions, for they have become your habits. Acknowledge and watch your habits, for they shall become your values. Understand and embrace your values, for they become your destiny."
Gandhi, Mohandas (1869 - 1948)

Abstract

The classical functions of the skeleton encompass locomotion, protection and mineral homeostasis. However, cell-specific gene deletions in the mouse and human genetic studies have recently identified bone as an endocrine organ possessing the capabilities to regulate both energy metabolism and reproduction. Preliminary data suggested that Phosphatase, Orphan 1 (PHOSPHO1) a bone specific phosphatase, indispensable for bone mineralisation, may crosstalk with osteotesticular protein tyrosine phosphatase (OST-PT, *Esp*), a signalling molecule that dephosphorylates the insulin receptor (InsR) on the osteoblast, negatively regulating the osteoblast insulin signalling cascade.

The work of this thesis has expanded upon preliminary data confirming that *Esp* was up-regulated 60-fold in *Phospho1*$^{-/-}$ osteoblasts. Furthermore *in silico* analysis revealed *Phospho1* ablation is significantly associated with insulin dependent diabetes mellitus. These data form the basis of this thesis examining the role of PHOSPHO1 in energy metabolism.

Initial *in vivo* characterisation of *Phospho1*$^{-/-}$ mice revealed that the ablation of *Phospho1* results in decreased blood glucose levels, improved insulin sensitivity and glucose tolerance in juvenile, adult and aged mice. Following high fat feeding, *Phospho1* ablation conferred a remarkable degree of protection against diet-induced-obesity and non-alcoholic fatty liver disease (NAFLD) despite the 60-fold increase in *Esp* expression.

The metabolic protection observed in *Phospho1*$^{-/-}$ mice served to strengthen PHOSPHO1's potential role in energy metabolism. However the mechanisms remained unclear. Mice overexpressing *Esp* specifically in osteoblasts are glucose intolerant and insulin resistant, due to the negative regulation of osteoblast-insulin-signalling, resulting in decreased undercarboxylated osteocalcin (GLU13-OCN)

release. This thesis identified however that the serum levels of a GLU13-OCN were normal in *Phospho1*$^{-/-}$ mice suggesting that there was a GLU13-OCN-independent mechanism for PHOSPHO1 regulated energy metabolism. Moreover, mass spectrometry analysis identified > 100 differentially expressed proteins in *Phospho1*$^{-/-}$ serum associated with the regulation of glycolysis and gluconeogenesis. These candidates displayed an enrichment for microRNA Mir34a and the transcription factor hepatocyte nuclear factor 1, both reported to regulate hepatic glucose homeostasis. These data therefore support the notion that further, yet undefined osteoblast derived factors contribute to whole body energy metabolism and highlight a new and unconventional role of *Esp* suggestive that it may act as a fine controller of insulin sensitivity in mice, offering protection from severe hypoglycaemia and dyslipidaemia.

Finally, this thesis also explored the notion that decreased levels of choline may contribute to the insulin sensitivity observed in *Phospho1*$^{-/-}$ mice. Phosphocholine (P-Cho) is a recognised substrate for PHOSPHO1 being hydrolysed into choline and inorganic phosphate (P_i). Phosphatase Orphan 1 deficient mice, hypothesised to have reduced choline levels were fed a 2% choline rich diet; mice displayed a normalisation in insulin sensitivity and fat mass. These data suggest that *Phospho1*-deficiency improves the metabolic profile of mice *in vivo* and confers resistance to obesity and diabetes via the alteration of serum/tissue choline levels.

The work described herein has characterised the metabolic phenotype of *Phospho1*$^{-/-}$ mice and began to unravel the mechanisms underlying the improved metabolic phenotype in *Phospho1*$^{-/-}$ mice.

Publications

Original peer reviewed papers

Oldknow KJ, Morton NM, Vary C, Yadav MC, Rajoanah S, Huesa C, Bunger L, Ball D, Guntur AR, Khavandgar Z, Ferron M, Karsenty G, , Monzur M, Rosen CJ, MacRae VE, Millán JL, Farquharson C (2015). PHOSPHO1, a novel skeletal regulator of insulin resistance and obesity. In preparation.

Oldknow KJ, MacRae VE, Farquharson C, Bünger L (2015). Evaluating invasive and non-invasive methods to determine fat content in the laboratory mouse. *Open Life Sciences* 10(1):81-88.

Javaheri B, Carriero A, Staines KA, Chang YM, Houston DA, **Oldknow KJ**, Millan JL, Kazeruni BN, Salmon P, Shefelbine S, Farquharson C, Pitsillides AA (2015). Phospho1 deficiency transiently modifies bone architecture yet produces consistent modification in osteocyte differentiation and vascular porosity with ageing. *Bone*. In press.

Rodriguez-Florez N, Garcia-Tunon E, Mukadam Q, Saiz E, **Oldknow KJ**, Farquharson C, Millán JL, Boyde A & Shefelbine SJ (2015). An investigation of the mineral in ductile and brittle cortical mouse bone. *Journal of Bone and Mineral Research* 30(5):786-795.

Carriero A, Bruse JL, **Oldknow KJ**, Millan JL, Farquharson C & Shefelbine SJ (2014). Reference point indentation is not indicative of whole mouse bone measures of stress intensity fracture toughness. *Bone* 69:174-179.

Eaton SL, Hurtado ML, **Oldknow KJ**, Graham LC, Marchant TW, Gillingwater TH, Farquharson C & Wishart TM (2014). A guide to modern quantitative fluorescent western blotting with troubleshooting strategies. *Journal* of *Visualized Experiments* 20:(93):e52099

Eaton SL, Roche SL, Llavero Hurtado M, **Oldknow KJ**, Farquharson C, Gillingwater TH & Wishart TM (2013). Total protein analysis as a reliable loading control for quantitative fluorescent Western blotting. *PLoS One* 8(8):e72457.

Reviews

Oldknow KJ, MacRae VE, Farquharson C (2015) The Endocrine role of bone: Recent and emerging perspectives beyond osteocalcin. *Journal of Endocrinology* 225(1):R1-19.

Book Chapters

Oldknow KJ, MacRae VE, Farquharson C, Bünger L (2014). Evaluating invasive and non-invasive methods to determine fat content in the laboratory mouse. *Farm Animal Imaging* Edinburgh: Scotland's Rural College (SRUC). 2014: 35-38. ISBN: 978-0-9931063-0-9.

Published Abstracts

Oldknow KJ, Morton NM, Yadav MC, Huesa C, Ferron M, Karsenty G, Khavandgar Z, Guntur AR, MacRae VE, Murshed M., Vary C, Rosen CJ, Millán JL, Farquharson C (2015). PHOSPHO1, a novel skeletal regulator of energy metabolism. *Journal of Bone and Mineral Research (pending publication)*. The American Society for Bone and Mineral Research, oral communication.

Oldknow KJ, Morton NM, Yadav MC, Huesa C, Ferron M, Karsenty G, Khavandgar Z, Guntur AR, MacRae VE, Murshed M., Vary C, Rosen CJ, Millán JL, Farquharson C (2015). Endocrine role of bone: PHOSPHO1 a novel regulator of energy metabolism. *Frontiers in Bone Research (pending publication)*. The Bone Research Society, oral communication.

Javaheri B, Carriero A, Shefelbine S, Millan J, **Oldknow KJ**, Farquharson C, Pitsillides A (2014). Phospho1 deficiency transiently modifies bone architecture yet produces consistent modification in osteocyte differentiation and vascularization with ageing. F*rontiers in Bone Research, Frontiers Abstract Book* (OP7) ISBN: 978-2-88919-300-4. The Bone Research Society, oral communication.

Oldknow KJ, MacRae VE, Farquharson C, Bünger L (2014). Evaluating invasive and non-invasive methods to determine fat content in the laboratory mouse. *Farm Animal Imaging* ISBN: 978-0-9931063-0-9. Farm Animal Imaging, oral communication.

Oldknow KJ, Morton NM, Yadav MC, Rajoanah S, Huesa C, Bunger L, Ball D, Ferron M, Karsenty G, MacRae VE, Millán JL, Farquharson C (2014). PHOSPHO1: An example of the interplay between bone mineralisation and energy metabolism. *Frontiers in Bone Research, Frontiers Abstract Book* (OC17) ISBN: 978-2-88919-300-4. The Bone Research Society, oral communication.

Oldknow KJ, Morton NM, Yadav MC, Rajoanah S, Huesa C, Bunger L, Ball D, Ferron M, Karsenty G, MacRae VE, Millán JL, Farquharson C (2014). PHOSPHO1: Roles beyond skeletal mineralisation. *Endocrine Abstracts* 34 (OC4.2). The Society for Endocrinology, oral communication.

Oldknow KJ, Morton NM, Yadav MC, Rajoanah S, Huesa C, Bunger L, Ball D, Ferron M, Karsenty G, MacRae VE, Millán JL, Farquharson C (2013). PHOSPHO1:

Recognition of roles beyond skeletal mineralization. *Journal of Bone and Mineral Research* 28:1. The American Society for Bone and Mineral Research, oral communication.

Oldknow KJ, Morton NM, Yadav MC, Rajoanah S, Huesa C, Bunger L, Ball D, Ferron M, Karsenty G, MacRae VE, Millán JL, Farquharson C (2013). Phospho1: An emerging role in energy metabolism. *Frontiers in Bone Research, Frontiers Abstract Book* (OC2) ISBN: 978-2-88919-174-1. The Bone Research Society, oral communication.

Oldknow KJ, Morton NM, Yadav MC, Rajoanah S, Huesa C, Bunger L, Ball D, Ferron M, Karsenty G, MacRae VE, Millán JL, Farquharson C (2013). An Emerging Role of PHOSPHO1 in the Regulation of Energy. *Bone Abstracts* 1 (OC6.6). The European Calcified Tissue Society, oral communication.

Oldknow KJ, Huesa C, Yadav MC, MacRae VE, Millan JL, Farquharson C (2012) Does Phospho1 regulate insulin signalling in osteoblasts? *Osteoporosis International* 23:5 (S579-S580). The Bone Research Society, poster presentation.

Awards

The American Society for Bone and Mineral Research Young Investigator Award – 2013.

The European Calcified Tissue Society New Investigator Award – 2013.

The Bone Research Society New Investigator Award – 2013, 2015.

Prizes

British Heart Foundation centre of Research Excellence Adipose Tissue Workshop and 40th UK Adipose Tissue Discussion Group (Poster prize – runner up) – 2013.

Society for Endocrinology Career Development Workshop (track 1) (Early career grant proposal winners) **–** 2014.

Scientific funding

Roslin Small project grant (£5500) – 2014.

Roslin Small project grant (£8100) – 2013.

Travel grants

The American Society for Bone and Mineral Research Young Investigator Travel Grant – 2015.

Practical Skills Grant Society of Endocrinology – 2015.

Farm Animal Imaging COST Action Grant – 2014.

International Bone and Mineral Society Travel Grant – 2014.

Page Travel Bursary – 2014.

Birrell-Gray Travelling Scholarship – 2013.

Practical Skills Grant Society of Endocrinology – 2013.

Farm Animal Imaging COST Action Grant – 2012.

Abbreviations

µCT	Micro computed tomography
Abhd	Abhydrolase domain containing 16
ADAMTS	A disintegrin and metalloproteinase with thrombospondin motifs
ADHR	Autosomal-dominant hypophosphatemic rickets
Adipoq	Adiponectin
ADP	Adenosine diphosphate
ADRB3	Adrenoceptor beta
AFT4	Activating transcription factor 4
Akp2	Tissue-nonspecific alkaline phosphatase (gene)
AKT	Protein kinase B
ALOX	Arachidonate 5-lipoxygenase-activating protein
ALP	Alkaline phosphatase
AMPK	AMP-activated protein kinase
ANK	Progressive ankylosis
ANOVA	Analysis of variance
ASARM	Acidic serine- and aspirate- rich motif
ATF4	Activating transcription factor 4
ATP	Adenosine triphosphate
Atp5b	ATP synthase, H+ transporting, mitochondrial F1 complex, beta polypeptide
BAT	Brown adipose tissue
BBB	Blood–brain-barrier
Bglap	Bone Gla protein
BM-40	Osteonectin
BMD	Bone mineral density
BMI	Body mass index
BMP	Bone morphogenetic protein
BMPR	Bone morphogenetic protein receptor
BRL	Beta 3-receptor agonist
BSA	Bovine serum albumin
BSP	Bone sialoprotein
BTB	Blood-testis-barrier
BV	Bone volume
BV/TV	bone volume fraction
BW	Body weight
Ca10(PO4)6(OH)2	Calcium hydroxyapatite
CART	Cocaine and amphetamine-regulated transcript
CD	Control diet
cDNA	Complimentary DNA
CE	Cholesteryl esters
Cfp	Complement factor properdin

Cidae	Cell death-inducing DFFA-like effector a
CII/CIII	Mitochondrial complex II/III
CLAMS	Comprehensive Lab Animal Monitoring System
Clec6a	C-type lectin domain family 6, member A
CNS	Central nervous system
CO_2	Carbon dioxide
Cor. BMD	Cortical bone mineral density
Cor. Por	Cortical porosity
Cor.Th.	Cortical thickness
COX	Cyclooxygenase
CRE	Carbapenem-resistant enterobacteriaceae
CREB	cAMP response element-binding protein
CT	Computer tomography
Cxcl	The chemokine (C-X-C motif) ligand 1
DA	Degree of anisotropy
DAB	Diaminobenzidine
DAPI	4',6-diamidino-2-phenylindole
DEPC	Diethylpyrocarbonate
DES1	Sphingolipid delta (4)-desaturase
dH_2O	Distilled water
DICOM	Digital Imaging and Communications in Medicine
Dio2	Deiodinase, iodothyronine, type II
Dlx5	Distal-Less homeobox 5
DM	Dry matter
DMEM	Dulbecco's modified eagle medium
DMP1	Dentin matrix protein 1
DMSO	Dimethyl sulfoxide
DNA	Deoxyribonucleic acid
dNTP	Deoxyribonucleotide triphosphate
DS	Dissected
DSPP	Dentin sialophosphoprotein
DTT	Dithiothreitol
DXA	Dual-energy X-ray absorptiometry
ECL	Electrochemiluminescence
ECM	Extracellular matrix
EDTA	Ethylenediaminetetraacetic acid
ELISA	Enzyme-linked immunosorbent assay
Enpp1	Ectonucleotide pyrophosphatase/phosphodiesterase family member 1 (NPP1 protein)
ENU	N-ethyl-N-nitrosourea mutagenesis
ERK	Extracellular signal-regulated kinases
ESI	Electrospray ionisation
Esp	Embryonic stem cell phosphatase
EUCOMM	European Conditional Mouse Mutagenesis Program
EV	Empty vector

FatP	Fat percentage
FatW	Fat weight
FBS	Fetal Bovine Serum
FCCP	Carbonyl cyanide-4-(trifluoromethoxy)phenylhydrazone
Fcer1g	Fc Fragment of IgE, high affinity I, receptor for gamma polypeptide
Fcgr	Low affinity immunoglobulin gamma Fc region receptor
FD	Freeze dried
FFM	Fat free mass
FGF	Fibroblast growth factor
Fmod	Fibromodulin
FOV	Field of view
FoxO1	Forkhead box protein O 1
FP1	Flag tagged PHOSPHO1 overexpressing virus
fro	Fragilitas ossium
GAG	Glycosaminoglycans
GF	Gonadal fat
GFP	Green fluorescent protein
GIGYF	GYF protein 1
GIGYF1	GYF protein 1
GLA	Vitamin K dependent carboxyglutamic acid residues
GLA13-OCN	Inactive osteocalcin
GLP-1	Glucagon-like peptide-1
GLU13-OCN	Metabolically active osteocalcin
GLUT	Glucose transporter facilitators
GPCR	G protein-coupled receptor
Gpnmb	Glycoprotein (transmembrane) nmb
GPRC6A	G protein-coupled receptor, class C, group 6, member A
GRB10	Growth factor receptor-bound protein 10
GSIS	Glucose stimulated insulin secretion tests
GSK	Glycogen synthase kinase 3
GTT	Glucose tolerance test
H&E	Haemotoxylin and eosin
HA	Hydroxyapatite
HAD	Haloacid dehalogenase
HBSS	Hank's Balanced Salt Solution
HEPES	4-(2-hydroxyethyl)-1-piperazineethanesulfonic acid
HFD	High fat diet
HLA-B	Major histocompatibility complex, class I, B
HOMAIR	Homeostasis model assessment of insulin resistance
HRP	Horseradish peroxidase
HSC	Hematopoietic stem cell
HU	Hounsfield unit
HZ	Hypertrophic zone
iBF	Interscapular brown fat

Ibsp	Bone sialoprotein (gene)
Icam	Intercellular adhesion molecule
IFN-γ	Interferon gamma
IGF-1	Insulin like growth factor – 1
IgG	Immunoglobulin G
IHC	Immunohistochemistry
Ihh	Indian hedgehog
InsR	Insulin receptor
IPA	Ingenuity pathway analysis
IRS	Insulin receptor substrate
ITT	Insulin tolerance test
LC	Liquid chromatography
LRP	Low-density lipoprotein receptors
LTW	Live tissue weight
Lum	Lumican
MAPK	Mitogen-activated protein kinase
MAR	Mineral apposition rate
MCP-1	Monocyte chemo-attractant protein-1
MEPE	Matrix extracellular phosphoglycoprotein
MF	Mesenteric Fat
MGP	Matrix gla protein
miRNA	Micro ribonucleic acid
MMCRI	Maine Medical Center Research Institute
MMP	Matrix metalloproteinase
MOPS	3-(N-morpholino)propanesulfonic acid
Mpeg1	Macrophage expressed gene 1
Mrc1	Mannose receptor, C Type 1
MRI	Magnetic resonance imaging
mRNA	Messenger ribonucleic acid
MS	Mass spectrometry
MSC	Mesenchymal stem cells
Msx2	Homeobox protein Hox-8
MV	Matrix vesicle
NAFLD	Non-alcoholic fatty liver disease
NASH	Non-alcoholic steatohepatits
NBF	Neutral buffered formalin
NCP	Non-collagenous protein
NF-kB	Nuclear factor-Kappa B
NFW	Nuclease free water
NHS	National Health Service
NMR	Nuclear magnetic resonance
nSMase2	Neutral sphingomyelinase 2
OA	Osteoarthritis
OCN	Osteocalcin
OCT	Optimal cutting temperature

ON	Osteonectin
OPG	Osteoprotegerin
OPN	Osteopontin
OST-PTP	Osteotesticular protein tyrosine phosphatase
Osx	Osterix
P_2	Purinergic receptor
PBS	Phosphate buffered solution
P-Cho	Phosphocholine
Pck1	Phosphoenolpyruvate carboxykinase 1
PCR	Polymerase chain reaction
PEA	Phosphoethanolamine
PFA	Paraformaldehyde
Pgc1	Peroxisome proliferator-activated receptor gamma, coactivator 1
PHOSPHO1	Phosphatase, Orphan 1
P_i	Inorganic phosphate
PiT	phosphate transporter 1
PlGF	Placental growth factor
PNPLA3	Patatin-like phospholipase domain-containing 3
PPAR	Peroxisome proliferator-activated receptor
PP_i	Inorganic pyrophosphate
PRDM16	PR domain containing 1
Prkaa1	Protein kinase, AMP-activated, alpha 1 catalytic subunit
PTHrP	Parathyroid hormone-related protein
PVA	Polyvinyl acetate
PZ	Proliferative zone
qPCR	Quantitative PCR
RANKL	Receptor for activation of nuclear factor kappa B ligand
RER	Respiratory exchange ratio
RIPA	Radio-immunoprecipitation assay
RNA	Ribonucleic acid
RNase	Ribonuclease
RT	Reverse transcription
Runx2	Runt-related transcription factor 2
SB	Subcutaneous fat
SDS	Sodium dodecyl sulphate
SEM	Standard error of the mean
Sglt	Sodium coupled glucose transporters
SIBLING	Small integrin-binding ligand N-linked glycoprotein
Slc	Solute carrier family
SMI	Structural model index
SMPD3	Sphingomyelin phosphodiesterase 3
SMURF	Smad ubiquitin regulatory factors
SNS	Sympathetic nervous system
SPARC	Secreted protein acidic and rich in cysteine

Spic	Spi-C transcription factor
Spp1	Secreted phosphoprotein 1
SRUC	Scotland's Rural College
STAR	Sheep tomogram analysis routines
STAT	Signal transducer and activator of transcription
TAE	Tris-actetic acid- ethylenediaminetetraacetic acid
TBE	Tris-borate-EDTA
TBS	Tris-buffered saline
TBS/T	Tris-buffered saline/Tween-20
TCRIG1	T cell, immune regulator 1, ATPase, H+ transporting, lysosomal V0 protein A3
TE	Echo Time
TEM	Transmission electron microscopy
TGF-β	Transforming growth factor beta
TNAP	Tissue-nonspecific alkaline phosphatase (gene)
TNF	Tumour necrosis factor
Tr. Sp.	Trabecular separation
Tr. Th.	Trabecular thickness
Tr.No.	Trabecular number
Tr.Pf	Trabecular pattern formation
TR	Repetition time
TRAP	Tartrate-resistant acid phosphatase
TV	Tissue volume
TW	Total Weight
Twist 2	Twist basic helix-loop-helix transcription factor
UCP	Uncoupling protein
UDP	Uridine diphosphate
UTP	Uridine triphosphate
VCO_2	Volume carbon dioxide
VDR	Vitamin D receptor
VEGF	Vascular endothelial growth factor
VIP	Vasoactive intestinal peptide
VO_2	Volume oxygen
WAT	White adipose tissue
WNT	Wingless
WT	Wild-type
XLH	X-linked hypophosphatemic rickets

Table of Contents

Chapter 1: Background

Chapter 2: Materials and Methods

Chapter 4: Characterising the *Phospho1* knock-out mouse metabolic phenotype

Chapter 5: Evaluating fat deposition and localisation

List of Figures

List of Tables

Chapter 1

Introduction

Preface

Traditionally the skeleton has been viewed as an inert structural organ essential for locomotion, ion homeostasis and maintenance of the hematopoietic niche. However, in the last decade, bone has been identified as a true endocrine organ, possessing the capabilities to regulate both energy metabolism and reproduction. These recent advances expand our understanding and identify a new and unconventional role of bone beyond its classical functions. However, much is still to be learned. This thesis will investigate the role of Phosphatase, Orphan 1 (PHOSPHO1) in energy metabolism. The bone specific phosphatase, PHOSPHO1 has a well-established role in bone mineralisation and excitingly preliminary data suggested that PHOSPHO1 may be involved in the regulation of global energy metabolism. Understanding the mechanisms in which bone specific proteins can influence whole body homeostasis is essential to identify potential therapeutic targets beyond the well accepted and reported candidates. It should be noted that sections of this introduction are based on the published review by Oldknow *et al*., highlighting the endocrine roles of bone (Oldknow *et al.*, 2015).

1.1 Skeleton form and function

The vertebrate skeleton is one of the largest mammalian organs, providing the framework of the body, supporting the softer tissues and creating points of attachment for most skeletal muscles. In addition, the skeleton provides protection for vital organs and blood cells, assists in movement and acts as a storage system for minerals, namely calcium and phosphorus, in order to repair micro-damage and participate in fracture healing, thus maintaining a high bone quality adequate to fulfil its major functions.

The structure of bone is adapted to its function. Bone is a composite material composed of living cells enmeshed in a mineralised collagenous matrix. These collagen fibres enable the bone to withstand torsion and tension, whereas the

inorganic mineral provides strength and resists compression (Fig. 1.1) (Farquharson, 2008).

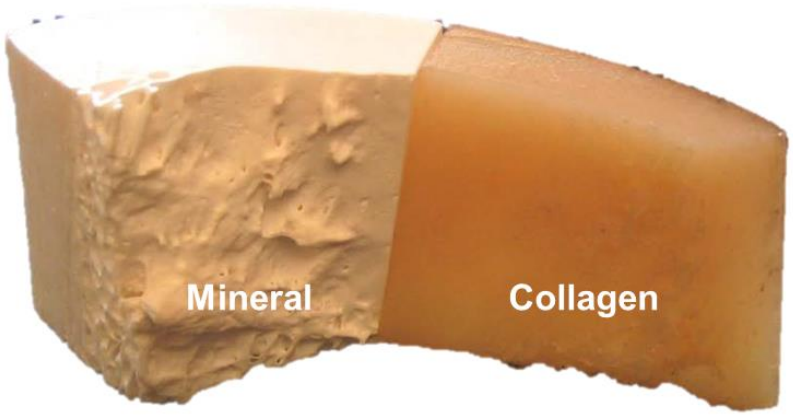

Figure 1.1 Bone as a composite material
Bone explant treated with hypochlorite (left) to digest collagen, leaving the mineral component intact and hydrochloric acid (right) to dissolve mineral, leaving the collagen component intact. With kind permission from Tim Arnett.

Bone is organised into two distinct structures, cortical (compact) and trabecular (cancellous). Cortical bone accounts for 80% of the total skeletal mass, primarily located in the shaft of the long bones (diaphysis) surrounding the medullary cavity. Cortical bone is highly organised; osteons, the chief structural unit of cortical bone consists of concentric lamellae organised in Haversian systems, resulting in a highly dense, poorly porous (2-5%) material. Central to the Haversian system is the Haversian canal. This canal contains blood vessels, connective tissues, nerve fibres and lymphatic vessels that supply osteocytes and nerves, this system proves advantageous when bone is subjected to high tensile forces from contracting muscles (Sommerfeldt and Rubin, 2001)(Fig 1.2). Unlike cortical bone, trabecular bone does not contain a Haversian system. As an alternative, trabeculae, accounting for 20% of the bone mass, form the functional units of trabecular bone. Arranged in a highly organised three dimensional manner, trabeculae provide continuous units of bony tissue aligned in parallel with the lines of major compressive or tensile forces. Accordingly, trabecular bone is less dense and more elastic than cortical bone, possessing 10 times the surface area of cortical bone. Due to this arrangement,

trabecular bone is more porous (30-90%) and has a higher bone turnover than cortical bone (Fig. 1.2).

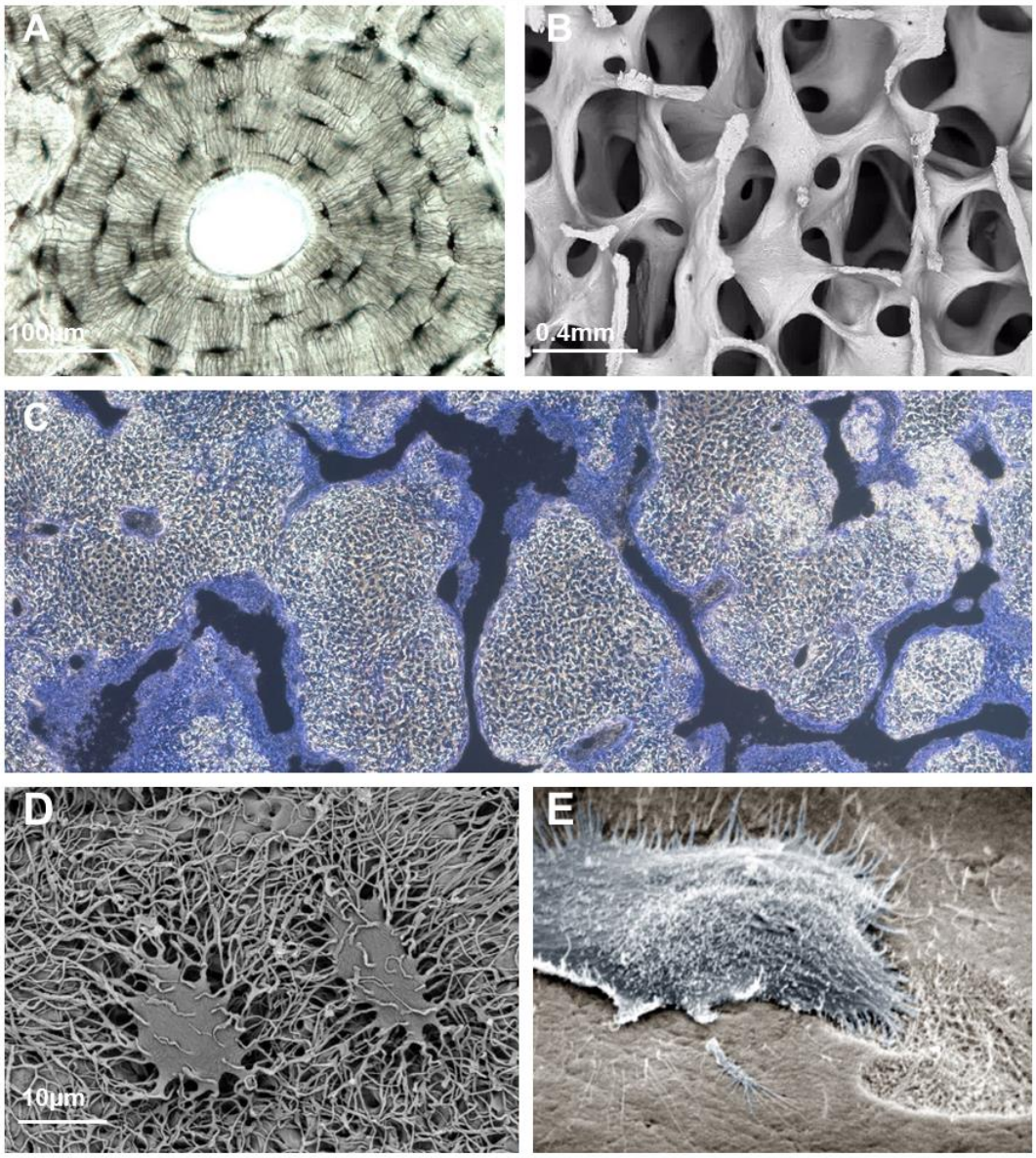

Figure 1.2 The bone structure and bone cells
The bone consists of two structures, cortical and trabecular bone. **(A)** Cortical bone with a central Haversian canal. Osteocytes are visible, present in the concentric layers of bone matrix. **(B)** Low power scanning electron microscope image showing normal bone architecture in the third lumbar vertebra of a 30 year old woman. Strong, interconnected plates of trabecular bone are visible allowing the bone to withstand compressive forces. **(C)** Mineralisation of osteoblast cells *in vitro*. **(D)** Scanning electron microscope image of osteocytes organised in functional syncytia collectively referred to as the osteocytic lacunar–canalicular system. **(E)** *S*canning electron micrograph showing an osteoclast resorbing bone. Images provided from the Bone Research Society, by kind permission of (A,C,E) Tim Arnett (B) Alan Boyde (D) Kevin Mackenzie.

1.2 Embryonic bone formation

Skeletal development involves the growth, expansion and remodelling of the bony structure. During development, bone is formed from three distinct cell lineages: the neural crest, paraxial mesoderm, and lateral plate mesoderm, which form the flat bones of the jaw and skull, vertebral column and appendicular skeleton respectively. Two mechanisms of bone formation (ossification) exist: endochondral and intramembranous, which are dependent upon a complex assimilation of biochemical and morphological events.

1.2.1 Intramembranous ossification

Intramembranous ossification is responsible for the formation of the frontal and parietal bone of the skull, mandible, maxilla and the periosteum of long bones. Ossification commences with mesenchymal condensations that secrete the early extra cellular matrix (ECM) and collagen concomitantly with mesenchymal cells that form a membrane of osteoprogenitor cells that differentiate into osteoblasts and osteocytes, secreting bone matrix resulting in the formation of spicules that fuse into trabeculae constituting primary bone (Samuelson, 2007). There is no intermediate cartilage template formed during the process of intramembranous ossification.

1.2.2 Endochondral ossification

Endochondral bone formation begins as a cartilaginous anlage and is observed during formation of long bones, such as those of the limbs. Long bones of the skeleton develop from limb buds comprised of an aggregate of undifferentiated mesenchymal cells (precartilage condensations). Upon differentiation into chondrocytes, cells secrete ECM forming the cartilaginous template of the bone; simultaneously the perichondral sheath is formed from mesenchymal cells at the periphery of the template. Proliferating chondrocytes within the cartilaginous template hypertrophy, concomitant with this, perichondral cells around the mid diaphyseal region of the cartilage model differentiate into osteoblasts and lay down

the supportive bony collar which is infiltrated by blood vessels transporting cells / elements that will form the bone marrow and osteoclasts. Osteoclasts resorb the cartilage template forming the primary ossification centre. Osteoblasts secrete bone matrix forming lamellar bone. Finally, the secondary ossification centre forms in the epiphyseal region of the cartilage, and a highly specialised epiphyseal growth plate forms between the two ossification centres.

The growth plate is essential postnataly, allowing the bone to grow in a longitudinal manner. The growth plate comprises chondrocytes arranged in columns that are parallel to the axis of the bone, and surrounded by their ECM (consisting of collagens, proteoglycans and numerous other non-collagenous proteins (NCP) (Gentili and Cancedda, 2009; Heinegard, 2009) (Fig. 1.3). Specifically, endochondral bone growth is characterised by the precise temporal and spatial organisation of chondrocytes (section 1.4) within the epiphyseal growth plate. These chondrocytes sit in distinct cellular zones of maturation, separated by longitudinal and transverse septa. The cells of each region can be distinguished by differences in their rate of proliferation and morphology. Chondrocytes proceed through these stages of differentiation whilst maintaining their spatially fixed locations (Hunziker *et al.* 1987). Resting chondrocytes and undifferentiated progenitors are situated in the resting zone located at the top of the growth plate, nearest the epiphysis, these cells progress through to the proliferating zone where they become proliferative and adopt a flattened and oblate shape; arranging themselves spatially into longitudinal columns (Hunziker *et al.*, 1987). Following the cessation of cell division, chondrocytes enter the hypertrophic zone, undergoing phenotypic changes. In brief, the cells become spherical and their volume increases approximately 10 times larger than that of the proliferative chondrocytes with increases in endoplasmic reticulum and Golgi apparatus, thus increasing matrix production. Associated with this hypertrophic phenotype is the increase in tissue non-specific alkaline phosphatase (TNAP) activity and expression of collagen type X, chondrocalcin, osteonectin (ON) and osteopontin (OPN) and decreased expression of collagen type II (early

chondrocyte marker), indicative of the final maturation phase (Buckwalter *et al.* 1986; Hunziker *et al.* 1987; Farnum *et al.* 2002). Finally, mineralisation of the ECM surrounding the hypertrophic chondrocytes of the longitudinal septa occurs allowing vascular invasion. This invasion facilitates the resorption of the transverse septa via osteoclast migration, allowing osteoblasts to replace this degraded cartilage with a bone matrix forming the primary spongiosa (Mackie *et al.* 2011). Upon sexual maturity, the primary and secondary ossification centres meet, fusion occurs and longitudinal bone growth ceases (Fig.1.3). Interestingly, in mice the growth plate never closes

1.2.3 Appositional bone growth

In addition to intramembranous and endochondral bone formation it is also important to address appositional bone growth. Appositional bone growth is the formation of new bone on the outer surfaces of existing bone to increase its width; necessary to allow the bone to withstand increasing loading pressures by increasing the cross sectional moment of inertia. Osteoblasts situated on the periosteum deposit bone in successive laminae, whilst osteoclasts resorb bone on the endosteal surface, resulting in a net increase in bone mass and marrow cavity diameter. Upon the termination of appositional growth, the periosteum is responsible for the maintenance of the bone surface (Farquharson, 2008).

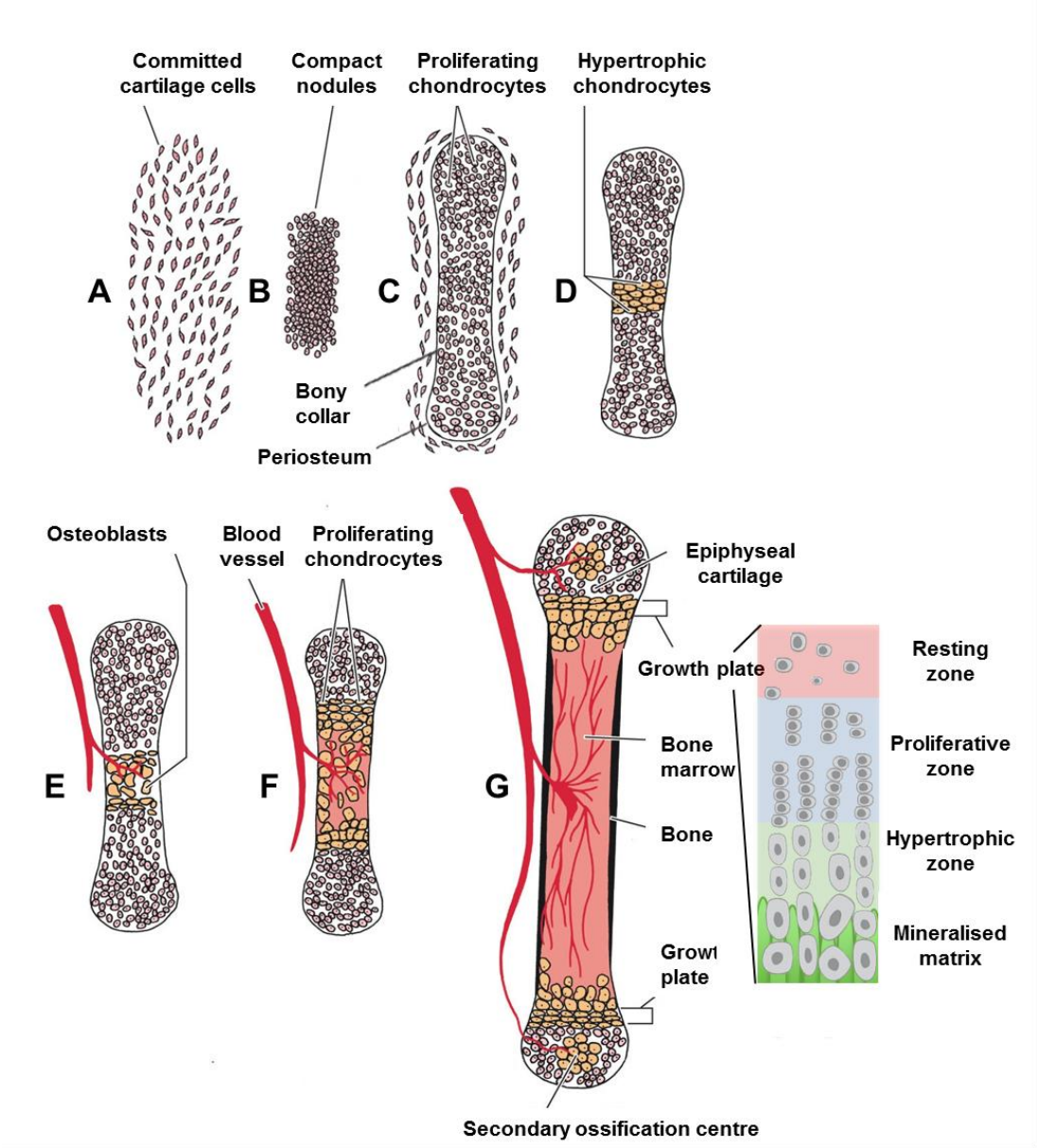

Figure 1.3 Endochondral ossification

Stages of endochondral ossification. **(A)** Mesenchymal stem cells **(B)** condense and aggregate to form the cartilage anlagen**. (C)** Pre-chondrocytes differentiate into chondrocytes and secrete ECM. The formation of a supportive bony collar is initiated. **(D)** Chondrocytes in the centre become hypertrophic and mineralise their surrounding matrix. **(E)** Invasion of the anlagen by blood vessels allows the infiltration of osteoblasts and osteoclasts leading to the formation of the primary ossification centre. **(F)** The primary ossification centre expands towards the epiphysis. **(G)** A secondary ossification centre and growth plate develops in the epiphysis. The epiphyseal growth plate is organised into distinct zones of the growth plate; the resting, proliferating, and hypertrophic zone, functioning until the point in which the two ossification centres fuse and growth ceases. Adapted from (Gilbert, 2006).

1.3 The process of bone remodelling and modelling

Bone remodelling is a biphasic process occurring throughout life in a constant and balanced manner, responsible for bone maintenance during adulthood, demonstrating a true homeostatic function. Bone remodelling is fully dependent upon the actions of two antagonistic cell populations: the osteoblasts and osteoclasts. The primary function of mesenchyme-derived osteoblasts is to deposit bone matrix that subsequently becomes mineralised (section 1.5). Conversely, the haematopoietic-tissue-derived osteoclasts are a unique cell type possessing the capability to destroy the host tissue by reabsorbing mineralised bone matrix (Rodan and Martin, 2000; Teitelbaum, 2000; Harada and Rodan, 2003; Teitelbaum and Ross, 2003; Karsenty, 2006). The misregulation of bone remodelling inevitably results in bone loss and disease, the most common, by far, is osteoporosis. These concepts will be discussed in greater detail hereafter.

Bone modelling differs from bone remodelling as bone resorption and formation occur on separate surfaces resulting in changes in the bone micro-structure (Frost, 1990) The process of bone modelling, unlike remodelling occurs from birth to adulthood and is responsible for adapting structure to loading by changing bone size and shape and removes damage thus maintaining bone strength (Seeman, 2009).

1.3.1 Osteoblasts

Constituting approximately 5% of all bone cells, osteoblasts are specialised 'bone building' cells, originating from pluripotent mesenchymal stem cells (MSC's) (Fig. 1.2 C). In addition to osteoblasts, MSC's are capable of differentiating into chondrocytes, adipocytes, fibroblasts, myoblasts and stromal cells; however, commitment of MSCs to these lineages is dependent upon the coordinated expression and activation of a number of transcription factors and cytokines including runt-related transcription factor 2 (Runx2), Osterix (Osx), Wnt, Transforming growth factor beta (TGFβ), β-catenin and bone morphogenetic

proteins (BMPs) (Table 1.1) (Ducy *et al.*, 2000b; Manolagas, 2000). Required at each stage of bone development, and throughout the remodelling process, osteoblasts are cuboidal in shape and contain abundant mitochondria, Golgi apparatus, ribosomes and endoplasmic reticulum, all characteristic of secretory cells (Dudley and Spiro, 1961). Ideally situated on the bone surface, the osteoblasts primary function is to synthesise bone matrix, termed the osteoid, predominantly consisting of collagen (94%) in addition to proteoglycans and other NCPs. Following matrix deposition and mineralisation, the osteoblast either remains on the surface of the bone as inactive lining cells, undergoes apoptosis, or becomes entombed by their secreted matrix and differentiate into osteocytes (section 1.3.3) (Dallas and Bonewald, 2010).

1.3.2 Osteoclasts

Osteoclasts act in a synchronised manner with osteoblasts, however, having opposite roles. Osteoclasts are responsible for the resorption of mineralised bone and together with the osteoblasts they regulate remodelling of bone tissue. Derived from the hematopoietic lineage, osteoclastogenesis is stimulated by factors such as macrophage colony-stimulating factor, and receptor for activation of receptor activator of nuclear factor kappa B ligand (RANKL) requiring contact with osteoblasts and stromal cells (Sommerfeldt and Rubin, 2001). Osteoclasts are multinucleated, rich in lysosomes, migratory giant cells. They have numerous mitochondria and a well-developed Golgi apparatus. Osteoclasts reside on the bone surface, ideally located for their function, where upon maturation osteoclasts become polarised and form a ruffled border that allows the osteoclast to attach to the bone surface forming a microenvironment which is key to the resorptive event. This compartment, isolated from the general extracellular space becomes acidified by an electrogenic proton pump, the Cl^- channel and secretion of acid proteases. The formation of the acid milieu (pH 4.5) mobilises the mineralised component of bone, exposing the organic matrix, mainly type 1 collagen that is degraded by the lysosomal enzyme cathepsin K. Furthermore, the secreted enzymes, tartrate-resistant acid phosphatase (TRAP) and matrix metalloproteinase (MMP) are also

responsible for the breakdown of the ECM. Diminished functions of osteoclast function in animals and human results in an excess of bone mass (osteopetrosis or pyknodysostosis). Conversely, increased activity or an imbalance between bone formation and resorption leads to bone loss and osteoporosis. Osteoclasts are known to be regulated in an endocrine manner e.g. through the secretion of calcitonin from the thyroid and parathyroid hormone (PTH) from the parathyroid gland (Samuelson, 2007; M. Lyons, 2013).

1.3.3 Osteocytes

Osteocytes are regarded as terminally differentiated osteoblasts and are the most abundant cell type, constituting over ninety percent of the cells in bone. It was previously thought that the osteoblast was the dynamic cell and upon maturation into an osteocyte, the cell became quiescent. However, it is now becoming clear that the osteocyte is also an important regulator of bone mass and a key endocrine regulator of phosphate metabolism (Dallas and Bonewald, 2010).

Osteocytes reside in lacunae and are immobilised in mature bone, they possess extensive filopodia, cellular processes that extend to adjacent osteocytes within canaliculi, allowing the passage of nutrients and metabolites. Gap junctions present between processes from different cells allow the osteocytes to form a functional network, communicating with osteoblasts and osteoclasts situated at the periosteum and endosteum. Ideally positioned within the bone matrix, osteocytes sense mechanical strain and translate that strain into biochemical signals of resorption or formation related to the intensity and distribution of the strain signals (Lanyon 1993). Osteocytes are also central to the regulation of system phosphate homeostasis and coordinate bone mineralisation with fibroblast growth factor 23 (FGF23) production and renal phosphate handling (Bonewald and Wacker, 2013). Furthermore, studies have highlighted that osteocytes and not osteoblasts or osteoblast progenitors are the major source of the osteoclastogenic cytokine receptor activator of nuclear factor kappa B (NF-kB), RANKL and the decoy receptor,

osteoprotegerin (OPG) (Nakashima *et al.*, 2011; Xiong *et al.*, 2011; Wysolmerski, 2012).

Molecule	Function	*In vivo* and *in vitro* effects
BMP2	Osteogenic factor	Osteochondrogenic factor; might initiate bone formation and bone healing and can induce expression of other BMPs.
BMP4	Osteogenic factor	Osteochondrogenic factor *in vivo* and *in vitro*.
BMP7	Osteogenic factor	Osteogenic factor in vivo and *in vitro*; active on more mature osteoblasts.
Dlx5	Osteogenic homeobox protein	Induces osteoblast maturation but inhibits osteocyte formation.
FGF	Angiogenic and mitogenic factor, osteogenic factor (controversial)	Mutations induce chondrodysplasia and craniosynostosis; can stimulate Sox9; might be a negative regulator of postnatal bone growth and remodelling.
IGF-I, II	Mitogenic factors, osteogenic factors	Stimulates growth plate formation, endochondrate ossification and bone formation by osteoblasts.
Ihh	Osteochondrogenic factor	Pivotal role for growth plate and endochondral formation; can inhibit osteoblast differentiation; might induce PTHrP expression.
MAPKs	Transduce osteogenic signalling by phosphorylation	Crucial for regulation of intracellular signalling induced by osteogenic factors (still remains controversial).
Msx2	Osteogenic homeobox protein	Induces proliferation of immature cells.
NF-kB	Inflammation transducer factor, inhibits osteogenesis	Inhibits the differentiation of MSCs and committed osteoblastic cells.
Noggin	BMP2, 4 and 7 specific inhibitor	Suppresses osteoblastic differentiation.
OPG	Decoy receptor of RANKL, inhibition of RANKL	Strongly inhibits bone resorption and has a pivotal role in bone remodelling.
Osterix	Late osteogenic transcription factor	Master regulator of late osteogenesis, inhibiting chondrogenesis.
PlGF	Angiogenic and vasculogenic factor	Induces proliferation and osteogenic differentiation of MSCs; crucial for vascularisation.
PTHrP	Osteochondrogenic factor	Pivotal role for growth plate and endochondral formation; can induce or inhibit osteogenesis.
RANKL	Induces osteoclastogenesis	Strongly stimulates bone resorption and has a pivotal role in bone remodelling.
Runx2	Early osteogenic transcription factor	Master regulator of early osteogenesis; *Runx2*$^{-/-}$ mice died, with no bone formation.
TGFβ	Mitogenic factor, osteogenic factor	Can induce osteoblast differentiation at the early stage of immature cells but can also inhibit osteogenesis in committed cells.
VEGF	Angiogenic and vasculogenic factor	Most potent angiogenic and vasculogenic factor; crucial at the onset of bone formation.
Wnt(s)	Mitogenic and osteogenic factors	Depending on Wnt type, crucial for osteoprogenitor proliferation; can also inhibit final osteoblast maturation.

Table 1.1 Molecules involved in bone formation
(Modified from (Deschaseaux *et al.*, 2009; Mohammad Hafiz *et al.*, 2010).

1.4 Chondrocytes and cartilage

Each cartilage subtype has a single cell type – the chondrocyte, which are referred to as chondroblasts during the initial production of 'ground material' and as they become less active they become chondrocytes, which are rounded in shape present in the central regions of hyaline and elastic cartilage and to a lesser extent in fibrocartilage. The role of chondrocytes in the process of endochondral bone growth is discussed in section 1.2.2. Cartilage is a specialised form of connective tissue that is neither innervated nor vascularised. Cartilage is subdivided into three types: hyaline or articular, elastic and fibrous or fibrocartilage. Hyaline cartilage is the most common type of cartilage occurring at most bone forming sites, joint surfaces of articulating bones and tracheal rings, functioning to disperse forces on joints caused by movement, form growth templates for pre- and post-natal long bone growth and is involved in fracture repair (Shum and Nuckolls, 2002). The ability of hyaline cartilage to withstand large compressive and tensile forces is due to the arrangement of the collagen type II fibres that are arranged in accordance with the stress placed on the body. Within articular cartilage collagen type II fibres form irregular bundles between the chondrocytes and near the surface they are orientated parallel to the surface. Elastic cartilage is found in the ear, larynx and epiglottis. Having a well-developed network of elastic fibres, elastic cartilage gives support to external structures. Finally fibrocartilage, the least common of the three forms, often associated with dense connective tissue and hyaline cartilage, aids in transferring loads between tendons and bone. Present at intervertebral disks and certain ligamentous and tendinous attachments to bones, fibrocartilage, is very similar to hyaline however type I collagen fibres predominate which form discrete bundles enabling cartilage to withstand large forces thus remaining resilient to deformation (Samuelson, 2007).

1.5 The mineralisation process

Bone predominantly consists of ECM, with approximately 70% (by weight) of this being inorganic. Of the inorganic matrix, calcium and inorganic phosphate (P_i) are

abundant. Derived from both nutritional sources and enzymatic activity, (e.g. P_i generation via TNAP and calcium via Vitamin D metabolites and PTH) calcium and phosphate form hydroxyapatite (HA) crystals ($Ca_{10}(PO_4)_6(OH)_2$), Hydroxyapatite crystals also contain other elements such as magnesium, sodium, potassium, copper, zinc and manganese. These HA crystals are arranged in an organised manner, deposited alongside and in close juxtaposition to type I collagen fibres in bone and within their gap regions and surrounded by aggrecan composites producing a hard but lightweight composite material (Millan, 2013). The proteoglycans within the amorphous aggrecan composites are instrumental in initiating and inhibiting bone mineralisation allowing water to contact HA crystals and ion exchange to occur. Glycoproteins such as osteocalcin (OCN) and OPN bind to HA crystals (section 1.5).

The mineralisation process occurs by a series of complex physio-chemical and biochemical processes that together facilitate the deposition of a solid phase HA (Houston *et al.*, 2004). Most simply, mineralisation is a two-step process (Fig 1.4):

1. De novo induction of mineral formation within the protective enclave of the matrix vesicles (MV) lumen (Anderson, 1995).
2. Propagation of induced mineral into the extravesicular matrix (Anderson *et al.*, 2005).

It is important to mention that although the formation of HA in cartilage is widely accepted to involve membrane-limited MV, an alternative mechanism is suggested to occur in bone termed collagen-mediated calcification, whereby collagen fibrils induce the deposition of apatite crystallites through a process of heterogeneous nucleation (Bonucci, 2012). Both mechanisms do however require the concentration of both calcium and phosphate to initiate HA formation.

1.5.1 The role of matrix vesicles

Matrix vesicles bud from distinct areas of the membrane on the surface of all mineralising cells. Within cartilage, MV's bud off from the hypertrophic chondrocyte plasma membrane whereas bone MV's are restricted to the freshly formed osteoid that is located at the basal plasma membrane of mineralising osteoblasts (Morris *et al.*, 1992). Within the MV lumen, calcium and P_i accumulate until sufficient amounts are present for precipitation to occur resulting in the formation of HA. Calcium accumulation is achieved by Ca^{2+} channels and the MV affinity for calcium binding lipids and proteins, whereas P_i accumulation remains highly controversial.

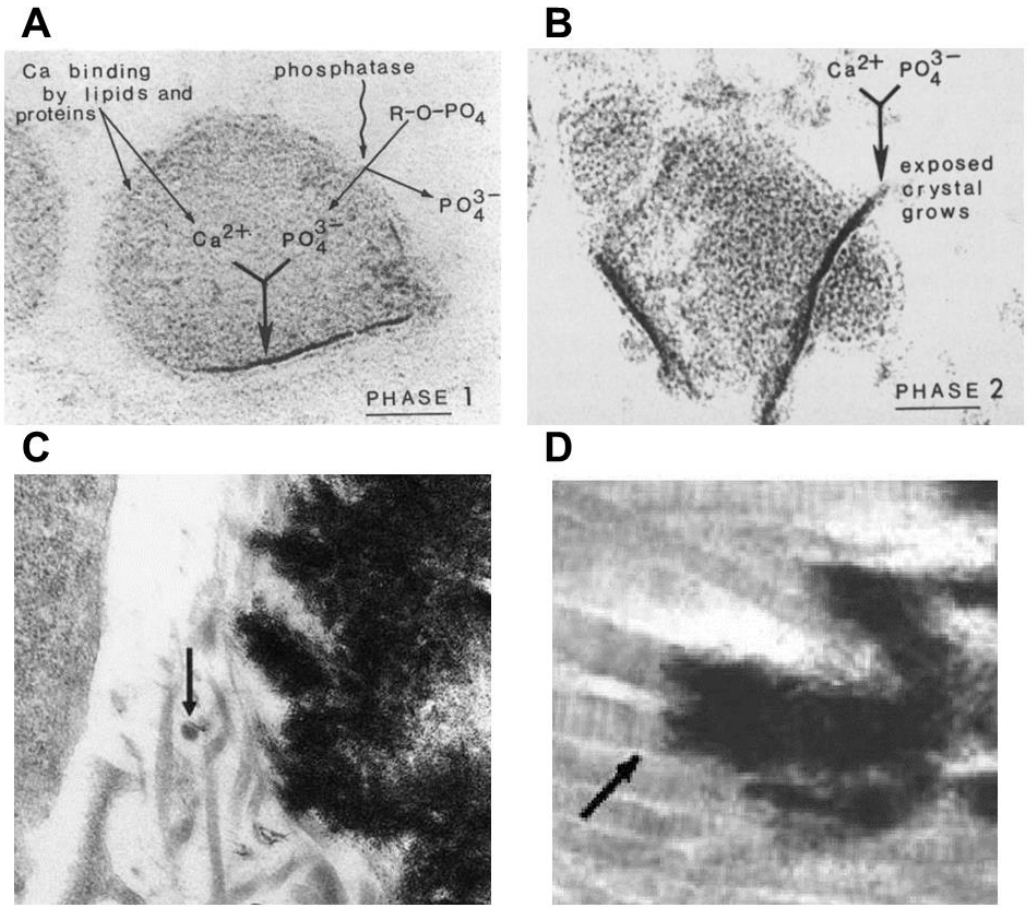

Figure 1.4 Mineral formation and alignment with collagen fibrils
(A) Accumulation of Calcium and P_i within the matrix vesicle instigating the formation of HA crystals within the protective enclave of the MV lumen **(B)** HA crystals grow in size and the pierce the MV membrane resulting in growth in the extravesicular matrix **(C)** Analysis of mineral in mice **(D)** Mineral is aligned with collagen fibrils of the ECM (Anderson, 1995; Millan, 2006).

1.5.2 The regulatory factors of matrix mineralisation

Traditionally, TNAP was solely recognised as the generator of high levels of P_i via its ATPase activity, however it was later observed that MV's from patients with hypophosphatasia (characterised by mutations in the TNAP gene - *Akp2*) contain apatite crystals, which is also observed in TNAP null (*Akp2*$^{-/-}$) mice. This observation therefore suggested that other phosphatases must work with TNAP to generate P_i and regulate matrix mineralisation. Following the identification of PHOSPHO1, this phosphatase has become recognised as an essential player in the bone mineralisation process.

1.5.2.1 PHOSPHO1

PHOSPHO1 is a bone specific phosphatase, identified over a decade ago at The Roslin Institute, University of Edinburgh (Houston *et al.*, 1999). Thereafter, work concentrated in characterising its role in bone mineralisation. More specifically, PHOSPHO1 is a member of the large family of the haloacid dehalogenase (HAD) superfamily of Mg^{2+} dependent hydrolases and its expression is upregulated in mineralising cells (Houston *et al.*, 1999; Roberts *et al.*, 2008). PHOSPHO1 shows high phosphohydrolase activity towards phosphoethanolamine (PEA) and phosphocholine (P-Cho) and is active inside chondrocyte and osteoblast derived MV's where it has been speculated to scavenge P_i from MV membrane phospholipids to favour intravesicular HA deposition (Stewart *et al.*, 2003; Roberts *et al.*, 2004; Stewart *et al.*, 2006; Roberts *et al.*, 2007).

Chemical inhibition of PHOSPHO1 by lansoprazole resulted in impaired skeletal mineralisation during limb development of the chick and markedly reducing mineralisation of the long bones of the leg and wings (MacRae *et al.*, 2010). Furthermore, genetic ablation of the *Phospho1* gene in mice resulted in significant skeletal pathology, spontaneous fractures, bowed long bones, osteomalacia, and scoliosis in early life (Fig. 1.5) (Huesa *et al.*, 2011; Yadav *et al.*, 2011). Curiously *Phospho1*$^{-/-}$ mice had reduced levels of TNAP and elevated pyrophosphate (PPi)

concentration (suppresses HA crystal formation and propagation and acts as a potent calcification inhibitor in biological fluids), however transgenic overexpression of TNAP did not correct the *Phospho1*$^{-/-}$ phenotype, despite correcting plasma PPi levels (Yadav MC, 2011). The superimposing haploinsufficiency of TNAP (*Akp2*$^{+/-}$) with *Phospho1*$^{-/-}$ caused a progressive worsening of the skeletal defects, whereas simultaneous ablation of *Phospho1* and *Akp2* results in the complete absence of skeletal mineralisation in the developing embryo and perinatal lethality. These data suggest that PHOSPHO1 and TNAP have complementary, non-redundant functional roles during skeletal mineralisation in the mouse (Yadav MC, 2011).

Using these models, a comprehensive paradigm of skeletal mineralisation was suggested, whereby PHOSPHO1 is responsible for intravesicular production of P_i and TNAP mediates extravesicular P_i transport into the MV, via phosphate transporter 1 (P_iT) (Yadav *et al.*, 2011; Millan, 2013).

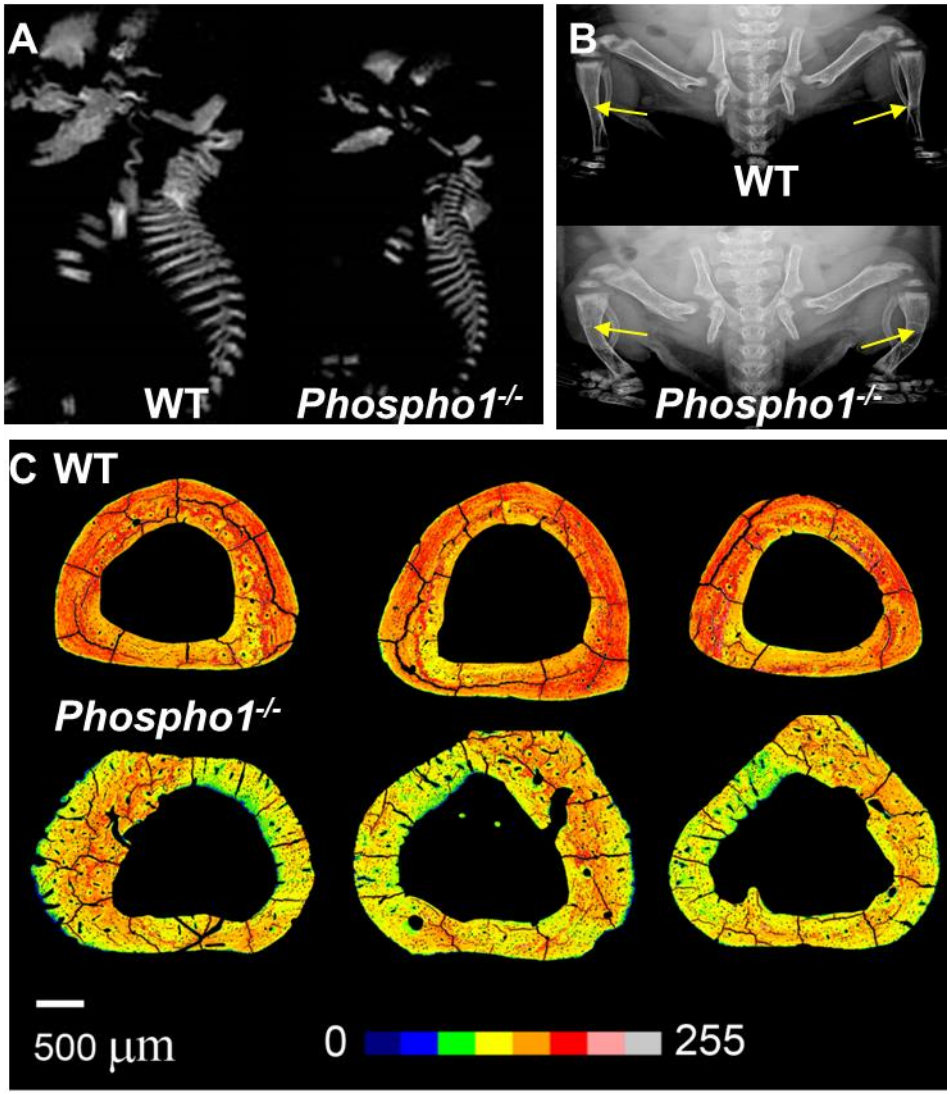

Figure 1.5. *Phospho1*$^{-/-}$ mouse bone phenotype
(A) Micro Computed tomography (µCT) image of a *Phospho1*$^{-/-}$ E16.5 shows reduced skeletal mineralisation compared with WT embryos **(B)** Radiographic images of WT and *Phospho1*$^{-/-}$ mice on postnatal days 10 and 25. *Phospho1*$^{-/-}$ mice show skeletal abnormalities including deformed long bones **(C)** Normalised backscattered electron intensity maps of tibial cross sections from non-mineralised (0, black) to high mineralisation (255, white). Bone matrix was hypomineralised in *Phospho1*$^{-/-}$ compared to WT (Yadav *et al.*, 2011) (Rodriguez-Florez *et al.*, 2015).

1.5.2.2 NPP1 & ANK

Ectonucleotide pyrophosphatase/phosphodiesterase 1 (NPP1) is the founding member of the NPP family. These glycoproteins have pleiotropic roles in hydrolysing phosphodiester or pyrophosphate bonds in various substrates, including nucleoside triphosphates, lysophospholipids and choline phosphate esters (Bollen *et al.*, 2000; Stefan *et al.*, 2005; Zimmermann *et al.*, 2012). Specifically, NPP1 forms disulphide-bonded homodimers and is highly expressed in the plasma membrane and mineral-depositing MV of osteoblasts (Johnson *et al.*, 1999; Vaingankar *et al.*, 2004; Terkeltaub, 2006). Mice lacking NPP1 (*Enpp1*$^{-/-}$) have severe mineralisation defects in long bones and calvariae, pathological soft tissue and medial arterial mineralisation associated with abnormally low pyrophosphate (PPi) levels (Anderson 2005; Mackenzie *et al.*, 2012a; Mackenzie *et al.*, 2012b; Oldknow *et al.*, 2015). Therefore NPP1 has been identified as a critical regulator of tissue mineralisation, hydrolysing nucleotides such as adenosine triphosphate into extracellular PPi (Terkeltaub, 2001). Ankylosis protein (ANK), whose expression is upregulated in osteoblasts and chondrocytes, mediates the channelling of the intracellularly produced PPi to traverse to the ECM (Hakim *et al.* 1984; Terkeltaub *et al.* 1994; Ho *et al.* 2000; Nurnberg *et al.* 2001). Mice lacking the ANK protein are characterised by pathological calcification of articular cartilage and the synovial fluid surrounding these regions (Fig. 1.6) (Hakim *et al.*, 1984).

1.5.2.3 Purinergic signalling

Purines can act as extra signalling molecules, and it is now accepted that extracellular nucleotides, signalling via P2 receptors, participate in a wide number of biological processes in both neuronal and non-neuronal tissues. P2 receptors existing in P2X ligand-gated ion channels and P2Y G-protein-coupled receptors respond to nucleotides including adenosine triphosphate (ATP), adenosine diphosphate (ADP), uridine triphosphate (UTP) and uridine diphosphate (UDP) (Burnstock and Kennedy, 1985; Abbracchio and Burnstock, 1994; Burnstock, 2007). Initial studies concerning purinergic signalling demonstrated that extracellular

nucleotides could induce increases in intracellular calcium in bone cells and inhibit bone formation whilst promoting bone resorption (Kumagai *et al.*, 1989; Kumagai *et al.*, 1991; Reimer and Dixon, 1992; Yu and Ferrier, 1993; Morrison *et al.*, 1998; Hoebertz *et al.*, 2002). New evidence suggests that ATP released from osteoblasts, stromal cells and osteocytes can act locally to inhibit bone mineralisation and stimulate osteoclast formation and activity (reviewed in (Orriss *et al.*, 2010). Specifically uridine-5'-triphosphate (UTP), the $P2Y_2$ receptor agonist strongly inhibits bone nodule formation, partly due to the decreased activity of TNAP (Hoebertz *et al.*, 2002; Orriss *et al.*, 2007). Moreover, osteoblasts have been shown to express P2X receptors, and P2X1 and P2X7 receptors within this class negatively regulate bone mineralisation (Orriss *et al.*, 2012). It has also been suggested that ATP released from osteocytes entombed in bone might help to prevent matrix mineralisation at the periphery of the osteocyte and prevent cell death (Orriss *et al.*, 2010).

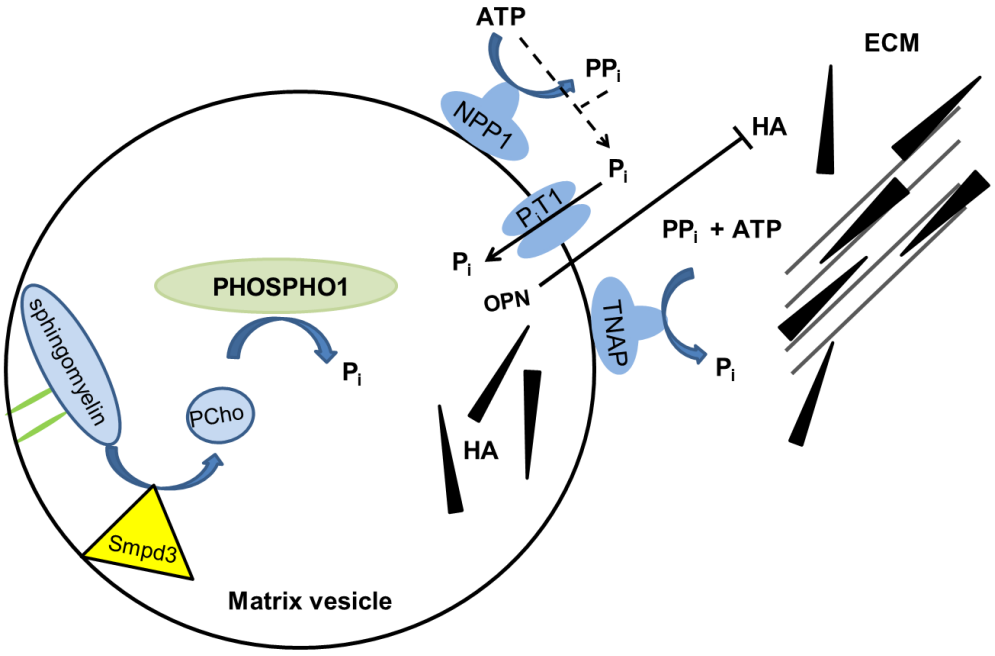

Figure 1.6 Model of initiation of skeletal mineralisation including the function of PHOSPHO1, TNAP, NPP1, and phosphate transporters.
The first step of MV-mediated mineralisation involves the convergence of two independent biochemical pathways **1)** intravesicular P_i generation by the enzymatic action of PHOSPHO1 hydrolysing P-Cho generated from sphingomyelin phosphodiesterase 3 (SMPD3). **2)** Influx of P_i via the P_it1 transporters, generated in the perivesicular space by the activities of TNAP and NPP1. OPN acts as a mineral inhibitor (Modified from (Zhou *et al.*, 2012; Millan, 2013).

1.5.2.4 Polyphosphate

Polyphosphates, predominantly located within nuclei, mitochondria and the plasma membrane, are long polymers of three to several hundred orthophosphates bound by energy-rich phosphoanhydride bonds (Kulaev, 1975; Kornberg, 1995; 1999). They have been implicated in phosphate storage (Harold, 1966), cation sequestration (Dunn *et al.*, 1994), counter-ion actions for basic amino acids (Cramer and Davis, 1984), regulation of intracellular adenylate nucleotides (Lorenz *et al.*, 1995) and modulation of cellular responses to stress (Lorenz *et al.*, 1997). Polyphosphates are found at high levels in osteoblast-like cells, and calcium/phosphate rich polyphosphate granules have been identified at sites of bone resorption and in calcified cartilage suggestive of an involvement of polyphosphates in matrix mineralisation (Casey *et al.*, 1972; Leyhausen *et al.*, 1998; Schroder *et al.*, 2000). Early studies showed that subcutaneous injection of polyphosphates inhibited ectopic calcification by direct binding to HA crystal thus halting crystal growth with equal or better potency than PP_i (Fleish and Neuman, 1961; Fleisch *et al.*, 1965; Francis, 1969). Most recently, in an osteoblast cell culture model polyphosphates (PolyP5 and PolyP65, polyphosphates of 5 and 65 phosphate residues in length) have been shown to be potent mineralisation inhibitors via direct binding to HA mineral crystals and by inhibition of TNAP activity (Hoac *et al.*, 2013).

1.5.2.5 SIBLING family of proteins

The small integrin binding ligand N-linked glycoprotein (SIBLING) family of proteins have been identified to be key in the regulation of HA crystal initiation and propagation. Comprising a structurally and phylogenetically homogeneous group of matricellular factors this family consists of OPN, bone sialoprotein (BSP), dentin sialophosphoprotein (DSPP), dentin matrix acidic phosphoprotein 1 (DMP1) and matrix extracellular phosphoglycoprotein (MEPE) (Malaval *et al.*, 2008). Briefly, OPN is secreted by both osteoblasts and osteoclasts and has been shown to inhibit the *in vitro* formation of HA (Hunter *et al.*, 1994). Supporting the role for OPN in mineralisation, mice lacking the OPN gene (*Spp1*$^{-/-}$) mice display a normal skeletal

phenotype, however have increased crystal size and crystallinity (Boskey *et al.*, 2002). Bone sialoprotein (BSP (encoded by the *Ibsp* gene)) is highly expressed by osteoblasts, hypertrophic chondrocytes and osteoclasts, acting as a local nucleator for HA production (Hunter *et al.*, 1994; Raynal *et al.*, 1996). Bone sialoprotein knockout mice (*Ibsp*$^{-/-}$) exhibit impaired bone growth and mineralisation, concomitant with dramatically reduced bone formation (Ganss *et al.*, 1999; Malaval *et al.*, 2008). First described in 1977, DSPP has since been shown to play a primary role in the formation and growth of HA crystals in an extracellular matrix of hard tissue such as bone and teeth (MacDougall *et al.*, 1997). The importance of DSPP in bio-mineralisation has been illustrated by human and mouse genetic studies, which showed the association of *Dspp* gene mutations or ablations with mineralisation defects in the dentin (Xiao *et al.*, 2001; Zhang *et al.*, 2001) and bone (Verdelis *et al.*, 2008). Current data suggests that BMP2, RUNX2, nuclear factor Y and DMP1 may be involved in the regulation of DSPP, however the exact molecular pathways governing the expression of DSPP are still poorly understood. Expression of DMP1 is primarily restricted to osteocyte however osteoblasts and hypertrophic chondrocytes also express DMP1 (Toyosawa *et al.*, 2001; Feng *et al.*, 2002). *In vitro*, DMP1 overexpression promotes ECM mineralisation, *in vivo Dmp1*$^{-/-}$ mice display significantly lower mineral content than control mice (Ling *et al.*, 2005). Furthermore, *Dmp1*$^{-/-}$ mice exhibit a dramatic increase in fibroblast growth factor 23 (*Fgf23*) expression in the osteocytes. Fibroblast growth factor 23 regulates kidney P_i homeostasis suggesting that DMP1 can indirectly control P_i levels via FGF23. These findings are consistent with the hypophosphatemia observed in the *Dmp1*$^{-/-}$ mice (Feng *et al.*, 2006). Similarly to DMP1, MEPE is primarily expressed by osteocytes however it is also expressed by osteoblasts (Nampei *et al.*, 2004). *In vitro*, during osteoblast matrix mineralisation *Mepe* mRNA expression is increased (Petersen *et al.*, 2000; Argiro *et al.*, 2001). *In vivo*, *Mepe*$^{-/-}$ mice had increased bone mass and were resistant to age associated trabecular bone loss. Furthermore, isolated osteoblasts produced significantly more mineralised nodules in *ex vivo* cell cultures than wild type (WT) osteoblasts, these mice also display a decrease in TNAP activity in the

growth plate and the primary spongiosa (Gowen *et al.*, 2003; David *et al.*, 2009a). The functional component of MEPE (acidic serine aspartate-rich MEPE-associated motif (ASARM) peptide), *in vitro* and *in vivo* has been shown *to* inhibit the uptake of P_i. (Liu *et al.*, 2007; Martin *et al.*, 2008; Shirley *et al.*, 2010). These data suggest that MEPE is involved in both bone mineralisation and P_i homoeostasis, however the pathways still remain somewhat elusive (Staines *et al.*, 2012).

1.5.2.6 Secreted protein acidic and rich in cysteine (SPARC)

Secreted protein acidic and rich in cysteine (SPARC) alternatively known as osteonection (ON) or BM-40, is a bone matrix non-collagenous calcium binding matricellular glycoprotein that is involved with, but not restricted to, tissue remodelling, repair, cell turnover and bone mineralisation and is secreted by many different types of cells, such as osteoblasts, fibroblasts, endothelial cells, and platelets (Termine *et al.*, 1981; Brekken and Sage, 2000; Alford and Hankenson, 2006). Its precise function in bone remains unclear, *in vitro* ON has the ability to inhibit HA crystal growth (Romberg *et al*, 1986). Osteonectin-deficient (*Sparc*$^{-/-}$) mice exhibit decreased bone formation, remodelling and osteopenia, due to a negative bone balance resulting from decreased osteoblast and osteoclast surface area and number. Furthermore, ON has been shown to be important for osteoblast formation, maturation, and survival (Delany *et al.*, 2000; Delany *et al.*, 2003).

1.5.2.7 SMPD3

Recent *in vitro* results have indicated that sphingolipids are implicated in osteoblast and chondrocyte apoptosis and in the regulation of osteoclastogenesis (Takeda *et al.*, 1998; MacRae *et al.*, 2006); reviewed by (Khavandgar and Murshed, 2015). *In vivo*, sphingolipid metabolism plays a critical role in skeletogenesis. Mouse models lacking the ceramide-generating neutral sphingomyelinase 2 enzyme (nSMase2/SMPD3 – gene-targeted *Smpd3*$^{-/-}$ and *fro/fro* mice (deletion mutation in *Smpd3* gene fragilitas ossium (fro))) display gross skeletal abnormalities, including deformed long bones, short-limb dwarfism, hypomineralisation, delayed dentin

mineralisation and enamel formation (Aubin *et al.*, 2005; Stoffel *et al.*, 2005; Alebrahim *et al.*, 2014). Conversely, the overexpression of *Smpd3* in osteoblasts only (*fro/fro*;Col1a1–*Smpd3* mice) corrects embryonic bone abnormalities, demonstrating a direct role of SMPD3 in skeletal mineralisation (Khavandgar *et al.*, 2011; Khavandgar *et al.*, 2013). However, the mechanisms underlying this role, while remaining unclear, are now becoming a little less hazy. It has now been proposed that SMPD3 hydrolyses sphingomyelin to P-Cho (Stoffel *et al.*, 2005), which is subsequently hydrolysed into choline and phosphate by the bone-specific phosphatase, PHOSPHO1 (Fig. 1.6) (McKee *et al.*, 2013). As described in section 1.5.2, ablation of *Phospho1* in mice results in a similar phenotype to that of *fro/fro* mice, with *Phospho1*$^{-/-}$ mice having significant skeletal pathology (Huesa *et al.*, 2011; Yadav *et al.*, 2011; Rodriguez-Florez *et al.*, 2015). These results suggest that PHOSPHO1 and SMPD3 are functional within the same metabolic pathway required for skeletal mineralisation in the mouse (Khavandgar, Oldknow, Murshed & Farquharson, unpublished observations). Interestingly, both *Phospho1* and *Smpd3* deficient models exhibit decreased body size, indicating that, in addition to the *de novo* pathway, the sphingomyelinase pathway may have the potential to regulate energy metabolism (Chapter 6) (Stoffel *et al.*, 2005; Oldknow *et al.*, 2013).

1.5.2.8 Vitamin K dependent proteins

Osteocalcin (OCN) or bone Gla-protein was isolated from bone over three decades ago by two independent groups (Hauschka *et al.*, 1975; Price *et al.*, 1976; Hauschka *et al.*, 1989b) and is the most abundant osteoblast-specific non-collagenous protein accounting for 10-20% of non-collagenous protein content (Hauschka *et al.*, 1989b). Named due to the presence of three vitamin K-dependent γ carboxyglutamic acid residues, OCN is a small protein (46 and 49 amino acids long in mice and humans respectively) initially synthesised in the osteoblast as a pre–pro molecule. Vitamin K-dependent post-translational modifications occur, causing three glutamic acid residues (GLU13, GLU17 and GLU20) to be γ carboxylated into carboxyglutamic acid (GLA) residues by a γ carboxylase. Final intracellular cleavages produce the

mature OCN, which is subsequently secreted (Hauschka *et al.*, 1989a). The presence of the three γ carboxyglutamic acid residues is critical for the structure and function of OCN in the fully carboxylated state allowing the binding of OCN to HA with a high affinity, regulating the maturation of bone mineral (Hauschka *et al.*, 1989b). In the fully carboxylated form, OCN is largely unstructured when calcium is not present, however in the presence of calcium the OCN protein becomes folded, allowing calcium sequestering thus inhibiting mineral formation and matrix mineralisation (Chenu *et al.*, 1994) . However, OCN also exists in the general circulation in fully carboxylated, partially carboxylated and completely uncarboxylated forms (Plantalech *et al.*, 1991; Cairns and Price, 1994; Vergnaud *et al.*, 1997; Schilling *et al.*, 2005). On the basis of results from human and rodent studies, serum OCN concentrations have been correlated with bone formation and osteoblast number, thus being used as a serum marker of bone formation (Brown *et al.*, 1984). To investigate the role of OCN in bone health, OCN-deficient mice (*Bglap3*$^{-/-}$) were generated and these mice were found to have a normal bone phenotype at birth but increased bone density and thickness at 6 months of age. This was due to the increased deposition of bone matrix without the impairment of bone resorption, thus OCN was concluded to be a negative regulator of bone formation (Ducy *et al.*, 1996; Wolf, 1996). Analogous to OCN, Matrix Gla protein (MGP) contains 5 vitamin K dependent GLA residues (Price and Williamson, 1985) and appreciably accumulates in the matrix of bone, cartilage, and dentin, functioning to promote the binding of HA through the affinity to calcium ions (Hale *et al.*, 1988). Despite this, OCN and MGP have non redundant and other unrelated functions. Mice that lack MGP are severely compromised and fatality is observed within two months of age as a result of arterial calcification which leads to blood-vessel rupture (Luo *et al.*, 1997). Mice also exhibit inappropriate calcification of the growth plate, which eventually leads to short stature, osteopenia and fractures (Luo *et al.*, 1997), thus MGP was concluded to inhibit calcification of arteries and cartilage. Interestingly expression of OCN at sites of ectopic mineralisation in MGP-deficient mice was not able to reverse the abnormal phenotype which is in contrast with the re-expression

of MGP at those same sites (Murshed *et al.*, 2004). Furthermore, overexpression of MGP in hypertrophic chondrocytes reduces their mineralisation potential (Newman *et al.*, 2001). However, the mode of action at the molecular level still remains somewhat elusive. Keutel syndrome, an autosomal recessive disease, is triggered by MGP loss of function mutations, and the disease is characterised by excessive cartilage (Cancela *et al.*, 1990; Munroe *et al.*, 1999; Cancela *et al.*, 2014).

1.6 Bone as an endocrine organ

Energy is required in all cells and organs, allowing biological processes to proceed; bone shows no exception to this rule. More specifically, bone is an energy-expensive organ due to the constant modelling and remodelling it undergoes. It is therefore logical to postulate that bone may have a means of regulating the flow/supply of energy storage to fulfil its metabolic needs. The initial realisation that leptin, an adipocyte-derived hormone inhibits both appetite (Flier and Elmquist, 1997; Friedman and Halaas, 1998) and bone mass accrual though a hypothalamic relay over a decade ago (Ducy *et al.*, 2000a), provided the basis for this potential link between bone remodelling and energy metabolism. Thereafter, a rapid expansion of evidence supporting this crosstalk has occurred, further elucidating the complex roles of leptin (Fig. 1.7) and identifying further adipocyte (adiponectin) and gut-derived hormones (glucagon-like peptides 1 and 2 and serotonin) that regulate bone mass, remodelling and energy homoeostasis. The revelation that bone itself regulates energy metabolism in a reciprocal manner via secreted OCN, which favours insulin secretion and insulin sensitivity and increased energy expenditure was uncovered several years ago (Lee *et al.*, 2007; Ferron *et al.*, 2010a; Rached *et al.*, 2010). Recently an explosion of avant-garde research has explored this concept, uncovering new and atypical roles of bone beyond its traditional functions. The field of bone and energy metabolism is therefore moving in at least 3 distinct but complementary directions:

I. How bone mass is controlled by the brain.

II. The role of insulin in the osteoblast.

III. Regulation of whole body energy metabolism by bone derived factors.

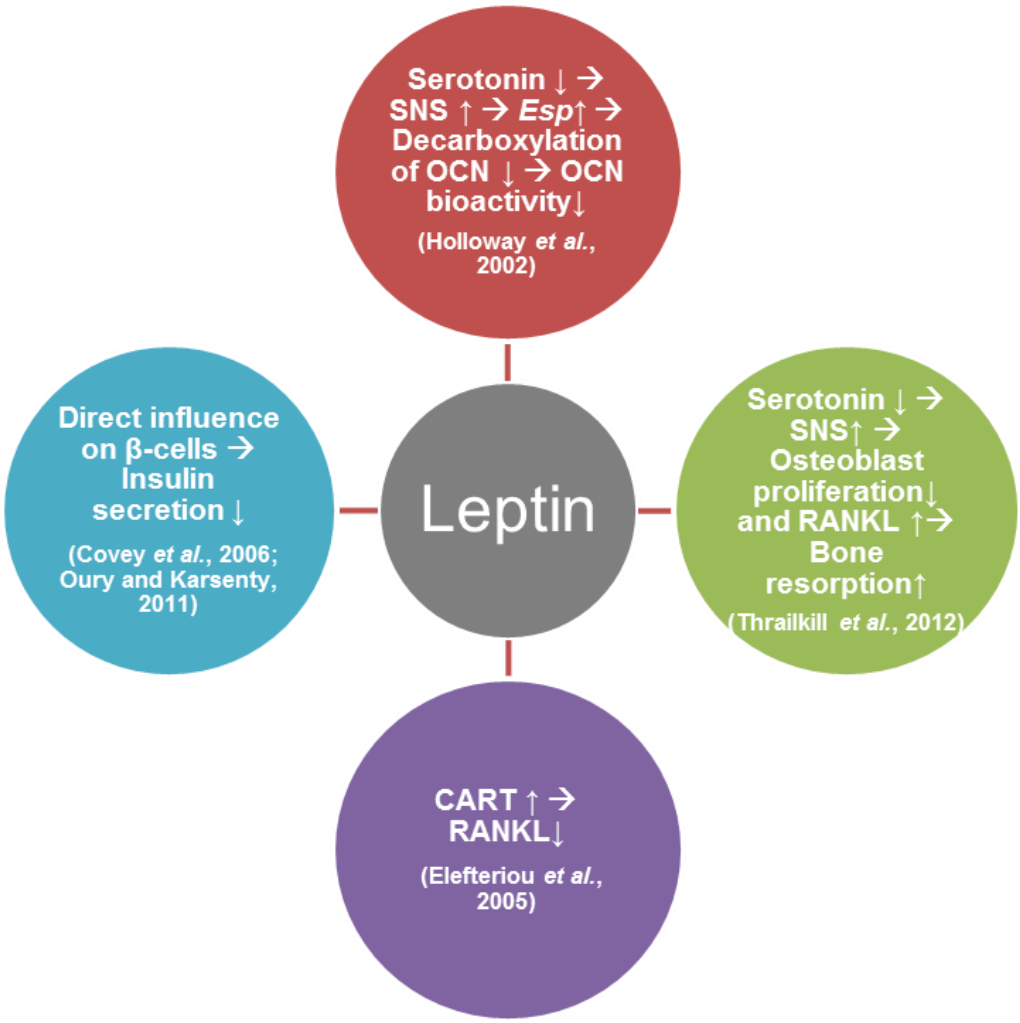

Figure 1.7. Bone related Functions of Leptin
↑ indicates up regulation or increase, ↓ indicates down-regulation or decrease, → Indicates results in.

1.6.1 The role of insulin in the osteoblast

Osteoblasts have very few specific genes, the most specific being *Bglap3* which codes for OCN (section 1.5.2.8). To investigate the role OCN in bone health, *Bglap3*$^{-/-}$ mice were generated, but surprisingly no major skeletal deformities were observed in these mice (Ducy *et al.*, 1996). In 2007, further phenotypic evaluation of these mice resulted in an unanticipated finding. OCN-deficient mice were hyperglycemic, hypoinsulinemic and had a reduced insulin secretion and sensitivity compared to the litter mate WT mice. Additionally, islet size, number, β cell mass, pancreas insulin content, and insulin immunoreactivity were all markedly decreased in *Bglap3*$^{-/-}$ mice. Moreover, *Bglap3*$^{-/-}$ mice had increased fat mass and adipocyte number, being insulin resistant in the liver, muscle, and white adipose (Table 1.2)(Lee *et al.*, 2007). In this same study the group took advantage of the small number of genes encoding secreted or signalling molecules that are expressed exclusively by the osteoblast in the hope to uncover further osteoblast-enriched genes affecting energy metabolism. One gene that was found to be of most interest was embryonic stem cell phosphatase (*Esp*), which is expressed by only two cell types, the osteoblast and the sertoli cells of the testis. Embryonic stem cell phosphatase encodes osteotesticular protein tyrosine phosphatase (OST-PTP) (Mauro *et al.*, 1994). *In vitro, Esp* coordinates the progression of the pre-osteoblast to a mature, mineralising cell, and *in vivo* may be a critical regulator of the commitment of mesenchymal cells to the ossification of new bones during skeletogenesis (Mauro *et al.*, 1994; Chengalvala *et al.*, 2001; Yunker *et al.*, 2004). However, it is well established, protein tyrosine phosphatases (PTPs) are key regulators of insulin receptor signalling (InsR) in many cell types dephosphorylating and inactivating the InsR within minutes of stimulation, maintaining glucose homeostasis (Mauro *et al.*, 1994; Hunter, 1995; Schlessinger, 2000; Tonks, 2006; Lee *et al.*, 2007). As a result, two mutant mice were created, a whole body knock out of *Esp* (Lee *et al.*, 1996) and an osteoblast specific knock down of the phosphatase domain of OST-PTP (Dacquin *et al.*, 2004). Both mutants exhibited severe hypoglycemia and hyperinsulinemia leading to postnatal lethality

in the first two weeks of life. Further analysis demonstrated the pancreas of *Esp*$^{-/-}$ had greater islet content, number of islets, islet size and β cell mass, resulting in increased insulin secretion. In addition, mutants were significantly more tolerant to glucose upon challenge, displaying an insulin sensitive phenotype (demonstrated by insulin tolerance testing), thus mice were protected from induced obesity and diabetes (Lee *et al.*, 2007; Ferron *et al.*, 2008). In parallel, mice overexpressing full-length *Esp* cDNA selectively in osteoblasts exhibited hyperglycemia, hypoinsulinemia, glucose intolerance, insulin resistance, decreased β cell proliferation, lower β cell mass, and impaired insulin secretion (Lee *et al.*, 2007). Subsequently, it was noted *Esp*$^{-/-}$ mice were a mirror image of *Bglap3*$^{-/-}$ mice, whilst the OST-PTP overexpressing mice were a phenocopy of *Bglap3*$^{-/-}$ mice. Further genetic studies revealed that the metabolic phenotype of *Esp*$^{-/-}$ mice was fully corrected by removing one allele of *Bglap3*, implying that *Esp*$^{-/-}$ mice are a model for a gain of function of OCN, providing solid evidence that OST-PTP and OCN reside in the same regulatory pathway (Lee *et al.*, 2007). Biochemical analysis revealed *Esp*$^{-/-}$ mice have significantly higher serum GLU13-OCN levels than WT controls, however, total *Ocn* gene expression and OCN serum levels was normal in *Esp*$^{-/-}$, suggestive that OST-PTP is involved in the decarboxylation of OCN and subsequent release of GLU13-OCN into the systemic circulation (Table 1.2) (Lee *et al.*, 2007; Ferron *et al.*, 2010b).

Notwithstanding, it still remained unclear how carboxylation status could regulate whole body energy metabolism. Clues came from several key studies concerning forkhead box protein O1 (FoxO1) and activating transcription factor 4 (ATF4). The transcription factor FoxO1 is targeted by insulin and regulates glucose homeostasis in tissues involved in energy metabolism including adipocytes and hepatocytes, yet its function in osteoblasts had not been explored until recently (Rached *et al.*, 2010). A *FoxO1* osteoblast conditional knockout mouse was generated, mice displayed decreased fasting blood glucose levels, increased insulin sensitivity and a 30% increase in serum OCN levels, coupled with a 75% reduction in *Esp* expression,

suggestive of an association between *Esp* and carboxylation status of OCN (Lee *et al.*, 2007). In the same study, it was demonstrated that mice lacking one allele of *FoxO1* and one allele of *Esp* in osteoblasts showed improved insulin sensitivity. Similarly, the metabolic phenotype was corrected in heterozygous mice lacking one allele of *FoxO1* in osteoblast by the removal of one allele of *Bglap.* Utilising these models to investigate the mechanisms underlying the phenotype, it was established that FoxO1 regulates the bioactivity of OCN via OST-PTP via direct binding to its promoter, reducing serum OCN (Rached *et al.*, 2010; Kousteni, 2011; 2012). Activating transcription factor 4 belongs to the subfamily of cAMP-response element-binding protein / ATF basic leucine zipper proteins broadly expressed throughout the body, however predominantly accumulates in osteoblast where it regulates virtually all functions of the osteoblast related to the control of bone mass including bone formation and matrix mineralisation (Yang and Karsenty, 2004; Elefteriou *et al.*, 2005; Yoshizawa *et al.*, 2009). Mice deficient in *Atf4* primarily show phenotypic abnormalities in the skeleton, however the global or osteoblast specific ablation of *Atf4* results in favourable metabolic changes, including improved glucose tolerance and insulin sensitivity associated with decreased *Esp* expression. Contrary, the overexpression of ATF4 in osteoblasts mirrored this phenotype, resulting in glucose intolerance associated with increased *Esp* expression. This effect was due to the direct regulation of *Esp* expression in osteoblasts by ATF4 which was established by a ChIP array confirming that ATF4 binds to the CRE element in the *Esp* promoter (Yoshizawa *et al.*, 2009). Finally, it has been shown that FoxO1 co-localises with ATF4 in the osteoblast nucleus, promoting the transcriptional activity of AFT4 thus up-regulating the expression of *Esp* in osteoblasts, resulting in OCN inactivation (Kode *et al.*, 2012).

But how does OST-PTP affect insulin signalling in osteoblasts? In the search for the OST-PTP substrate in osteoblasts, utilising multiple genetic and biochemical modalities the InsR was identified as a potential substrate. As a result, two studies conducted simultaneously by Professors Gerard Karsenty's and Thomas Clemens'

laboratories were initiated to explore the role of insulin signalling in osteoblasts. They generated InsR-deficient mice which presented with hyperglycemia, increased peripheral adiposity, reduced insulin secretion, severe glucose intolerance and decreased levels of circulating GLU13-OCN (Table 1.2). These mice also displayed a skeletal phenotype with a reduction in bone acquisition due to reduced bone formation; however the marker of bone resorption (CTx) was also decreased. Upon infusion of exogenous GLU13-OCN, the metabolic phenotype was fully corrected, suggestive that insulin signalling in osteoblasts has the potential to regulate whole body glucose homeostasis via carboxylation status of OCN (Ferron *et al.*, 2010a; Fulzele *et al.*, 2010). It was also suggested that insulin signalling in osteoblasts might favour bone resorption, due the observation of decreased CTx in osteoblast-specific *InsRosb*$^{-/-}$ mice which mirrored the increase in CTx observed in the *Esp*$^{-/-}$ mice. Utilising the *InsRosb*$^{-/-}$ *and Esp*$^{-/-}$, Ferron *et al.* established using a co-culture system, whereby WT osteoclast precursor cells cultured with osteoblasts isolated from *InsRosb*$^{-/-}$ mice decreased resorption pit formation whilst a 50% increase was seen utilising the *Esp*$^{-/-}$ primary osteoblasts. Moreover, *Opg* a negative regulator of osteoclast function, encoding the decoy receptor for RANKL was increased in *InsR*$^{-/-}$ and decreased 50% in *Esp*$^{-/-}$ osteoblasts. Further unravelling of this complex pathway found that insulin signalling in osteoblasts inhibited *FoxO1* expression, favouring bone resorption via suppression of *Opg*, as well as supressing twist basic helix-loop-helix transcription factor *(*Twist2*)* expression (Runx inhibitor) (Ferron *et al.*, 2010a; Fulzele *et al.*, 2010; Rached *et al.*, 2010). It appeared that osteoclasts were important in the connection between bone and energy metabolism, therefore Ferron and colleagues investigated genes associated with OPG dependent events in the osteoclast. It was found that T cell, immune regulator 1, ATPase, H+ transporting, lysosomal V0 protein A3 (*Tcirg1*) expression was decreased in osteoclast / *InsRosb*$^{-/-}$ osteoblast co-culture models. Present in acidification of the bone prior to bone resorption *Tcirg1* is present in osteoclasts (Teitelbaum, 2000; Teitelbaum and Ross, 2003; Bronckers *et al.*, 2012). These data suggested that insulin signalling in osteoblasts induces osteoclast acidification and consequently bone resorption. This

is via altered via both OPG and the OPG/RANKL ratio resulting in acidic pH which is known to decarboxylate proteins (Engelke *et al.*, 1991). Utilising biochemical and mass spectroscopy analysis it was established that an acidic environment generated by osteoclasts situated in osteoclast resorption lacuna can decarboxylate OCN present in the ECM.

In addition to the classical osteoblast specific PTP's, which has a specificity for phosphotyrosine (Alonso *et al.*, 2004; Barr *et al.*, 2009), 37 other mammalian classical PTP's exist. Of these, the only other identified PTP able to bind to the osteoblast InsR and respond to isoproterenol treatment similar to OST-PTP (Hinoi *et al.*, 2008) is T-cell PTP (TC-PTP). This finding further strengthens the notion that bone is involved in the regulation of glucose metabolism, increasing our understanding of the complex regulation of OCN mediated glucose homeostasis (Zee *et al.*, 2012).

1.6.2 Male fertility and the discovery of the osteocalcin receptor

The discovery of the OCN receptor (Gprc6a) occurred simultaneously with the elucidation of the role of OCN in fertility. Briefly, male and female patients with gonadal failure possess low bone mass and menopause favours bone loss (Riggs *et al.*, 1982; Wishart *et al.*, 1995; Riggs *et al.*, 1998). These clinical observations led to studies investigating the possible relationship between bone and fertility. Fortuitously it was noted that *Bglap3*$^{-/-}$ mice were poor breeders, resulting from decreased testes weight with a 50% reduction in sperm count. This was associated with impaired Leydig cell maturation and decreased circulating testosterone (Oury *et al.*, 2013). Mirroring this phenotype, *Esp*$^{-/-}$ mice had increased male reproductive organ weights with a 30% increase in sperm count and increased circulating testosterone (Oury *et al.*, 2011). This data suggested a link between OCN and testosterone production which was relevant to males only as no change in circulating oestrogen or the aromatase enzyme required to convert testosterone to oestrogen (Cyp19A1) was observed in the *Esp* or *Bglap3*-deficient mice. In an effort to elucidate the signalling mechanism underlying this pathway, several factors were

taken into consideration, namely, the target cells affected by OCN (β cells of the pancreas and Leydig cells of the testis) and the sexually dimorphic aspects of OCN. These clues led to the identification of GPRC6A, a G protein–coupled receptor (GPCR) linked to adenylate cyclase. Present in is present in the Leydig cells, GPRC6A inactivation in mice leads to a metabolic phenotype very similar to the *Bglap3*$^{-/-}$ mice characterised by glucose intolerance, decreased in β-cell area and β-cell mass. In addition, these mice demonstrate defective bone mineralisation (Pi *et al.*, 2008; Pi *et al.*, 2010). Moreover, the compound heterozygous mice lacking *Bglap3*$^{-/+}$ *Gprc6a*$^{-/+}$ had a reproductive phenotype identical in all aspects to the one seen in *Bglap3*$^{-/-}$ and *Gprc6a*-deficient mice models (Oury *et al.*, 2011). These data identified GPRC6A as an OCN receptor, demonstrating the importance of CREB in the regulation of OCN mediated testosterone biosynthesis. Additionally, utilising the *Gprc6a*$^{-/-}$ mouse model it was shown that intraperitoneal injection of OCN failed to markedly stimulate ERK activity, thus having only minor effects on circulating serum insulin levels, which was in contrast to WT mice whose insulin levels were increased when challenged with OCN (Yoshikawa *et al.*, 2011). The G protein–coupled receptor (Gprc6a) has been shown to be integral in the promotion of β cell proliferation during development and adulthood via OCN thus highlighting Gprc6a as an important receptor for skeletal mediated energy regulation via the pancreas (Pi *et al.*, 2011) (Wei *et al.*, 2014b). Most recently, Oury *et al.* demonstrated that OCN acts via the pancreas-bone-testis axis where OCN stimulated testosterone synthesis is positively regulated by insulin signalling in osteoblasts and is independent of luteinizing hormone (Oury *et al.*, 2013).

To highlight the importance of the role of bone in energy metabolism, Wei *et al.* evaluated the consequences of the overexpression or loss of the InsR in osteoblasts of high fat diet (HFD) fed mice. These studies revealed that insulin resistance in bone affects whole-body glucose homeostasis in mice fed a HFD by decreasing OCN activity; moreover they demonstrated that Smad Ubiquitination Regulatory Factor 1 (SMURF1)-mediated InsR ubiquitination contributes to the development of insulin

resistance in osteoblasts. This data underpins the notion that bone is a highly important site for the regulation of global energy homeostasis (summarised Fig. 1.8) (Wei *et al.*, 2014a).

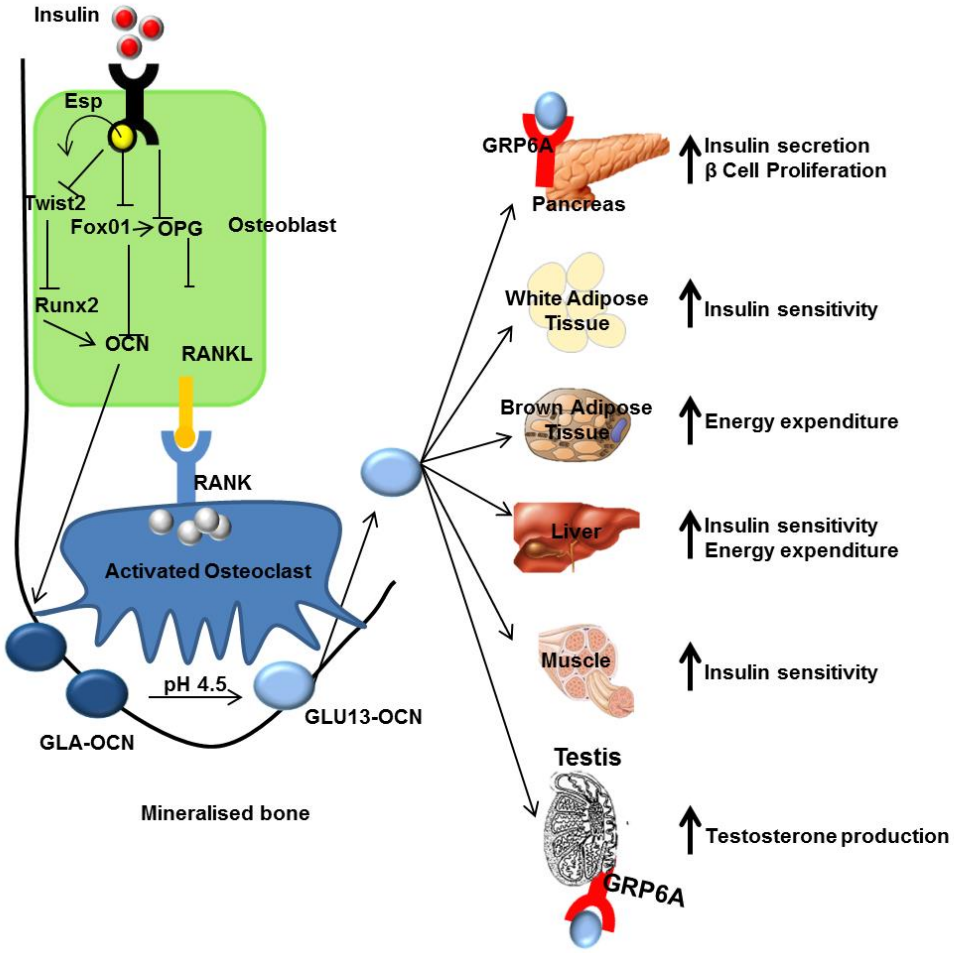

Figure 1.8 OCN a bone-derived multifunctional hormone
A feed forward loop links insulin, bone resorption and OCN activity. Insulin signalling in osteoblasts decreases OPG. The decrease in the ratio of OPG (a RANKL decoy receptor) to RANKL increases bone resorption by osteoclasts. The acidic pH (4.5) in resorption lacunae decarboxylates OCN stored in the bone extracellular matrix. Undercarboxylated active OCN stimulates insulin secretion by the β-cells of the pancreatic islets and promotes insulin sensitivity in peripheral organs. *Esp* acts as an inhibitor, dephosphorylating the insulin receptor, supressing the levels of GLU13-OCN. Undercarboxylated OCN stimulates insulin secretion and β cell proliferation in the pancreas, energy expenditure by muscle, and insulin sensitivity in adipose tissue, muscle and liver. In addition, it promotes male fertility by stimulating testosterone synthesis in leydig cells of the testis through the activation of its receptor, GPRC6A, in these cells ECM, extracellular matrix; InsR, insulin receptor. (Adapted from (Rosen and Motyl, 2010; Karsenty and Ferron, 2012)).

Bglap3$^{-/-}$	*Esp*-/- & *Esposb*$^{-/-}$	*Esp* Overexpression	*InsRosb*$^{-/-}$
• Hyperglycemia • Decreased insulin sensitivity • Decreased insulin secretion • Decreased pancreatic β cell mass and area • Decreased adiponectin expression • Decreased energy expenditure • Abnormally fat • Increased serum triglycerides • Susceptible to diabetes	• Neonatal death from severe hypoglycemia associated with hyperinsulinemia • Increased insulin sensitivity • Increased insulin secretion Increased pancreatic β cell mass and area • Increased adiponectin expression • Higher energy expenditure • Reduced body weight and fat accumulation • Lower serum triglycerides and free fatty acids • Higher serum GLU13-OCN • Protected from diabetes • Metabolic phenotype corrected upon removal of one allele of OCN	• Hyperglycemia • Decreased insulin secretion • Decrease Insulin sensitivity • Low circulating insulin • Decreased insulin responsiveness • Increased body fat	• Reduced bone formation • Reduced bone resorption • Low circulating total and GLU13-OCN • Hyperglycaemia • Reduced serum insulin levels • Severe glucose intolerance • Increased insulin resistance • Marked peripheral adiposity • Reduced energy expenditure

Table 1.2 Metabolic phenotype of *Bglap3*$^{-/-}$, *Esp*$^{-/-}$, *Esp* overexpression and InsR mutant mice
(Adapted from (Ng, 2011))

1.6.3 Clinical evidence: osteocalcin and metabolism/fertility

The first association between OCN and glucose metabolism in 1998 highlighted that OCN serum levels were significantly lower in diabetic patients and higher in patients with improved glycaemic control (Rosato *et al.*, 1998). Many human studies have since quantified both total circulating OCN and the hormonally active undercarboxylated OCN, yielding mixed results. A positive correlation between serum undercarboxylated OCN levels and enhanced β-cell function was observed in several studies (Hwang *et al.*, 2009; Prats-Puig *et al.*, 2010; Pollock *et al.*, 2011), however, in contrast, other studies have found no association between lower circulating uncarboxylated OCN levels and higher HOMA-IR (Shea *et al.*, 2009). These conflicting results are likely attributed to the lack of a commercially available undercarboxylated OCN assay (Ducy 2011). Similarly, it appears that the reproductive function of OCN translates to humans, with the identification of a positive association between OCN and testosterone serum levels in the general population, patients with bone disorders and patients with T2DM (Hannemann *et al.*, 2013; Kanazawa *et al.*, 2013). Furthermore, two subjects were identified from a cohort of patients displaying testicular failure that harboured a heterozygous missense variant in one of the transmembrane domains of GPRC6A, giving credence to a role of OCN function in humans (Oury *et al.*, 2013; Karsenty and Oury 2014; Oldknow *et al.*, 2015).

1.6.4 GLUT and bone

Cellular uptake of glucose is mediated by either of the two families of membrane-associated carrier proteins, namely the sodium coupled glucose transporters (SGLTs) via active transport and glucose transporter (GLUT) facilitators via facilitated diffusion (Bell *et al.*, 1990; Carruthers, 1990). The SGLT family comprises 12 members including co-transporters for sugars, anions, vitamins and short-chain fatty acids (Wright and Turk, 2004). Currently, the presence of SGLT in bone has not been reported; however, SGLT2 receptor inhibitors, acting as glucose-lowering agents in the management of type two diabetes mellitus (T2DM), have been

reported to have no significant effects on bone formation and resorption or BMD in humans (Ljunggren *et al.*, 2012). In contrast, GLUT receptors have recently been reported to be expressed in bone. To date, the GLUT family consists of 14 members sub-classified into three groups, according to sequence similarities and characteristic elements (Joost and Thorens, 2001; Mueckler and Thorens, 2013). GLUT receptors exhibit striking tissue-specific expression, each possessing differential sensitivities to stimuli such as insulin, thus allowing for complex and specific regulation of glucose uptake according to cellular requirements (Gould and Holman, 1993). It was first suggested that insulin promotes increased glucose uptake via GLUT1 in the osteoblast, independently of Insulin like growth factor – 1 (IGF-1) signalling to increase the metabolic activity of the osteoblast (Fulzele *et al.*, 2007). Most recently, solute carrier family 4 (*Slc2a4*) has been found to be expressed at similar levels to those in skeletal muscle in osteoblasts, osteocytes and chondrocytes, with the genetic ablation of *Slc2a4* in osteoblasts/osteocytes resulting in increased peripheral adiposity associated with mild hyperinsulinemia. These mice also presented with insulin resistance. These metabolic changes were assumed to originate from osteoblasts/osteocytes as no altered gene expression was identified in the liver or adipose tissue, indicating that decreased *Slc2a4*-mediated glucose uptake in bone is sufficient to influence whole-body metabolism (Zhu *et al.*, 2013). Emerging results from two independent laboratories have indicated that, in addition to GLUT4, GLUT1 is necessary for bone formation and whole-body glucose homoeostasis. Moreover, GLUT1 is modulated by high glucose levels (Wei *et al.*, 2014a; Wei *et al.*, 2014b; Wei J, 2014). Collectively, these results provide a deeper understanding of the role of bone in the regulation of glucose metabolism (Fig. 1.9).

Excitingly, recent evidence suggests that other osteoblast-derived hormones may contribute to the emerging function of the skeleton as a regulator of the energy metabolism. This was demonstrated by the partial ablation of osteoblasts in transgenic mice which resulted in profound affects in glucose metabolism, gonadal fat mass combined with increased energy expenditure. Administration of OCN

partly corrected the metabolic phenotype, however it did not improve the increased energy expenditure or decrease gonadal fat. This suggests that osteoblasts have the ability to affect glucose metabolism through both OCN dependent and independent mechanisms (Yoshikawa *et al.*, 2011). This observation forms the theme of this thesis.

1.6.5 Fibroblast growth factor 23

In addition to OCN, it is also important to highlight that osteocyte derived FGF23 has a central role in the regulation of energy metabolism (David *et al.*, 2009a; David *et al.*, 2009) in addition to its well documented roles in phosphate homeostasis and the coordination of bone mineralisation (section 1.3.3). Mouse models either overexpressing MEPE, ASARM peptides or infused with ASARM peptides display increased adiposity, are hyperglycaemic and have increased OCN, whereas FGF23-null mice are hypoglycaemic (ASARM peptide modulates PHEX–DMP1-mediated FGF23 expression; Rowe *et al.*, 1996; David *et al.*, 2009a; David *et al.*, 2009b; David *et al.*, 2011). Intriguingly, patients subjected to a 4 hour euglycaemic–hyperinsulinaemic clamp showed increased FGF23 that correlated positively with insulin infusion (Winther *et al.*, 2011). These combined data are indicative of key roles for FGF23 in energy metabolism (Oldknow *et al.*, 2015).

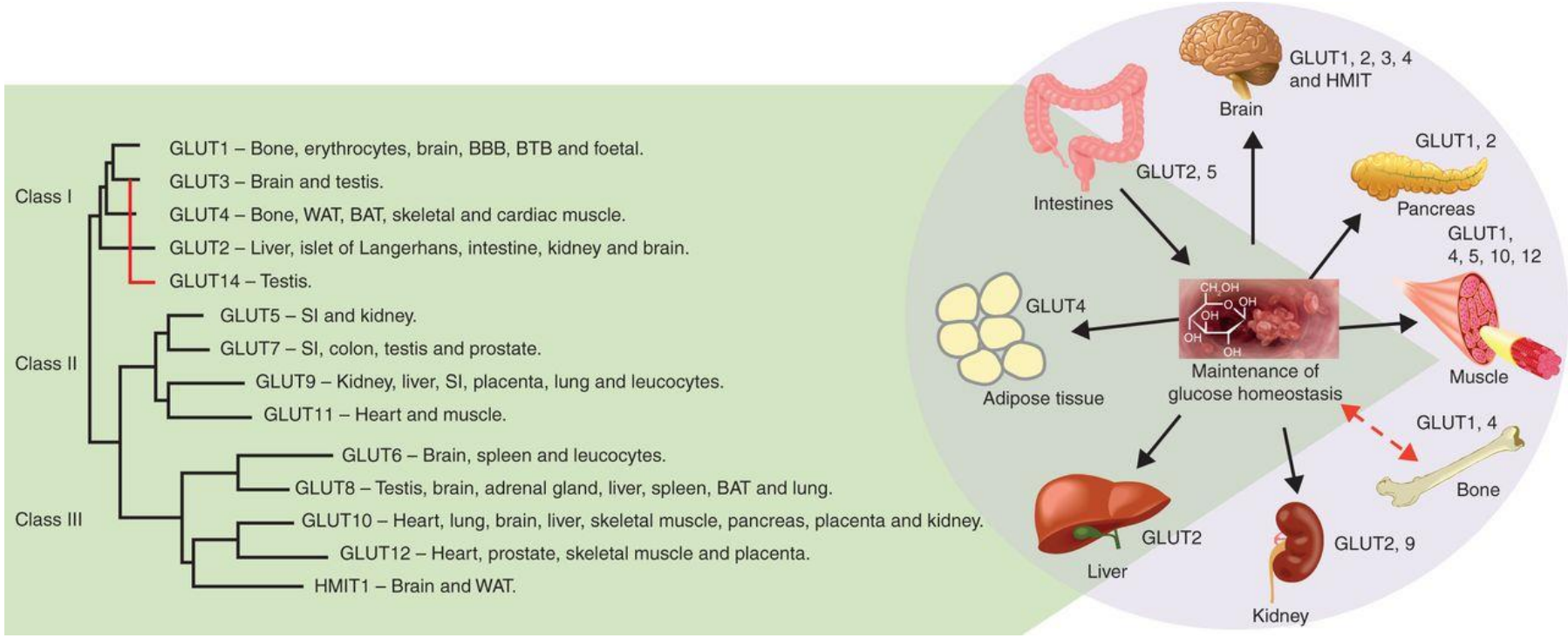

Figure 1.9 GLUT transporter family

Dendrogram of the extended GLUT family highlighting GLUT receptor tissue distribution and cellular/subcellular expression. Additionally, the role of GLUT proteins in the maintenance of glucose homoeostasis is summarised, outlining the relevant glucose-responsive tissues and the associated GLUT receptors (newly reported GLUT receptors in bone are also highlighted; figure adapted from (Joost and Thorens, 2001; Mueckler and Thorens, 2013). Potential similarities between GLUT3 and GLUT14 are indicated by a red line. The role of bone GLUT1 and GLUT4 in glucose homoeostasis is speculative and indicated by a red double-headed arrow. BBB, blood–brain barrier; BTB, blood–testis barrier; WAT, white adipose tissue; BAT, brown adipose tissue; SI, small intestine.

1.7 Aims and strategy

Whilst the functional importance of PHOSPHO1 in the regulation of skeletal mineralisation and in the formation of mechanically competent bones has been clearly demonstrated, the role of PHOSPHO1 in the regulation of energy metabolism has yet to be established. This potential role of PHOSPHO1 emerged from striking preliminary data obtained by Dr. Carmen Huesa, which suggested that:

I. *Phospho1*$^{-/-}$ osteoblasts have a 20-fold increase in *Esp* expression compared to WT osteoblasts.
II. PHOSPHO1 dephosphorylates the InsR at serine 1322.
III. PHOSPHO1 interacts with GYF protein 1 (GIGYF1), GIGYF1 forms a complex with GRB10 to regulate both insulin and IGF-1 receptor signalling.

Therefore, the aim of this thesis was to test the hypothesis that PHOSPHO1 regulates energy metabolism and PHOSPHO1 deficiency protects from obesity and insulin resistance. To address this I have completed the following aims:

I. Establish if PHOSPHO1 controls energy metabolism through cross talk with the InsR.
II. Determine if *Phospho1* overexpression in osteoblasts down regulates *Esp* expression and thereby regulate hormonally active GLU13-OCN.
III. Examine glucose metabolism and the energy status of *Phospho1*$^{-/-}$ mice.
IV. Investigate the potential regulation of energy metabolism by bone though PHOSPHO1 deficiency.

These aims have been achieved through the use of both *in vitro* and *in vivo* models. Prior to the phenotypic metabolic characterisation of *Phospho1*$^{-/-}$ mice it was first necessary to confirm/oppose preliminary data obtained by Dr. Carmen Huesa, suggestive that PHOSPHO1 controls energy metabolism through cross talk with the

InsR (Chapter 3). Furthermore, I ascertained that *Esp* which controls GLU 13-OCN secretion, was more highly expressed in *Phospho1*$^{-/-}$ osteoblasts (Chapter 3). This chapter highlighted that PHOSPHO1 was an interesting candidate for *in vivo* studies.

Thereafter, *Phospho1*$^{-/-}$ mice were examined under both normal and diet challenged (60% HFD) conditions, assessing multiple parameters inclusive, but not limited to, insulin sensitivity, activity monitoring, oxygen consumption, liver spectroscopy and whole body adiposity (Chapter 4 and 5).

The identification of candidates underlying the remarkable protection from obesity and insulin resistance observed in *Phospho1* deficiency would serve to cement *Phospho1*'s role in the regulation of the metabolic profile of mice. This role was examined both *in vitro* and *in vivo* using various cell lines (FAZA, INS1E, C2C12, 3T3-L1), primary calvarial osteoblasts and blood serum. Chapter 6 therefore provides a platform for future research.

In conclusion, these studies have revealed that the genetic ablation of *Phospho1* improves the metabolic profile of mice *in vivo* and confers a remarkable protection against obesity and diabetes. Specifically, *Phospho1*$^{-/-}$ mice are hypoglycaemic, show improved glucose and insulin tolerance and are protected from HFD induced obesity. These observations were not OCN dependent or related to increased physical activity and are consistent with the noted smaller fat deposits. Furthermore, preliminary *in vitro* studies indicated that conditioned medium (CM) from *Phospho1*$^{-/-}$ primary osteoblasts increased basal and insulin stimulated sensitivity in osteoblasts, adipocytes and β cells. These data are suggestive that the observed metabolic phenotype is primarily bone driven. Such data is essential to further unravel the links between energy metabolism, mineralisation and bone.

Chapter 2

Materials and Methods

2.1 Reagents and solutions

All chemicals were purchased from Sigma-Aldrich (Dorset, UK) and tissue culture medium and buffers were purchased from Life Technologies (Paisley, UK) unless otherwise stated. All medium and buffer recipes are shown in Appendix I.

2.2 Cell culture

2.2.1 Cell culture reagents

All tissue culture reagents were prepared in a sterile category 2 hood. Cell media was supplemented with the broad spectrum antibiotic gentamicin (0.05mg/ml, Life Technologies). Heat inactivated foetal bovine serum (FBS, Life Technologies) was filter-sterilised through a 0.22μm filter prior to use. Prepared medium was subsequently stored at 4°C prior to use.

2.2.2 Isolating primary osteoblasts

Under sterile conditions calvariae were dissected from 3-4 day old new-born WT and *Phospho1*$^{-/-}$ mice as previously described (Zhu *et al.*, 2011). Extracted calvaria were washed in Hank's Balanced Salt Solution and subject to successive cellular digestions with constant agitation at 37°C. Briefly, the digests consisted of:

I. 10 minute collagenase type II digestion (10mg/ml, Worthington, Lakewood, NJ) whereby the supernatant was discarded.
II. 30 minute collagenase digestion which was retained together with a phosphate-buffered saline (PBS) wash of the calvaria (fraction 1).
III. 10 minute ethylenediaminetetraacetic acid (EDTA, 4mM) digestion which was retained together with a HBSS wash (fraction 2).
IV. A 30 minute collagenase digestion (fraction 3).

Osteoblasts were isolated from the fractions by centrifuging (1800g, 5 minutes), resuspended in primary osteoblast medium (Appendix I) and finally pooled to obtain a single cell suspension. The extracted osteoblasts cells were expanded in flasks in a humidified atmosphere of 95% air/5% CO_2 and maintained at 37°C until

80–90% confluence and were then plated at 10000 cells/cm^2 in multi-well plates for individual experiments as described in section 2.2.3.2.

2.2.3 Freezing/thawing of cells

2.2.3.1 Cell lines

Cryopreservation of cell lines was carried out to maintain stocks. Upon confluency cells were trypsinised and counted as described in section 2.2.4. The cell suspension was then centrifuged at 2000g for 5 minutes and resuspended in 50/50 maintenance media and freezing mix 1 (Appendix I) to obtain the desired number of cells (3 x 10^6 cells per cryovial) (Corning, Surrey, UK). The cryovials were then wrapped in cotton wool, placed inside a polystyrene box and stored at -80°C for 4-7 days. For longer term storage, vials were transferred to -150°C. Upon requirement, stored cells were thawed quickly at 37°C and added drop wise to 5ml of pre-warmed appropriate maintenance media (Appendix I). The cell suspension was mixed and centrifuged for 5 minutes at 2000g to remove the toxic dimethyl sulfoxide (DMSO), which acts as a cryoprotectant to prevent cell death during the freezing process. The cell pellet was resuspended in maintenance media and transferred to a T175 tissue culture flask.

2.2.3.2 Primary Calvarial Osteoblasts

Primary osteoblasts were trypsinised and counted as described in section 2.2.4 and resuspended in 1.5 ml freezing mix 2 (Appendix I) to obtain the desired number of cells (3 x 10^6 cells per cryovial). The cryovials were placed in isopropanol at -20°C for two hours, transferred to -80°C overnight and for longer term storage, vials were transferred to -150°C. To thaw primary calvarial osteoblasts, cryovials were gently shaken in a 37°C water bath. The total contents of the cryovial (1.5ml) was and added drop wise to 4.5ml of pre-warmed primary osteoblast medium (Appendix I). The cell suspension was mixed and centrifuged for 5 minutes. The cell pellet was resuspended in primary osteoblast medium and transferred to a T175 tissue culture flask.

2.2.4 Maintenance and passaging of cells

Upon sub-confluence (70-80%), adherent cells were passaged by trypsinisation. Initially the culture medium was removed and the monolayer was washed with PBS. Cells were detached from the plastic by incubation with trypsin/EDTA for approximately 5 minutes at 37°C. The trypsin was neutralised by the addition of at least double the volume of appropriate cell medium containing the neutralising FBS. The cellular suspension was centrifuged at 2000g for 5 minutes in order to obtain a cellular pellet. The medium was removed and the cells were counted (if appropriate) using a Neubauer haemocytometer and then resuspended in a known volume of appropriate cell medium.

2.2.5 Conditioned media

Conditioned media was collected from WT and *Phospho1*$^{-/-}$ primary osteoblasts that were plated at a density of 10000 cells/cm^2 as described. Media was changed every 3 days and on at day 0 (upon plate confluency), 3, 6 and 9 was removed from the cells, centrifuged to remove particulates and frozen at -80°C until required. Collected conditioned media from *Phospho1*$^{-/-}$ primary osteoblasts was incubated for 1 hour with C2C12 (mouse myoblast cell line), FAZA (rat liver cell line), Ins1e (rat insulinoma cell line), MLOA5 (mouse postosteoblast / preosteocyte-like cell line), 3T3-L1 (mouse fibroblast cell line that were differentiated into to adipocytes), MC3T3 (mouse osteoblastic cell line) and WT primary osteoblast cultures. WT osteoblast conditioned medium was used as a control. Following incubation cells were subject to Insulin treatment as described in section 2.3.1. Protein and mRNA were then extracted (section 2.6.1 and 2.7.1).

2.2.6 Viral transduction of primary osteoblasts

For overexpression experiments, primary *Phospho1*$^{-/-}$ calvarial osteoblasts were cultured in T25 flasks and left to reach 75% confluency. Half of the media was removed from the flask and either 2.5µl of empty vector (EV), 5µl PHOSPHO1 overexpression or 5µl flag tagged PHOSPHO1 (FP1) lentivirus was added to the

media along with and 4μg/ml of FuGENE transfection reagent (Promega, Southampton, UK). Virus packaging was conducted by Dr. Carmen Huesa. Following 6 hours the media was replaced. In order to select for successfully transfected osteoblasts, 5mg/ml of puromycin was added to the osteoblast cultures for 3 days. Media was then replaced, supplemented with 2.5mg/ml of puromycin to maintain selection pressure and ensure successful transfection during the growing phase. Cell growth was observed every day until confluency had been achieved.

2.3 *In vitro* procedures for metabolic assessment of cells

2.3.1 Insulin treatment of cells

Following confluency the appropriate cells were washed three times in PBS and cultured for 24 hours in αMEM supplanted with 0.5% FBS. Medium was then changed to αMEM supplemented with 0.1% BSA (Fraction V) and 10mM HEPES 10mM (pH 7.4) for 3-6 hours. Cells were then stimulated with 10mM of insulin (Sigma) for 15 minutes, washed in ice-cold PBS and protein and mRNA was extraction described in sections 2.6.1 and 2.7.1.

2.3.2 Immunocytochemistry

Primary calvarial osteoblasts were plated on rat tail type I collagen coated plastic ware containing a sterile 22mmx22mm glass coverslip (Scientific Laboratory Supplies, Yorkshire, UK). Upon confluency, cells were stimulated with 100nM insulin (section 2.3.1), fixed with 4% paraformaldehyde (PFA) and subsequently washed in PBS 3 x 5 minutes. For permeabilisation, fixed cells were incubated with ice cold 100% methanol for 5 minutes at -20°C. Cells were then washed 3 x 5 minutes in PBS and blocked for 1 hour in blocking buffer (1xPBS, 5% normal goat serum, 0.3% triton X-100). The blocking buffer was removed and cells were incubated overnight at 4°C with the primary antibody against the InsR (Cell signalling, Boston, USA) diluted in blocking buffer overnight at 4°C. Cells were washed in PBS 3 x 5 minutes and incubated with the fluorochrome-conjugated goat-anti-rabbit secondary antibody (Life Technologies) diluted in blocking buffer for 90

minutes at room temperature in the dark (Appendix II). Finally, cells were washed 3 x 5 minutes in PBS and the coverslips were mounted using ProLong Gold Antifade Mountant with 4',6-diamidino-2-phenylindole (DAPI - Life Technologies). Slides were analysed using a Nikon EC-1 confocal microscope.

2.3.3 2-deoxyglucose [3H] *in vitro*

WT and *Phospho1*$^{-/-}$ primary osteoblasts were cultured in 6 well plates at a density of 10000 cells/cm^2 as described in section 2.2.4. Upon confluency primary osteoblasts were washed with PBS and incubated in in serum alpha MEM for 4 hours. Osteoblasts were washed in PBS again, and 2ml of PBS was added to each well. Osteoblasts were then treated with either 100nM insulin, 1000nM insulin or 10μM Cytochalasin B (PBS acted as the control) for 15 minutes at 37^{o}C. Radioactive 2-deoxyglucose [3H] (Glucose, 2DG-[3-^{3}H], PerkinElmer, Buckinghamshire, UK) was then added to each well (0.1 mM (9250 Bq/ml (0.25μCi/ml)) for 15min at 37°C. 2-deoxyglucose [3H] uptake was terminated by washing the osteoblasts 3 times with ice cold 0.9% saline. The osteoblasts were scraped in in 600μL PBS + 0.1% sodium dodecyl sulphate (SDS) and transferred to Eppendorf tubes where the cell extract was homogenised with a needle and syringe. Half the volume of the cell lysate (300μl) was transferred into a scintillation tube containing 4ml of scintillation liquid (Ecoscint Ultra, National Diagnostic's, Hessle, UK) and mixed well. Radioactivity was counted using the Hidex 300 SL Automatic Liquid Scintillation Counter (Turku, Finland) and the counts per minute (cpm), disintegrations per minute (dpm) were recorded. The remaining cell lysate was stored at -20°C and used for protein assay (DC) (section 2.7.2.1). Counts in the experimental wells were normalised to protein level following the subtraction of counts from the cytochalasin B control wells (cytochalasin B blocks GLUT-mediated transport and therefore any radioactivity demonstrates non-carrier mediated glucose entry).

2.3.4 Mitochondria stress test

Calvarial osteoblasts were extracted as described in section 2.2.2 and plated on a Seahorse XF24 microplate at a density of 25,000 and 50,000 cells per well in 100 μL of primary osteoblast medium. The plate was left in the hood for one hour to allow the osteoblasts to adhere and 150 μL of primary osteoblast medium was subsequently added to each well and the plate was transferred to a 37°C CO_2 incubator until 100% confluency was reached (approximately 1 day). Osteoblast were washed in 500μl XF assay media supplemented with 25 mM glucose and 10 mM pyruvate and placed in a non-CO_2 incubator at 37°C for 1 hour prior to start of assay. Calvarial osteoblasts were then exposed to oligomycin (1.2μM - a complex V inhibitor, that inhibits respiration by inhibiting ATP synthase), the uncoupling agent carbonyl cyanide p-trifluoromethoxyphenylhydrazone (FCCP -(0.56μM)), antimycin A (that inhibits respiration by inhibiting oxidation of ubiquinol in the electron transport chain) and rotenone (0.96μM - complex I inhibitor involved in the inhibition of the mitochondrial respiratory chain). All reagents were prepared for the assay from 2.5 mM Seahorse stock solutions (Seahorse Bioscience, Massachusetts, United States). Following equilibration the Seahorse plate was placed in the Seahorse XF24 Analyser and the protocol in Appendix III was followed. OCR values are shown as pMoles/min compared over time at 3 different time points per condition. All Seahorse experiments were repeated at least twice. All the data shown in the assays are an average of at least 3 different wells per group.

2.4 Histological analysis of cell cultures

2.4.1 Oil-Red-O

To observe and quantify fat droplets in cell culture, differentiated cells were washed in PBS and subsequently fixed with 10% Neutral buffered formalin (NBF) for 1 hour at room temperature. Following the removal of the fixative, cells were stained with freshly prepared Oil-Red-O working solution for 30 minutes (Appendix I), washed in PBS to remove excess stain and either visualised under a microscope or stored in PBS at 4°C until photography.

2.5 *In vivo* studies

2.5.1 Animal welfare and generation

All animal experiments were approved by The Roslin Institute's Animal Users Committee and the animals were maintained in accordance with Home Office guidelines for the care and use of laboratory animals. Animals were maintained under conventional housing conditions with a 12 hour light/dark cycle. *Phospho1* null mice were generated as previously described (Yadav MC, 2011) and separate colonies of WT and *Phospho1*$^{-/-}$ were maintained. This was preferable to using litter mates from *Phospho1*$^{-/+}$ breeding parents as the identity of the genotype of new-born mice was required for calvarial osteoblast preparations. Offspring carrying the mutant *Phospho1* gene were identified by genotyping (section 2.5.2).

2.5.2 DNA extraction and genotyping

Genotyping of *Phospho1*$^{-/-}$ mice was performed in house. Ear snips were collected and DNA was extracted using prepared solution 1 and 2 (Appendix IV). To each ear snip, 75µl solution 1 was added and incubated at 30 min at 95°C. To neutralise the reaction 75 µl solution 2 was added and extracted DNA was stored at -20°C until use. Extracted DNA was subject to direct PCR using primers and PCR conditions developed by Dr. Carmen Huesa (Appendix IV). To each DNA sample, 5µl of restriction digest master mix (Appendix IV) was added, and samples were subsequently incubated at 65°C for 1 hour. Samples were run on a 1.5% agarose Tris-borate-EDTA (TBE) gel made containing 3% ethidium bromide following the addition of 5x loading buffer (Bioline Reagents Ltd, London, UK). Hyper ladder 1 was used as a reference. Corresponding band patterns are show in Fig .2.1.

2.5.3 Metabolic analysis of animal models

Male juvenile (35 day old) adult (120 day old) and ageing (220 day old) WT and *Phospho1*$^{-/-}$ male mice were fed a control diet (CD - 6.2% fat; Harlan Laboratories, Indianapolis, IN, USA).

Adult mice diet challenged with:

I. A HFD (58% fat; DBM Scotland, Broxburn, UK) *Ad libitum* from 35 day old to until analysis at 120 day old.
II. 2% supplemented choline diet (Harlan Laboratories) from 85-days-old to 120 day old.

Food and water consumption was measured by housing mice individually for 5 days, whereby 200g of food and 250ml of water was given on day 0. Remaining food was subsequently weighed each day for 5 consecutive days at the same time each day (10am), obvious food remnants in the cage were recovered and weighed. The volume of water drank was also recorded. Average daily food and water intake was calculated over the 5-day time period. Observations on chewing of food pellets were also recorded. Due to the crumbly nature of the HFD it was not possible to weigh. Blood was extracted from mice via cardiac puncture. Collected blood was transferred to an EDTA coated tube and placed on ice for 30 minutes (Sarstedt, Nümbrecht Germany). Tubes were then centrifuged at 1000g which results in serum separation. Serum was carefully collected and stored at -80°C until use

2.5.3.1 XY activity monitor

Basal nocturnal activity was measured using an AM524 Single Layer X, Y IR activity monitor and associated Amonlite software (Linton Instrumentations, Norfolk, UK) These experiments were conducted at the Biological Resource Facility, Roslin, University of Edinburgh with help from Darren Smith. The AM524 uses an array of infrared beams to determine activity and mobility of a subject, which are arranged in an 8 x 16 pitched grid. The XY activity (fast, slow and total), active time, mobile time, distance travelled, mobile counts (fast and slow), static counts (fast and slow), static time, active time and front to back movement was automatically recorded. Prior to use with experimental mice, initial pilot studies were undertaken to ensure the results were reproducible, whereby the same mouse was placed in the activity for three consecutive overnight periods. These studies indicated no prior acquisition

period prior to experimental testing was necessary. Juvenile, adult (CD and HFD) and aged male mice were single housed placed inside the activity monitor on the evening of the experiment, nocturnal activity was subsequently recorded for 14.5 hours to encompass the dark phase (18:00 – 08:30 hours the following day). During testing, mice were undisturbed, had free access to chow and water and the cage had the normal bedding retained in order to minimise external stimuli that may alter the normal activity.

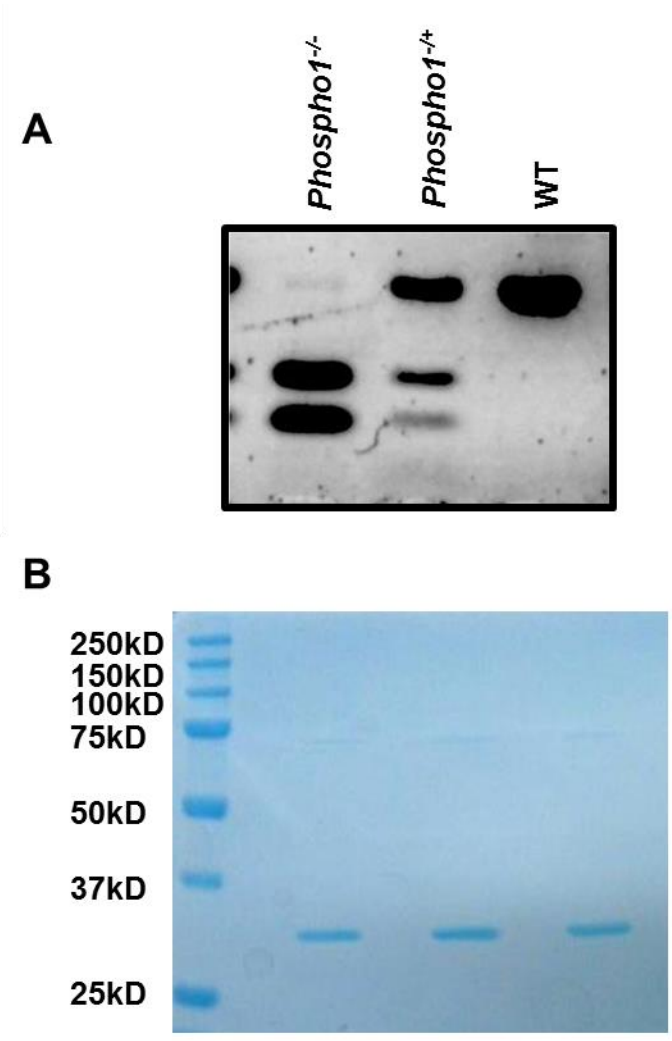

Figure 2.1 Genotyping of *Phospho1*$^{-/-}$ and WT mice using PCR and all Blue staining of polyacrylamide gel
(A) PCR analysis shows that *Phospho1*$^{-/-}$ mice have a product of two distinct dark bands, heterozygous mice have one distinct dark band and two fainter and WT mice have only one distinct dark band **(B)** Simply Blue Safe Stain used to visualise recombinant PHOSPHO1 protein run bands on a polyacrylamide gel.

2.5.3.2 Metabolic activity measurement using indirect calorimetry

The Oxymax Lab Animal Monitoring System: CLAMS (Columbus Instruments, OH USA), was used to measure heat production, volume (V) of CO_2, VO_2 and respiratory exchange rate (RER) via indirect calorimetry (Ridgman, 1988). These studies were completed at the McGill University, Montreal, Canada, in collaboration with Dr. Monuzur Murshed and Dr. Zohreh Khavandgar. Male 35 day old and 120 day old HFD mice were placed in the Oxymax system and supplied with a known flow of air. The consumption of O_2 and production of CO_2 during the metabolic process was recorded and the following formulae to calculate the desired parameters:

Oxygen consumption (VO2) = (InFlow x O_2in) – (OutFlow x O_2out).
Volume of carbon dioxide (VCO2) = (OutFlow x CO_2out) – (InFlow x CO_2in).
Respiratory exchange rate (RER) = (VCO_2 / VO_2).
HEAT = ((3.815 + 1.232) x RER) x (VO_2).

Prior to analysis an initial acclimatisation was undertaken which involved placing the mice in the Oxymax system for 2 hours for three consecutive days. The experiments were conducted over a 24 hour period, from 12pm until 12pm to obtain both day and night measurements. Associated CLAMS data eXamination Tool (CLAX) was used to assist in the analysis of the produced data.

2.5.3.3 Glucose and insulin tolerance tests

Mice were fasted for 4 hours and administered either 2mg of D-glucose (Sigma, Poole, UK) per g of body weight (BW) by gavage or 0.5mU of insulin per g of BW by intraperitoneal injection (IP) (Fig. 2.2). At 0, 15, 30 and 60 minutes after administration, blood glucose was measured with an Accu-Chek Aviva glucose meter (Roche Diagnostics Ltd, Lewes, UK) and insulin was measured by ELISA (ChrystalChem, Chicago, IL, USA) to obtain glucose-stimulated insulin secretion (GSIS) measurements. Animals were allowed to recover for two weeks prior to cull

and tissue removal to ensure glucose or insulin challenge did not bias further experimentation (serum measurements, gene expression etc.). However it is important to note 2% choline diet were sacrificed immediately after metabolic testing as a two week recover may have diluted diet induced changes.

2.5.3.4 *In vivo* 20 minute insulin treatment

To examine the effects of insulin treatment on the expression of known targets of insulin action. Juvenile male mice were fasted for 4 hours and administered 1mU of insulin per g of BW. At 0 and 19 minutes following administration, blood glucose was measured (detailed in section 2.5.3.3) to ensure insulin had been delivered successfully. At 20 minutes following insulin administration, mice were sacrificed and tissues including tibiae, pancreas, liver, quadriceps femoris and brown, subcutaneous (SB), mesenteric (MF) and gonadal (GF) fat pads, were collected for protein and gene expression analysis.

2.5.3.5 Beta 3-agonist-37344 administration

As an alternative to acute cold exposure juvenile WT and *Phospho1*$^{-/-}$ male mice were weighed and fasted for 4 hours between 9am and 1pm. Beta *3*-receptor agonist - 37344 (BRL-37344, Sigma) was administered IP 3 hours before euthanisa (1mg/kg BW) and adipose depots were collected for gene expression analysis (as described in 2.6) (Doucette and Rosen, 2014).

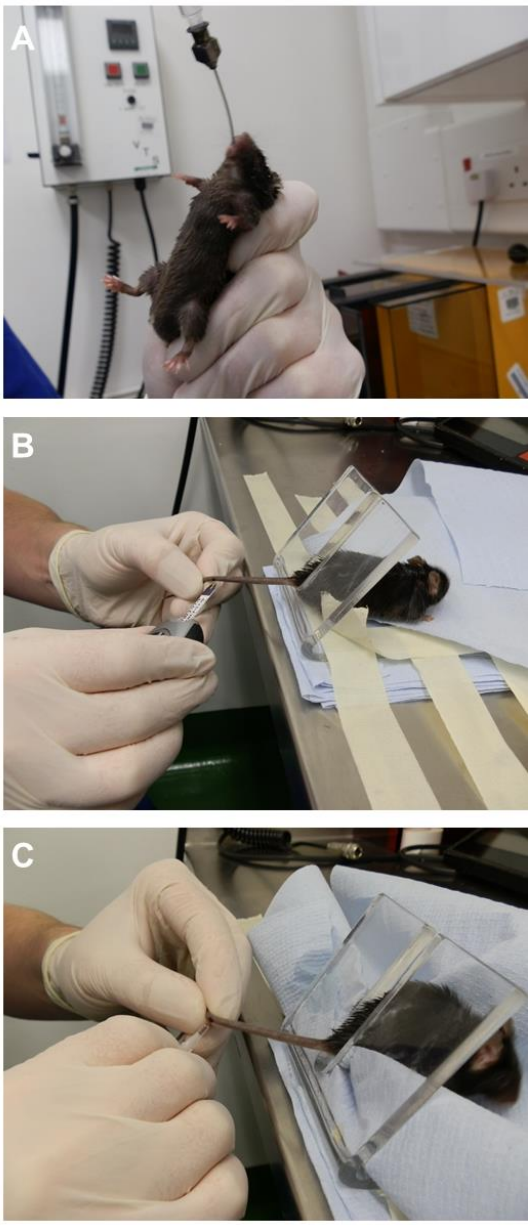

Figure 2.2 Metabolic testing of *Phospho1*$^{-/-}$ and WT mice
Representative photographs of oral gavage procedure **(A)**, Glucose measurement using the glucose meter **(B)** and blood collection for serum analysis **(C)**.

2.6 RNA methods

2.6.1 Isolation of RNA from cells and tissues

Prior to RNA extraction cultured primary osteoblasts and cell lines were washed and scraped from individual wells in PBS and stored at -80°C until use. Tissues were snap frozen and homogenised in QIAzol Lysis Reagent (RNeasy Lipid and

Tissue kit, Qiagen, Manchester, UK) using a hand held homogeniser (Cole-Parmer Instruments Ltd, London UK). Bone samples were submerged in liquid nitrogen and homogenised using a mortar and pestle followed by a hand held homogeniser in QIAzol Lysis Reagent. RNA was extracted using the RNeasy lipid tissue kit following manufactures instructions. The RNeasy lipid contains a phenol/guanidine-based sample lysis step which facilitates the breakdown of fatty tissues. An optional DNase treatment step was also included to completely remove any contaminating DNA (Qiagen). The concentration and quality (the ratio of wavelengths 260nm/280nm) of RNA was measured using a NanoDrop spectrophotometer (Labtech, Tampa, USA). Samples were diluted to the same concentration (that of the lowest sample) in nuclease-free water (NFW).

2.6.2 Reverse transcription

Complementary DNA (cDNA) was prepared from 10µl. of the diluted RNA using reverse transcription. Briefly, 2µl of random primers (1/60) was added to the diluted mRNA and heated for 10 minutes at 70°C in a Hybaid polymerase chain reaction (PCR) Express Thermal cycler (Thermo Scientific, Northumberland, UK). Samples were cooled on ice. The Superscript II kit was used to obtain cDNA following manufactures guidelines. The samples were run on the following programme in the Hybaid PCR machine: 25°C for 10 minutes; 42ºC for 50 minutes; 70°C for 15 minutes and held at 4°C. The neat cDNA samples were stored at -20°C. The cDNA was diluted with NFW to 5ng/µl and stored at -20°C.

2.6.3 Primer design

Primers were designed to span an exon to avoid amplifying genomic DNA. Using Primer BLAST, primer sequences were entered to check that the melting temperature (T_m) of the primers was between 65°C and 75°C and within 5°C of each other and the GC content was between 40% and 60%. *In silico* PCR was used to check primers before purchasing (http://genome-euro.ucsc.edu/cgiin/hgPcr?hgsid=202376389_vk1kEGcrSPgtiTvcQk9GXSRJtLMn).

PCR oligonucleotides were purchased from MWG Eurofins (Ebersberg, Germany). Primer sequences are disclosed in Appendix V.

2.6.4 Real time quantitative polymerase chain reaction and quantification of gene expression

Real time qPCR reactions were conducted in a 96 well plate (Thermo Scientific) and cycled in a Stratagene Mx3000P PCR cycler (Agilent Technologies, Santa Clara, USA). For each qPCR reaction, 1µl of primer (200mM forward and reverse primer), 10µl SYBR Green Master Mix (Primer Design, Southampton, UK), 4µl RNase/DNase free water was made up to a volume of 15µl and added to 5 µl of diluted cDNA (5ng/µl). The qPCR reaction was cycled using the following protocol: Initial hotstart enzyme activation (2 minutes 95°C) followed by 40 cycles of denaturation (15 seconds at 95°C) and data collection (60 seconds at 60°C). A post PCR run melt curve was run to ensure the primers produced only one product. Each sample was tested in triplicate and compared to the appropriate housekeeping gene using MxPro software (Agilent, Cheshire, UK). The relative expression of the analysed genes was calculated using the ΔΔCT method(Laakso *et al.*, 2001), whereby an arbitrary amplification threshold is set and relative expression levels of the samples are determined by comparison of the number of amplification cycles required to cross this threshold (CT).

2.6.5 Optimisation of qPCR primers and PCR product sequencing

Primers were tested for efficiency using serial dilutions of cDNA (known to express the gene of interest) to create a standard curve (Fig. 2.3). Primers were considered acceptable if the amplification efficiency was within the range of 90-110%, with an R^2 value between 0.99 and 1.00 and an amplification curve with sigmoid curves at regular intervals along the dilution series. Primer specificity was demonstrated by the generation of a single peak in the dissociation curve. Agarose gel electrophoresis was used to ensure the presence of one band following amplification. Bands were

cut from the gel and the DNA purified using a Qiaquick Gel Extraction Kit (Qiagen). To confirm primer specificity the purified DNA was sent for sequencing to Edinburgh Genomics (University of Edinburgh). NCBI Blast was used to match product sequence with sequence of interest.

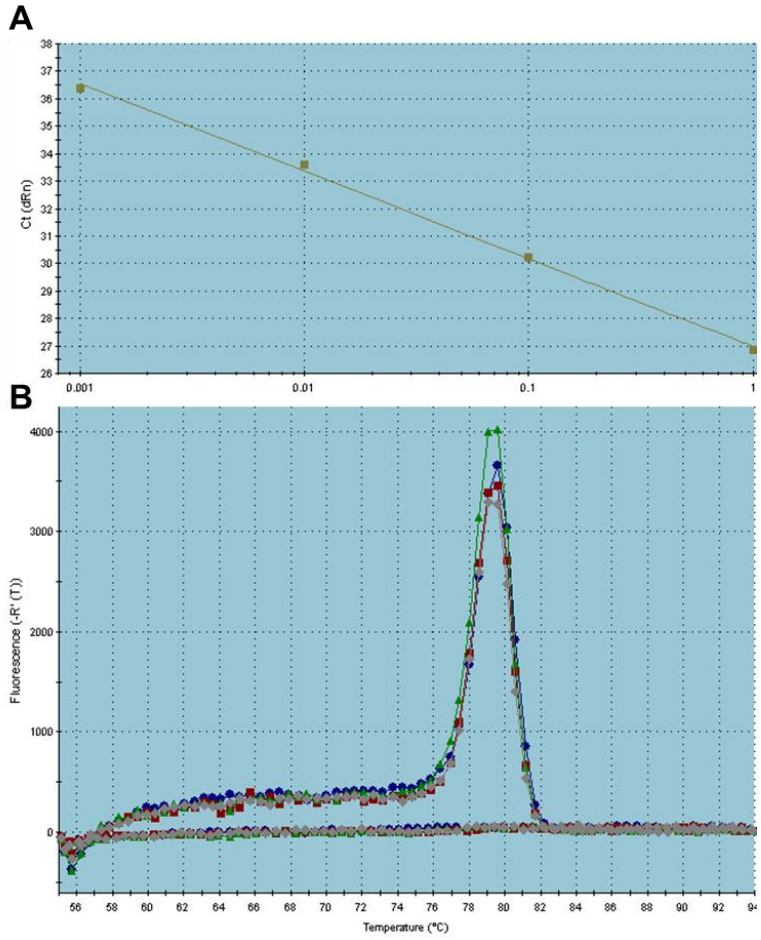

Figure 2.3 Validation of qPCR primer efficiency and specificity.
Representative image of **(A)** standard curve and **(B)** dissociation curve.

2.7 Protein methods

2.7.1 Protein extraction from cells and tissues

Cell monolayers were washed in ice-cold PBS to remove excess medium and scraped in an appropriate volume of radio-immunoprecipitation assay (RIPA) buffer (Appendix I) containing 0.15 x volume of complete mini protease inhibitor cocktail (Roche). Tissue samples were homogenised in the appropriate volume of RIPA buffer. All samples were vortexed further and subjected to one freeze thaw

cycle to ensure cell disruption and protein release. Prior to quantification of protein concentration, samples were centrifuged and the supernatant removed and stored at -20°C to ensure no further protein release from the cell pellet/tissue material.

2.7.2Quantification of protein concentration

2.7.2.1 DC assay

To quantify protein concentration in each sample, the Bio-Rad DC protein assay (Bio-Rad, Hertfordshire, UK) was used (similar to the well-documented Lowry assay) following manufactures instructions. Briefly, a protein standard (γ globulin) was used to generate a standard curve. Duplicates of 5µl of standard or sample was added to a well of a 96-well plate followed by 25µl alkaline copper tartrate (reagent A) and 200µl Folin's reagent (reagent B). The plate was shaken and incubated at room temperature for 15 minutes prior to the measurement of absorbance (750nm) using a Multiskan Ascent microplate reader. The unknown sample protein concentrations were extracted using the generated standard curve.

2.7.2.2 Bradford assay

For samples containing high detergent levels, the Bradford protein assay was used to measure protein concentration (Bio-Rad). γ globulin protein standards were prepared ranging from 10 -90µg/ml and used to generate a standard curve to which unknown sample values were extrapolated as described in 2.7.2.1. Standard or diluted sample (160µl) were added in duplicate into a 96-well plate, followed by 40µl Bradford dye reagent concentrate. The plate was shaken briefly and incubated at room temperature for 5 minutes prior to the measurement of absorbance (595nm) using a Multiskan Ascent microplate reader.

2.7.3 Western blotting

Following protein concentration quantification (section 2.7.2), protein samples were diluted to the same concentration (between 10-30µg) and the appropriate volume of 4x lithium dodecyl sulphate (LDS) sample buffer and reducing agent DTT was

added to each sample. Diluted protein samples were then denatured at 70°C for 10 minutes. The denatured protein samples and a pre-stained molecular weight marker to accurately determine protein size (All Blue, Bio-Rad) were chilled on ice for 5 minutes before being loaded onto pre-cast 3-8% Tris –Acetate or 10% Bis-Tris gels (Invitrogen, Paisley, UK - depending upon protein of interest molecular weight). Gels were run in a Novex Gel Tank (Invitrogen) containing 1x Tris Acetate or 1x MOPS running buffer, respectively. Anti-oxidant was added to the centre compartment of the tank to preserve reduced proteins (2.5µl/ml; Invitrogen). Proteins were separated by electrophoresis at 200V for 50mins. If necessary, to visualise protein bands on polyacrylamide gels prior to transfer the gel was washed 3 x 5 minutes in 100ml of ultrapure water, covered with 20ml of SafeStain (Life Technologies) and allowed to shake for 1 hour at room temperature. The gel was then washed with ultrapure water for at least 1 hour prior to visualisation either using a light box, or an Odyssey CLx scanner (LI-COR Biosciences, Lincoln, Nebraska) using the 700 channel (Fig. 2.1). Proteins were transferred onto a Hybound-ECL nitrocellulose membrane (GE Healthcare, Amersham), sandwiched between transfer buffer (Appendix I) soaked filter paper and sponges. This created a wet transfer within a transfer module (Invitrogen). Transfer was run on ice at 30V for 90mins. Following transfer, nitrocellulose was washed several times in a mixture of Tris-Buffered Saline and Tween 20 (TBST). Depending on western blot method (LICOR or ECL) the membrane was then blocked in Odyssey blocking buffer (LICOR) or 5% milk block, respectively. Primary antibodies were applied either overnight at 4°C with agitation or for 1 hour at room temperature (Primary and secondary antibodies listed in Appendix II). Membranes were then washed in PBS/TBST and secondary antibody applied in blocking buffer for 1.5 hours at room temperature (LICOR - 55 minutes with protection from light). Bound antibody was either detected using chemiluminescence detection or using the Odyssey infrared detection system were imaged directly on the LICOR Odyssey® scanner (Eaton *et al.*, 2013). For chemiluminescence detection Amersham ECL western blotting detection reagents A and B (GE Healthcare) were used. The nitrocellulose was

covered with the reagents in a ratio of 1:1 for 1min and chemiluminescence was detected with Amersham ECL Hyperfilm (GE Healthcare), which was developed using a Medical Film Processor (SRX-101A; Konica Minolta, Banbury, UK).

2.7.4 Stripping nitrocellulose

Antibodies were stripped from the nitrocellulose membranes using restore plus stripping buffer (Thermo Scientific) at 37°C for 30 minutes. To ensure complete antibody removal, membranes were probed with the appropriate secondary antibody and chemiluminescence was repeated.

2.7.5 Protein expression quantification

For ECL detected proteins, Image J was used to compare the density of bands on the scanned x-ray films. Imported images were converted to grayscale (8-bit). Using the rectangular selections tool, a rectangle was drawn around the first lane, and using the gel tool, the remaining lanes were step wise selected. Following selection, the lanes were plotted, which produces a profile plot representing the relative density of the contents of the rectangle over each lane. The peaks were closed and the area measured. These measurements were then exported into an excel sheet where the relevant statistics were performed. LICOR scanned blots were quantified on single channels using Image Studio Lite.

2.8 Histology

2.8.1 Paraffin embedded tissue

For wax sections all tissue was fixed in 4% PFA for 24-48 hours and then transferred to 70% ethanol. However calcified tissue was decalcified in 10% EDTA (pH 7.4) with gentle agitation at 4°C for approximately 3 weeks, with regular EDTA changes prior to transfer to 70% ethanol. Fixed tissue (PFA) were placed in cassettes, and subjected to the following automated protocol: two changes of each of the following: 70% ethanol for 1 hour; 80% ethanol for 1 hour; 95% ethanol for 1 hour; 100% ethanol for 1 hour; xylene (VWR, Leicester, UK) for 1 hour; and overnight in paraffin wax

(VWR) at 60°C, followed by fresh paraffin wax for 1 hour. Processed tissues was embedded in paraffin wax using plastic moulds and allowed to set at 4°C. All Wax blocks were trimmed to size and stored at 4°C until required. Prior to sectioning, paraffin blocks were cooled on an ice block overlaid with a wet paper towel for 30 minutes. Using a microtome (Ernst Leitz AG, Germany; blades used were MX35 Premier+ Microtome Blades, Thermo Scientific, Cheshire, UK), Blocks were then sectioned at a 5μm thickness and sections were floated for 1 minute in a 40°C water bath and transferred to a poly-l-lysine coated microscope slide (VWR International Ltd, Lutterworth, UK). Slides were dried at 37°C overnight to ensure attachment of the sections to the slide and stored at room temperature until required.

2.8.2 Frozen tissue

For frozen sections proximal tibiae were coated in 5% polyvinyl acetate (PVA) and livers from WT and *Phospho1*$^{-/-}$ mice were snap frozen in a cooled hexane bath, and stored at -80°C. Frozen tissue was embedded in optimal cutting temperature (OCT) embedding medium (Brights, Huntingdon, UK) and attached to a metal chuck. A cryostat (OTF500/HS-001, Brights) was used to section tissue. Excess OCT was removed and the tungsten carbon knife (Brights) blade angle was set to 25°C, chamber temperature to 25°C and specimen temperature to 23°C. 10μm sections were taken and transferred to Superfrost slides (Fisher, Loughborough) and stored at -80°C. For bone sample's, the Cryojane tape-transfer system was used (Instrumedics Inc, Richmond, IL, US) to allow preservation of the calcified bone. Briefly, after the block was trimmed, a piece of transfer tape was adhered to the block face, the adhesive tape is placed section-side-down on the adhesive-coated slide, and is laminated to the adhesive layer using a cold roller, a flash of ultraviolet light passes through the slide to polymerise the adhesive layer on the slide into a hard, solvent-resistant plastic, tightly anchoring the section to the slide, the tape is peeled away leaving the still frozen section tightly bonded to the plastic layer. The slides were finally air-dried and fixed in 100% ice cold acetone and stored at -80°C until use.

2.8.3 Haematoxylin and eosin

Paraffin embedded sections (section 2.8.1) of adipose tissue were stained with haematoxylin and eosin (H&E) such that morphology of adipocytes could be measured. Slides were first de-waxed in xylene and rehydrated through a series of alcohols to dH_2O and stained with H&E using Leica Autostainer and mounted in DePeX (VWR, Lutterworth, UK). Slides were mounted with DPX and visualised using a Nikon E600microscope with a digital camera attached, using Image Tool (Image Tool Version 3.00). The adipocyte diameters of 100 adipocytes per section (sections were take every 120μm throughout the tissue) were measured using ImageJ software (Lee *et al.*, 2007).

2.8.4 Oil-Red O

Frozen liver sections (section 2.8.2) were washed with running tap water for 10 minutes, rinsed with 60% isopropanol and stained with freshly prepared Oil-Red-O working solution for 5 minutes (Appendix I). Slides were then washed with 60% isopropanol and nuclei was lightly stained with haematoxylin (5 dips), rinsed with distilled water and mounted in aqueous mountant (Life Technologies).

2.8.5 Quantification of pancreatic β-cell islet size number and size

Paraffin embedded pancreata (as detailed in section 2.8.1) from 120 day male CD WT and *Phospho1*$^{-/-}$ mice were sent to Dr. Sophie Turban (University of Edinburgh), who kindly immunostained sections with guinea pig anti-insulin (1:300) (AbCam, Cambridge, UK) prior to image quantification of islet areas using KS300 software (3.0 CarlZeiss Vision, GmBH).

2.9 Fat phenotypic analysis

2.9.1 Computed tomography

The bodies of freshly sacrificed male mice (35, 120 180 and 200 day old C57BL/6 mice and 120 day old male WT and *Phospho1*$^{-/-}$ control and HFD mice) were immediately CT-scanned using a Siemens Somatom Esprit Computer Tomography

(CT) Scanner. Multi-object (6 mice/scan), cross-sectional CT images were taken along the length of the body (3 mm apart, field of view 450 mm, approximately 70 images per mouse) (Luu *et al.*, 2009). Sheep Tomogram Analysis Routines (STAR) software (BioSS - V.4.8; STAR: Sheep Tomogram Analysis Routines, University of Edinburgh, http://www.ed.ac.uk) was used to calculate the total area and average densities of fat, muscle and bone in each carcass image without segmenting out guts and organs, based on density thresholds (low fat: -174 Hounsfield units **(**HU), high fat: -12 HU, low muscle:-10 HU, high muscle: 92 HU, bone: < 94 HU)). These values were established from sheep calibration trials in which lambs underwent CT scanning followed by slaughter and full dissection (Glasbey and Robinson, 2002). Sheep thresholds were used as mouse specific thresholds have not been reported in the literature to the best of my knowledge.

2.9.2 Freeze drying

Whole mouse carcasses and corresponding isolated adipose tissue were freeze dried to determine the dry matter weight (DM) of the carcass. The predication of individual fat percentage values was calculated by regression on DM content (DM/BW) using an equation (FatP _DM/BW (%) x 113 - 30.2) derived by Hastings & Hill (Hastings and Hill, 1989). The CT based measures of tissue weights were then compared to the DM-based estimates for the fat content (fat %) and the fat free mass (FFM) in (%) using simple linear regression:

$y_i = b_0 + b_1 x_i$,

with b_1= regression coefficient and b_0 = intercept

2.9.3 Micro magnetic resonance imaging and liver spectroscopy

Dr. Jansen (University of Edinburgh, Preclinical Imaging) conducted micro-magnetic resonance imaging (μMRI) and liver spectroscopy on male 120 day-old WT and *Phospho1*$^{-/-}$ CD and HFD mice. Mice were sacrificed at the Roslin Institute and placed in a plastic bag, weighed and transported to the preclinical imaging facility at the Little France campus to avoid quarantine restrictions. The Varian 7

Tesla magnet using VnmrJ Pre-Clinical MRI Software was used to acquire T2 weighted images in both the axial (1mm thickness, 192x192 pixels, TR – 3000ms, TE 24ms, 1 average, FOV – 38.4 x38.4) and coronal planes (0.5mm Thickness, 512x256 pixels, TR – 3000ms, TE 24ms, 4 averages, FOV – 102.4 x51.2) (Fig. 2.4). Liver spectroscopy was conducted on user defined areas (TR - 1800ms, TE – 11.5 ms, 16 averages, Vauxhall 3x3x3). Acquired DICOM images were analysed using sliceOmatic (TomoVision). This software was used to tag user defined areas allowing the quantification of total SB and MF. Tagging was done blind and the same images from one mouse were analysed twice to ensure reproducibility. Liver spectra were analysed by fitting Lorentzian and Gaussian lineshapes to fit peaks to MR data using jMRUI (Graphical User Interface that allows time-domain analysis of *in vivo* MR data http://www.mrui.uab.es/mrui/mrui).

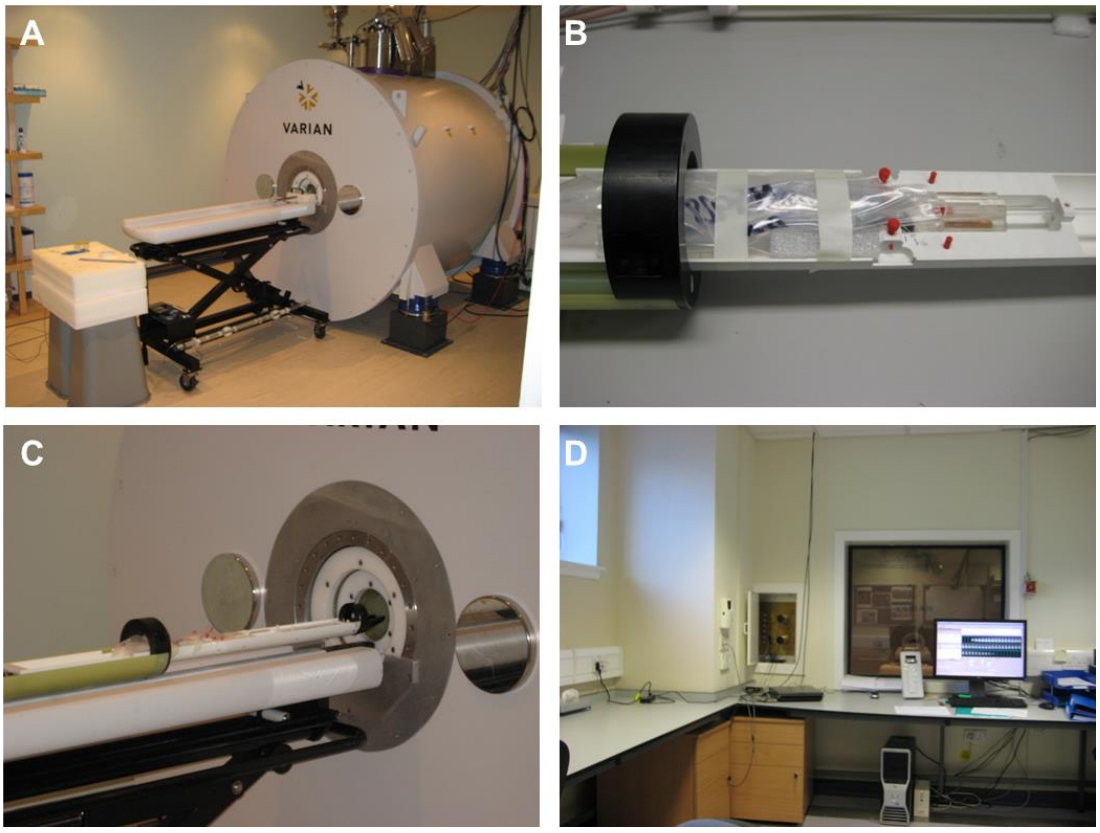

Figure 2.4 Micro magnetic resonance imaging (μMRI) in mice
Representative image of **(A)** Varian 7 Tesla μMRI instrumentation **(B-C)** insert for micro-imaging **(D)** image reconstruction and post-processing facility.

2.10 Biochemical Methods

2.10.1 Choline assay

Serum from 35 day old and 120 day old CD and HFD mice was collected as described in section 2.5.3. The choline/Acetylcholine Assay Kit (Abcam) was used to determine serum choline. The assay was carried out in accordance with the manufacturer's instruction. The serum samples used in the assay were plated in duplicate and absorbance (750nm) was measured using a Multiskan Ascent microplate reader.

2.10.2 Pancreas insulin content

Pancreases from 120 day old WT and *Phospho1*$^{-/-}$ mice were dissected, weighed and submerged in 2ml of pancreata lysis buffer (Appendix I). Pancreata were homogenised using a small hand-held homogeniser. The homogenate (100µl) was diluted in 2ml of acidified ethanol (1.5% HCl in 70% ethanol) overnight at -20°C. The next day samples were centrifuged at 2000g for 15 minutes at 4°C. The aqueous solution neutralised by the addition of 100µl 1M Tris (pH 7.5). Insulin content was measured by ELISA (as described in section 2.10.6) and normalised to protein content as measure by the Bradford assay (section 2.7.2.2).

2.10.3 Malachite green phosphatase assay

The BIOMOL Green reagent (Enzo Life sciences, Exeter, UK) was used to measure free-phosphate released during enzymatic phosphatase assays. This assay is a modification of the classic Malachite green assay (Martin *et al.*, 1985; Harder *et al.*, 1994). Briefly the reactions were measured in 96-well plates with a total volume of 50µl. Serial dilutions of the phosphate standards were made using the assay buffer (20mM Tris, 2mM $MgCl_2$, 25µg/ml BSA (Fraction V)). Substrates and the enzyme (rec human PHOSPHO1 – already available in the lab) were also diluted in assay buffer. Reactions were allowed to proceed at 37°C for 30 minutes. The reaction was then terminated by the addition of 100µl BIOMOL green reagent and left at room temperature for 20-30 minutes to allow for development of the green colour. The

absorbance of each well at 620 nm was measured and the specific activity was calculated in units of activity per mg of enzyme, where 1 unit of activity represents the hydrolysis of 1 nmol of phosphate per minute (Roberts *et al.*, 2004).

2.10.4 Triglyceride colorimetric assay

The triglyceride colorimetric assay kit (Cayman Chemicals, Michigan, and USA) was used to measure triglyceride levels present in blood serum from 120 day old WT and *Phospho1*$^{-/-}$ mice. This assay is based on the enzymatic hydrolysis of the triglycerides by lipase to produce glycerol and free fatty acids. Briefly, 10µl of the prepared standards and serum was added to the provided plate in duplicate and the assay was initiated by the addition of 150 µl of diluted triglyceride enzyme mixture. The plate was then shaken, covered and incubated at room temperature for 15 minutes. The glycerol released was measured by a coupled enzymatic reaction system with a colorimetric readout at 540 nm (Multiskan Ascent) and total triglyceride content was calculated.

2.10.5 Osteocalcin carboxylation status

Serum from 56 day old and 120 day old male WT and *Phospho1*$^{-/-}$ CD mice were collected as described in section 2.5.3 and sent to Prof. Karsenty and Dr. Ferron (Columbia University, USA) who conducted an ELISA-based method to quantify osteocalcin carboxylation in mice (Ferron *et al.*, 2010b). Briefly, ELISA plates (R&D systems, Minneapolis, MN, USA) were coated with 100µl of a 12 µg/ml solution of affinity purified anti-GLU-OCN, anti-GLA13-OCN or anti-MID-OCN, washed and blocked. 5µl of blank, standards (purified GLU-OCN or synthetic GLA-OCN) or serum samples were added to the plate and incubated overnight at 4°C. HRP-conjugated anti-CT-OCN was added to each well and the plate incubated for 1 hour at room temperature, further washes were conducted prior to the addition of a 3,3′,5,5′-tetramethylbenzidine substrate and the final stop solution. Absorbance (450nm) was measured using a plate reader (Biorad). Concentrations of GLU-OCN, GLA13-OCN and total OCN in the samples were calculated from polynomial

second order or exponential standard curve obtained from the standard included in each assay.

2.10.6 Enzyme-linked Immunosorbent Assay (ELISA)

To measure serum leptin, insulin and adiponectin serum was collect (described in section 2.5.3) and sample was analysed in duplicate using commercially available ELISA's following manufacturer's instructions (ChrystalChem, Chicago, IL, USA).

2.11 Mass Spectroscopy

2.11.1 Protein sequencing

To determine if PHOSPHO1 was present in various tissues recombinant PHOSPHO1 protein was first sent to the Mr Dougie Lamont at the FingerPrints Proteomics Facility (College of Life Sciences, University of Dundee) to generate a purpose built inclusion list that was used to detect PHOSPHO1 in protein tissue samples (pancreas, quadriceps femoris and calvaria). Following completion protein samples from the tissues of interest were sent to Mr Dougie Lamont and a mass spectroscopy search was performed using proteome discovery software (Thermo Scientific) against both IPI mouse database and purpose built inclusion list.

2.11.2 Quantification of ceramide species in serum samples

To quantify serum ceramide in 120 day old male WT and *Phospho1*$^{-/-}$ CD mice serum lipids were extracted according to the method of Folch *et al.* (Folch *et al.*, 1957) fully supervised by Professor Phillip Whitfield (University of the Highlands and Islands, Inverness). Briefly, 50µl of serum was extracted with 4 ml chloroform/methanol (2/1, v/v) containing 10µl 1nmol D2, 10pmol D3 and 10pmols D2 as internal standards (C17 ceramide was used as a control as this species is not present in humans). The mixture was stood at room temperature for 1 hour and subsequently partitioned by the addition of 1.3ml of 0.1M KCL. The mixture was centrifuged to facilitate phase separation removing the lower chloroform layer which was then evaporated under nitrogen gas. The lipid extract was then reconstituted in 2 ml

prior to solid-phase extraction. A silica solid-phase extraction cartridge (100mg/3 ml) was attached to the chamber and primed with 5ml chloroform, the serum chloroform extract was then applied to the column, and the column was then washed with 5ml of chloroform and 10ml of chloroform/ethyl acetate (1/1, v/v) before elution of the glycolipid fraction with 5 ml of acetone/methanol (9/1, v/v) and the fraction was dried down and reconstituted in 200µl methanol containing 5mM ammonium formate glycolipid analysis and quantification was performed by Professor Phillip Whitfield via electrospray ionisation-tandem mass spectrometry (ESI-MS/MS) using a TSQ Quantum Ultra triple quadrupole mass spectrometer equipped with a heated electrospray source (HESI) and coupled to a Accela 1250 UHPLC system (Thermo Scientific, Hemel Hempstead, UK)(Whitfield *et al.*, 2002) (Fig. 2.5). Data were analysed using software driven algorithm (thermo Xcalibur Quad Browser) imputing known ceramide species (Appendix VI).

Figure 2.5 Mass spectrometer
Representative image of **(A)** TSQ Quantum Ultra triple quadrupole mass spectrometer **(B)** Heated electrospray source (HESI).

2.11.3 Identification of differential expressed serum proteins

Proteins from 120 day old male WT and *Phospho1*$^{-/-}$ CD and HFD male mice serum were be extracted and prepared. Protein samples were precipitated using cold acetone, and gently dried. Samples were dissolved in ICAT denaturing buffer containing the reducing agent trichloroethyl phosphine, alkylated (iodoacetamide), and digested with sequencing grade trypsin (Sigma). Extracted peptides were analysed by Dr. Cal Vary, MMCRI according to published methods (Romero *et al.*, 2011). Quantitation was accomplished by analysis of peak area. The search parameters allowed for cysteine modification by the ICAT reagent and biological modifications programmed in the algorithm (i.e., phosphorylation, amidation, tryptic fragments). The detected protein threshold was set to 2.0 to achieve 99% confidence. Identified proteins were grouped by the Paragon algorithm (Life Technologies) to minimise redundancy, and following bias correction (method kindly provided by Dr. Cal Vary) Functional pathway and causal network analysis was performed using QIAGEN's Ingenuity (IPA), GeneMANIA and EXPANDER (EXpression Analyzer and DisplayER) following training from Dr. Jacqueline Smith, University of Edinburgh.

2.11.4 Identification of differential expressed serum lipids.

Total lipids were extracted from serum using the Bligh-Dyer method for total lipid extraction (Bligh and Dyer, 1959) and silica based solid phase extraction was employed for sample clean up and fractionation prior to analysis. This was done by myself with assistance from Dr. Cal Vary, MMCRI. Lipids were subsequently analysed by direct infusion on a hybrid quadrupole time-of-flight (TOF) mass spectrometer (TripleTOF 5600, ABSciex, MA, USA) using the MS/MSALL technique in positive mode essentially as described (Simons *et al.*, 2012) Lipid species were identified using LipidView software (ABSciex), and principle component analysis (ABSciex) was used to identify and group lipid species according to contribution to sample differences. Lipid identification was corroborated by precursor ion scanning

using a 4000QTRAP triple quadrupole mass spectrometer (ABSciex) (Stohn *et al.*, 2015).

2.12 Bone analysis

2.12.1 X-ray and 3 Point bending

Male 35 day CD, 120 day CD and 120 day HFD WT and *Phospho1*$^{-/-}$ bones were x-rayed using a Faxitron (Biooptics, Arizona, USA). The exposure was set to 15 seconds at 22kV. 3-point bending was conducted on male tibias from the defined groups using a LXR materials testing machine (Lloyd Instruments, West Sussex, UK) fitted with a 500N load cell (Huesa *et al*. 2011). The span of the anvil was set to 7.5mm with the lowering of the cross-head at a speed of 1 mm/min. Tibiae were placed on the anvil in a pre-determined orientation. Data was recorded after every 0.2 N change in load and every 0.1 mm change in deflection. Tibiae were tested until fracture (if possible). From the load extension curve, failure (point of maximum load), fracture (load rapidly decreases to 0), maximum stiffness (maximum gradient of the rising portion of the curve) and yield (95% of the maximum stiffness) were defined (Aspden, 2003) (Fig. 2.6). Tibia lengths were measured using callipers.

2.12.2 Micro-computed tomography imaging

To assess the trabecular architecture, cortical geometry and relative density of bone mineral, micro-computed tomography (μCT) imaging was carried out with guidance from Professor Rob Van't Hof and Dr. Camen Huesa. Bone specimens were dissected, placed into H_20 and stored at -20°C pending analysis. High-resolution scans with an isotropic voxel size of 5 μm (trabecular) or 10μm cortical scanning were acquired with a micro-computed tomography system (μCT, 60 kV, 0.5 mm aluminum filter, 0.6° rotation, Skyscan 1172, Brukker microCT, Kontich, Belgium). Two images were averaged at each rotation angle to reduce noise. Scans were reconstructed using NRecon software (Brukker microCT). The base of the growth plate was used as a standard reference point, and a 1000μm section of the metaphysis was taken for analysis of trabecular bone. For analysis of cortical

structure a 400 μm section of the mid-diaphysis was scanned 1500μm below the base of the metaphysis section. CTAn software (Bruker) was used to analyse appropriate parameters (bone volume fraction (BV/TV), trabecular thickness (Tr. Th.), trabecular separation (Tr. Sp.), trabecular number (Tr. No.), trabecular pattern formation (Tr. Pf.), structural model index (SMI), degree of anisotropy (DA), cortical porosity (Cor. Por. %), cortical thickness (Cor.Th.) and cortical bone mineral density (Cor. BMD) and reduce noise in the reconstructed images by applying a median filter with a radius of 1 pixel. Appropriate thresholds were set to ensure only bone was analysed. Calcium hydroxyapatite phantoms of a known density were scanned using the same settings as above for calibration, from which BMD values were calculated.

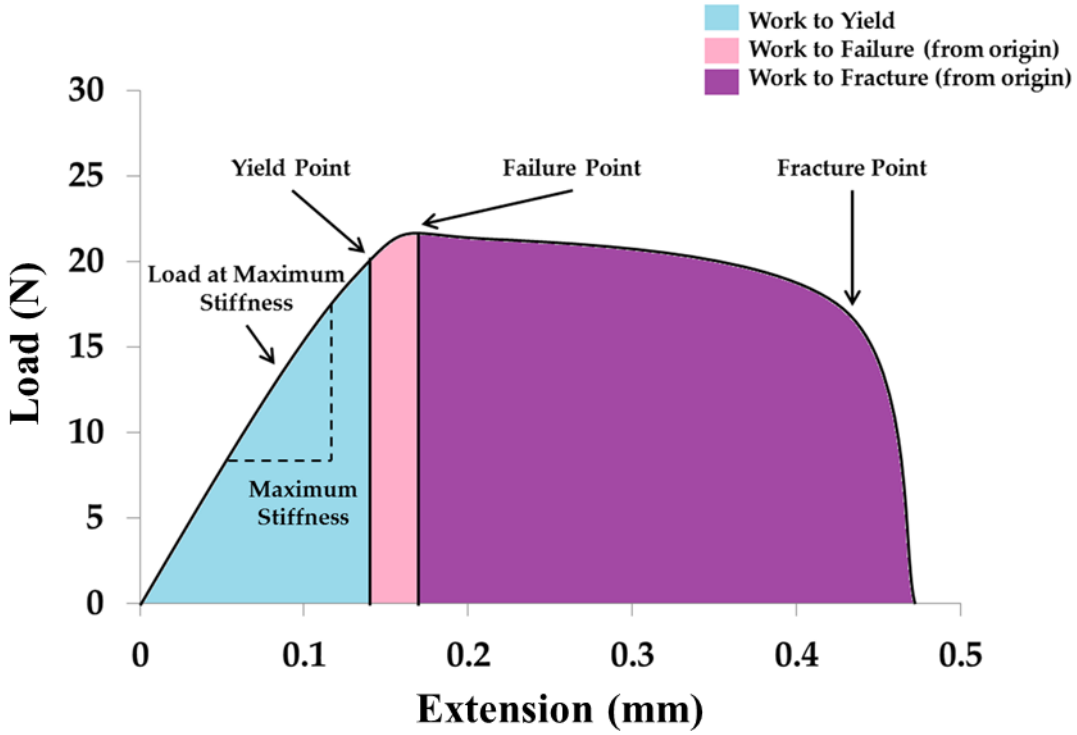

Figure 2.6 Three point bending load extension curve
Diagram of a typical load extension curve obtained with 3-point bending. The measured parameters are highlighted.

2.13 Statistical analysis

Data was analysed in this thesis using various statistical models. All data were checked for normality and equal variance. Linear regression and correlation analysis based on Excel (Microsoft Office 10) built-in functions with interval of confidence and testing of the correlation coefficients were performed according to standard procedures described in the statistical literature (Rasch *et al.*, 1978a; 1978b). The SAS software was used to fit the generalised linear model, and the Gompertz growth model was performed using Excel (Microsoft Office 10) built-in functions. The Student's *t*-test, ANOVA and a Two Way Repeated Measures ANOVA (two factor repetition with Holm-Sidak pairwise multiple comparison procedures) for normally distributed data and non-parametric data was analysed using a Mann–Whitney Rank Sum test using Sigma Plot software v11.0 (Systat Software Inc., London, UK) Data are presented as means ± standard error (SEM) were appropriate. Regression and correlation coefficient's are given with the intervals of confidence ($P = 0.05$) and $P < 0.05$ was considered to be significant.

Chapter 3

Initial observations on the importance of PHOSPHO1 in the regulation of energy metabolism

3.1 Introduction

Matrix mineralisation is a tightly regulated physicochemical/biochemical biphasic process localised within terminally differentiating growth plate chondrocytes, osteoblasts and odontoblast, facilitating cartilage, bone and tooth formation (Cecil and Anderson, 1978; Anderson *et al.*, 1990). Mineralisation is dependent upon the accumulation of calcium and P_i which are permissive for the initiation of HA crystals. This process requires both non-collagenous and collagenous matrix proteins as well as a balance of mineralisation promoters and inhibitors such as include TNAP, NPP1, SIBLING proteins, ANK and PHOSPHO1 (section 1.5.2).

Phosphatase, Orphan 1 is a member of the HAD superfamily of Mg^{2+} dependent hydrolases, localised in sites of mineralisation whereby *Phospho1* is expressed 100-fold higher in differentiating chondrocytes compared to non-chondrogenic tissue (Houston *et al.*, 1999; Roberts *et al.*, 2008). PHOSPHO1 shows high phosphohydrolase activity towards MV membrane phospholipids (e.g. P-Cho), whereby it scavenges P_i. This first phase of mineralisation occurs simultaneously with the accumulation of calcium ions in the MV, regulated by calcium binding molecules such as annexin I and phosphatidylserine (Stewart *et al.*, 2003; Roberts *et al.*, 2004; Stewart *et al.*, 2006; Roberts *et al.*, 2007) (Wu *et al.*, 1995; Anderson, 2003) resulting in the formation of HA crystal's. Upon MV membrane breakdown, preformed HA is exposed to the extracellular fluid allowing propagation into the collagenous ECM.

To further understand the roles of PHOSPHO1, *Phospho1*$^{-/-}$ mutant mice were generated by N-ethyl-N-nitrosourea mutagenesis (ENU) (Yadav *et al.*, 2011). These mice presented with significant skeletal pathology, growth plate abnormalities, spontaneous fractures, bowed long bones, osteomalacia, and scoliosis in early life (Huesa *et al.*, 2011; Yadav *et al.*, 2011). To uncover gene changes engendered in the *Phospho1*$^{-/-}$ mutant mice, a microarray study was conducted using WT and *Phospho1*$^{-/-}$ primary calvarial osteoblasts (unpublished data). The key finding was

that *Esp*, the gene encoding the protein osteotesticular protein tyrosine phosphatase, was up regulated 20-fold in *Phospho1*$^{-/-}$ osteoblasts compared to WT osteoblasts. *In vitro*, *Esp* coordinates the differentiation of the pre-osteoblast to a mature, mineralising cell, and *in vivo* may be a critical regulator of the commitment of mesenchymal cells to the ossification of new bones during skeletogenesis (Mauro *et al.*, 1994; Chengalvala *et al.*, 2001; Yunker *et al.*, 2004). Interestingly, PTPs are key regulators of InsR signalling, dephosphorylating and inactivating the InsR within minutes of stimulation to maintain glucose homeostasis (Mauro *et al.*, 1994; Hunter, 1995; Schlessinger, 2000; Dacquin *et al.*, 2004; Tonks, 2006; Lee *et al.*, 2007). Thus two models have been generated by others to explore the function of *Esp*:

I. Global knock out of *Esp* (Lee *et al.*, 1996).
II. Osteoblast specific knock out of *Esp* (Dacquin *et al.*, 2004).

Both mutants exhibited severe hypoglycemia and hyperinsulinemia resulting in postnatal lethality in the first two weeks of life. Further mechanistic characterisation identified that OST-PTP dephosphorylates the InsR, negatively regulating the osteoblast insulin signalling cascade. These data were therefore suggestive that OST-PTP and PHOSPHO1 may crosstalk in regulating energy metabolism.

Upon the commencement of my PhD two key preliminary pieces of evidence emerged strengthening the hypothesis that indeed PHOSPHO1 may regulate global energy metabolism. Firstly, utilising a commercial phosphatase profiling assay (JPT Peptide Technologies, Berlin, Germany), PHOSPHO1 displayed the highest hydrolysing activity towards the InsR S (P) 1322, suggesting PHOSPHO1 can potentially dephosphorylate the InsR at serine 1322. Secondly, yeast 2 hybrid studies revealed a potential interaction between PHOSPHO1 and GRB10 interacting GIGYF1 which, as the name suggests forms a complex with GRB10 to regulate both insulin and IGF-1 receptor signalling. In the absence of *Phospho1* it could therefore be hypothesised that there would be increased IGF-1 receptor phosphorylation under insulin stimulation, as well as increased phosphorylation of IRS1 and Src

homology 2 domain-containing transforming protein 1 (UniProt, 2011). Therefore the overarching aim of this chapter was to confirm / oppose preliminary data obtained by Dr. Carmen Huesa.

3.2 Hypothesis

PHOSPHO1 directly mediates the dephosphorylation and deactivation of InsR situated on the osteoblast.

3.3 Aims

I. Re-analysis of microarray data.
II. Establish if *Phospho1* overexpression in osteoblasts down regulates *Esp* expression.
III. Determine if PHOSPHO1 dephosphorylates the InsR.
IV. Investigate the effects of insulin stimulation in calvarial osteoblast cultures.
V. Comparison of PHOSPHO1 expression levels in murine tissues.

3.4 Materials and Methods

3.4.1 Microarray analysis of WT and *Phospho1*$^{-/-}$ osteoblasts

Analysed microarray data from WT and *Phospho1*$^{-/-}$ osteoblasts was kindly provided from Dr. Manisha Yadav (Sanford Children's Health Research Center, Sanford-Burnham Medical Research Institute, La Jolla, CA, USA) in the form of a spreadsheet depicting fold changes. Quantitative PCR was used to confirm gene expression changes in *Esp* as described in section 2.6. Functional pathway and causal network analysis was performed using QIAGEN's IPA and GeneMANIA using the query genes: *Adamts4, Bmp4, Cd68, Cfp, Fmod, Lum, Mpeg1, Phospho1, Runx2, Slc1a3, Spic* and *Vdr*.

3.4.2 Primary osteoblasts

Under sterile conditions calvariae were dissected from 3-4 day old new-born WT and *Phospho1*$^{-/-}$ mice as described in section 2.2.2. Extracted cells were resuspended

in osteoblast medium (Appendix I) and pooled to obtain a single cell suspension. The cells were expanded in flasks in a humidified atmosphere of 95% air/5% CO_2 and maintained at 37°C until 80–90% confluence and were then plated at 10000 cells/cm^2 in multi-well plates.

3.4.3 Viral transduction of primary osteoblasts

Lentivirus' were a kind gift from Dr. Carmen Huesa who conducted virus packaging. Primary osteoblasts were maintained in osteoblast medium in T25 flasks as described in section 2.2.4. At 75% confluency 50% of the osteoblast media was removed and either empty vector (EV), PHOSPHO1 overexpressing virus (P1) or flag tagged PHOSPHO1 overexpressing virus (FP1) was added. Following transfection successfully transfected primary osteoblasts were selected and expanded (section 2.2.6).

3.4.4 Malachite green phosphatase assay

The BIOMOL Green reagent was used to measure free-phosphate released during enzymatic phosphatase assays (section 2.10.3). The absorbance of each well at 620nm was measured and the specific activity was calculated in units of activity per mg of enzyme, where 1 unit of activity represents the hydrolysis of 1 nmol of phosphate per minute.

3.4.5 mRNA analysis of primary osteoblasts cells

Ribonucleic acid was isolated from viral transduced calvarial primary cell cultures using a Qiagen RNeasy Lipid Tissue Mini Kit, mRNA concentration of each sample was determined (section 2.6.1) and samples were reverse transcribed to produce cDNA which was diluted to 5ng/μl for RT-qPCR analysis described in section 2.6.2 and 2.6.4. Results were normalised to the *Atp5b* housekeeping gene and the dissociation curve was checked for the presence of one product. Relative gene expression was calculated using the ΔΔCt method (Livak & Schmittgen 2001). All primers used are detailed in Appendix V.

3.4.6 Protein analysis of primary osteoblast cells

Protein was extracted from viral transduced calvarial primary cell cultures (section 2.7.1) and total protein content was assessed using the Bio-Rad DC protein assay according to the manufacturer's instructions (section 2.7.2.1). PHOSPHO1 protein expression was determined using an anti-human anti-PHOSPHO1 HuCAL Fab bivalent antibody at a dilution of 1:1000 and a HRP-labelled goat anti-human secondary antibody (1:5000). The ECL detection kit was used to detect antibody labelling. To allow for protein expression quantification and conformation of accurate protein loading, nitrocellulose membranes were stripped and probed with mouse monoclonal HRP-labelled anti-β actin antibody (1:50000).

3.4.7 Insulin treatment of primary osteoblasts

Primary calvarial osteoblasts were extracted as described in (2.2.2). Osteoblasts were plated at 10000cells/cm^2 in 6 well plates in osteoblast medium (Appendix I). Upon confluency, cells were serum starved for 4 hours in serum free medium (αMEM) and stimulated with insulin (10nM; Sigma) for 10 minutes before lysis (non-stimulated cells acted as controls). Protein was extracted for analysis as described in section 2.7.1. Membranes were probed with specific antibodies against phospho-Aktser473, total Akt, phospho-GSK3βser9, total GSK3β phospho-Erk 1/2thr202/tyr204 and total Erk1/2 and protein expression was visualised using the ECL western blotting detection system.

3.4.8 Immunocytochemistry

Osteoblasts were plated in collagen coated 6 well plates. At confluency, cells were fixed in in 4% paraformaldehyde for 15 minutes, permeabilised and blocked as described in (section 2.3.2). Following removal of blocking buffer, cells were incubated with the primary antibody (1xPBS, 1% BSA (Faction V), 0.3% Triton X-100)) overnight at 4°C. Cells were washed in PBS 3 x 5 minutes and the fluorochrome-conjugated secondary antibody diluted in antibody dilution buffer was added to the cells for 90 minutes at room temperature in the dark. Following a

final 3 x 5 minutes wash in PBS, coverslips were mounted using ProLong Gold Antifade Mountant with DAPI (Invitrogen). Slides were analysed using a Nikon EC-1 confocal microscope.

3.5 Results

3.5.1 Microarray analysis

To determine possible functional roles of PHOSPHO1 in energy metabolism, the osteoblast microarray data obtained by Dr. Manisha Yadav was subjected to re-analysis. Raw data was arranged into the correct format and inputted into the IPA software. Intriguingly, 21 of the 309 inputted genes significantly were significantly associated with T2DM ($P = 1.04x10^{-6}$) (Table 3.1). This therefore warranted a deeper gene regulatory pathway analysis using IPA inbuilt knowledge database. Ingenuity knowledge database is a vast repository of biological interactions and functional annotations originating from original peer reviewed articles which allow the integration of predicted upstream and downstream regulators of the inputted microarray data associated with insulin dependent diabetes mellitus. Using this tool, an array of 45 indirect interactions were identified between insulin dependent diabetes mellitus, inputted genes and various cytokines, growth factors, enzymes, kinases, peptidases, phosphatases, transcriptional regulators, transmembrane receptors and transporters (Fig. 3.1A). To establish whether the predicted molecules were indeed associated with diabetes and/or bone an *in silico* search was performed using PubMed (Gene + Key words: adiposity, bone, diabetes, glucose, osteoblasts, osteocalcin, and obesity). Of the 45 molecules identified only 10 genes were found to be associated with both diabetes and bone and one gene, solute carrier family 1 (glial high affinity glutamate transporter), member 3 (*Slc1a3*), was only associated with diabetes. However, glutamate transporters are known to play important roles in osteoblast and osteoclast differentiation and activity, bone mass regulation and response to osteogenic mechanical load; therefore *Slc1a3* was retained in the cohort (reviewed in (Brakspear and Mason, 2012) (Table 3.2). Upon completion of the *in silico* search, gene expression of the selected molecules were examined by RT-qPCR.

Validation using RT-qPCR ascertained that all genes (*Vdr, Slc1a3, Adamts4, Bmp4, Cd68, Cfp, Cxcl4. Fmod and Lum*) except *Mpeg1* were up/down regulated as predicted by IPA (Fig. 3.1 B and Table 3.2).

Gene in Dataset	Fold From WT
Abhd16a	-14.224
Alox5ap	-3.427
Ccl9	-3.863
Clec6a	-3.787
Ctss	-2.372
Fcer1g	-15.853
Fcgr2a	-3.299
Fcgr2b	-2.432
Gp49a/Lilrb4	-3.138
Gp49a/Lilrb4	-3.138
Gpnmb	-13.704
Hla-b	-18.680
Icam1	2.527
Ifi202b	11.328
Lyz1/Lyz2	-11.330
Mpeg1	-7.108
Mrc1	-2.510
Ms4a6a	-4.583
Serping1	1.993
Tyrobp	-2.971
Vdr	2.297
VIP	2.093

Table 3.1 Osteoblast microarray candidates involved associated with insulin dependent diabetes mellitus
21 genes from the WT and *Phospho1*$^{-/-}$ osteoblast microarray were identified by Ingenuity Pathway Analysis to be associated with type two diabetes mellitus $P = 1.04 \times 10^{-6}$.

To further establish genetic interactions and associations between the genes identified from the *in silico* output search; the identified 10 genes were inputted into the online network creator, GeneMANIA. Similarly to Ingenuity's knowledge database, GeneMANIA searches publicly available biological datasets to identify related genes via protein-protein, protein-DNA and genetic interactions, protein expression data, protein domains and phenotypic screening profiles, producing a gene network (Fig. 3.2).

Intriguingly, the GeneMANIA generated gene network highlighted that *Phospho1* may indeed interact with *Grb10* and *Insr* to regulate the glucose metabolic process. Excitingly, *Atf4* and *FoxO1* were also highlighted in the gene network. FoxO1 has been shown to co-localise with *Atf4* in the osteoblast nucleus, promoting the transcriptional activity of *Atf4*, thus up-regulating *Esp* expression in osteoblasts and osteocalcin (OCN) inactivation (Kode *et al.*, 2012). These gene network data are suggestive of a PHOSPHO1, OST-PTP and OCN mutual regulation.

Taken together the IPA and GeneMANIA network analysis highlight a potential role for PHOSPHO1 in the regulation of whole body glucose metabolism.

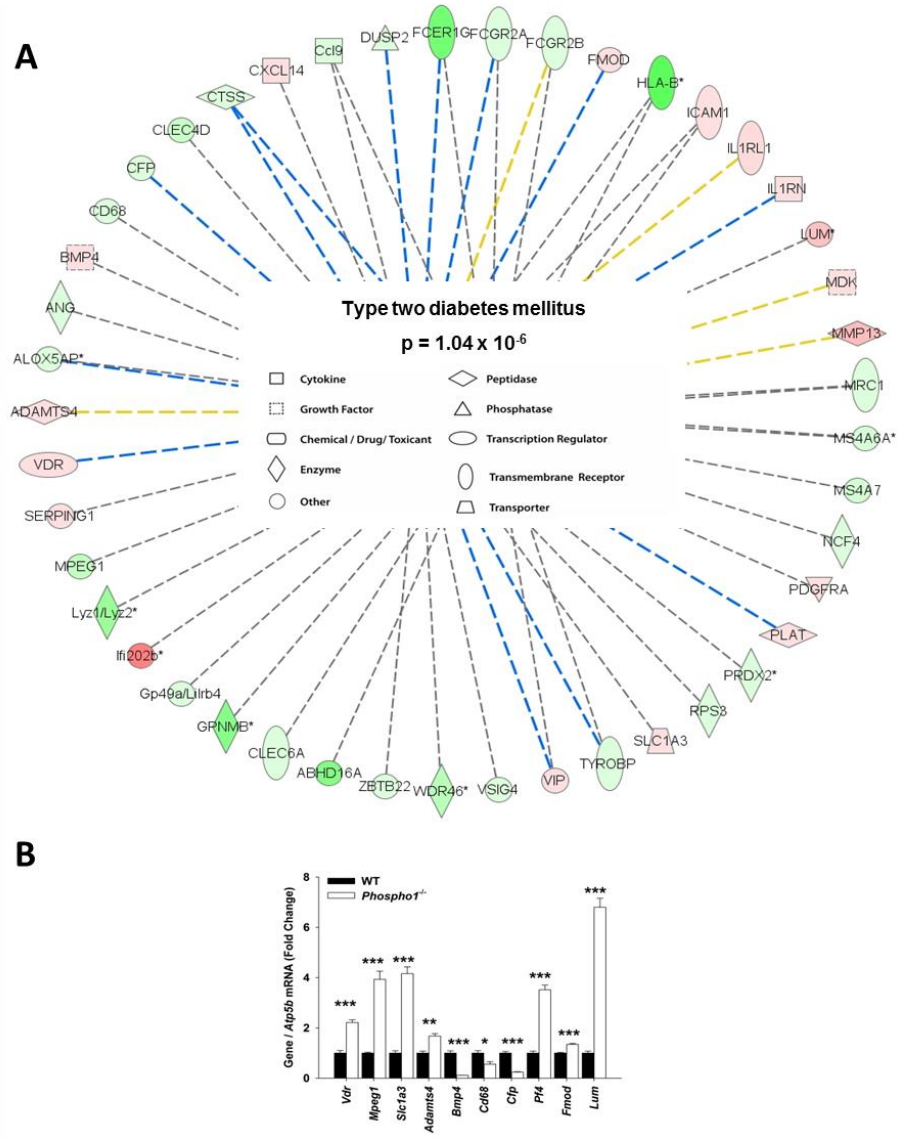

Figure 3.1 Ingenuity Pathways Analysis network summary predictions
To identify further genes which may be involved in the regulation of energy metabolism via the osteoblast, IPA was used to predict further genes associated with type two diabetes mellitus based upon the 21 genes found to be differentially expressed in the microarray **(A)**. **(B)** Predicated genes were confirmed by RT-qPCR in WT and *Phospho1*$^{-/-}$ primary calvarial osteoblast's. Results were normalised to the *Atp5b* housekeeping gene. Data are represented as mean ±S.E.M n = 3, t-test. * $P < 0.05$, ** $P < 0.01$, ***$P < 0.01$. Red = Up regulated. Green = Down regulated (the darker the shade of green and red colour indicates a more extreme up/down regulation, conversely the paler the shade indicates a more subtle up/down regulation. Dashed line = indirect interaction (blue = inhibition, yellow = findings underlying the relationship are inconsistent with the state of the downstream node, grey = IPA prediction).

Gene	Function in Diabetes	Function in Bone	Ingenuity Prediction	Fold From WT	Fold	p value	References
Vdr	Deficiency associated with T1DM.	The active form, 1alpha 25-(OH)2D, binds to the vitamin D receptor (VDR) to modulate gene transcription and regulate mineral ion homeostasis.	↑	↑	2.21	0.00017	(Basit, 2013; Girgis *et al.*, 2014)
Mpeg1	WAT-associated inflammation in HFD is accompanied by reduced expression of immune and inflammatory response genes including MPEG1.	Correlated with correlation femur ultimate force.	↓	↑	3.93	0.00011	(Alam *et al.*, 2009; Kang *et al.*, 2011)
Slc1a3 (glutamate transporter)	Alterations in glutamate transport during diabetes (retina).		↑	↑	4.16	0.00003	(Ward *et al.*, 2005)
Adamts4	ADAMTS families are regulated by PPARγ, which increases insulin sensitivity.	Key enzymes involved in the cleavage of aggrecan and the degradation of cartilage	↑	↑	1.67	0.00164	(Worley *et al.*, 2003; Wainwright *et al.*, 2013)
Bmp4	*BMP4* has been suggested to play an important role in adipogenesis, especially the white adipocyte differentiation through interaction with BMP receptor (BMPR) and subsequently activating the Smad signalling pathways.	BMP4 stimulates osteocalcin synthesis in osteoblast-like MC3T3-E1 cells.	↓	↓	0.12	0.00004	(Kozawa *et al.*, 2002; Tang *et al.*, 2013)
Cd68 (macrophage transmembrane protein)	Obesity is associated with significant infiltration of adipose tissue by macrophages. Treatment with pioglitazone reduces expression of CD68 and MCP-1 in adipose tissue, apparently by reducing macrophage numbers, resulting in reduced inflammatory cytokine production and improvement in insulin sensitivity. Higher CD68 mRNA levels with obesity and insulin resistance.	Genetic ablation of CD68 results in mice with increased bone and dysfunctional osteoclasts.	↓	↓	0.56	0.01518	(Weisberg *et al.*, 2003; Xu *et al.*, 2003; Di Gregorio *et al.*, 2005; Ashley *et al.*, 2011)
Cfp (complement factor properdin)	Elevated properdin and enhanced complement activation in first-degree relatives of South Asian subjects with T2DM.	Complement proteins are present in developing endochondral bone and may mediate cartilage cell death and vascularisation - is localised in the resting and hypertrophic zone but not in the proliferating zone is localised in the resting and hypertrophic zone but not in the proliferating zone.	↓	↓	0.24	0.00002	(Andrades *et al.*, 1996; Somani *et al.*, 2012)
Cxcl4	Incubation of 3T3-L1 adipocytes with CXCL14 stimulated insulin-dependent glucose uptake CXCL14 plays a causal role in HFD induced obesity	*Ex vivo* expansion of HSCs may be highly effective through osteoblast-differentiated MSCs acting as a feeder layer, and likely operates through the CXCL12 chemokine's signalling pathway.	↑	↑	3.51	0.00002	(Takahashi *et al.*, 2007; Mishima *et al.*, 2010)
Fmod	Fibromodulin were found to be down regulated after 40 weeks of diabetes.	Important in maintaining periodontal homeostasis through regulation of TGFβ/BMP signalling, matrix turnover, and collagen organisation.	↑	↑	1.34	0.00031	(Jeansson *et al.*, 2006; Wang *et al.*, 2014)
Lum (lumican)	Collagen-associated proteoglycan. In the present study, increased deposition of collagen types I and V and decreased deposition of collagen type III, biglycan and lumican was observed in the decidua of the diabetic group (uterine lining (endometrium).	Lumican is a significant proteoglycan component of bone matrix, which is secreted by differentiating and mature osteoblasts only and therefore it can be used as a marker to distinguish proliferating pre-osteoblasts from the differentiating osteoblasts.	↑	↑	6.80	0.00000	(Raouf *et al.*, 2002; Favaro *et al.*, 2013)

Table 3.2 *In Silico* analysis of Ingenuity pathways prediction

In Silico analysis of genes predicated to be associated with bone and diabetes mellitus. List of relevant references associated with PubMed key word search. (n = 3, t-test).

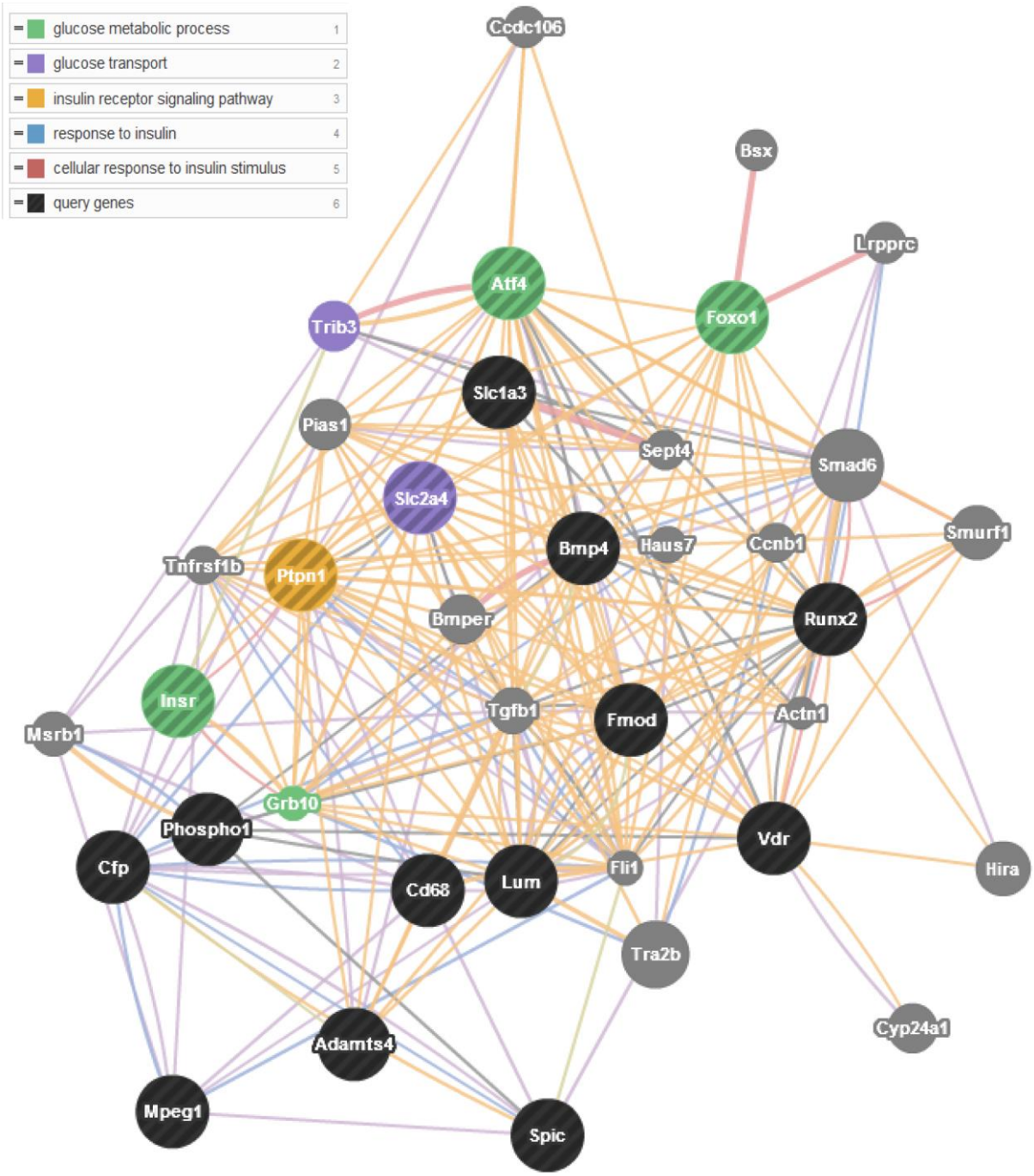

Figure 3.2 GeneMANIA network summary predictions

GeneMANIA network generated using Ingenuity Pathways Analysis gene predictions. The network highlights potential interactions between *Phospho1* and related osteoblast genes in the glucose metabolic process, encompassing; glucose transport, InsR signalling, response to insulin and cellular response to insulin stimulus. Query genes (black) with the exception of *Spic* and *Runx2* which were inputted manually, other genes (grey) were generated by the programme using a large set of inbuilt functional association data. Node size are based on GO terms. Network line colour corresponds to interaction: purple = co-expression, pink = physical interactions, blue = co-localisation, green = shared protein domains orange = predicted, grey = other.

3.5.2 Confirmation of *Esp* expression

To validate if indeed, *Esp* was truly up regulated 20-fold in *Phospho1*$^{-/-}$ osteoblasts compared to WT osteoblasts as suggested by the microarray study, gene expression of *Esp* was examined in WT and *Phospho1*$^{-/-}$ osteoblasts by RT-qPCR. There was approximately a 60-fold increase in *Esp* mRNA expression in *Phospho1*$^{-/-}$ osteoblasts in comparison to WT osteoblasts (Fig. 3.3A). Conversely, *Phospho1*$^{-/-}$ osteoblasts overexpressing PHOSPHO1 were generated and *Esp* mRNA was decreased by 2.5-fold compared to the EV control (Fig. 3.3B). Furthermore, assessment of PHOSPHO1 gene and protein expression by western blotting showed a significant increase in PHOSPHO1 between EV and PHOSPHO1 overexpressing osteoblasts (Fig. 3.3C-D). These data confirm the success of the *Phospho1* over expression strategy. It is important to note that a flag tag PHOSPHO1 lentivirus was also used in this study due to the intermittent nature of the PHOSPHO1 antibody.

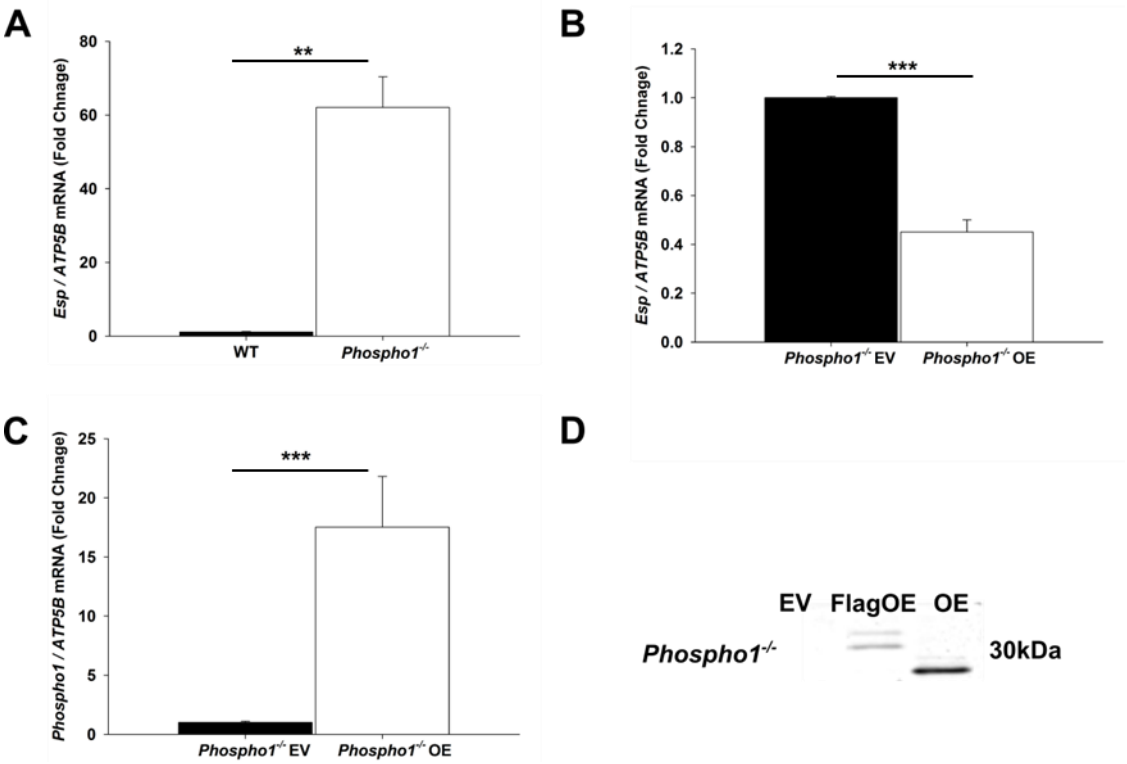

Figure 3.3 Conformation of *Esp* overexpression in *Phospho1*$^{-/-}$ osteoblasts
To assess the relative change in *Esp* mRNA expression in primary calvarial osteoblasts, RT-qPCR was conducted. **(A)** Non transfected primary WT and *Phospho1*$^{-/-}$ osteoblasts **(B)** *Phospho1*$^{-/-}$ osteoblasts empty vector control and *Phospho1*$^{-/-}$ osteoblasts overexpressing PHOSPHO1 empty vector. To confirm PHOSPHO1 gene and protein overexpression RT-qPCR **(C)** and western blotting **(D)** was conducted in *Phospho1*$^{-/-}$ osteoblasts empty vector control and *Phospho1*$^{-/-}$ osteoblasts overexpressing *Phospho1* (with and without the flag tag). mRNA values generated were normalised to the *Atp5b* housekeeping gene. Data are represented as mean ±S.E.M n = 3, t-test. * $P < 0.05$, ** $P < 0.01$, ***$P < 0.001$.

3.5.3 PHOSPHO1 peptide specificities

To examine whether PHOSPHO1 has specific activity towards the InsR S (P) 1322 and GIGYF1 as suggested by the preliminary phosphatase screen and yeast 2 hybrid analysis, a commercially available phosphatase assay adapted from the classic malachite green assay was used (Fig. 3.4A). The phosphatase assay has been previously employed to successfully identify two phosphomonoesters which PHOSPHO1 exhibits high specific activities toward PEA and P-Cho (Roberts *et al.*, 2004). To determine the optimal concentration of recombinant PHOSPHO1 to use in these assays, varying concentrations of PHOSPHO1 (0ng, 50ng, 125ng, 250ng, 625ng) were used in addition to varying concentrations of PEA (1mM, 100μM, 10 μM). It was concluded that 200ng of recombinant PHOSPHO1 was sufficient to hydrolyse PEA releasing free phosphate (Fig. 3.4B). To select the optimum incubation time, 200ng of recombinant PHOSPHO1 was incubated with varying concentrations of PEA (1mM, 100μM, 10 μM) at 37°C for 5, 15, 30, 40 and 60 minutes (Fig. 3.3C), at 30 minutes sufficiently high levels of free phosphate was produced, therefore 30 minutes was the selected incubation time and used in future experiments.

Following the successful optimisation of the phosphatase assay, peptides from the desired substrates (20mM GIGYF1 and serine containing InsR), positive control (PEA 1mM, 100μM, 10 μM) and negative control (tyrosine containing InsR – GFKRSY* EEHIP) were incubated with both 200ng and 625ng of recombinant PHOSPHO1. Little phosphate was released from the GIGYF1 and serine containing InsRin both experiments suggestive that PHOSPHO1 is unable to hydrolyse phosphate from these substrates (Fig. 3.4D-E). The specific activities (unit/mg) for the positive, negative and GIGYF1 and serine containing InsR were calculated, confirming that PHOSPHO1 does not hydrolyse free phosphate from GIGYF1 and serine containing InsR (Fig. 3.4F).

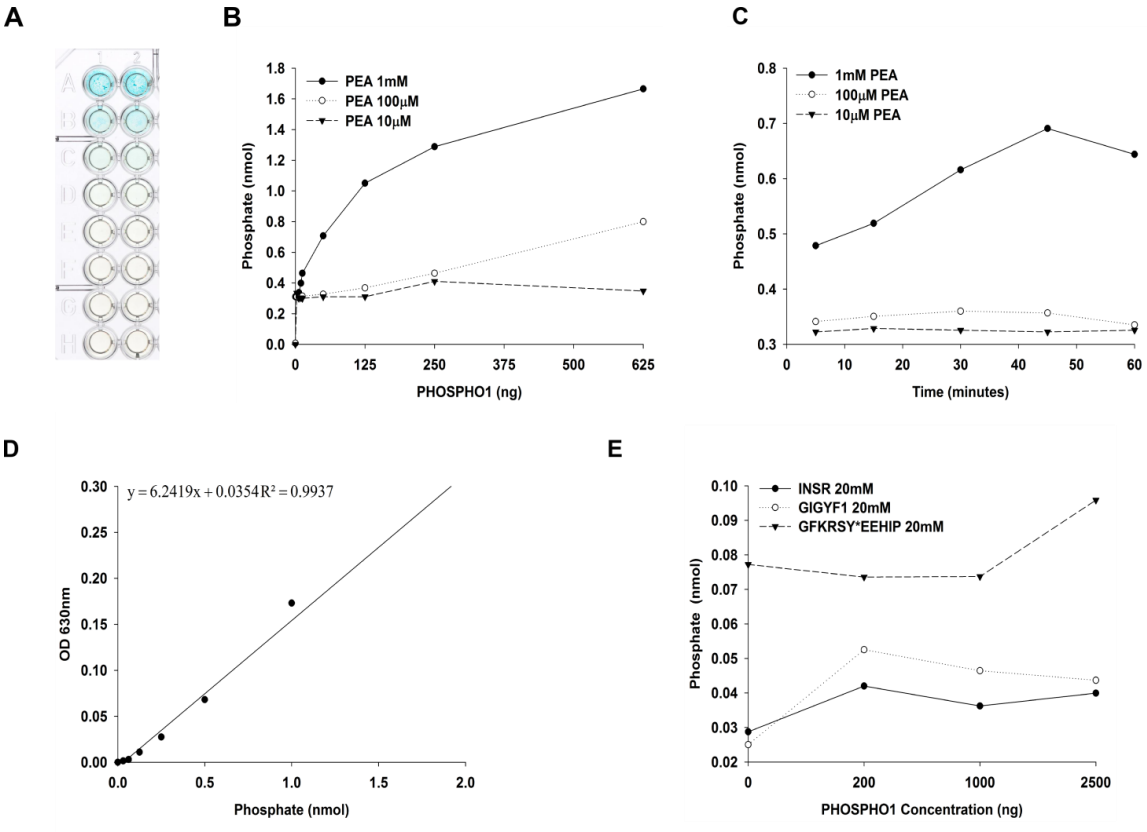

F

Peptide	Phosphate (nmol)	Units of activity	Specific activity (units/mg)
INSR 20mM	0.0420	0.0014	7.0000
GIGYF1 20mM	0.0525	0.0018	8.7535
GFKRSY*EEHIP 20mM	0.0736	0.0025	12.2604
PEA 1mM	1.0485	0.0349	174.7491
PEA 100uM	0.1402	0.0047	23.3658
PEA 10 uM	0.0560	0.0019	9.3380

Figure 3.4 PHOSPHO1 substrates

Phosphatase assay to determine if PHOSPHO1 hydrolyses phosphate from GIGYF1 and serine containing InsR. **(A)** Representative malachite green assay plate containing blank reactions and standards in duplicate (From top of plate: 2nmol, 1nmol, 0.5 nmol, 0.25 nmol, 0.125 nmol, 0.063 nmol, 0.031nmol, 0nmol) **(B)** Concentration curve using PHOSPHO1 (0ng, 50ng, 125ng, 250ng, 625ng) and PEA (1mM, 100μM, 10 μM) as substrate. **(C)** Time course of BIOMOL green assay (200ng of rec enzyme) to determine optimal incubation time for future reactions. **(D)** Standard curve showing linear absorbencies utilising known concentrations of phosphate (BML-KI102) **(E)** Phosphate released from substrates of interest following incubation with varying concentrations of PHOSPHO1. **(F)** Specific units of activity (units/mg) of substrates of interest and reference substrate (PEA). Units of activity = hydrolysis of 1nmol phosphate per minute. Specific activity = units / mg enzyme.

3.5.4 Effects of insulin on primary osteoblasts

To determine if *in vitro* osteoblast insulin signalling was altered in *Phospho1* deficiency, primary WT and *Phospho1*$^{-/-}$ osteoblasts were stimulated with 100nM, 10nM and 1nM of insulin. As expected insulin stimulated AKT and ERK1/2 phosphorylation in a concentration dependent manner in both genotypes, however *Phospho1*$^{-/-}$ osteoblasts exhibited a lesser response to 100nM insulin-stimulation AKT phosphorylation than WT cells. Similarly all concentrations of insulin stimulated ERK1/2 phosphorylation in *Phospho1*$^{-/-}$ cells was also decreased compared to WT cells (Fig. 3.5A). Surprisingly, the distribution of the InsR in primary WT and *Phospho1*$^{-/-}$ osteoblasts was not altered in both basal and stimulated conditions (Fig. 3.5B).

3.5.5 Determination of PHOSPHO1 protein/mRNA expression in murine tissues

It has been reported that gene expression of *Phospho1* by RT-qPCR was 120-fold higher in bone than the lowest expression tissue (liver) and low transcript levels were also detected in all other tissues examined: heart (5.67), bone marrow (3.57), adipose tissue (3.38), brain (1.96), and gut (1.20) (fold difference compared with PHOSPHO1 expression in liver, which was arbitrarily set as 1 for comparison) (Roberts *et al.*, 2007). However, using the online BioGPS, Gene Atlas portal (http://biogps.org), it appears that *Phospho1* is expressed highly in skeletal muscle, bone marrow and testis (Fig. 3.5) but poorly in bone. Some of tissues were not initially screened in the study by Roberts and colleagues (2007) and therefore the tissue expression of *Phospho1* was examined in an expanded tissue list (Fig. 3.6A). *Phospho1* was found to be expressed at high levels in the gonad, interscapular brown fat (iBF) and quadriceps femoris. However, protein expression did not match this distribution and PHOSPHO1, as determined by western blotting was most highly expressed in mouse calvariae and bone with significantly lower levels observed in the brain, lung, heart and quadriceps femoris, suggestive that *Phospho1* transcript levels are not indicative of translated PHOSPHO1 protein. As expected, expression bands in calvariae, bone, brain, lung, heart and quadriceps femoris were not present

in *Phospho1*$^{-/-}$ tissue. However, a double band, approximately 1kDa lower than the expected PHOSPHO1 band was observed in both WT and *Phospho1*$^{-/-}$ pancreata (Fig. 3.6A). Sequencing confirmed this was not PHOSPHO1. Unfortunately I was unable to perform successful immunohistochemistry (IHC) to confirm this tissue distribution of PHOSPHO1 protein. In brief, expected PHOSPHO1 labelling was observed in the tibial shaft, however the same, yet faint staining was observed in *Phospho1*$^{-/-}$ tibiae despite protocol optimisation and antibody repurchase. Furthermore, attempts by others out with the group reported that PHOSPHO1 expression was present in odontoblasts, however later, unpublished analysis of *Phospho1*$^{-/-}$ teeth showed they had similar staining (McKee *et al.*, 2013). It is likely that the commercially available antibody whilst (usually) good for western blotting is unpredictable for IHC.

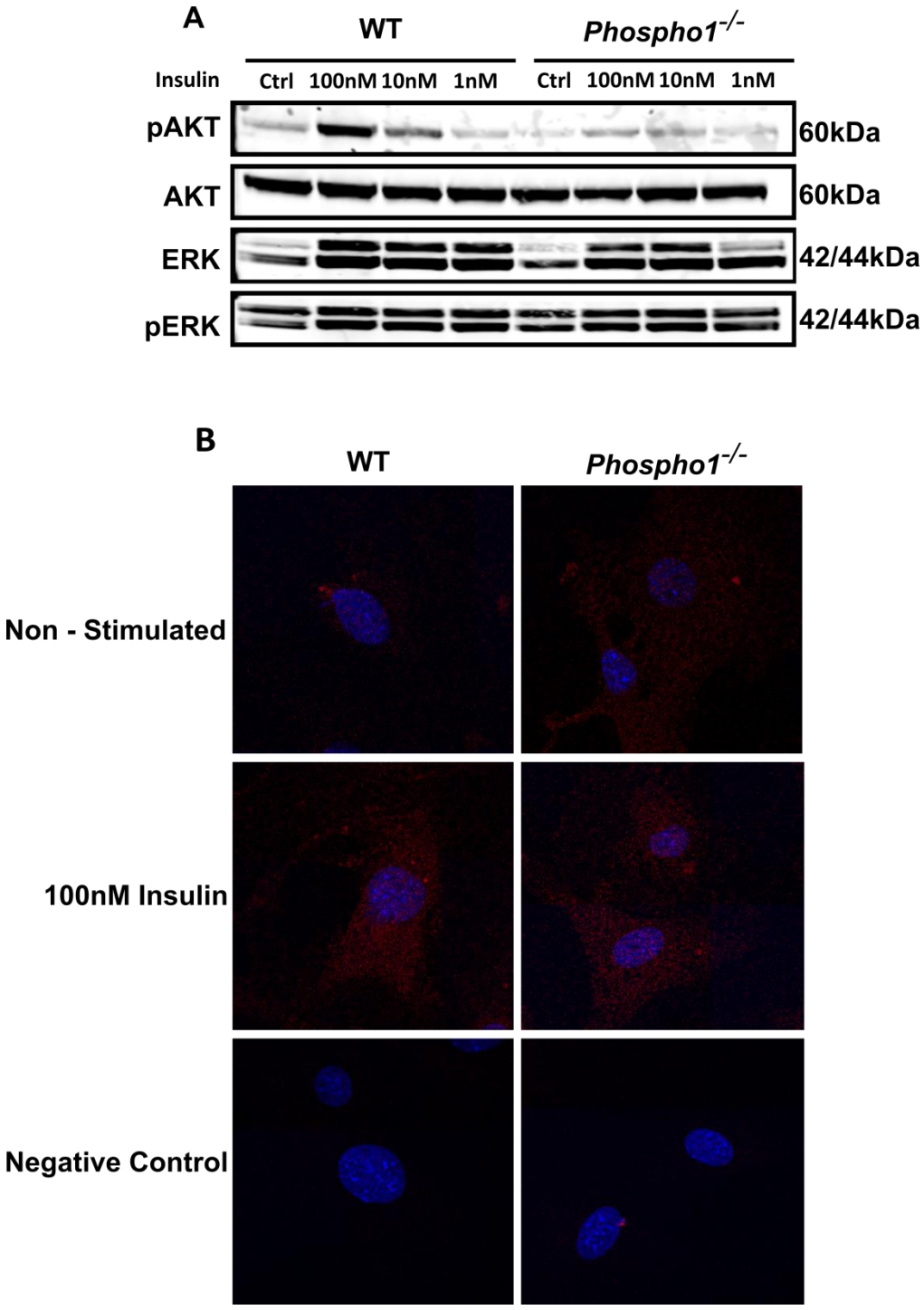

Figure 3.5 *Phospho1*$^{-/-}$ primary calvarial osteoblasts display reduced AKT phosphorylation in response to insulin signalling.
(A) Representative immunoblots demonstrating the effects of insulin (100nM, 10nM and 1nM) on the phosphorylation of AKT and ERK1/2 in calvarial osteoblast cultures ($n \geq 3$). **(B)** Immunofluorescent staining of the InsR (red) on the surface of WT and *Phospho1*$^{-/-}$ neonatal calvarial primary osteoblast cultures. Nuclei are shown in blue.

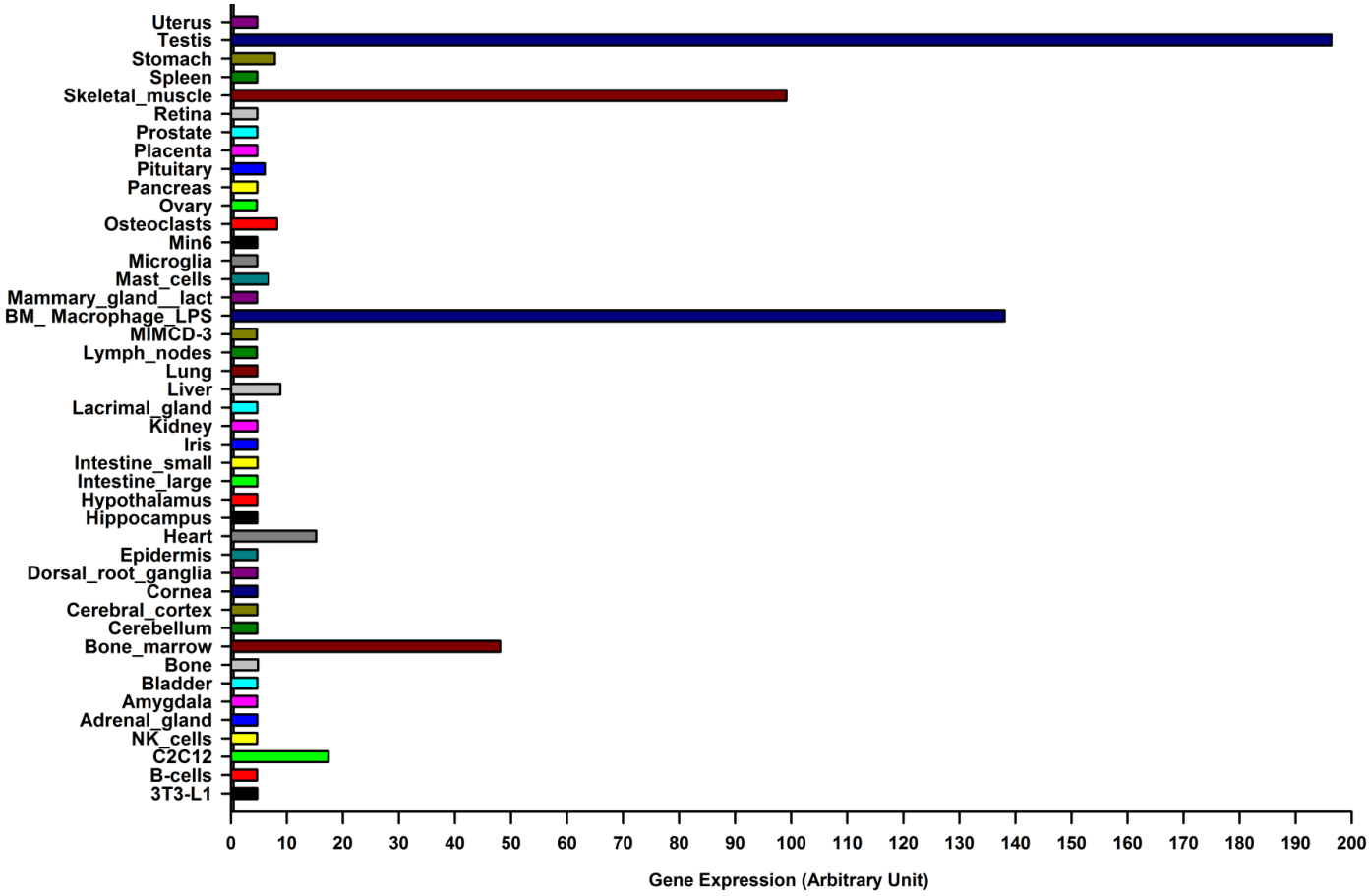

Figure 3.6 BioGPS expression of *Phospho1* in mice
High-throughput gene expression profiling from a diverse array of cell lines and normal tissues, organs of mice, and cell lines. Adapted from: GeneAtlas MOE430, gcrma, species: Mouse.

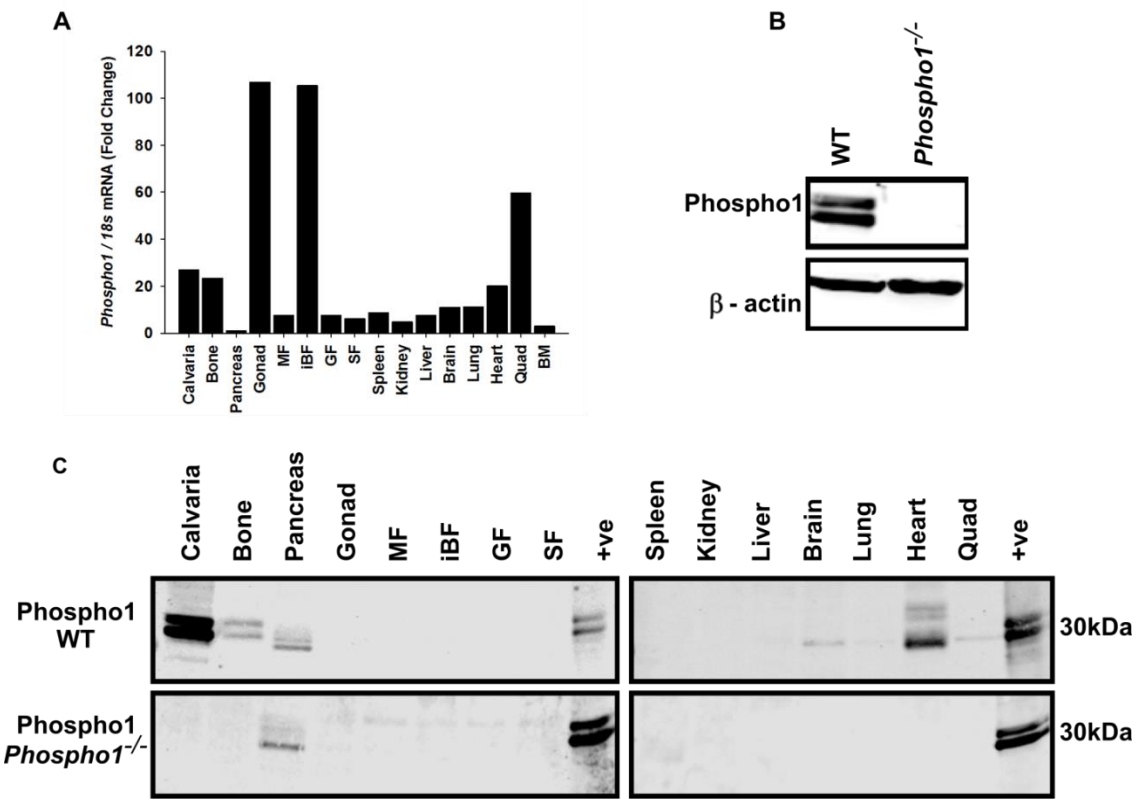

Figure 3.7 The expression of *Phospho1* mRNA and PHOSPHO1 protein in murine tissue
(A) RT-qPCR of *Phospho1* in murine tissues. *Phospho1* was found to be expressed at high levels in the gonad, iBF and quadriceps femoris. **(B)** Protein expression of PHOSPHO1 was shown to be only present in WT bone, illustrating complete ablation in bone. **(C)** PHOSPHO1 was highly expressed in mouse calvaria and bone, with significantly lower levels observed in the brain, lung, heart and quadriceps femoris. Mesenteric fat (MF), intra-scapular brown fat (iBF), gonadal fat (GF), subcutaneous fat (SB) and bone marrow (BM).

3.6 Discussion

The bone specific phosphatase, PHOSPHO1 has previously been shown to be essential for the initiation of HA crystal formation inside MVs during endochondral ossification (reviewed in (Millan, 2013). Through the study of *in vivo* models, PHOSPHO1 was revealed to be crucial in the production of mechanically competent mineralisation enabling the skeleton to withstand habitual load thus avoiding spontaneous fractures (Huesa *et al.*, 2011). However the underlying biochemical details whereby PHOSPHO1 generates P_i remains largely unknown. In an attempt to provide a deeper understanding to how PHOSPHO1 contributes to HA crystal formation, a microarray study was conducted in WT and *Phospho1*$^{-/-}$ primary calvarial osteoblasts. The data from this comparison have subsequently been pivotal to the focus of this thesis. The embryonic stem cell protein-tyrosine phosphatase was found to be up regulated 60-fold in *Phospho1*$^{-/-}$ osteoblasts, confirmed by elevated mRNA levels in *Phospho1*$^{-/-}$ osteoblasts and conversely decreased in *Phospho1*$^{-/-}$ osteoblasts overexpressing PHOSPHO1, suggestive that PHOSPHO1 is involved in global energy metabolism (Fig. 3.3). Thus, a more compressive *in silico* analysis was performed to determine if indeed PHOSPHO1 had alternate roles out-with bone mineralisation. Unquestionably, IPA revealed that *Phospho1* ablation is significantly associated with insulin dependent diabetes mellitus. Further analysis by GeneMANIA a complimentary *in silico* data mining software highlighted 10 genes which were associated with both diabetes and bone. The identification of this subset of genes therefore warrants future investigation by genetic manipulation (e.g. the generation of gene specific osteoblast conditional knockout mice) which was outside the possibilities of this PhD. However, in the midst of the era of integrative physiology, these data add to the rapid and expanding body of evidence linking bone with global energy regulation.

Preliminary data suggested that PHOSPHO1 may directly dephosphorylate the InsR S (P) 1322 and interact with GIGYF1. However, upon further investigation a phosphatase assay showed recPHOSPHO1 released little phosphate from both InsR

S (P) 1322 and GIGYF1 peptides, demonstrating the inability of PHOPSHO1 to dephosphorylate the outlined candidates. Furthermore, InsR S (P) 1322 and InsR Y (P) 1322 appear to have synonymous names in the literature. Insulin has been shown to stimulate autophosphorylation of the InsR on multiple tyrosines, including Tyr 1322 on the COOH-terminus (Fig. 3.8) (King and Sale, 1990; White and Kahn, 1994). However, deletion of tyrosine (Tyr1322, Tyr1316) and threonine (Thr1336) phosphorylation sites of the COOH terminal has no effect on insulin stimulated receptor kinase activity or biological activity, suggesting the COOH terminus does not modulate the kinase function of the insulin receptor. Whilst not essential for signalling these tyrosine residues including Tyr 1322 may play a regulatory role as they autophosphorylated in native receptors (Myers *et al.*, 1991; Takata *et al.*, 1991).

In contrast to the *in vitro* experiments, *in silico* analysis suggested that *Phospho1* may interact with *Grb10* and the *InsR* to regulate the glucose metabolic process. It is important however to recognise the limitations associated with *in silico* network analysis. Networks are created based upon large sets of functional association data. These association data encompass protein and genetic interactions, pathways, co-expression, co-localisation and protein domain similarity. These pathways are based upon predictions and similar to microarray studies, require further *in vitro* and/or *in vivo* experimentation to confirm predictions. A united effort of experimental biology and theory therefore must be applied. It remains unclear if PHOSPHO1 has a direct effect on the insulin receptor.

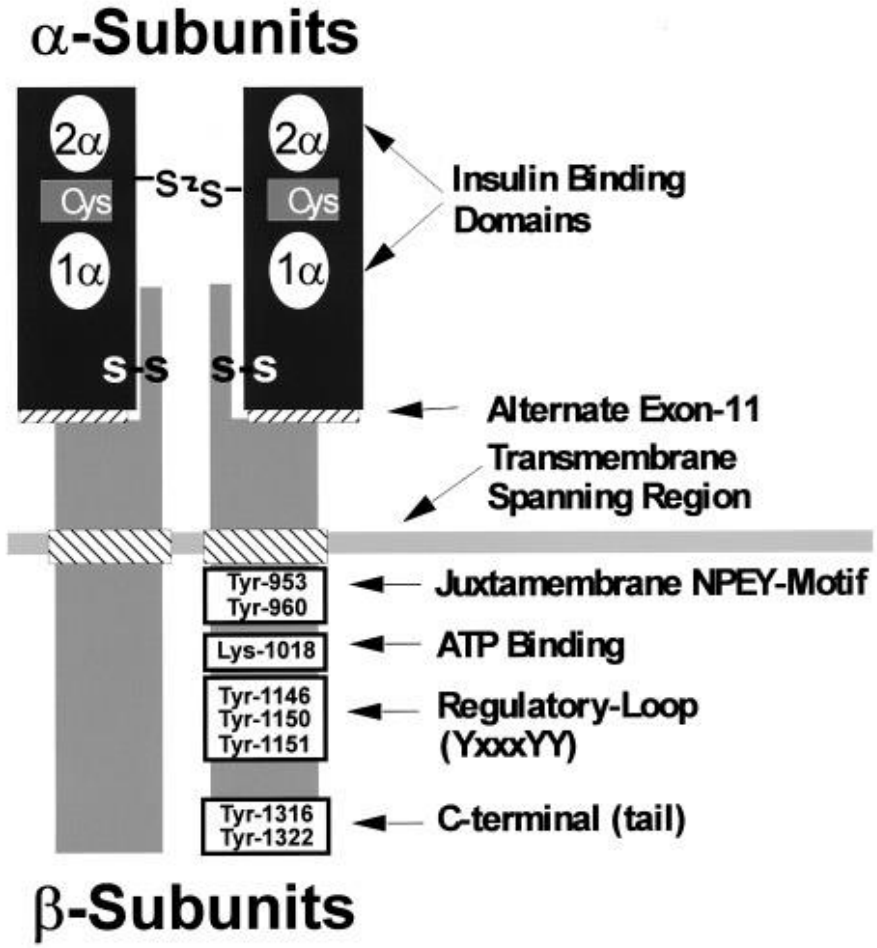

Figure 3.8 Model of the InsR
Tyr01322 is situated on the COOH terminus of the β subunit linked to the α subunit by disulphide bonds (adapted from (White and Kahn, 1994)).

To try to unravel these complex data, primary calvarial osteoblasts were stimulated with insulin. Intriguingly, *Phospho1*$^{-/-}$ osteoblasts exhibited decreased AKT phosphorylation in response to 100nM insulin. This observation however this was not a result of an altered distribution of the *InsR* mRNA expression levels between the two genotypes. These conflicting data may be as a consequence of the 60-fold increase of *Esp* in *Phospho1*$^{-/-}$ osteoblasts leading to greater dephosphorylation of the InsR. This is discussed fully in Chapter 6.

All data available indicated that PHOSPHO1 is preferentially expressed by bone. Indeed in the avian model, IHC localised PHOSPHO1 protein to the osteoid layer of the periosteum, forming surfaces of growing osteons, newly formed osteocytes, cartilage remnants and trabecular bone. All soft tissues analysed were negative. Moreover whole-mount in situ hybridisation showed that *Phospho1* expression occurred prior to E6.5, restricted to the bone collar within the mid-shaft of the diaphysis of long bones but by E11.5 expression was observed over the entire length of the diaphysis (Houston *et al.*, 2004; Stewart *et al.*, 2006; Roberts *et al.*, 2007). Further evidence from the online transcriptome atlas database for mouse embryo (Eurexpress -http://www.eurexpress.org/ee/databases/assay.jsp?assayID=euxassay_007708&image=01) revealed that in the E15.5 mouse the strongest hybridisation for *Phospho1* was in the skeletal elements (Fig. 3.8). However, contradictory to these data, the BioGPS, Gene Atlas portal highlighted *Phospho1* is expressed at high levels in skeletal muscle, BAT, and testis. If this wider expression pattern is indeed true, any metabolic phenotype of the *Phosho1*$^{-/-}$ mice may not be due to bone derived PHOSPHO1 but potentially a consequence of non-osseous tissue derived PHOSPHO1. Quantification of mRNA expression in a large panel of tissues not previously analysed, demonstrated *Phospho1* was found to be expressed at high levels in the gonad, iBF and quadriceps femoris however this did not translate to PHOSPHO1 protein expression. These data were not in accordance with previously reported expression of *Phospho1* (Roberts *et al.*, 2007), this is likely due to the primer sequence used. Roberts *et al.* selected primers that were specific to *Phospho1*,

however the amplicon obtained was 2070 base pairs, dramatically above the desired 50-150 base pairs for optimal PCR efficiency. Similarly, expression of *Esp* in murine tissue is widespread (data not shown), however protein levels of OST-PTP are restricted to osseous and testicular tissue as suggested by the name osteotesticular protein tyrosine phosphatase (Lee *et al.*, 2007).

It is not uncommon for genes to be transcribed into mRNA but not translated into protein due to various regulatory mechanisms, encompassing post-transcriptional or post-translational regulation. These processes usually occur due to errors during protein synthesis and sensitivity to environmental changes, allowing only a small percentage of proteins to reach their intended functional state (Medicherla and Goldberg, 2008). However, some mRNA is translated and rapidly degraded which may contribute to the lack of PHOSPHO1 being observed in the gonad, iBF and quadriceps femoris. As protein synthesis and maturation requires up to 75% of the total cellular energy budget this degradation is a somewhat wasteful process (Kim *et al.*, 2013b). Specifically, 15-30% of newly synthesised proteins are rapidly degraded in a ubiquitin-proteasome dependent manner in which substrates are tagged with ubiquitin prior to transportation to the 26S proteasome for degradation (Schubert *et al.*, 2000; Vabulas and Hartl, 2005; Welchman *et al.*, 2005). Alternatively, autophagy is a further mechanism for both non-specific and specific protein degradation. This protein degradation pathway occurs within the lumen of the lysosomes, following transportation via macroautophagy, microautophagy or chaperone-mediated autophagy (reviewed in (Wang *et al.*, 2015).

In addition to the post-translational regulation described above, post-transcriptional regulation may also explain the disparity observed between mRNA and protein levels. Short endogenous RNAs, microRNAs (miRNAs), pair to sites in the 3′ untranslated region to regulate protein expression (Welchman *et al.*, 2005). Studies have suggested that miRNAs chiefly affect protein expression and may not have measurable effects on mRNA abundance (Welchman *et al.*, 2005). The investigation

of the process underlying the disparity between PHOSPHO1 mRNA and protein expression was not investigated in this thesis but such information would be informative in future studies.

In conclusion, the conflicting data obtained from both *in vitro* and *in silico* work make it difficult to confirm if PHOSPHO1 affects osteoblast InsR signalling or if the upregulation of *Esp* expression in the *Phospho1*$^{-/-}$ osteoblasts offers protection from excessive insulin signalling. The subsequent chapters aim to determine if *Phospho1*$^{-/-}$ mice have a metabolic phenotype *in vivo* as suggested by the altered *Esp* expression noted in cultured *Phospho1*$^{-/-}$ osteoblasts.

Figure 3.9 Skeletal specific expression of *Phospho1* in the E14.5 mouse
High-throughput transcriptome-wide acquisition of expression patterns by in situ hybridisation of sagittal sections from E14.5 wild type murine embryos. The strongest hybridisation for *Phospho1* was in the skeletal elements (e.g. radius, ulna, humorous, fibular, tibiae, femur, mandible, maxilla, rib, axial skeleton, clavicle, scapular, pelvic girdle) indicated by dark purple staining. Adapted from:
http://www.eurexpress.org/ee/databases/assay.jsp?assayID=euxassay_007708.

Chapter 4

Characterising the *Phospho1* knock-out mouse metabolic phenotype

4.1 Introduction

The bone specific phosphatase PHOSPHO1 is present in MV's of osteoblasts and chondrocytes (Houston *et al.*, 2004; Stewart *et al.*, 2006). Analysis of mice lacking PHOSPHO1 showed that these animals had significant skeletal pathology, spontaneous fractures, bowed long bones, osteomalacia, and scoliosis in early life (Huesa *et al.*, 2011; Yadav *et al.*, 2011). Further investigation revealed that the double ablation of both PHOSPHO1 and tissue-nonspecific alkaline phosphatase (TNAP) is perinatally lethal and that these mice display a complete absence of skeletal mineralisation at embryonic day 18 (E18), suggestive that PHOSPHO1 and TNAP have complementary, non-redundant functional roles during endochondral ossification (Yadav *et al*. 2011). Using these models a comprehensive paradigm of skeletal mineralisation was suggested, whereby PHOSPHO1 is responsible for intravesicular production of P_i and TNAP mediates extravesicular P_i transport into the MV, via phosphate transporter 1 (P_iT) (Yadav *et al.*, 2011; Millan, 2013). Despite the advances that have made been made in generating this inclusive model for the initiation of skeletal mineralisation, the intimate biochemical details of how PHOSPHO1 is implicated in intravesicular P_i generation have yet to be elucidated. As outlined in Chapter 3 a microarray was used to provide clues to the molecular pathways underlying the functional role of PHOSPHO1. The key finding was that *Esp*, the gene encoding the OST-PTP, was up regulated 20-fold in *Phospho1*$^{-/-}$ osteoblasts compared to WT osteoblasts, which was later confirmed by RT-qPCR (60-fold) and lentivirus overexpression studies (Chapter 3). Embryonic stem cell protein-tyrosine phosphatase is expressed by only two cell types, the osteoblast and the sertoli cells of the testis. *In vitro*, *Esp* coordinates the progression of the pre-osteoblast to a mature, mineralising cell, and *in vivo* may be a critical regulator of the commitment of mesenchymal cells to the ossification of new bones during skeletogenesis (Mauro *et al.*, 1994; Chengalvala *et al.*, 2001; Yunker *et al.*, 2004). Protein tyrosine phosphatases are master regulators of InsR signalling. Osteotesticular protein tyrosine phosphatase has been recently shown to be involved in the decarboxylation of OCN, whereby *Esp* dephosphorylates the InsR

situated on the osteoblast, negatively regulating the osteoblast-insulin-signalling cascade and subsequent release of GLU13-OCN into the systemic circulation (Mauro *et al.*, 1994; Hunter, 1995; Schlessinger, 2000; Dacquin *et al.*, 2004; Tonks, 2006; Lee *et al.*, 2007; Ferron *et al.*, 2010b). The fully carboxylated OCN regulates mineral formation and matrix mineralisation (Chenu *et al.*, 1994), however upon decarboxylation of OCN on its three glutamic acid residues (GLU13, GLU17 and GLU20) OCN is realised into the general circulation and regulates global energy metabolism via the stimulation of insulin secretion and β cell proliferation in the pancreas, energy expenditure by muscle, and insulin sensitivity in adipose tissue, muscle and liver (Rosen and Motyl, 2010; Karsenty and Ferron, 2012). Indeed, the 60-fold increase in *Esp* in *Phospho1*$^{-/-}$ mice is therefore suggestive that *Phospho1*$^{-/-}$ mice may resemble OST-PTP overexpression mice and OCN-deficient mice; Both OST-PTP overexpression and OCN-deficient mice are phenocopies; the mice are hyperglycemic, hypoinsulinemic and have reduced insulin secretion and sensitivity compared to the litter mate WT mice (Lee *et al.*, 2007). These data indicate that there may be a reciprocal regulation between OST-PTP and PHOSPHO1, whereby global energy metabolism is affected via circulating GLU13-OCN. Certainly to add credence to this hypothesis, pathway analysis of the existing microarray data obtained from WT and *Phospho1*$^{-/-}$ primary calvaria osteoblasts highlighted that PHOSPHO1 is associated with T2DM (P = 1.04x10^{-6}). Furthermore, 10 genes (*Vdr, Slc1a3, Mpeg1, Adamts4, Bmp4, Cd68, Cfp, Cxcl4. Fmod and Lum*) were found to be associated with both diabetes and bone following an *in silico* search (validated by RT-qPCR) and GeneMANIA network analysis predicted *Phospho1* interacts with *Grb10, Insr, Atf4* and *FoxO1* (involved in the GLU13-OCN regulation) (Chapter 3). Therefore the overarching aim of this chapter was to characterise the metabolic phenotype of *Phospho1*$^{-/-}$ mice.

4.2 Hypothesis

Phospho1$^{-/-}$ mice are hyperglycaemic, have decreased insulin secretion and sensitivity.

4.3 Aims

I. Analyse the metabolic phenotype of juvenile and aged *Phospho1*$^{-/-}$ mice.

II. Examine the effect of a HFD on the metabolic phenotype of WT and *Phospho1*$^{-/-}$ mice

III. Study *Phospho1* heterozygote mice to explore the possibility that PHOSPHO1 may represent a druggable target.

IV. Determine if a HFD affects the skeletal phenotype of WT and *Phospho1*$^{-/-}$ mice.

4.4 Materials and Methods

4.4.1 Glucose tolerance and insulin tolerance test

Male juvenile, adult and aged mice were weighed and fasted for 4 hours between 9am and 1pm. 2 mg of D-glucose per g of BW was administered by gavage or 0.5mU of insulin per g of BW was administered IP and blood glucose and circulating insulin was measured (detailed in section 2.5.3.3). Animals were allowed to recover for two weeks prior to euthanasia. Tissues were collected for protein, gene and histological analysis.

4.4.2 Growth curves

WT and *Phospho1*$^{-/-}$ mice on both CD and HFD were weighed every week from weaning until 120 days of age.

4.4.3 Food consumption, activity and energy expenditure

Ad libitum food consumption was monitored for 6 days and basal nocturnal activity was quantified using an AM524 Single Layer X, Y IR activity monitor and associated Amonlite software (Linton Instrumentations, Norfolk, UK). Metabolic activity was measured using indirect calorimetry (Oxymax Lab Animal Monitoring System: CLAMS (Columbus Instruments, OH USA). This was done in collaboration with Dr. Monzur Murshed and Dr. Zohreh Khavandgar, University of Montreal, Canada. All experiments were conducted blind to the operator.

4.4.4 mRNA analysis of primary osteoblasts cells and cell lines

RNA samples were extracted from primary calvarial osteoblasts, using a Qiagen RNeasy lipid kit according to the manufacturer's instructions. cDNA was prepared (section 2.6.1) and was used at 5ng/μl for RT-qPCR analysis, as detailed in section 2.6.4. Results were normalised to the *Atp5b* housekeeping gene and the relative gene expression level was calculated using the ΔΔCt method (Livak & Schmittgen 2001).

4.4.5 Protein analysis of primary osteoblasts cells and cell lines

Protein was extracted from primary calvarial osteoblasts in RIPA buffer as detailed in section 2.7.1. Protein concentration was quantified (section 2.7.2) and appropriate quantities were used for western blot analysis (section 2.7.3). UCP1 protein expression was determined using an anti-rabbit anti-UCP1 antibody at a dilution of 1:1000 and a HRP-labelled goat anti-rabbit secondary antibody (1:5000). Antibody labelling was visualized using the ECL detection kit. Equality of protein loading was confirmed by also probing the membrane with mouse monoclonal HRP-labelled anti-β actin antibody (1:50000).

4.4.6 Tissue histology

Male juvenile, adult and aged mice (35, 120 and 220 day-old, respectively) CD and HFD were sacrificed by cervical dislocation. Tissue was fixed in 4% PFA and embedded in paraffin wax. 5-μm sections were stained with haematoxylin and

eosin (H&E) using the Leica Autostainer and mounted in DePeX (VWR, Lutterworth, UK). Adipocyte diameter and pancreatic β-cell islet number and size was quantified using ImageJ software as previously described (section 2.8.5) (Lee *et al.*, 2007; Huesa *et al.*, 2014).

4.4.7 Serum isolation from whole blood samples

Blood was extracted from mice via cardiac puncture and blood was transferred to an EDTA coated tube, serum was collected and stored at -80°C until use.

4.4.8 Pancreas insulin content

Dissected pancreata from 120 day old WT and *Phospho1*$^{-/-}$ mice were homogenised and diluted in 2ml of acidified ethanol overnight at -20°C. Samples were neutralised by the addition of 100µl 1M Tris (pH 7.5) and insulin content was measured by ELISA (section 2.10.6) and normalised to protein content as measure by the Bradford assay (section 2.7.2.2).

4.4.9 µCT x-ray and 3 point bending

µCT imaging was carried on 35 day CD, 120 day CD and 120 day HFD tibiae. High-resolution scans with an isotropic voxel size of 5 µm (trabecular) or 10µm cortical scanning were acquired with a micro-computed tomography system (µCT, 60 kV, 0.5 mm aluminum filter, 0.6° rotation, Skyscan 1172, Brukker microCT, Kontich, Belgium). Scans were reconstructed and using CTAn software (Bruker) was used to analyse appropriate parameters (section 2.12.2). Calcium hydroxyapatite phantoms of a known density were scanned using the same settings to calculate BMD. Bones were then x-rayed (section 2.12.1) and subsequently loaded until fracture (where indicated) using a LXR materials testing machine fitted with a 500N load cell. Data was recorded after every 0.2 N change in load and every 0.1 mm change in deflection. From the load extension curve, failure, fracture, maximum stiffness and yield were defined (Aspden, 2003).

4.5 Results

4.5.1 *Phospho1* inactivation improves glucose tolerance and insulin sensitivity in juvenile mice

I reasoned that if the ablation of *Phospho1* was associated with T2DM and caused a 60-fold up-regulation of *Esp* expression in osteoblasts (Chapter 3) *Phospho1*$^{-/-}$ mice would have a similar phenotype to transgenic mice overexpressing full-length *Esp* cDNA selectively in osteoblasts (α1(I)-*Esp* mice). α1(I)-*Esp* mice are hyperglycemic, glucose intolerant and insulin resistant as a result of impaired insulin secretion in response to glucose (Lee *et al.*, 2007). Unexpectedly, metabolic analysis revealed that juvenile (35 day old) *Phospho1*$^{-/-}$ mice had a significant reduction in blood glucose levels (WT: 9.31±0.31 mmol/L, *Phospho1*$^{-/-}$: 7.76±0.32 mmol/L; $P < 0.01$) (Fig. 4.1A). *Phospho1*$^{-/-}$ mice also showed an improvement in glucose tolerance (Fig. 4.1B) and were more insulin sensitive compared to WT counterparts (Fig. 4.1C). These observations were consistent with a significantly decreased body mass (g) of *Phospho1*$^{-/-}$ mice (WT: 22.58±0.96, *Phospho1*$^{-/-}$: 19.03±0.10; $P < 0.05$)(Fig. 4.2A)and the finding of smaller (mg/g BW) SB (WT: 4.31±0.27, *Phospho1*$^{-/-}$: 2.58±0.20; $P < 0.01$), MF (WT: 5.30±0.30, *Phospho1*$^{-/-}$: 3.39±0.40; $P < 0.01$), GF (WT: 4.31±0.27, *Phospho1*$^{-/-}$: 2.58±0.20; $P < 0.01$) and interscapular brown (iBF) (WT: 5.11±0.57, *Phospho1*$^{-/-}$: 3.05±0.40; $P < 0.01$) fat depots noted in *Phospho1*$^{-/-}$ mice at necropsy (Fig. 4.2B). Consistent with these observations, histological analysis revealed smaller gonadal adipocytes in *Phospho1*$^{-/-}$ mice ($P < 0.05$) (Fig. 4.2C). These changes were not a consequence of altered food intake (g/gBW/day) (WT: 0.13±0.01; *Phospho1*-/-: 0.12± 0.01) (Fig. 4.3A), but may be partly explained by a significant increase in total activity of *Phospho1*$^{-/-}$ mice (beam breaks) (WT: 4048.33±238.58; *Phospho1*-/-:9176.33±901.03; $P < 0.01$) (Fig. 4.3B). However, no change in energy expenditure was observed between WT and *Phospho1*$^{-/-}$ mice (Fig. 4.3C-F).

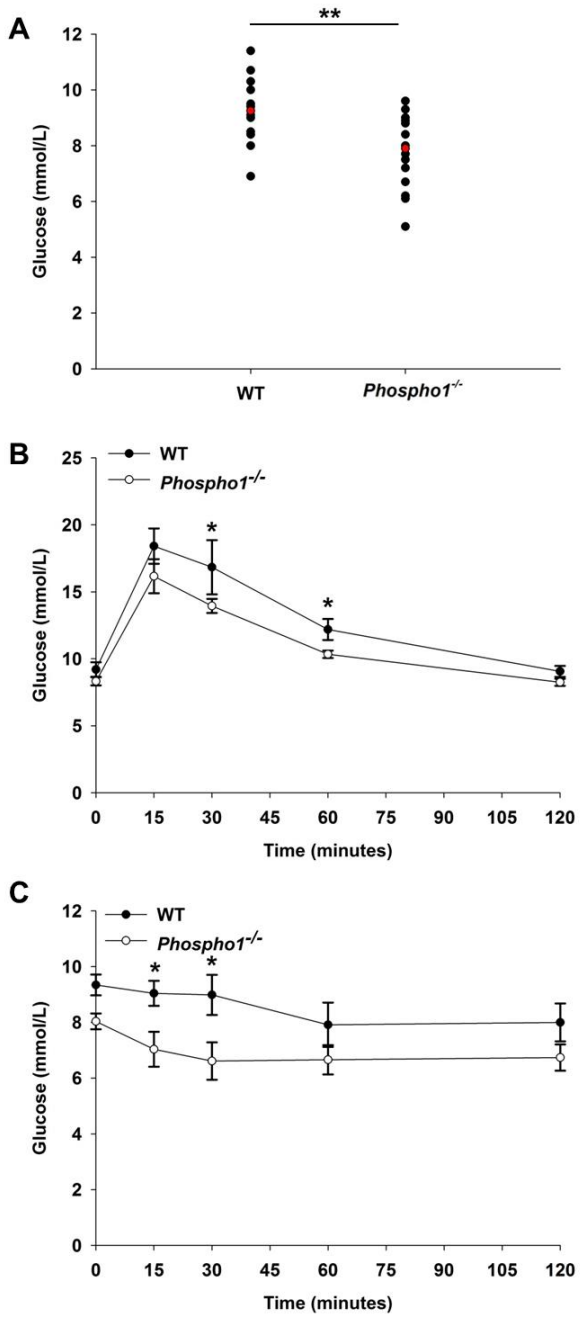

Figure 4.1 Juvenile *Phospho1*$^{-/-}$ male mice are protected from glucose intolerance
Metabolic analysis of 35 day old WT and *Phospho1*$^{-/-}$ male mice. **(A)** *Phospho1*$^{-/-}$ mice had a reduction in blood glucose levels compared to WT counterparts. **(B)** GTT tests revealed that *Phospho1*$^{-/-}$ mice also showed an improvement in glucose tolerance and **(C)** were significantly more insulin sensitive compared to WT counterparts as determined by an insulin tolerance test. n ≥ 10, t-test (A), two way repeated measures ANOVA (B&C). Data are represented as mean ±S.E.M. * $P < 0.05$, ** $P < 0.01$, ***$P < 0.001$.

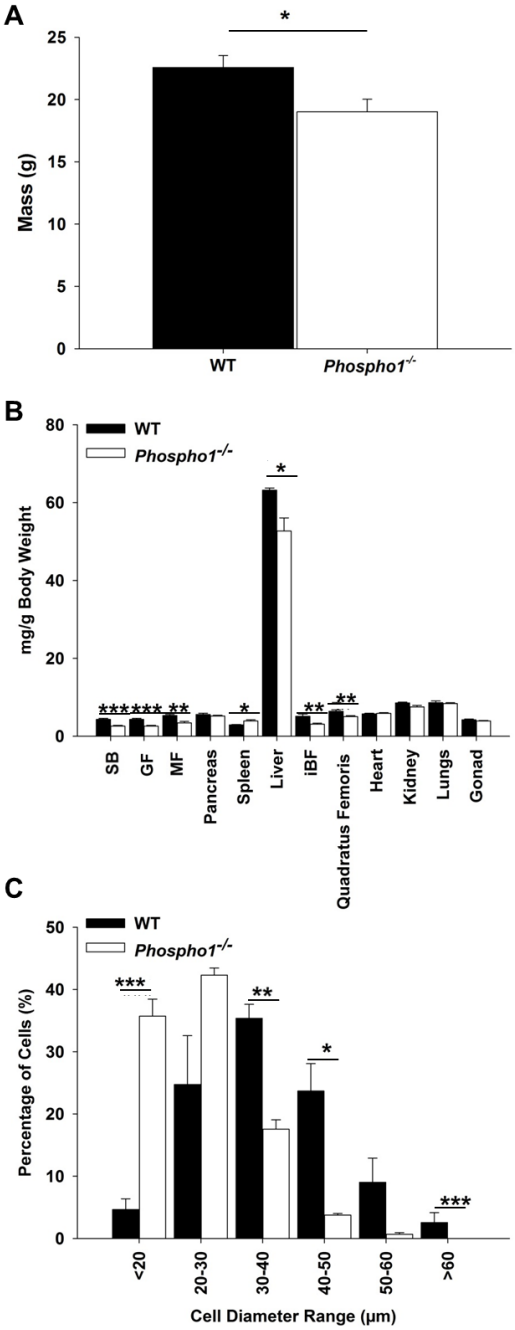

Figure 4.2 Juvenile *Phospho1*$^{-/-}$ male mice are smaller than WT counterparts having decreased adipose tissue stores

Simple weighing of 35 day old WT and *Phospho1*$^{-/-}$ male mice revealed **(A)** *Phospho1*$^{-/-}$ mice are smaller than WT counterparts. **(B)** These mice were then dissected and the outlined tissues were removed and weighed: Subcutaneous fat (SB), gonadal fat (GF), mesenteric fat (MF), pancreas, spleen, liver, intra-scapular brown fat (iBF), quadriceps femoris, heart, kidney, lungs and gonad. Dissection analysis revealed that all fat depots weighed (mg/g BW) in *Phospho1*$^{-/-}$ were smaller than WT counterpart mice. The GF were then fixed, processed and sectioned and used to examine the adipocyte size in these mice. **(C)** Histological analysis revealed smaller gonadal adipocytes in *Phospho1*$^{-/-}$ mice. n ≥ 5, t-test. Data are represented as mean ±S.E.M. * $P < 0.05$, ** $P < 0.01$, ***$P < 0.001$.

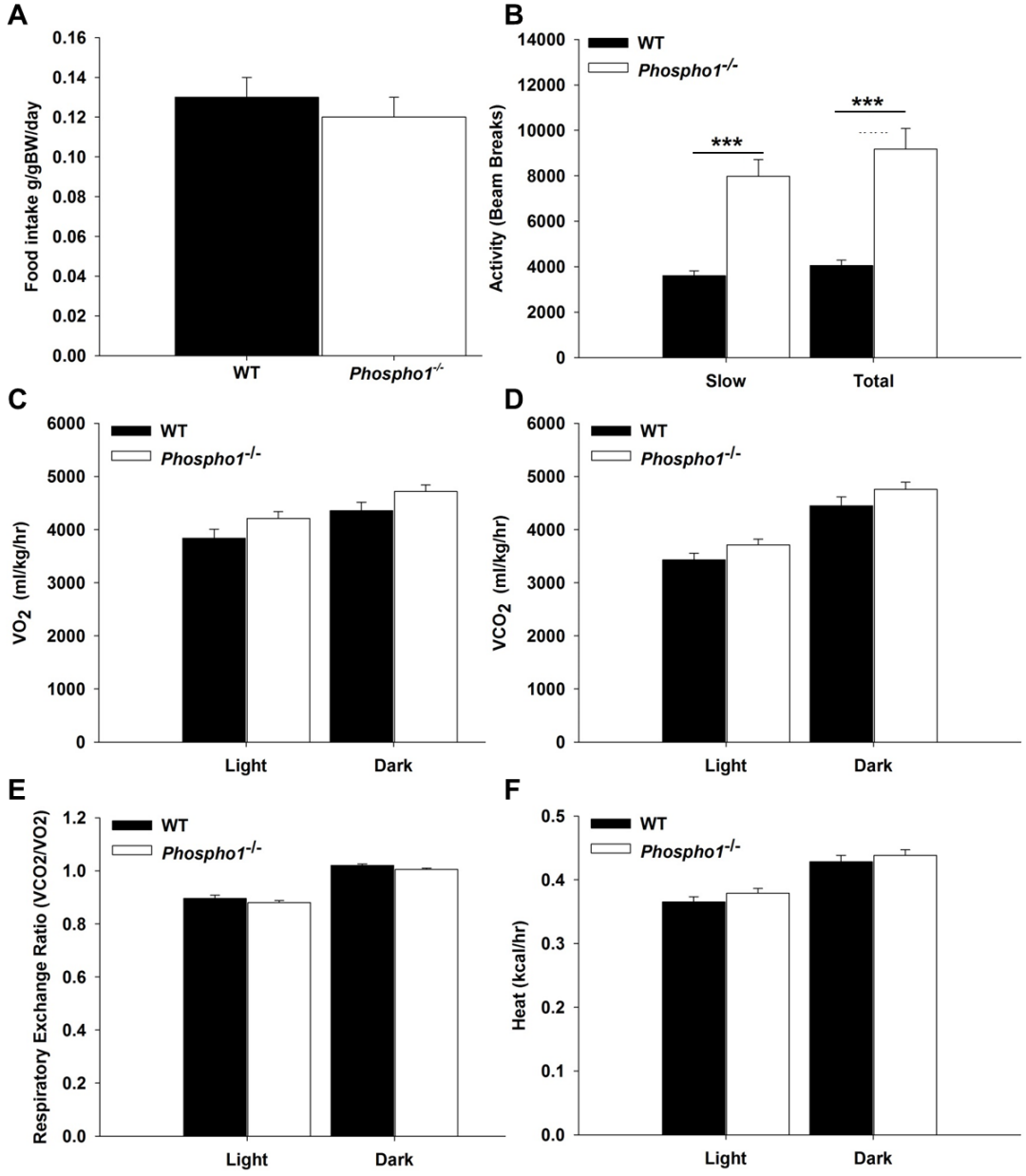

Figure 4.3 Energy expenditure and activity analysis of Juvenile *Phospho1*$^{-/-}$ male mice
Food intake was measured in 35 day old WT and *Phospho1*$^{-/-}$ male mice, no difference was observed when normalised to BW **(A)**. **(B)** An increase in slow activity was observed in *Phospho1*$^{-/-}$ mice which results in an increased in total activity, measure by beam breaking. **(C-F)** No change in energy expenditure, measured by indirect calorimetry was observed between WT and *Phospho1*$^{-/-}$ mice. n ≥ 3, t-test. Data are represented as mean ±S.E.M. * $P < 0.05$, ** $P < 0.01$, ***$P < 0.001$.

4.5.2 *Phospho1* inactivation improves glucose tolerance and insulin sensitivity in aged mice

It is likely, that as the genetic ablation of *Phospho1* results in a hypomineralised, fracture-prone skeleton in juvenile mice (Huesa *et al.* 2011) aged *Phospho1*$^{-/-}$ mice may not display any metabolic abnormalities. Therefore to discern if aged *Phospho1*$^{-/-}$ mice are also protected from obesity and insulin resistance aged (220 day old) *Phospho1*$^{-/-}$ mice were subject to metabolic analysis. Indeed, aged *Phospho1*$^{-/-}$ mice had improved glucose tolerance compared to WT counterparts, however the fasting glucose levels were unchanged between the genotypes (WT: 8.33±1.20, *Phospho1*$^{-/-}$: 8.60±0.15; $P = 0.61$) (Fig. 4.4A). In accordance with juvenile mice, aged *Phospho1*$^{-/-}$ mice had smaller (mg/g BW) subcutaneous (WT:6.13±0.51, *Phospho1*$^{-/-}$: 4.12±0.12; $P < 0.05$), gonadal (WT: 10.54±0.52, *Phospho1*$^{-/-}$: 5.98±0.43; $P < 0.05$) and iBF (WT: 5.49±0.10, *Phospho1*$^{-/-}$: 3.75±0.18; $P < 0.05$) fat depots compared to WT controls (Fig. 4.4B). Furthermore, improved metabolic activity seen in aged *Phospho1*$^{-/-}$: mice was not a consequence of altered food intake (g/gBW/day) (WT: 0.12±0.004; *Phospho1*$^{-/-}$: 0.103± 0.005 p = 0.15) (data not shown) or altered activity (Table 4.1). Unfortunately mice were not available to measure energy expenditure at this age.

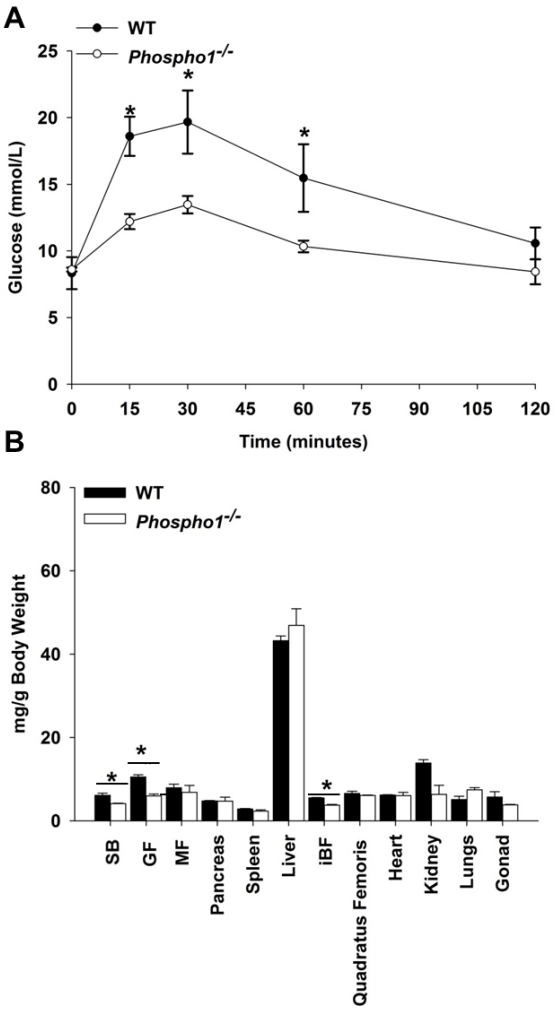

Figure 4.4 Aged *Phospho1*$^{-/-}$ male mice are insulin sensitive and have decreased adipose tissue stores

Metabolic analysis of 220 day old WT and *Phospho1*$^{-/-}$ male mice. **(A)** *Phospho1*$^{-/-}$ mice had no change in fasting blood glucose levels compared to WT counterparts however they showed an improvement in glucose tolerance as determined by glucose tolerance testing. **(B)** These experimental mice were then dissected and the outlined tissues were removed and weighed: Subcutaneous fat (SB), gonadal fat (GF), mesenteric fat (MF), pancreas, spleen, liver, intra-scapular brown fat (iBF), quadriceps femoris, heart, kidney, lungs and gonad. Dissection analysis revealed that (B) SB, GF and iBF fat depots (mg/g BW) were smaller in *Phospho1*$^{-/-}$ mice than WT counterpart mice. n ≥ 3, two way repeated measures ANOVA (A), t-test (B). Data are represented as mean ±S.E.M. * $P < 0.05$, ** $P < 0.01$, ***$P < 0.001$.

Activity	WT	*Phospho1*$^{-/-}$
Total Activity (BB)	1905.667±778.691	1670.333±1061.422
Fast Activity (BB)	233.667±109.152	158.000±105.929
Slow Activity (BB)	1672.000±674.959	1512.333±955.562
Total Static Counts (BB)	1656.333±648.334	1496.333±945.839
Fast Static Counts (BB)	103.333±32.845	81.333±54.606
Slow Static Counts (BB)	1553.000±615.593	1415.000±891.278
Total Mobile Counts (BB)	249.333±141.921	174.000±115.717
Fast Mobile Counts (BB)	130.333±78.318	76.667±51.324
Slow Mobile Counts (BB)	119.000±63.799	97.333±64.398
Active Time (s)	1392.000±557.557	1247.667±786.385
Static Time (s)	1245.000±483.327	1144.000±718.062
Mobile Time (s)	147.000±82.008	103.667±68.489
Front to back (BB)	114.000±65.248	82.333±52.097
Inactive Time (s)	50208.000±557.557	35152.333±14663.542
Distance travelled (m)	65.047±26.109	54.157±33.594

Table 4.1 Activity analysis of aged *Phospho1*$^{-/-}$ male mice

No change in activity of any of the parameter measured was observed in 220 day old *Phospho1*$^{-/-}$ mice compared to WT counterparts (measured by beam breaking). Beam breaks (BB), seconds (s), metres (s). n = 5, t-test. Data are represented as mean ±S.E.M.

4.5.3 *Phospho1* deficiency protects from diet induced hyperglycemia and insulin resistance

As *Phospho1*$^{-/-}$ mice disclosed an improvement in glucose tolerance it is likely that these mutant mice may be protected from hyperglycemia and insulin resistance. Wild type and *Phospho1*$^{-/-}$ mice were therefore fed mice a HFD from weaning until 120 days of age (data summarised in Table 4.2). In agreement with data from juvenile and aged mice, *Phospho1*$^{-/-}$ mice fed a CD remained leaner then WT counterparts until adulthood (Fig. 4.5A). Furthermore *Phospho1*$^{-/-}$ mice had decreased fasting glucose levels compared to WT mice which were not increased with HFD feeding (CD: WT:9.50 ±0.37, *Phospho1*$^{-/-}$:8.59±0.27;HFD: WT 10.3±0.53 mmol/L, *Phospho1*$^{-/-}$ 9.27±0.77 mmol/L; $P < 0.05$) and *Phospho1*$^{-/-}$ mice resisted the pronounced HFD induced weight gain (CD: WT:34.20 ±1.12, *Phospho1*$^{-/-}$:28.30±0.59; HFD: WT: 38.0±1.54 g, *Phospho1*$^{-/-}$: 32.4±1.26 g; $P < 0.05$) (Fig. 4.5 B-C). Indeed, *Phospho1*$^{-/-}$ mice displayed an improvement in glucose tolerance on the CD which persisted when *Phospho1*$^{-/-}$ mice were fed the chronic HFD (Fig. 4.6A). It is important to highlight the fasting glucose levels observed in the WT mice are very similar with previously reported fasted (5 hours) glucose levels of C57BL/6 mice (9.1±0.2 mmol/L) which had the highest fasting blood glucose compared to 3 commonly used imbred mouse stains (129X1/Sv, FVB/N and DBA/2 mice) (Berglund *et al.*, 2008).

To assess if the improved glucose tolerance was due to increased insulin secretion in response to glucose, GSIS were performed. In comparison to WT mice the GSIS revealed decreased insulin secretion in response to an IP injection of glucose in *Phospho1*$^{-/-}$ mice fed either a CD or HFD, suggestive of a highly insulin sensitive phenotype (Fig. 4.6B). Insulin tolerance tests revealed *Phospho1*$^{-/-}$ mice remained insulin sensitive on the HFD, which was unlike WT mice that became insulin resistance when fed a HFD (Fig. 4.6 C-D). These observations were consistent with the significant decrease in the HOMA-IR reading (a clinical method to quantify insulin resistance and beta-cell function) in *Phospho1*$^{-/-}$ HFD mice compared

to WT HFD controls, indicative that *Phospho1*$^{-/-}$ resist diet induced insulin resistance (HFD: WT 0.90±0.26, *Phospho1*$^{-/-}$ 0.33±0.04; $P < 0.05$)(Fig. 4.6 E). These observations were not explained by altered food intake (no data available for HFD due to crumbly nature of food deeming it impossible to measure without specialist equipment) (Fig. 4.6F). The detailed evaluation of fat deposition and localisation adult WT and *Phospho1*$^{-/-}$ is presented in Chapter 5).

Interestingly, histological analysis of pancreata from adult WT and *Phospho1*$^{-/-}$ male mice revealed CD adult *Phospho1*$^{-/-}$ mice had a significant decrease in islet number (CD: WT 1.40 ±0.10, *Phospho1*$^{-/-}$ 1.10±0.001; $P < 0.05$) however this did not translate to a decrease in islet area, indicative that *Phospho1*$^{-/-}$ mice have larger islets than WT controls (Fig. 4.7 & 4.8A-B). Moreover, no change in pancreas insulin content between the genotypes was observed in the CD cohort, but WT HFD mice had a significant decrease in insulin content (μg/mg protein) compared to *Phospho1*$^{-/-}$ HFD mice (HFD: WT 280.00 ±11.32, *Phospho1*$^{-/-}$ 258.01±6.12; $P < 0.05$) (Fig. 4.8C).

Intriguingly, histological analysis of BAT from all ages indicate that *Phospho1*$^{-/-}$ mice had a markedly decreased lipid content and increased cellular nuclei number(Fig. 4.9 and 4.10A). Importantly no differences were observed in the expression of *Ucp1* and other BAT enriched genes e.g. *Pparα*, *dio2*, *Pgc1α*, *prdm16*, *Cidae* and *Adipoq* (Fig. 4.10B). UCP1 was also found to be normally expressed at the protein level (Fig. 4.10C). Since UCP1 is responsible for the majority of non-shivering thermogenesis, this suggests that canonical thermogenesis through UCP1 does not underlie the metabolic protection seen in *Phospho1*$^{-/-}$ mice

To deduce if increased energy expenditure/activity or decreased food intake could offer a simple explanation for the metabolic protection observed in *Phospho1*$^{-/-}$ mice these parameters were measured. No change in slow or total activity was seen between the genotypes as observed in juvenile mice (Fig. 4.11 A-B). Intriguingly *Phospho1*$^{-/-}$ HFD mice had significantly increased oxygen consumption (ml/kg/hr)

(HFD Dark: WT 3835.77 ±168.54, *Phospho1*$^{-/-}$ 4263.99±;72.05 $P < 0.05$), produced significantly less heat (kcal/hr)than WT counterparts (Dark HFD: WT 0.68 ± 0.014, *Phospho1*$^{-/-}$ 0.65±; 0.01$P < 0.01$) despite the dramatic change in BAT histology (Fig. 4.9) and had a decreased respiratory exchange ratio (RER) (VCO_2/VO_2), suggestive of switch to fatty acid oxidation (Dark HFD: WT 0.83± 0.006, *Phospho1*$^{-/-}$ 0.81±; 0.005$P < 0.05$) (Fig. 4.11 C-F).

4.5.4 PHOSPH01 may represent a druggable target for the treatment of insulin resistance and diabetes

Finally if the observed metabolic phenotype in *Phospho1*$^{-/-}$ mice was primarily bone driven and not due to food intake or activity, it was of interest to ascertain if *Phospho1* heterozygote (*Phospho1*$^{-/+}$) mice displayed an intermediate insulin sensitive phenotype. Glucose and ITT revealed that juvenile *Phospho1*$^{-/+}$ male mice displayed an intermediate insulin sensitive phenotype, showing improvement in glucose tolerance and insulin sensitivity compared to WT mice (Fig. 4.12A-B), however no significant difference between WT and *Phospho1*$^{-/+}$ mice fat depots (mg/g BW) were seen at necropsy, subcutaneous (WT:4.31 ±0.28, *Phospho1*$^{-/+}$:4.26 ±0.35;), MF (WT:5.30 ±0.30, *Phospho1*$^{-/+}$:6.45±1.63), GF (WT:4.31 ±0.28, *Phospho1*$^{-/+}$: 4.26±0.35) and iBF (WT:5.11 ±0.56, *Phospho1*$^{-/+}$:4.69 ±0.44) These data suggest that PHOSPHO1 may represent a druggable target which may be of importance in the global epidemic of insulin resistance and diabetes.

Trait	WTCD	KOCD	WTHFD	KOHFD	WT.	KO.	CD.	HFD.	Genotype	Diet	Genotype x Diet
Weight at 21 days (g)	13.595±1.151 a,b	11.360±1.337 a,b	11.221±0.580 b	13.200±0.590 a	12.401±0.646	12.283±0.731	12.480±0.889	12.200±0.410	0.907	0.779	0.036
Weight at 120 days (g)	35.245±0.961 a	28.021±1.024 c	38.000±1.080 a	31.561±1.116 d	36.623±0.720	29.799±0.758	31.638±0.790	34.781±0.781	**<0.001**	**0.003**	0.708
Fasting glucose (mmol/L)	9.443±0.370 a,b	8.311±0.387 c	10.281±0.375 a	8.560±0.389 b,c	9.867±0.262	8.434±0.278	8.873±0.260	9.421±0.267	**<0.001**	0.149	0.436
Max weight (g)	43.221±6.436 a,b	28.684±7.436 b	48.252±3.327 a	33.937±3.323 b	45.735±3.621	31.312±4.070	35.954±4.914	41.096±2.354	**0.012**	0.352	0.984
Max weight gain (g/day)	0.369±0.050 b	0.634±0.064 a	0.417±0.033 b	0.387±0.039 b	0.384±0.037	0.500±0.039	0.497±0.046	0.398±0.025	**0.010**	**0.025**	**0.002**
Age at max weight gain (days)	18.399±5.958 b	16.636±6.873 b	33.600±3.071 a	13.243±3.070 b	25.998±3.358	14.944±3.763	17.516±4.557	23.424±2.175	**0.035**	0.249	**0.073**
Age at half max weight (days)	48.216±9.326 a,b	13.732±10.771 c	28.481±4.826 b,c	43.044±4.821 a	38.343±5.253	28.399±5.902	30.971±7.120	35.768±3.400	0.216	0.548	**0.004**

Table 4.2 General linear model summary table of the effect of genotype (WT and *Phospho1*$^{-/-}$) and diet (CD and HFD) on the growth parameters in mice

White columns contain least square means are presented with their SEM from wild type mice (WT), *Phospho1*$^{-/-}$ mice (KO), control diet (CD) and high fat diet (HFD). Orange columns contain least square means with their SEM of WT data from all diets (WT.), *Phospho1*$^{-/-}$ data from all diets (KO.), CD data from all genotypes (CD.) and HFD from all genotypes (HFD.). Green columns contain *P* values of the genotype effect only (Genotype) on growth parameters, diet effect only (Diet) and the combination of genotype and diet effect (Genotype x Diet). Values assigned the same letter show no significant difference from one another ($P < 0.05$) white columns). Significances denoted in bold (green columns). n = 12, parameters calculated by linear regression, Gompertz growth model and analysed using the generalised linear model.

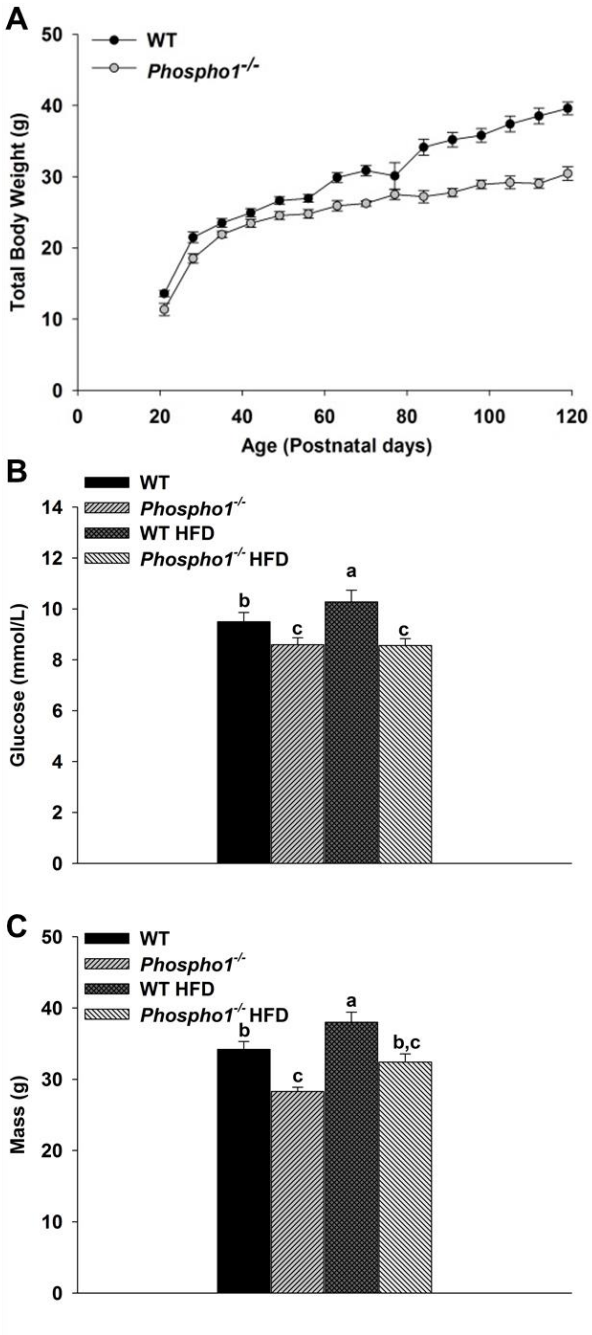

Figure 4.5 Adult *Phospho1*$^{-/-}$ male mice are protected from hyperglycemia and weight gain following the administration of a HFD

WT **and** *Phospho1*$^{-/-}$ mice on the CD were weighed once a week on the same day and time. *Phospho1*$^{-/-}$ mice remained leaner then WT counterparts until adulthood (120 days) (A). Following administration of a HFD from weaning until 120 days of age the fasting glucose levels and mass of WT and *Phospho1*$^{-/-}$ mice on the CD and HFD were measured. *Phospho1*$^{-/-}$ mice had decreased fasting glucose levels compared to WT mice which were not increased with HFD feeding (B), likewise there was no significant increase in BW following HFD feeding which was observed in WT mice (C). $n \geq 3$, one way ANOVA. Data are represented as mean ±S.E.M. Values assigned the same letter show no significant difference from one another ($P < 0.05$).

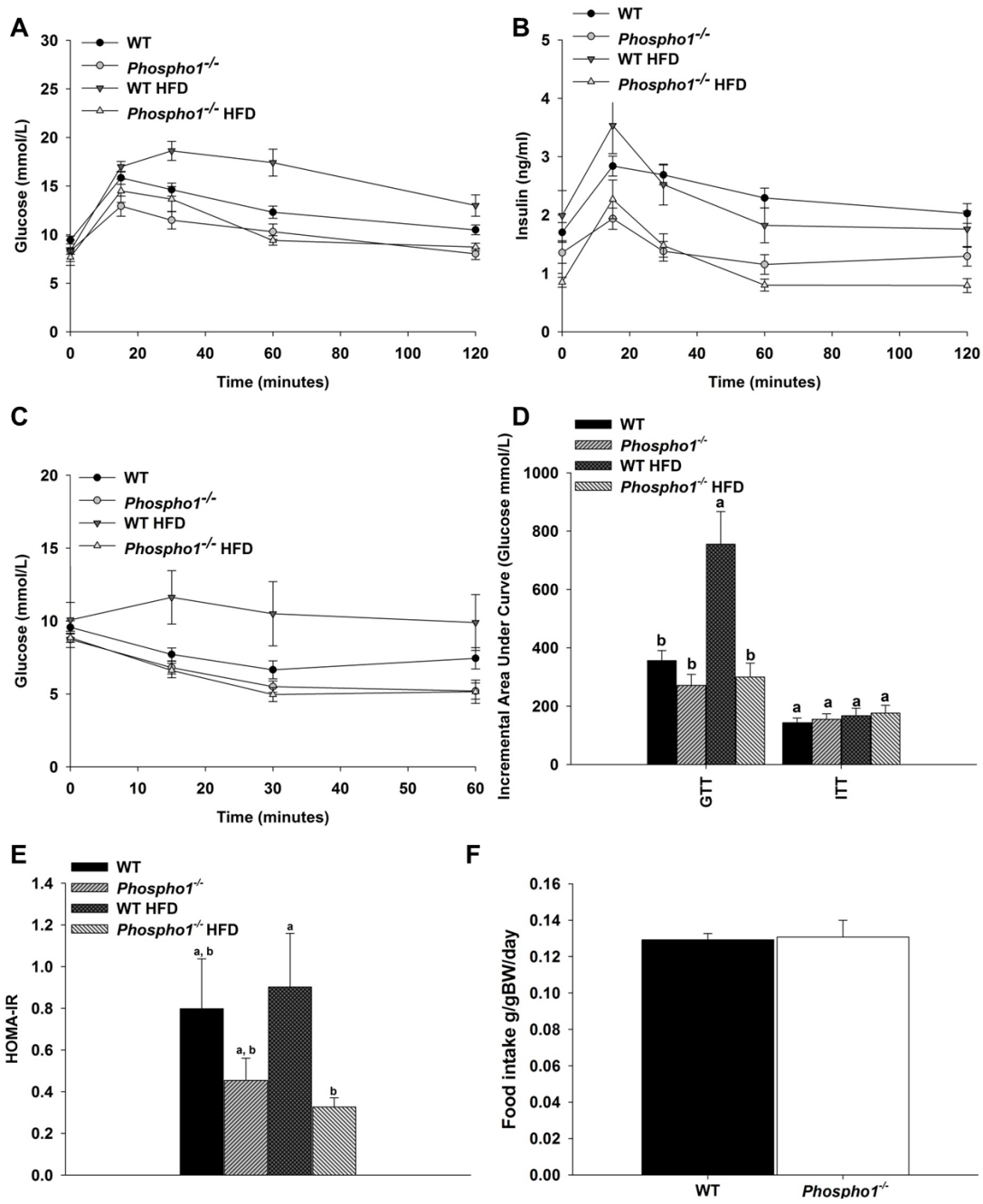

Figure 4.6 Adult *Phospho1*$^{-/-}$ male mice are protected from diet induced glucose intolerance and insulin resistance

WT and *Phospho1*$^{-/-}$ were fed a HFD from weaning until 120 days of age. Glucose tolerance tests **(A)** and insulin tolerance tests **(B)** revealed WT mice fed a HFD became insulin resistant whereas *Phospho1*$^{-/-}$ mice showed an improvement in glucose tolerance on the CD compared to WT mice which then persisted when *Phospho1*$^{-/-}$ mice were fed the chronic HFD. Furthermore GSIS revealed the improved glucose tolerance in *Phospho1*$^{-/-}$ mice fed either a CD or HFD was accompanied by a decreased insulin response in response to glucose. *Phospho1*$^{-/-}$ mice resist insulin resistance observed in WT HFD mice **(C)**. There was a significant decrease in the area under the curve (GTT) on the HFD between WT and

Phospho1$^{-/-}$ mice **(D)** which translated into a significant decrease in the HOMA-IR reading in *Phospho1*$^{-/-}$ HFD mice compared to WT HFD controls **(E)**. These changes were independent on altered food intake **(F)**. n ≥ 3, two way repeated measures ANOVA (A-C), one way ANOVA (D&E) t-test (F).Data are represented as mean ±S.E.M. Values assigned the same letter show no significant difference from one another ($P < 0.05$).

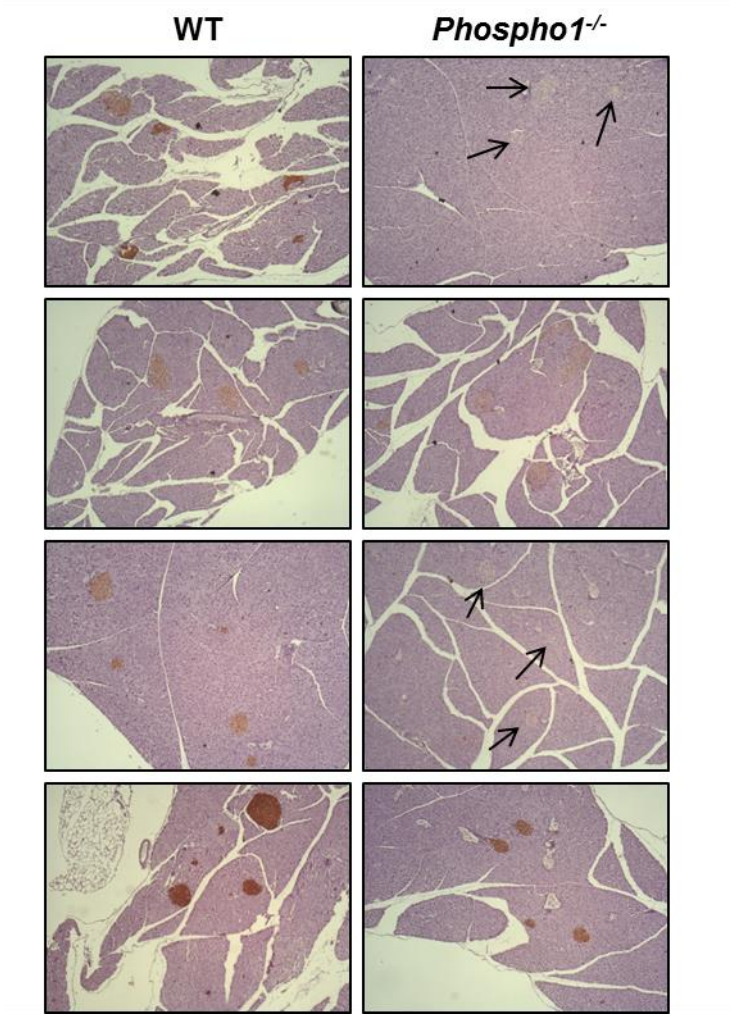

Figure 4.7 Immunolocalisation of insulin in the pancreas of adult WT and *Phospho1*$^{-/-}$ male mice

Immunohistochemistry showed insulin present in WT and *Phospho1*$^{-/-}$ islets (positive insulin protein is indicated by brown stain). Arrows indicate insulin negative islets (n = 4).

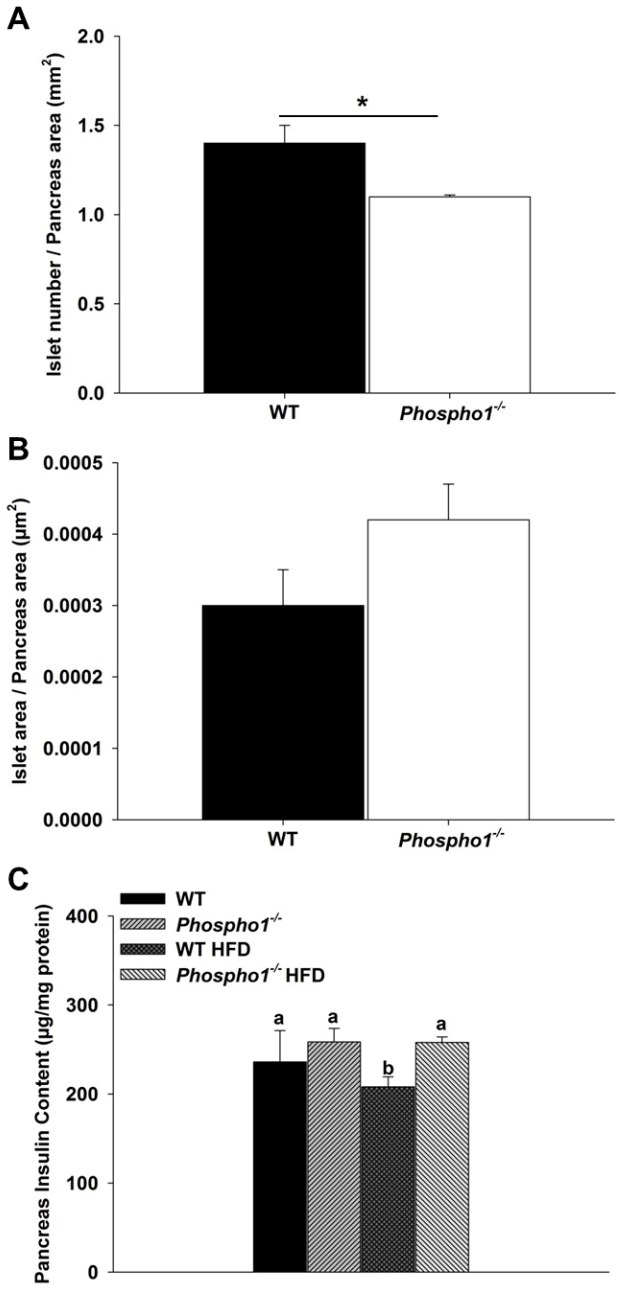

Figure 4.8 Quantification of Immunolocalisation of Insulin in the adult WT and *Phospho1*$^{-/-}$ male mice

Insulin immunohistochemistry analysis revealed that 120 day old *Phospho1*$^{-/-}$ mice have a significant decrease in islet number **(A)** however no change in islet area. **(B)** No change in insulin content between the genotypes was observed in the CD cohort; however WT HFD mice had a significant decrease in insulin content compared to *Phospho1*$^{-/-}$ HFD mice **(C)**. n = 4, t-test (A&B), one way ANOVA (C). Data are represented as mean ±S.E.M. Values assigned the same letter show no significant difference from one another ($P < 0.05$).* $P < 0.05$, ** $P < 0.01$, ***$P < 0.001$.

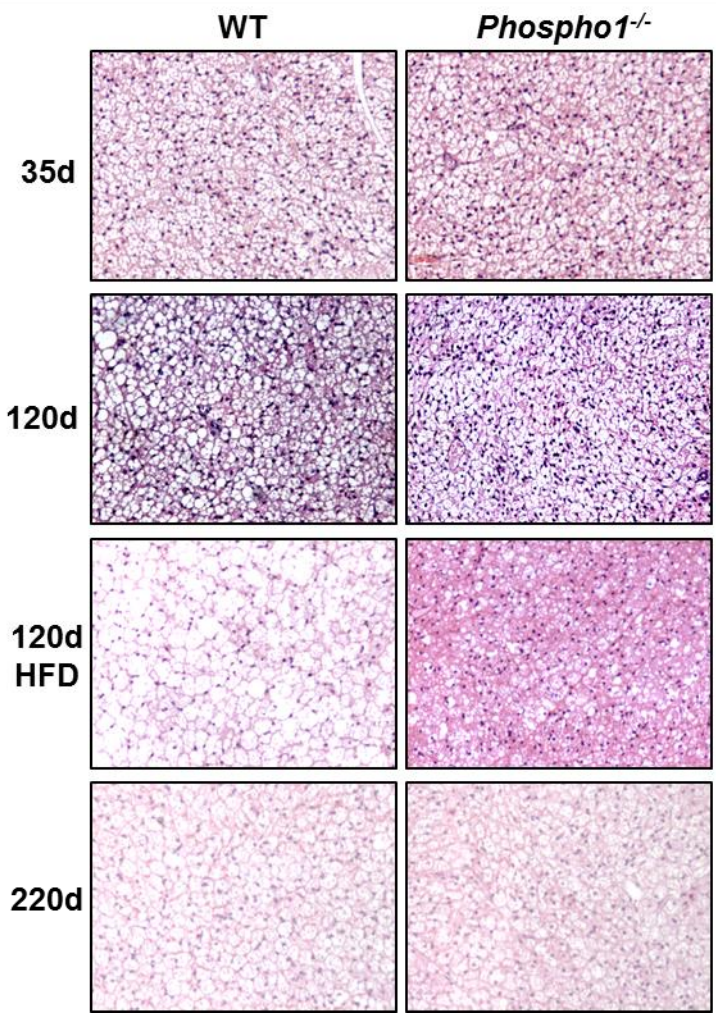

Figure 4.9 *Phospho1*$^{-/-}$ male mice have smaller brown fat adipocytes compared to WT controls
Representative histology of juvenile, adult (CD and HFD) and aged WT and *Phospho1*$^{-/-}$ mice.

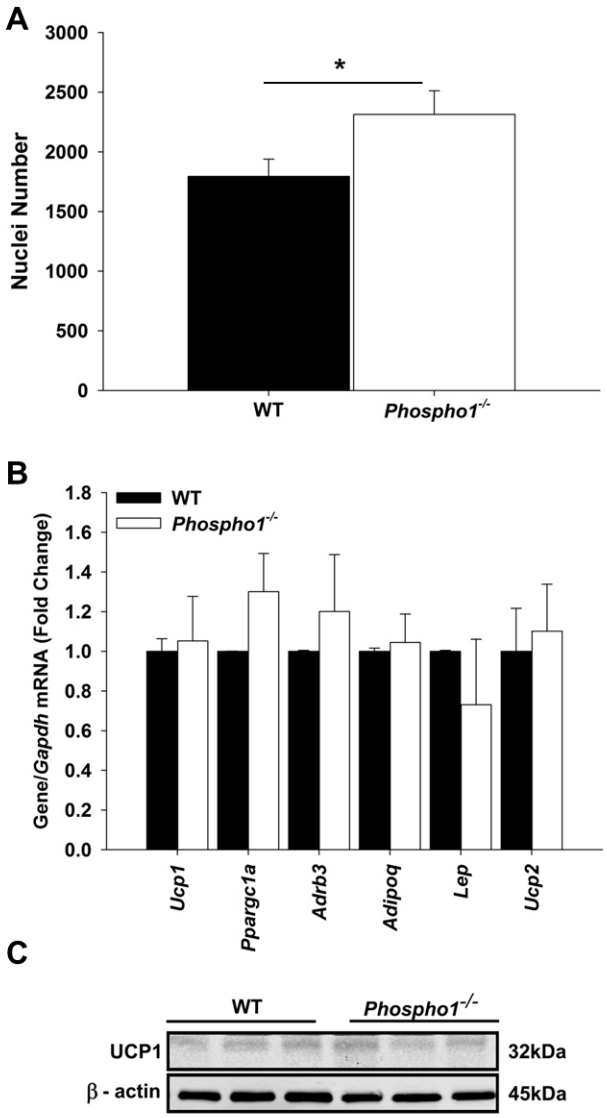

Figure 4.10 Brown fat characterisation of adult mice

(A) 120 day old *Phospho1*$^{-/-}$ mice had a significant increase in brown fat nuclei number indicative of an increase number of small brown adipocytes. However this was not accompanies by mRNA expression of brown fat specific genes **(B)** or **(C)** UCP1 protein expression. n ≥ 3, t-test (A&B). Data are represented as mean ±S.E.M. **P < 0.05*, ** *P < 0.01*, ****P < 0.001*.

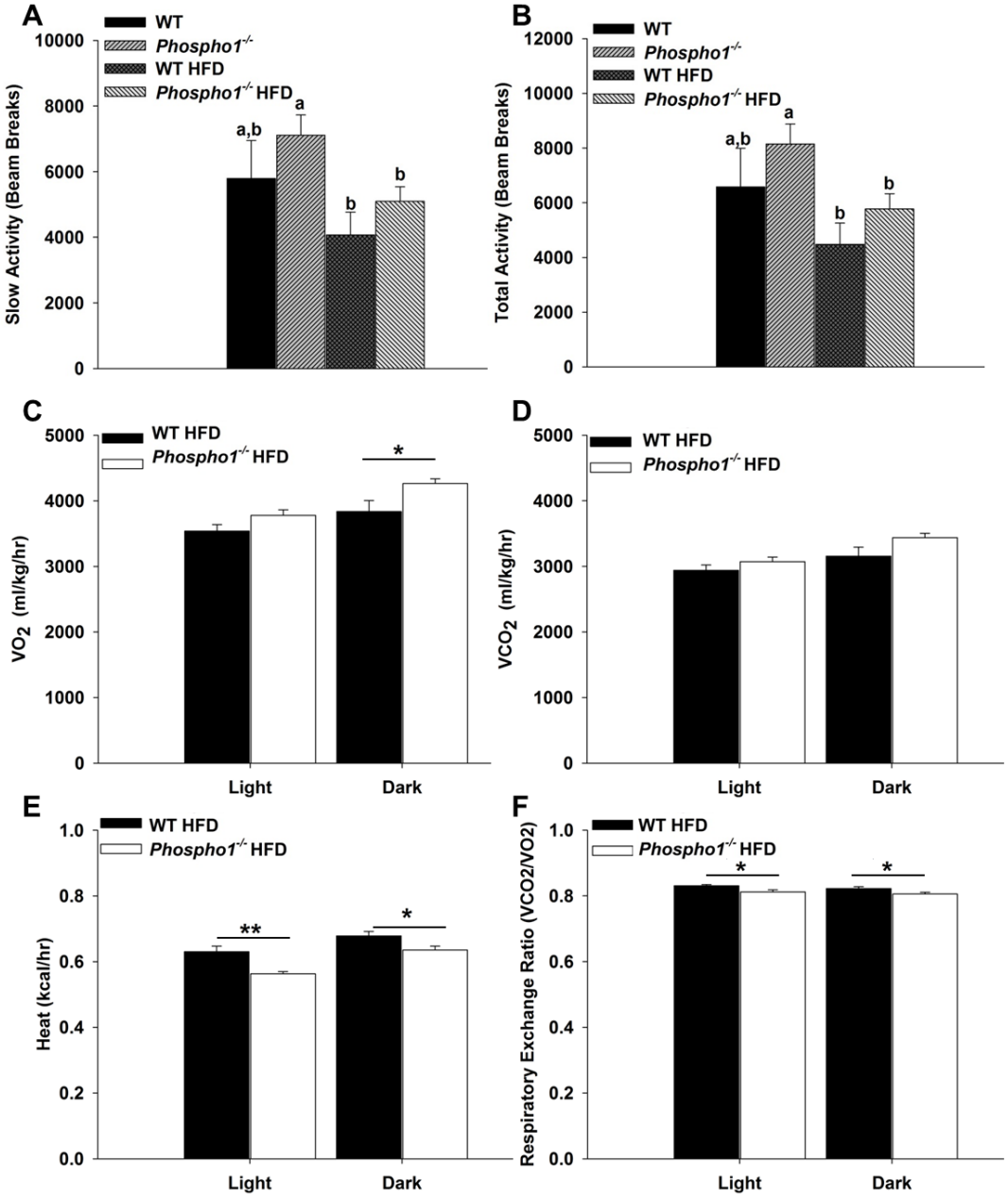

Figure 4.11 Energy expenditure and activity analysis of adult *Phospho1*$^{-/-}$ male mice
(A) No major changes in slow activity or **(B)** total activity was observed between the genotypes however HFD significantly decreased activity in both genotypes. *Phospho1*$^{-/-}$ HFD mice had a significantly increased VO_2 in the dark **(C)**, however no change in VCO_2 was observed **(D)**. *Phospho1*$^{-/-}$ HFD mice produced significantly less heat than WT counterparts both in the light and dark **(E).** Furthermore *Phospho1*$^{-/-}$ respiratory exchange ratio (RER) was significantly decreased compared to WT counterparts both in the light and dark suggestive of a switch to fatty acid oxidation **(F)**. **)**. n ≥ 3, one way ANOVA (A&B), t-test (C-F).Data are represented as mean ±S.E.M. * $P < 0.05$, ** $P < 0.01$, ***$P < 0.001$.

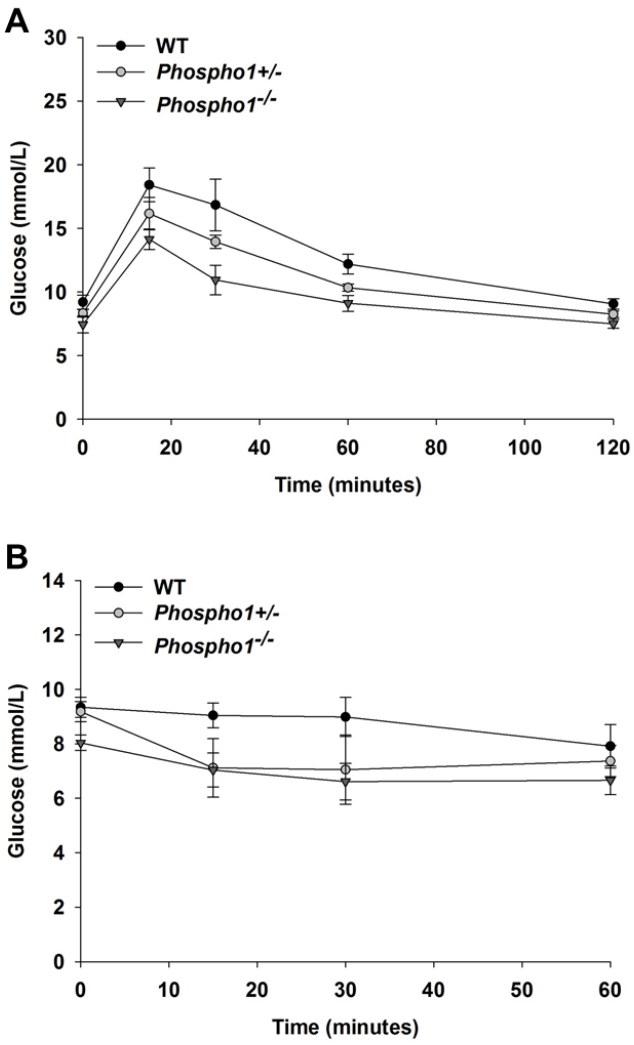

Figure 4.12 Juvenile *Phospho1*$^{-/+}$ male mice display an intermediate insulin sensitive phenotype

Metabolic analysis of 35 day old WT, *Phospho1*$^{+/-}$ and *Phospho1*$^{-/-}$ male mice. **(A)** Glucose tolerance tests revealed that *Phospho1*$^{-/+}$ mice also showed an improvement in glucose tolerance compared to WT mice and were **(B)** more insulin sensitive compared to WT counterparts as determined by an ITT. These data are suggestive that PHOSPHO1 may represent a druggable target. n = 5, two way repeated measures ANOVA. Data are represented as mean ±S.E.M.

4.5.5 Analysis of HFD feeding on the phenotype of WT and *Phospho1*$^{-/-}$ adult bone

There is a clear disparity in the literature regarding the relationship between HFD feeding and bone mineral density (BMD) in murine models. Whilst some murine models lose bone with a HFD others do not (Doucette *et al.*, 2015). It is also important to highlight that in genetically homogenous mice, HFD feeding leads to different metabolic adaptations which may affect bone parameters (Burcelin *et al*., 2002). Therefore, to investigate the interrelationship of diet, age and bone in male WT and *Phospho1*$^{-/-}$, we first x-rayed tibiae of juvenile (35-days-old) and adult (120-days-old) WT and *Phospho1*$^{-/-}$ tibiae (CD and HFD). All *Phospho1*$^{-/-}$ tibiae irrespective of age/diet show clear deformation (Fig. 4.13). Densitometry analysis confirmed that *Phospho1*$^{-/-}$ tibia are shorter in length and have increased width, this was not changed by the administration of a HFD (Fig. 4.14 A-B). However HFD feeding normalised the increased OD seen in 120 day old CD *Phospho1*$^{-/-}$ tibiae to the WT basal state (Fig. 4.14 C), indicative that HFD lowers mineral content in *Phospho1*$^{-/-}$ tibiae but does not affect WT tibiae.

Next juvenile (35 day old) WT and *Phospho1*$^{-/-}$ male mice tibiae were subject to 3-pont-bending and μCT to assess the biomechanical, trabecular and cortical parameters. Previous analysis revealed that long bones of 30 day old *Phospho1*$^{-/-}$ mice undergo plastic deformation and do not fracture upon bending. Furthermore these bones had reduced accumulation of osteoid in the long bones, reduced ash mineral content and reduced BMD of cortical bone (Huesa *et al.*, 2011; Yadav *et al.*, 2011). In this present study however, only subtle changes in bone architecture and biomechanistic properties were seen between juvenile tibiae from *Phospho1*$^{-/-}$ and WT mice. The *Phospho1*$^{-/-}$ mice had a significant reduction in cortical thickness and increase in maximum stiffness (Table 4.3).

To determine if HFD had an effect on biomechanical, trabecular and cortical parameters of tibiae from WT and *Phospho1*$^{-/-}$ mice, tibiae were again subjected to 3-point-bending and μCT analysis. The general linear model was used to ascertain if

the differences in biomechanical, trabecular and cortical parameters were due to a genotype effect only, diet effect only or the combination of genotype and diet (Table 4.4). The expected the genetic ablation of *Phospho1* in mice significantly decreased cortical porosity and increased the load and slope to maximum stiffness, yield, failure and fracture. Interestingly diet had the greatest effect on trabecular bone, increasing trabecular separation, trabecular pattern formation and structural model index, but reduced trabecular number and the degree of anisotropy. Indeed HFD also significantly reduced bone volume fraction. Surprisingly the combination of genotype and diet only had a significant effect the trabecular degree of anisotropy and cortical porosity (*P* values outlined in Table 4.4).

Combining the data from juvenile and CD adult mice it was then possible to ascertain if the differences in biomechanical, trabecular and cortical parameters were due to a genotype effect only, age effect only or the combination of genotype and age (Table 4.5). Most surprisingly, genotype only had a significant effect on structural model index, load and slope to maximum stiffness. As anticipated age had an effect on most of the parameters measured, whereas the combination of genotype and age have no significant effect on any of the parameters measured (Table 4.5).

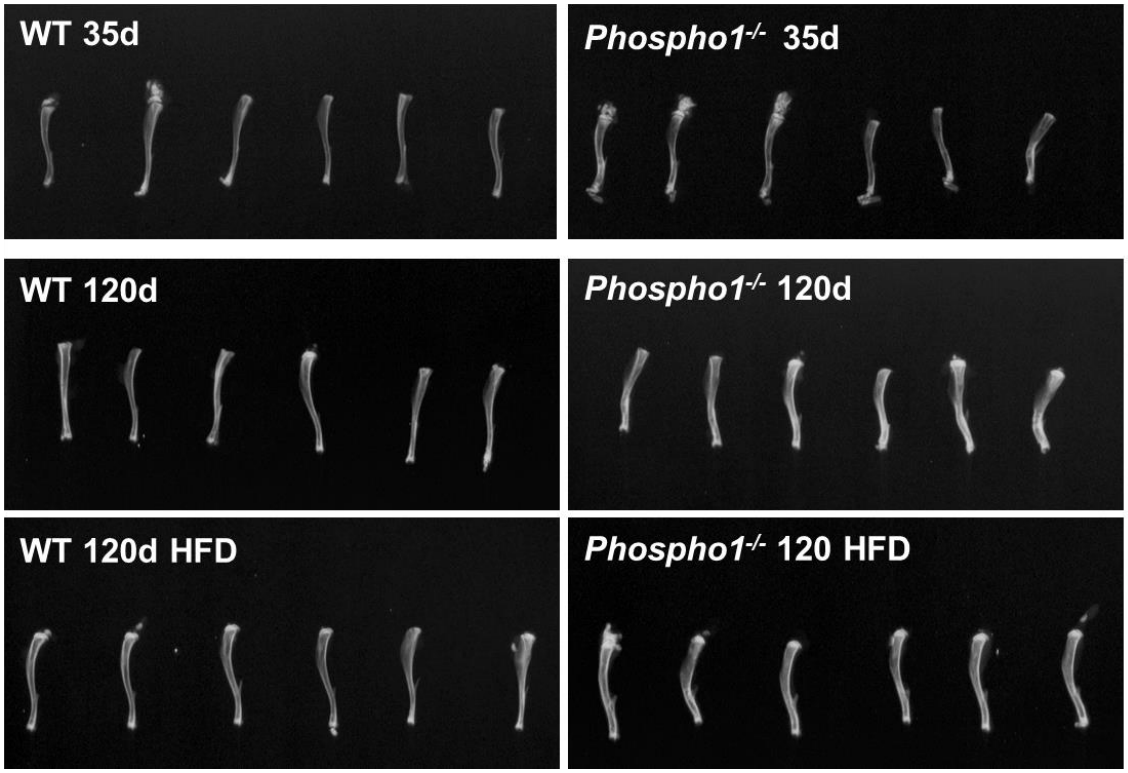

Figure 4.13 X-rays of WT and *Phospho1*$^{-/-}$ tibiae
X-rays of juvenile (35-days-old) and adult (120-days-old) WT and *Phospho1*$^{-/-}$ tibiae. All Phospho1$^{-/-}$ tibiae show clear deformation irrespective of diet (n = 6).

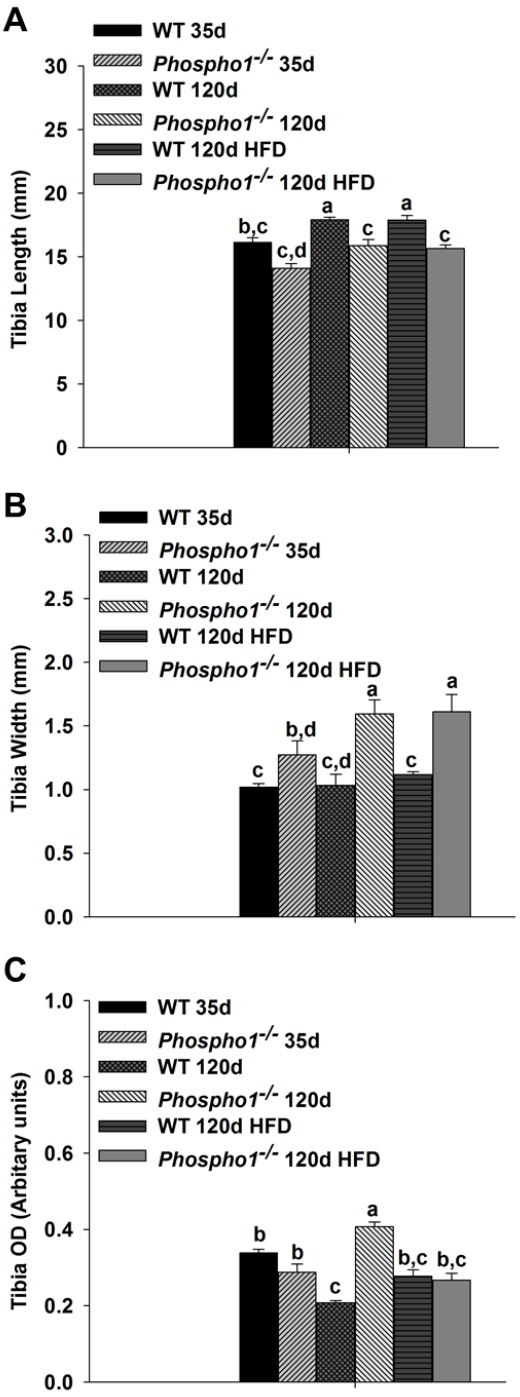

Figure 4.14 X-ray densitometry analysis

X-ray of densitometry of juvenile (35-days-old) and adult (120-days-old) WT and Phospho1$^{-/-}$ tibia. *All Phospho1$^{-/-}$* tibiae have are significantly decreased length **(A)** and increased in width **(B)** irrespective of diet compared to WT tibiae. Optical density measurements of juvenile and HFD mice were unchanged between the genotypes however *Phospho1$^{-/-}$* CD adult tibiae were significantly more dense than WT controls **(C)**. n = 6, one way ANOVA. Data are represented as mean ±S.E.M. Values assigned the same letter show no significant difference from one another *($P < 0.05$).*

Trait	WT	*Phospho1*$^{-/-}$
BV/TV	10.403±1.186	10.240±1.299
Tr. Th.	34.063±1.014	32.868±1.110
Tr. Sp.	186.457±9.743	204.320±10.673
Tr. No.	0.003±0.000	0.003±0.000
Tr. Pf.	0.032±0.003	0.027±0.003
SMI	1.969 ±0.093	1.787±0.102
DA*	2.679±0.413	2.584±0.452
Cor. Por total %	48.946±4.385	57.585±4.804
Cor.Th	**171.848±7.219**	**144.576±7.908**
Cor. BMD	1.213±0.055	1.095±0.060
Load to Max (N)	**2.784±0.429**	**4.382±0.470**
Slope to Max	14.017±1.582	17.204±1.733
Yield	4.021±0.599	5.090±0.657
Failure (N)	7.984±0.882	8.219±0.967
Fracture (N)	5.541±0.939	6.005±1.028
Work to Failure	4.059±0.699	3.547±0.766
Work to Fracture	6.634±0.995	6.974±1.090
Post-Failure Work	2.575±0.896	3.427±0.981

Table 4.3 μCT and 3-point-bending analysis of tibiae from 35 day male WT and *Phospho1*$^{-/-}$ mice
Least square means are presented with their standard errors of the mean (SEM); n = 6 per group. The following parameters were measured - μCT analysis : bone volume fraction (BV/TV), trabecular thickness (Tr. Th.), trabecular separation (Tr. Sp.), trabecular number (Tr. No.), trabecular pattern formation (Tr. Pf.), structural model index (SMI), degree of anisotropy (DA), cortical porosity (Cor. Por. %), cortical thickness (Cor.Th.) and cortical bone mineral density (Cor. BMD). 3-point-bending analysis – Load to max, slope to max, yield, failure, fracture, work to failure, work to fracture. n = 6, t-test. Significances denoted in bold $P < 0.05$.

Trait	WTCD	KOCD	WTHFD	KOHFD	WT.	KO.	CD.	HFD.	Genotype	Diet	Genotype x Diet
BV/TV	14.073±0.819 a	14.073±0.819 a	8.405±0.819 b	8.675±0.819 b	11.239±0.579	11.374±0.579	14.073±0.579	8.540±0.579	0.871	**< 0.001**	0.871
Tr. Th.	47.660±1.893 c	49.698±1.893 b,c	48.81±1.893 b,c	54.275±1.893 a,b	48.236±1.339	51.986±1.339	48.679±1.339	51.544±1.339	0.062	0.146	0.377
Tr. Sp.	190.938±15.479 b	188.815±15.479 b	254.407±15.479 a	296.357±15.479 a	222.673±10.946	242.586±10.946	189.877±10.946	275.382±10.946	0.213	**< 0.001**	0.170
Tr. No.	0.003±0.000 a	0.003±0.000 a	0.002±0.000 b	0.002±0.000 b	0.002±0.000	0.003±0.000	0.003±0.000	0.002±0.000	0.391	**< 0.001**	0.095
Tr. Pf.	0.022±0.002 b,c	0.017±0.002 b	0.030±0.002 a	0.026±0.002 a,c	0.026±0.001	0.022±0.001	0.020±0.001	0.028±0.001	0.031	**< 0.001**	0.966
SMI	1.817±0.098 b	1.591±0.098 b,c	2.306±0.098 a	2.246±0.098 a	2.061±0.069	1.918±0.069	1.704±0.069	2.276±0.069	0.158	**< 0.001**	0.405
DA*	2.755±0.065 a	2.614±0.065 a,c	2.420±0.065 b	2.559±0.065 b,c	2.588±0.046	2.587±0.046	2.685±0.046	2.490±0.046	0.987	**0.007**	**0.043**
Cor. Por total %	52.038±1.435 b,c	52.991±1.435 b	57.478±1.435 a	47.803±1.435 d	54.758±1.014	50.397±1.014	52.514±1.014	52.640±1.014	**0.007**	0.931	**0.001**
Cor.Th	186.975±15.728 a	188.550±15.78 a	157.491±15.728 a	190.328±15.728 a	172.233±11.121	189.439±11.121	187.763±11.121	173.910±11.121	0.287	0.389	0.332
Cor. BMD	1.196±0.054 a	1.341±0.054 a	1.213±0.054 a	1.196±0.054 a	1.204±0.038	1.268±0.038	1.268±0.038	1.205±0.038	0.251	0.252	0.150
Load to Max (N)	5.428±1.032 b,c	7.615±0.942 a,c	4.669±0.942 b	8.927±0.942 a	5.048±0.698	8.271±0.666	6.521±0.698	6.798±0.666	**0.003**	0.777	0.297
Slope to Max	22.605±3.960 c	34.314±3.615 a,b	27.316±3.615 b,c	44.190±3.615 a	24.961±2.681	39.252±2.556	28.460±2.681	35.753±2.556	**0.001**	0.064	0.494
Yield	7.479±1.467 a,d	11.182±1.339 a	6.747±1.339 b,c,d	10.454±1.339 a,c	7.113±0.993	10.818±0.947	9.331±0.993	8.600±0.947	**0.014**	0.601	0.999
Failure (N)	12.192±1.511 b	16.847±1.379 a	11.568±1.379 b	17.072±1.379 a	11.880±1.023	16.959±0.975	14.519±1.023	14.320±0.975	**0.002**	0.889	0.767
Fracture (N)	6.678±1.664 a	11.218±1.519 a	7.011±1.519 a	10.807±1.519 a	6.844±1.127	11.012±1.074	8.948±1.127	8.909±1.074	**0.015**	0.980	0.814
Work to Failure	5.078±0.850 a	5.470±0.776 a	3.774±0.776 a	4.808±0.776 a	4.426±0.576	5.139±0.549	5.274±0.576	4.291±0.549	0.382	0.232	0.691
Work to Fracture	8.654±1.329 a,b	10.201±1.213 a	5.313±1.213 b	9.610±1.213 a	6.983±0.900	9.906±0.858	9.428±0.9	7.461±0.858	**0.030**	0.130	0.282
Post-Failure Work	3.576±1.261 a	4.731±1.151 a	1.538±1.151 a	4.802±1.151 a	2.557±0.853	4.767±0.814	4.153±0.853	3.170±0.814	0.076	0.415	0.382

Table 4.4 µCT and 3-point-bending analysis of tibiae from 120 day male CD and HFD WT and *Phospho1*$^{-/-}$ mice

µCT analysis : bone volume fraction (BV/TV), trabecular thickness (Tr. Th.), trabecular separation (Tr. Sp.), trabecular number (Tr. No.), trabecular pattern formation (Tr. Pf.), structural model index (SMI), degree of anisotropy (DA), cortical porosity (Cor. Por. %), cortical thickness (Cor.Th.) and cortical bone mineral density (Cor. BMD). 3-point-bending analysis – Load to max, slope to max, yield, failure, fracture, work to failure, work to fracture. White columns contain least square means presented with their SEM from wild type mice (WT), *Phospho1*$^{-/-}$ mice (KO), control diet (CD) and high fat diet (HFD). Orange columns contain least square means with their SEM of WT data from all diets (WT.), *Phospho1*$^{-/-}$ data from all diets (KO.), CD data from all genotypes (CD.) and HFD from all genotypes (HFD.). Green columns contain *P* values of the genotype effect only (Genotype) on bone parameters, diet effect only (Diet) and the combination of genotype and diet effect (Genotype x Diet). Values assigned the same letter show no significant difference from one another ($(P < 0.05)$ white columns). Significances denoted in bold (green columns). n = 6, generalised linear model.

Trait	WT35d	KO35d	WT120d	KO120d	WT.	KO.	35d.	120d.	Genotype	Age	Genotype x Age
BV/TV	10.403±1.018 b	10.240±1.116 b	14.073±1.018 a	14.073±1.018 a	12.238±0.72	12.157±0.755	10.322±0.755	14.073±0.72	0.939	**0.002**	0.939
Tr. Th.	34.063±1.335 b	32.868±1.463 b	47.660±1.335 a	49.698±1.335 a	40.861±0.944	41.283±0.99	33.465±0.99	48.679±0.944	0.762	**< 0.001**	0.252
Tr. Sp.	186.457±7.606 a	204.320±8.332 a	190.938±7.606 a	188.815±7.606 a	188.698±5.378	196.568±5.641	195.388±5.641	189.877±5.378	0.325	0.488	0.215
Tr. No.	0.003±0.000 a	0.003±0.000 a	0.003±0.000 a	0.003±0.000 a	0.003±0.000	0.003±0.000	0.003±0.000	0.003±0.000	0.447	0.386	0.386
Tr. Pf.	0.032±0.002 a	0.027±0.003 a,c	0.022±0.002 a,b	0.017±0.002 b,c	0.027±0.002	0.022±0.002	0.03±0.002	0.02±0.002	0.058	**0.001**	0.917
SMI	1.969±0.091 a	1.787±0.100 a,c	1.817±0.091 a,c	1.591±0.091 a,c	1.893±0.064	1.689±0.067	1.878±0.067	1.704±0.064	**0.041**	0.077	0.814
DA*	2.679±0.287 a	2.584±0.314 a	2.755±0.287 a	2.614±0.287 a	2.717±0.203	2.599±0.213	2.631±0.213	2.685±0.203	0.692	0.858	0.938
Cor. Por total %	48.946±3.143 a	57.585±3.443 a	52.038±3.143 a	52.991±3.143 a	50.492±2.222	55.288±2.331	53.266±2.331	52.514±2.222	0.153	0.818	0.247
Cor.Th	171.848±6.320 a	144.576±6.923 b	186.975±6.320 a	188.550±6.320 a	179.412±4.469	166.563±4.687	158.212±4.687	187.763±4.469	0.062	**< 0.001**	**0.038**
Cor. BMD	1.213±0.067 a,b	1.095±0.073 a	1.196±0.067 a,b	1.341±0.067 a,b	1.204±0.047	1.218±0.05	1.154±0.05	1.268±0.047	0.844	0.112	0.071
Load to Max (N)	2.784±0.694 c	4.382±0.761 b,c	5.428±0.761 b	7.615±0.694 a	4.106±0.515	5.998±0.515	3.583±0.515	6.521±0.515	**0.018**	**0.001**	0.691
Slope to Max	14.017±2.491 c	17.204±2.729 b,c	22.605±2.729 b	34.314±2.491 a	18.311±1.848	25.759±1.848	15.61±1.848	28.46±1.848	**0.011**	**< 0.001**	0.120
Yield	4.021±1.166 b	5.090±1.278 b	7.479±1.278 b	11.182±1.166 a	5.75±0.865	8.136±0.865	4.555±0.865	9.331±0.865	0.067	**0.001**	0.296
Failure (N)	7.984±1.213 c	8.219±1.329 c	12.19±1.329 b	16.847±1.213 a	10.088±0.9	12.533±0.9	8.101±0.9	14.519±0.9	0.071	**< 0.001**	0.100
Fracture (N)	5.541±1.316 b	6.005±1.441 b	6.678±1.441 b	11.218±1.316 a	6.11±0.976	8.611±0.976	5.773±0.976	8.948±0.976	0.087	**0.034**	0.157
Work to Failure	4.059±0.666 a	3.547±0.730 a	5.078±0.730 a	5.470±0.666 a	4.569±0.494	4.508±0.494	3.803±0.494	5.274±0.494	0.932	**0.050**	0.526
Work to Fracture	6.634±1.160 b	6.974±1.271 a,b	8.654±1.271 a,b	10.201±1.160 a	7.644±0.861	8.588±0.861	6.804±0.861	9.428±0.861	0.448	**0.045**	0.626
Post-Failure Work	2.575±1.022 a	3.427±1.119 a	3.576±1.119 a	4.731±1.022 a	3.075±0.758	4.079±0.758	4.079±0.758	3.001±0.758	0.361	0.296	0.889

Table 4.5 µCT and 3-point-bending analysis of tibiae from 35 day old and 120 day male CD WT and *Phospho1*$^{-/-}$ mice

µCT analysis : bone volume fraction (BV/TV), trabecular thickness (Tr. Th.), trabecular separation (Tr. Sp.), trabecular number (Tr. No.), trabecular pattern formation (Tr. Pf.), structural model index (SMI), degree of anisotropy (DA), cortical porosity (Cor. Por. %), cortical thickness (Cor.Th.) and cortical bone mineral density (Cor. BMD). 3-point-bending analysis – Load to max, slope to max, yield, failure, fracture, work to failure, work to fracture. White columns contain least square means presented with their SEM from 35 day old wild type mice (WT35d), *Phospho1*$^{-/-}$ mice (KO35d) and 120 day old wild type mice (WT120d), *Phospho1*$^{-/-}$ mice (KO120d). Orange columns contain least square means with their SEM of WT data from all diets (WT.), *Phospho1*$^{-/-}$ data from all diets (KO.), 35 day old data from all genotypes (35d.) and 120 day old data from all genotypes (120d.). Green columns contain *P* values of the genotype effect only (Genotype) on bone parameters, age effect only (Age) and the combination of genotype and diet effect (Genotype x Age). Values assigned the same letter show no significant difference from one another ($P < 0.05$) white columns). Significances denoted in bold (green columns). n = 6, generalised linear model.

4.6 Discussion

Recent developments in endocrinology made possible by the combination of mouse genetics, integrative physiology and clinical observations have resulted in rapid and unanticipated advances in the field of skeletal biology. Indeed, the skeleton, classically viewed as a structural scaffold necessary for mobility and regulator of calcium–phosphorus homoeostasis and maintenance of the haematopoietic niche has now been identified as a more complex organ involved in the regulation of male fertility and whole-body glucose metabolism which is in addition to the classical insulin target tissues (Ducy *et al.*, 2000a; Lee *et al.*, 2007; Ferron *et al.*, 2008; Confavreux *et al.*, 2009; Ferron *et al.*, 2010a; Clemens and Karsenty, 2011; Karsenty, 2012). These seminal data have established the skeleton as a bona fide endocrine organ.

Data presented in Chapter 3 revealed that *Esp,* the gene encoding the protein OST-PTP, was up regulated 60 fold in *Phospho1*$^{-/-}$ osteoblasts. OST-PTP dephosphorylates the InsR, negatively regulating osteoblast-insulin-signalling and thereby controlling GLU13-OCN release (Mauro *et al.*, 1994; Hunter, 1995; Schlessinger, 2000; Dacquin *et al.*, 2004; Tonks, 2006; Lee *et al.*, 2007). Furthermore mice lacking *Esp* in osteoblasts have severe hypoglycemia and hyperinsulinemia (Lee *et al.*, 2007). Conversely, mice overexpressing *Esp* only in osteoblasts were glucose intolerant and insulin resistant (Lee *et al.*, 2007). Therefore the identification of increased *Esp* expression in *Phospho1*$^{-/-}$ mice has important implications for osteoblast differentiation and glucose homeostasis, possibly identifying a novel link between bone and energy metabolism.

Indeed, the results presented in this Chapter reveal that the ablation of *Phospho1* results in decreased blood glucose levels, improved insulin sensitivity and glucose tolerance in juvenile, adult and aged mice. Furthermore following HFD feeding, *Phospho1* ablation confers a remarkable degree of protection against insulin resistance in mice despite the 60-fold increase in *Esp* expression. These data support

the notion that the osteoblast is an important target used by insulin to control whole-body glucose homeostasis and suggest that *Esp* may act as a fine controller of insulin sensitivity, offering protection from severe hypoglycemia and dyslipidaemia.

Following the comprehensive phenotypic analysis of WT and *Phospho1*$^{-/-}$ mice it is apparent that changes in food intake are not responsible for the improved metabolic phenotype as no change in food intake was seen in all three age groups. However juvenile *Phospho1*$^{-/-}$ mice displayed increased activity which was not seen at adulthood or during ageing. This initial increase in activity may result in improved life-long insulin sensitivity; however this seems unlikely as no change in energy expenditure was observed. It is also possible that the ablation of *Phospho1* expression in the developing embryo can have long lasting effects, effectively "priming" the mice for an insulin sensitive phenotype throughout life. To discern if aged *Phospho1*$^{-/-}$ mice are protected from obesity and insulin resistance, a tamoxifen inducible *Phospho1* knockout model would be required (Chapter 7). It is also likely that bone architecture composition including fracture incidence does not influence the metabolic phenotype in this model. It has been reported that the genetic ablation of *Phospho1* produces significant skeletal deficits, which are transiently suppressed during skeletal maturity, therefore if bone architecture was the sole determinant of this phenotype it would have been expected to note a normalisation at 120 day old mice (Javaheri *et al.*, 2015).

An alternative explanation for the improved metabolic phenotype in *Phospho1*$^{-/-}$ mice may be due to the increased nuclei number and decreased lipid content of BAT from *Phospho1*$^{-/-}$ mice, possibly indicating increased mitochondria number. An increase in mitochondria number would lead to elevated canonical thermogenesis. BAT regulates metabolism and energy expenditure. Specifically, BAT dissipates large amounts of energy as heat, thus maintaining the energy balance of the whole body, but crucially only when the ambient temperature is below the thermoneutral range

for mice (30°C) (Richard and Picard, 2011). Since no differences were observed in the expression of BAT enriched genes e.g. *Ucp1* this suggests that canonical thermogenesis through *Ucp1* does not underlie the metabolic protection we see in *Phospho1*$^{-/-}$ mice. However, as these experiments were conducted in temperatures (23°C) which are below the rodent thermoneutral temperature (30°C), mice housed at this sub-thermoneutrality were potentially mildly cold-stressed, hyper-metabolic, hypertensive and obesity-resistant and therefore gene expression may have been altered. It would be therefore beneficial to study mice at thermoneutrality, which would be of more direct relevance to energy balance in humans (unfortunately this was not possible but discussed fully in Chapter 7) (Maloney *et al.*, 2014). However, if the observation that *Ucp1* expression is unchanged at thermoneutrality, these data would suggest the existence of a new non-canonical BAT protective pathway.

Finally in an effort to investigate the controversial effect of HFD on mice, WT and *Phospho1*$^{-/-}$ mice were fed a HFD from weaning until 120-days of age and subject to 3-point-bending and μCT analysis. Bone microarchitecture of trabecular bone was significantly influenced by HFD feeding, specifically the HFD resulted in bone loss in *Phospho1*$^{-/-}$ mice. These skeletal changes are in agreement with previous studies that demonstrate that bone loss occurs in C57BL/6J following HFD feeding (Cao *et al.*, 2010; Patsch *et al.*, 2011; Huesa *et al.*, 2014) but, are in contrast to a recent study that suggested that bone mass is not altered in C57BL/6J mice fed a HFD (Doucette *et al.*, 2015). The loss of bone in our model is consistent with the dogma that that HFD feeding increases adipocyte size and proliferation leading to the secretion of adipokines and cytokines such as TNFα, IL-6, Pref-1, resistin, leptin, that influence bone remodelling (Skurk *et al.*, 2007; Doucette *et al.*, 2015).

In conclusion, the results presented in this chapter highlight that the ablation of *Phospho1* in mice offers protection against diet induced hyperglycemia and insulin resistance. Importantly, the improved metabolic phenotype observed in *Phospho1*$^{-/-}$ mice is present in both juvenile and aged mice on a CD, highlighting that *Phospho1*$^{-/-}$

mice display lifelong protection from metabolic disease. Importantly, *Phospho1*$^{-/+}$ mice display an intermediate insulin sensitive phenotype suggesting PHOSPHO1 may represent a druggable target. Following the quantification of fat mass in *Phospho1*$^{-/+}$ mice (Chapter 5), Chapter 6 will aim to elucidate the mechanisms regulating PHOSPHO1 mediated energy metabolism.

Chapter 5

Evaluating fat deposition and localisation in WT and *Phospho1* knock-out mice

5.1 Introduction

Body weight coupled with dissection is the simplest and most common predictor of fat mass, however it has been previously reported that body weight (BW) alone is a poor predictor of fat percentage especially in leaner mice (Rogers and Webb, 1980). The dissection of single fat pads, exemplified by GF, has been shown to be highly correlated with total body fat percentage, but the experimental animals need to be sacrificed (Sharp *et al*., 1984). The gold standard methods for evaluating fat mass include freeze drying and chemical analyses. Briefly, freeze dried mass / wet weight allows for the prediction of fat percentage from dry matter content (FatP_FD) (Hastings and Hill, 1989; Bunger and Hill, 1997) and subsequent chemical analysis of the dried and ground animal allows for the prediction of protein content (from nitrogen)(Reynolds *et al.*, 2001). These methods are time consuming and destructive implying they can only be used *post mortem* (with the exception of BW) and therefore cannot be used in longitudinal studies.

In the last decade many sophisticated modalities have emerged to quantify adiposity in both rodent and larger animal models in a non-invasive way, including both standard and small animal dual-energy X-ray absorptiometry (DXA), PIXImus DXA, *in-vivo* CT and μCT and standard and μMRI. Whilst these modalities have a high resolution, are quantifiable and allow for longitudinal studies, they have a low throughput and are relatively expensive (Table 5.1). They also require initial calibration against accepted gold standard methods such as dissection, freeze drying and chemical analysis (Hastings and Hill, 1989; Bunger and Hill, 1997).

The genetic ablation of *Phospho1* dramatically improves glucose and insulin tolerance (Chapter 4), suggesting that lack of *Phospho1* may protect against diet induced obesity in mice. Therefore the overarching aim of this chapter was to quantify total fat mass and adipose localisation in WT and *Phospho1*$^{-/-}$mice. However, due to the small cohort of mice available it was first necessary to evaluate the robustness of simple dissection, freeze drying and multi-object *in vivo* CT in

mice. These data would not only extend Prof. Lutz Bunger's (SRUC) preliminary data indicating that multi-object *in vivo* CT in the ovine model was capable of providing precise and robust quantification of adipose tissue in C57BL/6 mice, the most widely used of all inbred strains (Clelland *et al.*, 2013), but also determine if the simplistic weighing of SB, GF, MF and iBF fat pads is indeed an accurate method to predict whole body adiposity. Following validation, it would be then possible to exploit these findings and precisely quantify fat in the WT and *Phospho1*$^{-/-}$ control and HFD cohort. As imaging is of great importance within The University of Edinburgh, I was awarded a small project grant from the Roslin Institute to expand upon these initial aims and establish if the use of μCT and μMRI in murine models was a good predictor of total fat mass and indeed if these modalities provided additional advantages to CT, dissection and freeze drying methods.

5.2 Hypothesis

Phospho1$^{-/-}$ mice are leaner than their WT counterparts in both subcutaneous and visceral fat deposits.

5.3 Aims

I. To assess the repeatability, reproducibility and accuracy of multi-object *in vivo* CT in mice.
II. To evaluate the robustness of simple dissection and freeze drying in mice.
III. To quantify total fat mass and adipose localisation in WT and *Phospho1*$^{-/-}$ mice using the selected method from aim I and II.
IV. To assess if μCT and μMRI provide additional advantages to CT, dissection and freeze drying methods.

	Dissection / Freeze Drying	PIXImus DXA	μMRI	CT	μCT
Brief Description	Individual fat pads removed from carcass and weighed. Whole carcass dried together with removed tissues.	Low energy X-rays to produce high-resolution (0.18 × 0.18 mm pixel) images.	Application of a strong magnetic field, combined with radio waves result in a detectable signal utilising the body's natural magnetic properties.	X-rays used to generate cross-sectional 2D models via rapid rotation of the X-ray tube 360° around the animal.	Synonymous to conventional CT, however produces very high resolution images allowing for "3d" microscopy.
Cost	Low	Medium	High	Medium	High
Image acquisition time (individual mice)	N/A	≈ 5 minutes	≈ 30 minutes	≈ 5 minutes (6 mice)	< 60 minutes
Manual / Automated analysis	Manual	Automated	Manual	Automated	Manual – Some automated functions.
Expertise /Software	Dissection skills, access to freeze dryer.	Software included	Require MRI Radiographer, free software available for analysis.	Radiographer, Software included.	Training required. Software included.
Outcomes	Isolated fat pads highly correlated to total fat mass. Dry matter gold standard predictor of fat %.	Estimated density and mass of lean, adipose, mineralised tissue.	Precise quantification of individual fat depots. Production of 2D/ 3D models. Further detailed analysis possible.	Estimated mass of lean, adipose and mineralised tissue. Production of 2D/ 3D models.	Precise quantification of individual fat depots. Production of 2D/ 3D models. Further detailed analysis possible.
Destructive	Yes	No	No	No	No (*in vivo* ◎CT)
References	(Sharp *et al.*, 1984; Hastings and Hill, 1989; Bunger and Hill, 1997)	(Johnston *et al.*, 2005; Stevenson and van Tets, 2008)	(Berger, 2002; Hamilton *et al.*, 2011; Bao *et al.*, 2013; Peng *et al.*, 2013)	(Rampersad and Bunger, 2005; Bunger *et al.*, 2011; Clelland *et al.*, 2013)	(Chapman *et al.*, 2011; Kanasaki and Koya, 2011; http://www.bruker.com/products/x-ray-diffraction-and-elemental-analysis/x-ray-micro-ct.html)

Table 5.1 - Comparison of Invasive and Non-invasive methods for measuring adiposity in rodents

5.4 Materials and Methods

5.4.1 CT

35, 120 180 and 200 day old (n = 5) C57BL/6 mice and 120 day old male WT and *Phospho1*$^{-/-}$ control and HFD (n = 6) mice were sacrificed by cervical dislocation immediately prior to CT-scanning. Cross-sectional CT images were taken along the length of the body and Sheep Tomogram Analysis Routines (STAR) software was used to calculate the total area and average densities of fat, muscle and bone in each carcass image without gutting as outlined in section 2.9.1.

5.4.2 Freeze Drying

Individual fat pads (SB, GF, MF & iBF) were extracted and weighed (Fig. 5.1B and C). Whole mouse carcasses and corresponding isolated adipose tissue were freeze dried to determine the dry matter weight (DM) of the carcass and the predication of individual fat percentage values was calculated by regression on dry matter content as outlined in section 2.9.2. The CT based measures of tissue weights were compared to the DM-based estimates for the fat content (fat %) and the fat free mass (FFM) in (%) using simple linear regression: $y_i = b_0 + b_1x_i$, with b_1= regression coefficient and b_0 = intercept.

5.4.3 μMRI

Following sacrifice, 120 day old WT and *Phospho1*$^{-/-}$ male mice (n = 4) on both the control and HFD were subject to MRI. T2 weighted images were acquired both in the axial and coronal planes. Acquired DICOM images were analysed blind using sliceOmatic.

5.4.4 Spectroscopy

Spectra were obtained from livers from 120 day old WT and *Phospho1*$^{-/-}$ male mice on both the control and HFD (n = 4). Two peaks were fitted using jMRUI with either a Lorentzian and Gaussian lineshapes.

5.4.5 *In vivo* μCT

Frozen 120 day old WT and *Phospho1*$^{-/-}$ mice (n = 3) were scanned using the Skyscan 1076 *in vivo* scanner. Scans were performed at a resolution of 35 μm with the X-ray source set to 40kV, 250 μA and using a 0.5mm Al filter, step size of 0.4° combined with frame averaging set to 3.

5.4.6 Histological staining of fat depots

Following sacrifice by cervical dislocation, fat pads were dissected from 35, 120 and 220 day old WT and *Phospho1*$^{-/-}$ male mice on both the control (n = 5) and HFD (120 day old mice) (n = 4) and fixed in 5% PFA for 24 hours and stored in 70% ethanol. The fat depots were processed into wax as described in section 2.8.1 and stained with haematoxylin and eosin (section 2.8.3).

5.4.7 Oil-Red-O staining of the liver *in vivo*

Adult (120 day old) WT and *Phospho1*$^{-/-}$ mice on both the control and HFD (n = 4) were sacrificed by cervical dislocation and livers were snap frozen in a cooled hexane bath. Oil-Red-O staining of 10μm-thick liver cryo-sections was performed as outlined in section 2.8.4. Nuclei were lightly stained with haematoxylin and sections were mounted in aqueous mountant prior to visualisation.

5.4.8 Statistical analysis

The data analysis has used linear regression and correlation analysis based on Excel (Microsoft Office 10) built-in functions with interval of confidence and testing of the correlation coefficients according to standard procedures described in the statistical literature (Rasch *et al.*, 1978a; 1978b). Data are presented as means ± SEM where appropriate. Regression and correlation coefficient's are given with the intervals of confidence ($P = 0.05$).

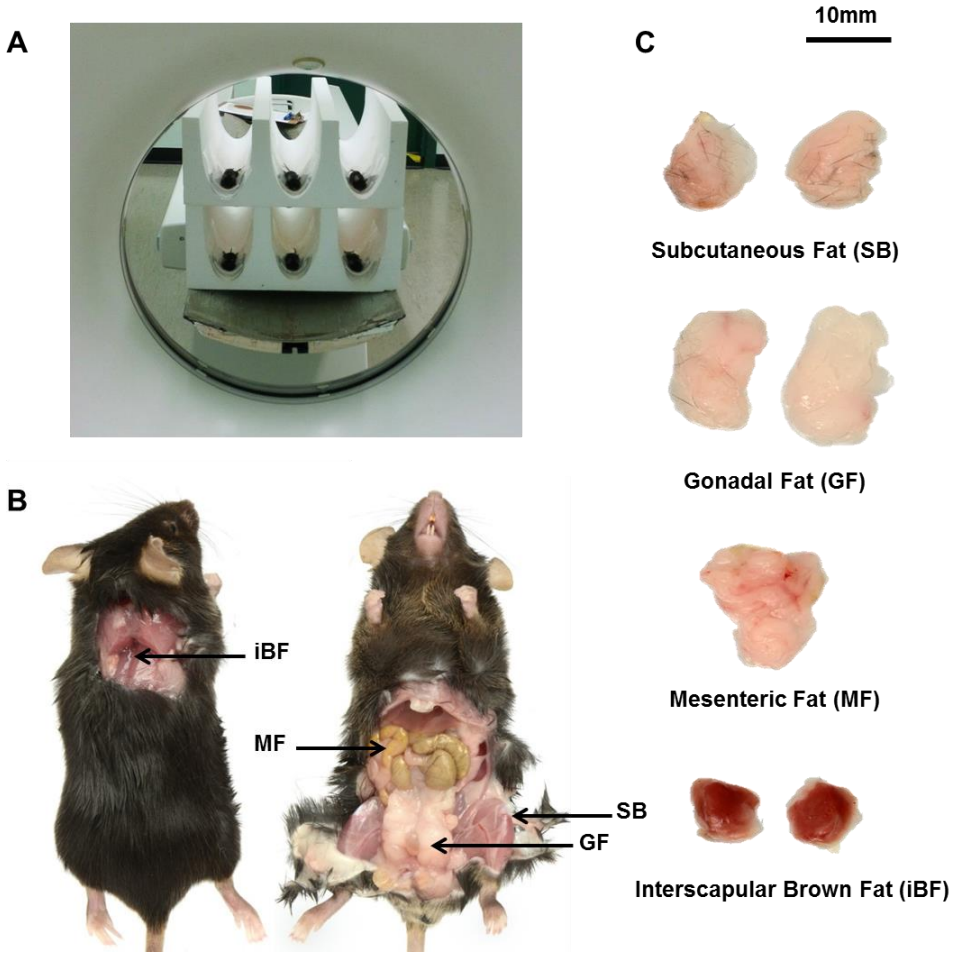

Figure 5.1 – Multi-object CT scanning
(A) Multi-object CT scanning. **(B)** Photograph depicting locations of fat depots. **(C)** Representative images of the dissected fat depots. From top to bottom: subcutaneous fat (SB), gonadal fat (GF), mesenteric fat (MF), interscapular brown fat (iBF). Scale bar = 10mm.

5.5 Results

5.5.1 Live weight, fat and non-fat traits measured by freeze drying, CT and dissection

The description of the dataset regarding these traits in terms of simple means and their standard errors is given in Table 5.2. The live tissue weight (LTW) of the mice was on average 31.5g, but splitting into the age groups shows a high variation between the age group means (20.9g to 41.1g). This produced the required variation in the fat traits, with fatness increasing with age. Taking the FatP_FD as an example, the fat content increases from about zero % (-1.1%) at 35 days to 18% at 200 days (with an average of 9%). Given the different methods to measure the size of the fat and non-fat compartment of the body it is not unexpected to find that the magnitude of the measured quantities of fat and non-fat differed between the methods used. The total estimated fat by FD across all ages amounts to 3.4g (9.0%). The value obtained from CT is 6.5g (23.6%) and thus much higher, probably indicating that the thresholds derived from sheep dissection trials need to be refined for mice. Another opportunity is to use the obtained CT values in suitable regression equations to predict accurately the fat values obtained by freeze drying; the gold standard. Similarly, it is not unexpected to find the lowest total fat amount from dissecting out the 4 above mentioned fat depots (SB, GF, MF and iBF). This method finds on average 1.5g of the total fat (sum of the 4 depots), which is less than half of the existing body fat. Again, the total body fat can be easily predicted from appropriate regression equations which either use the information from one or all dissected fat depots.

	35 days		120 days		180 days		200 days		All Ages	
Trait	**Mean**	**SEM**	**Mean**	**SEM**	**Mean**	**SEM**	**Mean**	**SEM**	**Mean**	**SEM**
LTW (g)	20.88	0.373	30.18	0.946	33.88	1.130	41.12	0.900	31.525	1.970
FatW_FD (g)	-0.244	0.172	2.251	0.478	3.9630	0.893	7.576	0.468	3.387	0.681
FatP_FD (%)	-1.141	0.818	7.400	1.426	11.416	2.264	18.401	0.946	9.019	1.994
NFatW_FD (g)	20.76	0.430	27.65	0.848	29.35	0.495	32.47	0.610	27.56	3.237
NFatW_FD (%)	100.78	0.412	92.34	1.391	88.05	2.115	80.62	0.778	90.45	5.636
FatW_CT (g)	2.640	0.120	4.87	0.618	7.07	1.181	11.34	0.698	6.48	0.709
FatP_CT (%)	16.06	1.030	19.86	2.030	51.77	1.560	32.48	1.850	23.58	1.660
NFatW_CT (g)	13.91	0.577	19.39	0.221	19.90	0.881	23.57	0.841	19.19	2.692
NFatW_CT (%)	83.94	1.032	80.14	2.033	74.08	3.708	67.52	1.853	76.42	2.033
TW_CT (g)	16.55	0.520	24.25	0.656	26.97	0.980	34.91	0.742	25.67	1.729
M_DS (g)	0.050	0.006	0.151	0.013	0.194	0.022	0.468	0.053	0.216	0.031
GF_DS (g)	0.143	0.006	0.508	0.057	0.784	0.176	1.680	0.120	0.779	0.116
SB_DS (g)	0.126	0.007	0.237	0.031	0.383	0.057	0.645	0.108	0.348	0.041
iBF_DS (g)	0.096	0.011	0.156	0.007	0.179	0.023	0.257	0.019	0.172	0.017
NFatW_DS(g)	20.47	0.367	29.13	0.889	32.34	0.876	38.07	0.767	30.00	4.749
NFatW_DS (%)	98.02	0.068	96.53	0.235	95.53	0.608	92.60	0.557	95.67	1.565
TW_DS (g)	0.414	0.016	1.052	0.092	1.540	0.258	3.050	0.270	1.514	0.201

Table 5.2 Simple means from freezer drying, CT and dissection

Simple means for live weight, fat and non-fat traits measured by freeze drying, CT and dissection with their standard errors of the mean (SEM); n = 5 per age group). Note: Animals of different ages have been chosen to enlarge the variability in the fat traits. Live tissue weight (LTW), Fat weight (FatW), Fat percentage (FatP), Non-fat weight (NFatW), Mesenteric fat (M), Gonadal fat (GF), Subcutaneous fat (SB), Interscapular brown fat (iBF), Freeze dried (_FD), Computed tomography (_CT) and Dissected (DS).

5.5.2 Live weight as a predictor for fat and non-fat

The simplest predictor of fatness is often LTW (Table 5.3). This assumes however that there is a wide variation in fatness. This was the case in the present cohort where mice aged between 35 and 200 days of age were studied. Both, FatW_FD and FatP_FD are highly correlated with LTW, r = 0.95 and 0.95, respectively, indicating that LTW alone allows good prediction of the fat weight and content in this sample of mice. LTW also correlates highly with the non-fat weight and content estimated by FD: r= 0.98 and 0.95. It is of note that these seemingly good prediction abilities of LTW will be diminished when looking at mice at one age or animals with a small age span only, although the low sample sizes per age group in this study did not allow me to prove this. As the FD measures of fatness are highly correlated with those obtained from CT it is not surprising to find that LTW is also a good predictor for the CT based traits, with the correlations slightly lower (r = 0.85 to 0.94; Table 5.3).

5.5.3 Benchmarking CT predictions against freeze drying

Water content is a robust indicator of fat proportion as described previously and can be easily measured by freeze drying (Sharp *et al.*, 1984). This method is cheaper and quicker than the equivalent chemical analysis. As the latter was not available in this study, freeze drying was the chosen benchmarking method. The initial use of both methods on the same sample allows the derivation of prediction equations, which can be utilised to allow the use of subsequent CT measures alone to predict fat and non-fat traits given the results of both methods correlate highly. Here, high positive correlations between CT measured fat (FatW_CT and FatP_CT) and the corresponding traits quantified by FD (r = 0.91 to 0.98) was shown. Moreover, high positive and just slightly lower correlations between the non-fat traits measured by FD and CT were observed. Interestingly, the correlations between the measures expressed as a percentage are always slightly lower than the correlations between absolute values.

	Correlation Coefficients	95 % Confidence Interval (lower bound)	95 % Confidence Interval (upper bound)	Regression Coefficients (b_1)	5% Lower Limit	5% Upper Limit	Intercept (b_0)
LTW (g) vs. FatW_FD (g)	0.950	0.876	0.980	0.387	0.325	0.450	-8.824
LTW (g) vs. FatP_FD (%)	0.947	0.869	0.979	0.967	0.806	1.127	-21.445
LTW (g) vs. NFatW_FD (g)	0.979	0.947	0.992	0.613	0.550	0.675	8.824
LTW (g) vs. NFatP_FD (%)	0.947	0.979	0.869	0.967	0.806	1.127	121.445
LTW (g) vs. FatW_CT (g)	0.936	0.842	0.975	0.443	0.361	0.525	-7.745
LTW (g) vs. FatP_CT (%)	0.850	0.654	0.939	0.886	0.616	1.156	-4.438
LTW (g) vs. NFatW_CT (g)	0.894	0.747	0.958	0.442	0.333	0.551	5.258
LTW (g) vs. NFatP_CT (%)	0.850	0.939	0.654	0.886	0.616	1.156	104.348
FatW_CT (g) vs. FatW_FD (g)	0.983	0.957	0.994	0.848	0.771	0.925	-2.105
FatP_CT (%) vs. FatP_FD (%)	0.905	0.770	0.962	0.886	0.681	1.091	-11.867
NFatW_CT (g) vs. NFatW_FD (g)	0.915	0.794	0.966	1.158	0.907	1.408	20.804
NFatP_CT (%) vs. NFatP_FD (%)	0.905	0.770	0.962	0.886	0.681	1.091	111.867
TW_ CT (g) vs. TW_FD (g)	0.987	0.966	0.995	1.100	1.012	1.189	-5.978
SB_DS (g) vs. FatW_FD (g)	0.918	0.800	0.967	12.117	9.54	14.694	-0.829
M_DS (g) vs. FatW_FD (g)	0.931	0.830	0.973	17.202	13.873	20.531	-0.322
GF_DS (g) vs. FatW_FD (g)	0.982	0.954	0.993	4.931	4.463	5.400	-0.454
iBF_DS (g) vs. FatW_FD (g)	0.891	0.741	0.957	41.115	30.839	51.391	-3.682
SB_DS (g) vs. FatW_CT (g)	0.938	0.846	0.975	14.358	11.74	16.976	1.483
M_DS (g) vs. FatW_CT (g)	0.932	0.832	0.973	19.98	16.151	23.808	2.171
GF_DS (g) vs. FatW_CT (g)	0.981	0.952	0.993	5.716	5.163	6.269	2.027
iBF_DS (g) vs. FatW_CT (g)	0.862	0.677	0.944	46.092	32.736	59.447	-1.445
TW_DS (g) vs. FatW_FD (g)	0.979	0.947	0.992	2.865	2.574	3.157	-0.952
TW_DS (g) vs. FatP_FD (%)	0.938	0.848	0.976	6.870	5.625	8.115	-1.383
TW_DS (g) vs. FatW_CT (g)	0.982	0.953	0.993	3.332	3.013	3.650	1.434
TW_DS (g) vs. FatP_CT (%)	0.908	0.777	0.963	6.787	5.244	8.329	13.303

Table 5.3 Correlation coefficients and confidence intervals for CT and dissected fat predictions

Dissected (DS), Fat percentage (FatP), Fat weight (FatW), Freeze dried (FD), live tissue weight (LTW), Total Weight (TW). n = 20, data analysed by using the generalised linear model.

5.5.4 Benchmarking isolated dissected fat pad mass against freeze drying and CT

The dissection of a single isolated fat pad from mice is a very common, invasive but highly simplistic and rapid exercise to evaluate total fat mass in mice. However the accuracy of this in C57BL/6 mice has not yet been reported. High positive correlations (r = 0.92, 0.93, 0.98 and 0.89, respectively) were found between all isolated fad pads and the FatW_FD(g) with the highest correlation between GF_DS and FatW_FD indicating that the GF pad seems the best single trait predictor for the total body fat in a mouse (r = 0.98; Table 5.3). Again, as the FD and CT measured fat traits are highly correlated it is expected that the mass of the individual fat depots also correlates highly with the CT based fat mass measures, with the highest value (r = 0.98) between the GF_DS and FatW_CT emphasising the good prediction opportunities if only one depot is being used, and highlighting the accuracy of multi-object CT.

The last 4 rows of Table 5.3 highlight that the prediction accuracy can be increased if the fat weight found in all 4 depots is summed up and all correlated to FD and CT measured fat mass. The correlations are both 0.98 and therefore comparable to the GF_DS vs. FatW ones.

These data highlight that there is a strong correlation between BW alone and fat mass / percentage. Moreover, simplistic dissection is sufficient to quantify whole body adiposity in mice and CT can accurately predict the degree of adiposity in the murine model. Thus these techniques were applied to the experimental WT and *Phospho1*$^{-/-}$ cohort.

5.5.5 WT and *Phospho1*$^{-/-}$ control and HFD dissection analysis

Phospho1 deficient mice had significantly decreased fat accumulation in SB, GF, MF depots than the WT mice on the CD. Upon HFD feeding WT mice became obese and had a significant increase in fat accumulation in all depots measured; however *Phospho1*$^{-/-}$ mice only accumulated fat in the SB and GF depots with no change in fat

accumulation noted in the MF depot between the control and HFD fed *Phospho1*$^{-/-}$ mice. No change in fat mass accrual was seen in the iBF deport between genotypes on the two diets (Fig. 5.2). There was no significant change in the size of adipocytes from GF of *Phospho1*$^{-/-}$ mice on the control and HFD with both groups having significantly more smaller adipocytes (< 20μm diameter) than the WT groups on both diets. Wild type HFD mice had significantly more larger adipocytes (> 60μm diameter) ($P < 0.05$) that WT CD mice suggestive that the HFD does not affect the size of *Phospho1*$^{-/-}$ adipocytes, however HFD increased the number of larger and decreased the number of smaller adipocytes in WT mice, consistent with obesity (Fig.5.2).

5.5.6 WT and *Phospho1*$^{-/-}$ control and HFD CT analysis

Multi-object CT values from the WT and *Phospho1*$^{-/-}$ were calculated from non-segmented mouse carcass (Fig. 5.3A) (preliminary data suggested that time consuming segmentation did not improve fat prediction accuracy). Computed tomography based fat predictions indicated that WT mice regardless of diet had increased total fat mass compared to *Phospho1*$^{-/-}$ mice and diet did not increase fat mass of the two genotypes. Interestingly, CD *Phospho1*$^{-/-}$ mice had increased muscle and bone mass compered to CD WT mice ($P < 0.05$) (Fig. 5.3B). Micro computed tomography confirmed the decrease of SB fat mass of CD *Phospho1*$^{-/-}$ mice to WT mice (Fig. 5.4).

5.5.7 μMRI adiposity and hepatic analysis

The mass of iBF predicted by μMRI did not significantly change between the genotypes however iBF did show a tendency to increase with HFD feeding similar to dissection analysis (Fig. 5.5B, Fig. 5.2C). The mass of SB and MF was not increased in *Phospho1*$^{-/-}$ mice between the two diets, whereas a HFD increased WT SB by 27.1% and MF by 64.5% ($P < 0.05$) indicating that *Phospho1*$^{-/-}$ mice are protected from diet induced obesity. Following conventional μMRI, MR spectroscopy was then conducted using time-domain analysis of *in vivo* MR data. Fitting both

Lorentzian and Gaussian lineshapes revealed that fat content was unchanged in the liver of *Phospho1*$^{-/-}$ mice between the two diets, consistent with μMRI fat depot analysis. Concomitant to this, fat content was significantly increased (84.8%) in WT HFD mice compared to *Phospho1*$^{-/-}$ HFD mice resulting in non-alcoholic fatty liver (NAFLD) disease which was visualised by both gross dissection and increased Oil-red-O staining in WT HFD livers (Fig. 5.6).

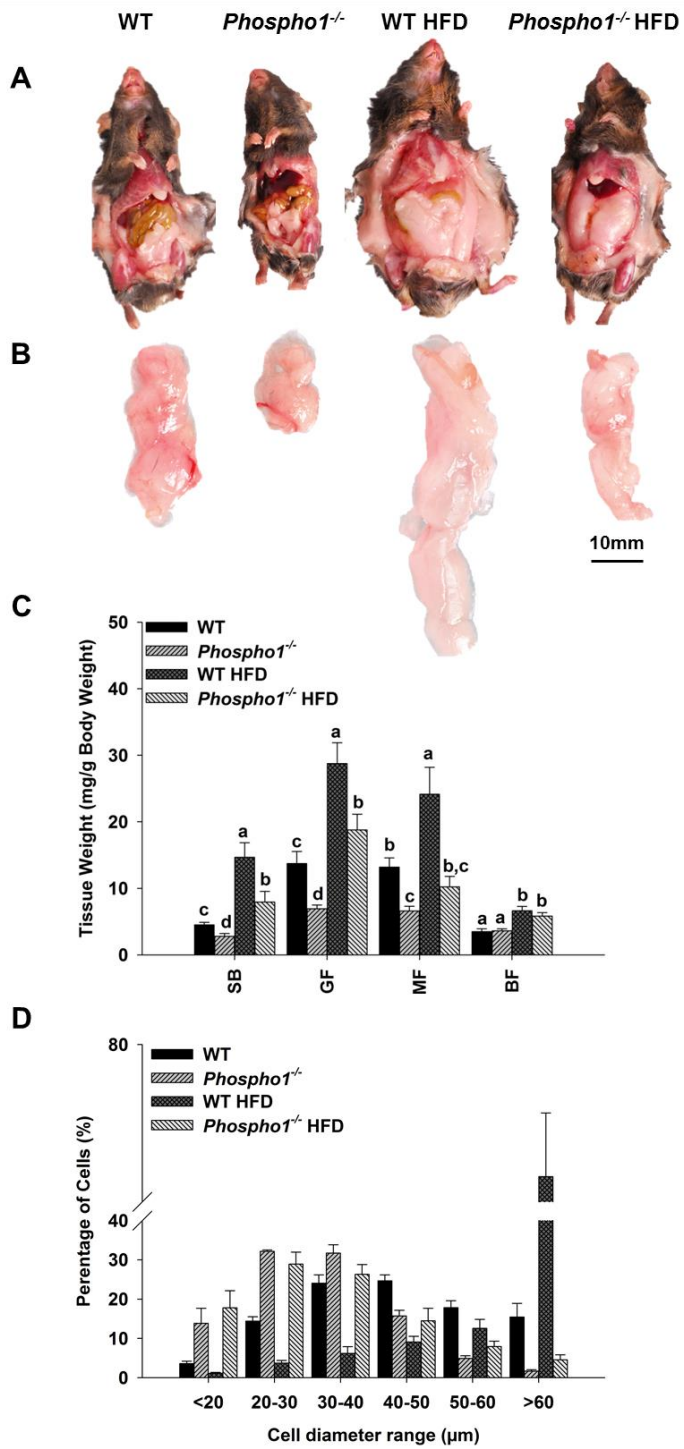

Figure 5.2 Dissection based fat quantification from WT and *Phospho1*$^{-/-}$ mice on both a control and HFD

(A) Photograph depicting fat accumulation in WT and *Phospho1*$^{-/-}$ mice on both a control and HFD. **(B)** Representative Images of the dissected GF fat depots. **(C)** Fat depots were dissected from WT and *Phospho1*$^{-/-}$ control and HFD mice. Results were normalised to BW (mg/g). **(D)** Percent of total GF adipocytes per 10µm diameter size class. n = 3 replicates, one way ANOVA. Data are represented as mean ±S.E.M. Values assigned the same letter show no significant difference from one another ($P < 0.05$).

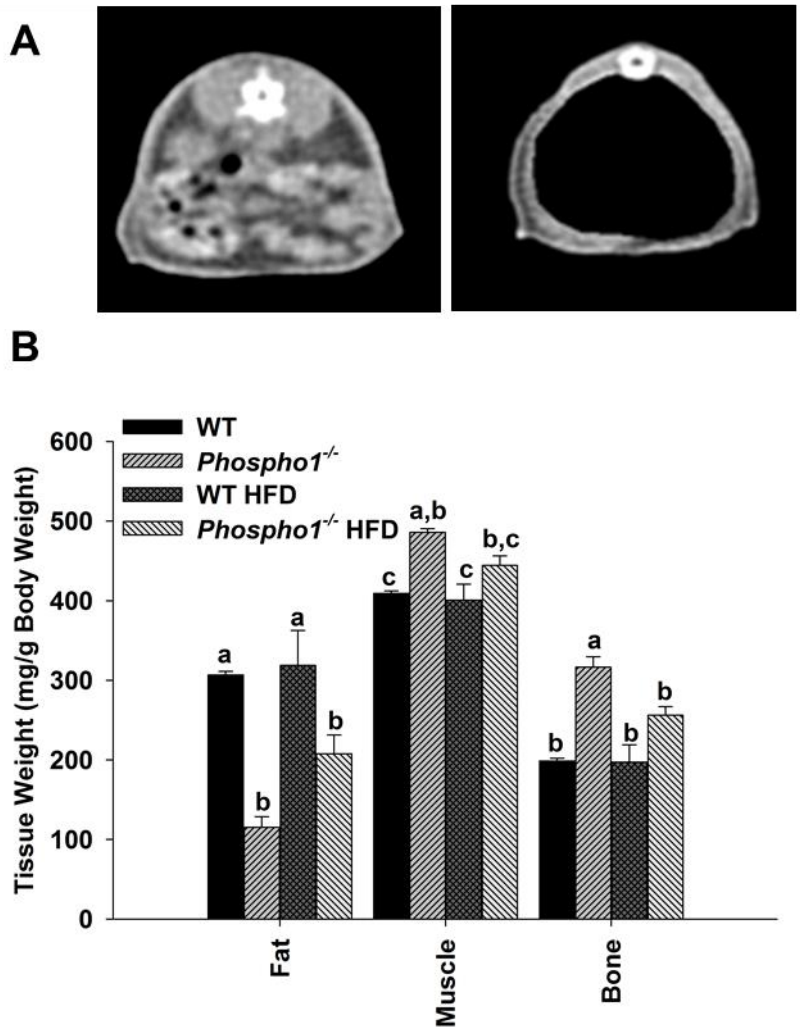

Figure 5.3 CT based fat quantification from WT and *Phospho1*$^{-/-}$ mice on both a control and HFD

(A) Multi-object CT scanning. Left non-segmented, right segmented mouse carcass. **(B)** Fat, muscle and bone mass determined by non-segmented multi-object CT scanning. Results were normalised to BW (mg/g). n = 6, one way ANOVA. Data are represented as mean ±S.E.M. Values assigned the same letter show no significant difference from one another ($P < 0.05$).

.

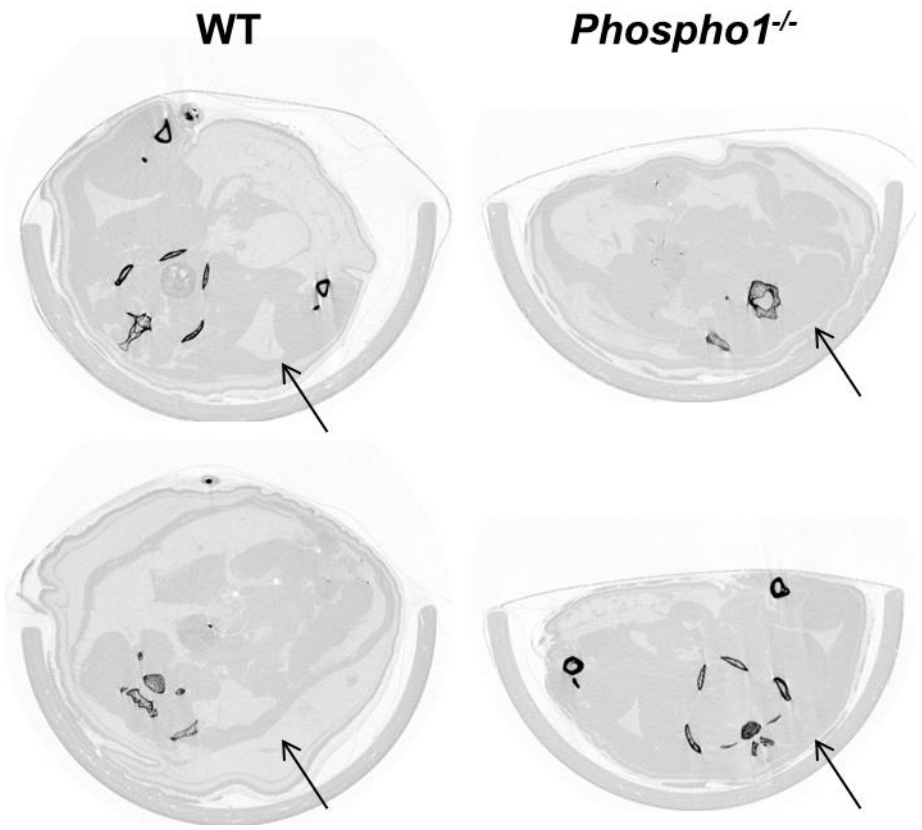

Figure 5.4 Cross section μCT scans of WT and *Phospho1*$^{-/-}$ mice
Representative μCT scans of two mice per genotype. Arrows depict subcutaneous fat accumulation.

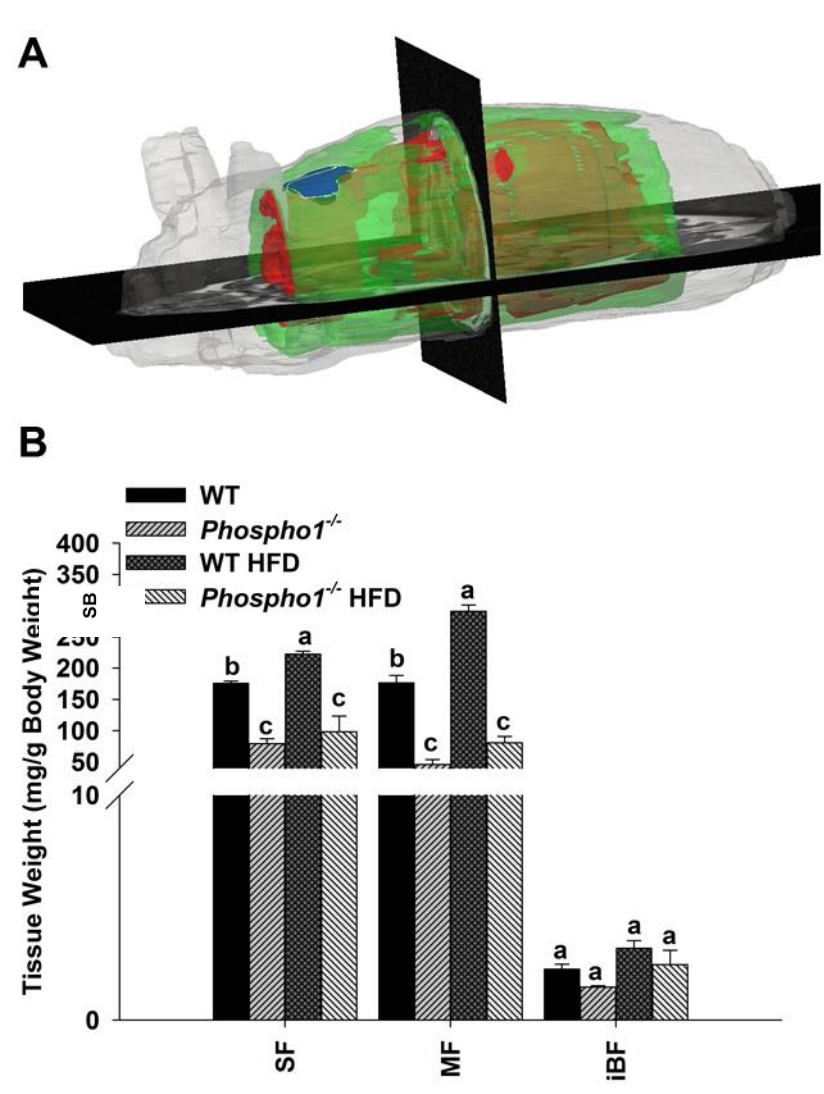

Figure 5.5 μMRI fat quantification from WT and *Phospho1*$^{-/-}$ mice on both a control and HFD

(A) Representative reconstructed μMRI scan. Green = SB fat, red = MF fat, blue = iBF. **(B)** SB, MF and iBF mass determined by μMRI. Results were normalised to BW (mg/g). n = 6, one way ANOVA. Data are represented as mean ±S.E.M. Values assigned the same letter show no significant difference from one another ($P < 0.05$).

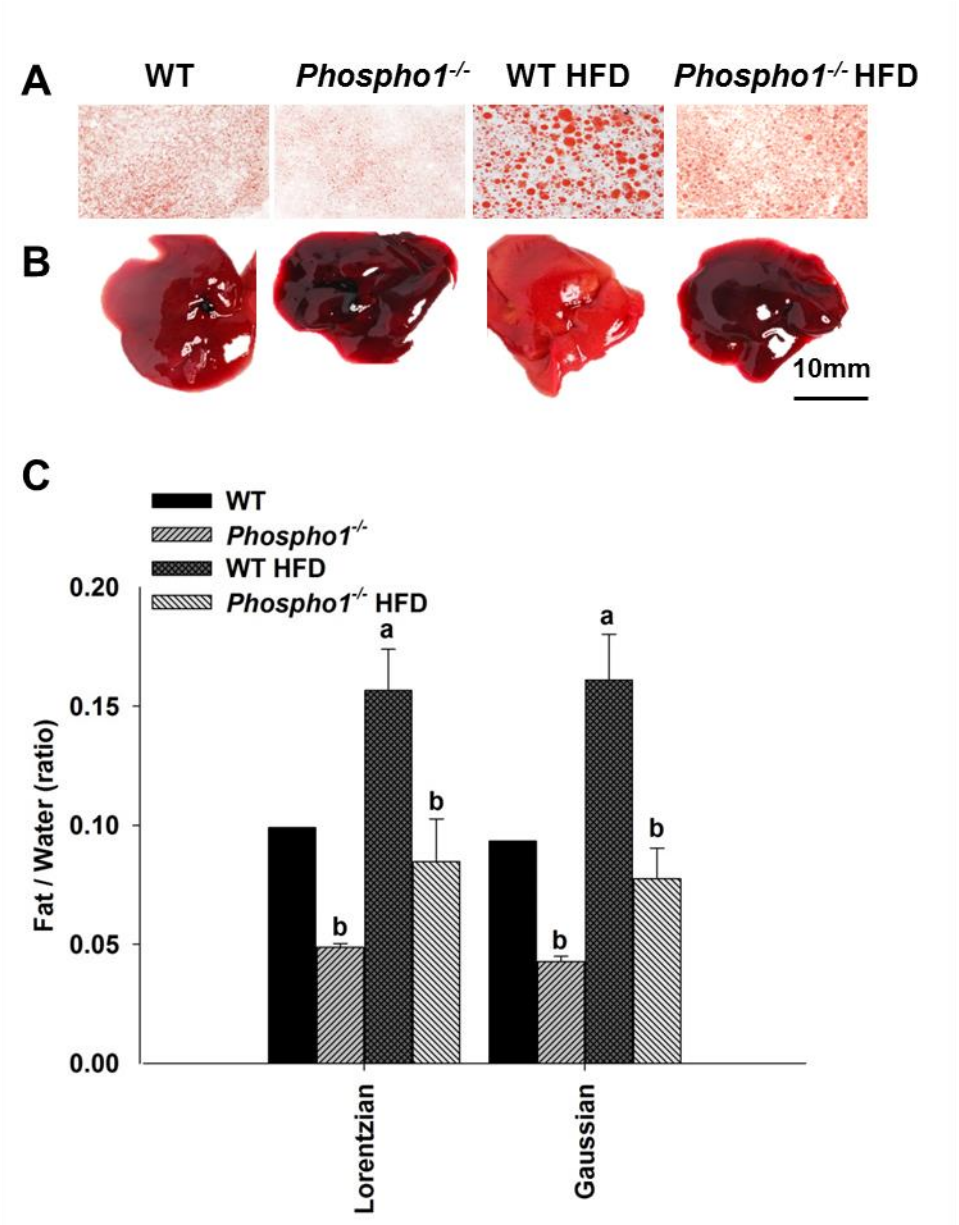

Figure 5.6 WT and *Phospho1*$^{-/-}$ mice liver analysis from both a control and HFD
(A) Typical photographs of liver histology (Oil-Red-O stained) from each group. **(B)** Representative photographs of dissected liver. **(C)** Quantitative assessment of liver fat utilising spectroscopy. Water and fat peak areas were defined with the assumption of either Gaussian or Lorentzian line shapes. n = 2 WT, n = 3 for remaining groups, one way ANOVA. Data are represented as mean ±S.E.M (n = 3 replicates). Values assigned the same letter show no significant difference from one another ($P < 0.05$).

5.6 Discussion

PHOSPHO1, the bone specific phosphatase has been previously been shown to be essential for the initiation of bone mineralisation (Houston *et al.*, 2004; MacRae *et al.*, 2010; Huesa *et al.*, 2011; Yadav *et al.*, 2011). Moreover, I have shown that in addition to the roles in bone mineralisation *Phospho1* ablation confers a remarkable insulin resistance and diabetes in mice (Chapter 4). Here, the fat deposition and localisation in WT and *Phospho1*$^{-/-}$ control and HFD mice was determined (Fig. 5.2-5.6). Prior to these studies it was first necessary to compare both invasive and non-invasive methods for measuring adiposity in young to old C57BL/6 male mice. These parameters were necessary as the WT and *Phospho1*$^{-/-}$ experimental mice were predominantly C57BL/6 male mice with a large variation of fat traits. Previous publications have evaluated the use of BW alone as predictor of fat mass or fat percentage, reporting a good correlation in obese mice, yet a poor correlation in very lean mice (Rogers and Webb, 1980). Contrary to this, a strong correlation between BW alone and fat mass and percentage in mice of 20g (35 days of age) to 40g (200days of age) measured by freeze drying and by multi-object CT was observed in the cohort of this present study. There was a tendency for the r values to be slightly lower for the relative measures (%) compared to the absolute values (g), and the correlation to FD measures seem slightly higher compared to the CT based measures. These high correlations are likely due to the large age span present in the cohort, selected to produce a large variation in fat traits. However, in mice with similar BW's, this may not be the case and the use of LTW as solely predictor of fat mass is not recommended.

Compared to the LTW as a fat predictor, the multi-object CT yielded slightly higher accuracies, e.g. the FatW_CT is a very good predictor for the total fat mass in the body (r = 0.98). The chosen approach in this study to CT scan freshly killed mice allows conclusions for CT scanning mice *in vivo*. This study shows the fat amount in live animals can be predicted very well with multi-object spiral CT. There was only limited research exploring the use of multi-object CT in fat mass prediction in mice.

This study now provides prediction equations based on one predictor (Table 5.3), indicating that CT can accurately predict the degree of adiposity in the murine model. Moreover, with the use of multiple regression analysis, a further small increase in accuracy could be expected.

This study highlighted that simplistic dissection is also sufficient to quantify whole body adiposity, and the measurement of one depot (GF pad) achieves the same predicted accuracy than the dissection of all 4 depots. These results are in agreement with previous work (Hull, 1960) and are based on the strong positive correlation between isolated fat depots and predicted fat mass. Therefore it was concluded that LTW, dissection and multi-object *in vivo* CT fat quantification are highly valuable techniques to evaluate fat mass. Multi-object *in vivo* CT offers the clear advantages of being a minimally invasive technique allowing longitudinal studies to be completed in a high throughput manner.

With these insights, simplistic dissection was first employed to quantify whole body adiposity. These data were suggestive that *Phospho1*$^{-/-}$ mice had smaller (mg/g BW) GF, SB and MF fat deposits compared to the WT counterparts. Indeed *Phospho1*$^{-/-}$ mice resisted MF accumulation when fed the chronic HFD. In concordance with these data, multi-object CT based fat predictions indicated that WT mice had increased total fat mass compared to *Phospho1*$^{-/-}$ mice however diet did not increase fat mass of the two genotypes. The lack of a detectable effect of HFD feeding on mice may be due to the fact that the thresholds derived from sheep dissection trials need to be refined for mice to more accurately detect small changes in fat mass or the mice used in this study may have developed adaptive mechanisms that participated in in the protection against diet induced obesity (Burcelin *et al.*, 2002). However, these data are consistent with the insulin sensitivity and hypoglycemia observed in *Phospho1*$^{-/-}$ mice (Chapter 3),but this phenotype was not expected due to the 60-fold increase in *Esp* mRNA expression in *Phospho1*$^{-/-}$ osteoblasts that has been

reported to be associated with InsR inactivation, thus insulin resistance and obesity (Lee *et al.*, 2007).

Coincidently, additional funding became available to evaluate μCT and μMRI imaging modalities in mice. Both μCT and μMRI were in concordance with dissection and CT fat predictions, indicating that *Phospho1*$^{-/-}$ mice were leaner than WT mice. However these modalities, specifically μMRI provided the ability to delineate between different fat depots, with the additional benefit of MR spectroscopy, not possible with conventional CT, freeze drying and dissection. μMRI revealed that *Phospho1*$^{-/-}$ mice resisted diet induced obesity and NAFLD.

The discrepancy between hypothesised fat mass and actual fat mass evaluated by dissection, CT, μCT and μMRI highlighted that PHOSPHO1 regulates global energy metabolism despite the 60-fold increase in *Esp*, strengthening the notion that a novel pathway may exist between osteoblasts and glucose homeostasis, and like other studies points towards further osteoblast-derived hormones that regulate glucose metabolism (Yoshikawa *et al.*, 2011). This study also revealed that both μCT (qualitative) and μMRI (quantitative) were good predictors of total fat mass in mice and indeed provided additional advantages to conventional CT, dissection and freeze drying methods, such as the ability to accurately dissect fat tissue *in silico* (allowing total fat quantification), the ability to delineate between different tissues thus providing high resolution, longitudinal tools to study fat distribution in mice, muscle shape and hepatic fat / water ratios.

In conclusion this study highlights that simple dissection and BW is an accurate predictor of whole body fat mass; however for longitudinal studies multi-object CT has the capability to accurately predict total fat mass and with appropriate bench marking muscle and bone mass (as shown in other species), thus replacing time consuming dissection in experimental design. Furthermore, this study has highlighted that μMRI and μCT provide high spatial resolution and contrast,

allowing not only quantification of adiposity in longitudinal studies, but also the ability to distinguish between normal and pathological tissues. Specifically μMRI is quantifiable, and provides the additional benefit of MR spectroscopy, however further work is required to benchmark both μMRI and μCT to DM based prediction or chemical analyses in allow for the dissection of the genetic basis of diet induced obesity and study of diet effects over age. Utilising these various imaging modalities I have shown that PHOSPHO1 ablation is protective against obesity and NAFLD likely via OCN independent mechanism that will be explored in Chapter 6.

Chapter 6

Elucidating the mechanism(s) by which PHOSPHO1 regulates energy metabolism

6.1 Introduction

Energy metabolism is a precisely regulated process, involving intricate paracrine, autocrine and endocrine signalling pathways that work in synergy to coordinate energy expenditure and storage in metabolically active tissues. In the last decade, bone has been identified as a true endocrine organ, possessing the capabilities to regulate energy metabolism, expanding our understanding and identifying a new and unconventional role of bone beyond its classical functions (section 1.6). Whilst this thesis has identified and characterised the role of PHOSPHO1 in this phenomenon, the underlying mechanisms have not yet been examined. Of particular interest was OCN, the most abundant osteoblast-specific non-collagenous protein accounting for 10-20% of the non-collagenous protein content of bone (Hauschka *et al.*, 1989b). Initially synthesised in the osteoblast as a pre–pro molecule, OCN is largely unstructured when calcium is not present. In the presence of calcium the OCN protein becomes folded regulating the maturation of bone mineral (detailed in section 1.5.2.8) (Hauschka *et al.*, 1989b; Chenu *et al.*, 1994). However, OCN also exists in partially carboxylated and completely uncarboxylated forms in the circulation which has recently been shown to regulate energy metabolism by stimulating insulin sensitivity, insulin secretion and energy expenditure (Plantalech *et al.*, 1991; Cairns and Price, 1994; Vergnaud *et al.*, 1997; Schilling *et al.*, 2005; Ferron *et al.*, 2008). Indeed, the bioactivity of OCN is tightly regulated by OST-PTP, the product of the *Esp* gene, mutations of which result in insulin sensitivity and protection from induced obesity and diabetes due to increased circulating GLU13-OCN (Lee *et al.*, 2007; Ferron *et al.*, 2008). More recently, FoxO1 has been implicated as a regulator of *Esp.* In the osteoblast nucleus FoxO1 co-localises with ATF4, promoting the transcriptional activity of ATF4 resulting in the up-regulation of *Esp* in osteoblasts, leading to OCN inactivation (Kode *et al.*, 2012). Indeed, a 60-fold increase in *Esp* mRNA expression was observed in *Phospho1*$^{-/-}$ osteoblasts and *in silico* gene network analysis was suggestive that *Atf4* and *Fox01* were differentially expressed between WT and *Phospho1*$^{-/-}$ osteoblasts indicative of PHOSPHO1, OST-PTP and OCN mutual regulation. However,

contrary to the established dogma, *Phospho1*$^{-/-}$ mice have lower blood glucose, improved glucose and insulin tolerance and resist obesity on a HFD despite the 60-fold increase in *Esp* expression which is indicative of a hyperglycemic, insulin resistant and obese phenotype (section 1.6.1) (Lee *et al.*, 2007). These observations point towards an OCN-independent influence of osteoblasts on energy metabolism with *Esp* possibly offering protection against excessive insulin signalling. It is therefore plausible to suggest that in addition to OCN, other bone-derived hormones may contribute to the function of the skeleton as a regulator of energy metabolism (Yoshikawa *et al.*, 2011). Mindful of this, SMPD3 catalyses the hydrolysis of sphingomyelin to from ceramide and phosphocholine (section 1.5.2.7) (Stoffel *et al.*, 2005). Phosphocholine is subsequently hydrolysed to choline and phosphate by PHOSPHO1. Elevated levels of both ceramide and choline result in insulin resistance in mice (Yang *et al.*, 2009; Wu *et al.*, 2013). Ceramide may have direct effects on genes (e.g. *Ucp3*) involved in energy metabolism and expenditure and induce the suppressor of cytokine signalling-3 which plays a central mechanistic role in the development of both leptin and insulin signalling pathways. It does this by attenuating phosphorylated signal transducer and activator of transcription (STAT) proteins binding to the InsR (Ueki *et al.*, 2004; Kanatani *et al.*, 2007), inhibiting IRS-1 phosphorylation and downstream insulin signalling (Lebrun and Van Obberghen, 2008) and targeting both IRS-1 and IRS-2 for proteosomal degradation (Lebrun and Van Obberghen, 2008). Furthermore, choline has been shown to induce hyperglycemia and insulin intolerance in mice via the modulation of plasma glucagon. Glucagon subsequently enhances hepatic gluconeogenesis, concomitant with increasing mitochondrial fatty acid uptake and oxidative stress that increases phosphorylation of IRS1-s-307, thereby inhibiting insulin-mediated signal transduction (Nakatani *et al.*, 2004; Wu *et al.*, 2013). Theoretically, the genetic ablation of *Phospho1* would result in decreased choline and preliminary mass spectroscopy analysis indicated that plasma ceramide was reduced in *Phospho1*$^{-/-}$ mice. Choline and / or ceramide deficiency may therefore provide an alternative hypothesis for the improved metabolic profile of *Phospho1*$^{-/-}$ mice *in viv*o.

Therefore the overarching aim of this chapter was to elucidate the mechanisms regulating PHOSPHO1 mediated energy metabolism. This will provide new insights into the molecular mechanisms surrounding the dynamic interplay between bone and glucose regulation.

6.2 Hypothesis

Phospho1 ablation regulates whole body glucose metabolism through an OCN in-dependent mechanism.

6.3 Aims

I. Quantify serum OCN levels in WT and *Phospho1*$^{-/-}$ mice.

II. Analyse the effects of *Phospho1*$^{-/-}$ and WT osteoblast conditioned medium on hepatic, pancreatic, myoblast, osteoblastic and adipogenic cell lines.

III. Examine whether ceramide species are decreased in *Phospho1*$^{-/-}$ serum

IV. Determine if choline supplementation normalises glucose metabolism in *Phospho1*$^{-/-}$ mice.

V. Identify the candidates underlying the protection from obesity and insulin resistance in *Phospho1* deficiency.

6.4 Materials and Methods

6.4.1 Primary osteoblasts

Under sterile conditions calvariae were dissected from 3-4 day old new-born WT and *Phospho1*$^{-/-}$ mice as described in section (2.2.2). Extracted cells were resuspended in osteoblast medium (Appendix I) and pooled to obtain a single cell suspension. The cells were expanded in flasks in a humidified atmosphere of 95% air/5% CO_2

and maintained at 37°C until 80–90% confluence before being plated at 10,000 cells/cm^2 in multi-well plates.

6.4.2 Cell lines (FAZA, Ins1e, C2C12, 3T3-L1)

Under sterile conditions cells lines (FAZA - rat liver cell line, Ins1e - rat insulinoma cell line, C2C12 - mouse myoblast cell line and 3T3-L1 maintained at -160°C were thawed quickly at 37°C and 5ml of pre-warmed appropriate maintenance media (Appendix I) was added slowly and centrifuged. The cell pellet was resuspended in maintenance media and transferred to a T175 tissue culture flask (T75 for C2C12 cells) and expanded in flasks in a humidified atmosphere of 95% air/5% CO_2 and maintained at 37°C. When the cells were 80–90% confluent they were plated at 10,000 cells/cm^2 in multi-well plates until differentiated.

6.4.3 Conditioned medium with insulin treatment

Following differentiation, C2C12, FAZA, Ins1e, 3T3-L1 and primary WT osteoblast cells were cultured for 24 hours in αMEM containing 0.5% FBS. Medium was changed to serum free αMEM containing 0.1% BSA (Fraction V) and HEPES 10mM pH 7.4. 1 hour prior to insulin stimulation, cells were incubated with 1ml WT or *Phospho1*$^{-/-}$ osteoblast conditioned medium. Cells were finally stimulated with 10nM insulin or vehicle control (PBS) for 15 minutes and washed in ice-cold PBS prior to protein and mRNA extraction (section 2.6, 1.7).

6.4.4 mRNA analysis of primary osteoblasts cells and cell lines

RNA samples were extracted from primary calvarial osteoblasts, using a Qiagen RNeasy lipid kit according to the manufacturer's instructions. cDNA was prepared and was used at 5ng/µl for RT-qPCR analysis, as detailed in section 2.6 Results were normalised to the appropriate housekeeping gene and the relative gene expression level was calculated using the ΔΔCt method (Livak & Schmittgen 2001).

6.4.5 Protein analysis of primary osteoblasts cells and cell lines

Protein was extracted from primary calvarial osteoblasts and cell lines in RIPA buffer as detailed in section 2.7.1. Protein concentration was quantified (section 2.7.2) and appropriate quantities were used for western blot analysis (section 2.7.3). pAKT, AKT, GLUT 4, pGSK3 and GSK3 expression was determined using a goat anti-rabbit (goat anti-mouse GLUT4) antibody at a dilution of 1:1000 and the appropriately HRP-labelled donkey anti-rabbit/mouse secondary antibody (1:5000) (Appendix II). Antibody labelling was visualised using the ECL detection kit. Equality of protein loading was confirmed by also probing the membrane with mouse monoclonal HRP-labelled anti-β actin antibody (1:50000).

6.4.6 ELISA analysis of serum OCN, adiponectin and leptin

Serum from 8 week and 120 day old male WT and *Phospho1*$^{-/-}$ CD mice was collected via cardiac puncture and transferred to an EDTA coated tube and stored at -80°C until use. An ELISA-based method to quantify osteocalcin carboxylation was used (section 2.10.5) (Ferron *et al.*, 2010b). Commercially available ELISA kits were used to measure leptin, adiponectin and insulin in serum from 120 day old male WT and *Phospho1*$^{-/-}$ CD and HFD (section 2.10.6).

6.4.7 Analysis of serum triglyceride

A triglyceride colorimetric assay kit was used to measure triglyceride levels present in blood serum from 120 day old male WT and *Phospho1*$^{-/-}$ CD and HFD mice. This assay was based on the enzymatic hydrolysis of the triglycerides by lipase to produce glycerol and free fatty acids. The glycerol released was measured by a coupled enzymatic reaction system with a colorimetric readout at 540 nm (detailed in section 2.10.4).

6.4.8 Ceramide mass spectrometry

Serum was collected as described in section 2.5.3 from 120 WT and *Phospho1*$^{-/-}$ mice. 50µl of serum was used to extract lipids according to the method of Folch *et al.*

(Folch *et al.*, 1957). Glycolipid analysis and quantification was performed by Professor Phillip Whitfield (University if Highland and Islands) via electrospray ionization-tandem mass spectrometry (ESI-MS/MS) (detailed in section 2.11.2). Data were analysed using software driven algorithm (thermo Xcalibur Quad Browser) imputing known ceramide species (Appendix VI).

6.4.9 *In vitro* 2-deoxyglucose [3H]

WT and *Phospho1*$^{-/-}$ primary osteoblasts were extracted and expanded as described in section 2.2.2 and 2.2.4. Cells were then incubated in serum free medium for 4 hours and washed in PBS. Either basal (2ml PBS), 100nM insulin (in 2ml PBS), 1000nM insulin (in 2 ml PBS) or 10μM Cytochalasin B (in 2 ml PBS) was added for 15 minutes at 37^{o}C. Following insulin treatment 0.1 mM (9250 Bq/ml (0.25μCi/ml)) 2-DG (^{3}H-labelled) was then added to each well for 15min at 37°C. Glucose uptake was terminated by washing the cells 3 times with ice cold 0.9% saline with the plates on ice. Cells were scraped in PBS+0.1% SDS and homogenised. Radioactivity was measured and normalised to protein content (section 2.3.3).

6.4.10 BRL-37344

Male juvenile, adult and aged mice (35, 120 and 220 day-old) were weighed and fasted for 4 hours between 9am and 1pm. 1mg/kg BW of BRL-37344 was administered IP for 3 hours. Mice were later euthanised and tissues were collected for protein and gene analysis (2.6 and 2.7).

6.4.11 Mitochondria stress test

Osteoblasts were plated at a density of 25,000 and 50,000 cell's per well (24 well plate) and transferred to a 37°C CO_2 incubator until 100% confluency was reached. Cells were washed in 500μl XF assay media supplemented with 25 mM glucose and 10 mM pyruvate and placed in a non-CO_2 incubator at 37°C for 1 hour prior to start of assay. Oligomycin (1.2μM), FCCP (0.56μM), antimycin A / rotenone (0.96μM)

were prepared and following equilibration the Seahorse plate was placed in the Seahorse XF24 Analyser for analysis (section 2.3.4).

6.4.12 2% choline diet

Male mice were fed a 2% supplemented choline diet (Harlan Laboratories) or CD (Harlan Laboratories) for 5 weeks prior to cull at 120 days. Metabolic tests were conducted as detailed in section 2.5.3.3.

6.4.13 Proteomics

Proteins from serum were extracted and prepared (section 2.5.3) and the extracted proteins were analysed using a RSLC 3000 nanoscale capillary LC followed by qTOF mass spectrometry (QSTAR, ABSciex). This was done by Dr. Cal Vary (Center for Molecular Medicine, Maine Medical Center Research Institute (MMCRI), ME, USA)). ProteinPilot™ was used for protein identification and quantitation, as well as visualising peptide-protein associations and relationships. Functional pathway and causal network analysis was performed using QIAGEN's Ingenuity (IPA), GeneMANIA and EXPANDER (EXpression Analyzer and DisplayER) following training from Dr. Jacqueline Smith.

6.4.14 Lipidomics

Total lipids were extracted from serum and osteoblast conditioned medium and silica based solid phase extraction was employed for sample clean up and fractionation prior to analysis. Resulting mass spectra was analysed by LC-MS in both positive and negative ion scanning modes. This was done by myself with assistance from Dr. Cal Vary, MMCRI. LipidView™ was used for the molecular characterisation and quantification of lipid species and principle component multivariate data analysis established preliminary lipid classes and their contribution to sample differences.

6.5 Results

6.5.1 Quantification of serum adipokines

To uncover the mechanism leading to the increase in insulin sensitivity in *Phospho1*$^{-/-}$ mice, various serum adipokines were first studied. Adiponectin, an adipokine that plays an important role in the modulation of glucose and lipid metabolism in insulin-sensitive tissues (Chandran *et al.*, 2003) was decreased 2.62 and 1.92 fold respectively in *Phospho1*$^{-/-}$ mice on both the CD and HFD (Fig. 6.1A), suggestive that insulin sensitivity and protection from obesity is independent of elevated adiponectin. Serum leptin levels were unaffected between WT and *Phospho1*$^{-/-}$ mice on a CD, however in the diet challenged study leptin was decreased by 1.31-fold in HFD *Phospho1*$^{-/-}$ mice compared to HFD WT controls (Fig. 6.1B). Circulating triglycerides were increased 1.30-fold in CD *Phospho1*$^{-/-}$ mice compared to CD WT mice (Fig. 6.1C).

6.5.2 Expression of genes metabolic target genes

The expression of target genes involved in metabolism was next evaluated. Surprisingly, selected metabolic target genes were largely unaltered in SB adipose, quadriceps femoris and liver tissue of *Phospho1* deficient mice. Specifically, lipoprotein lipase (*lpl*) which is involved in the regulation of fatty acid turnover was up regulated 2.16-fold in *Phospho1*$^{-/-}$ adipose tissue compared to controls (Fig. 6.2A). *Irisin,* an exercise-induced myokine suggested to induce browning of white adipocytes (Huh *et al.*, 2014), was up regulated 1.62-fold in *Phospho1*$^{-/-}$ quadriceps femoris compared to controls (Fig. 6.2B) and AMP-activated protein kinase (*Prkaa1*), phosphoenolpyruvate carboxykinase 1 (*Pck1*) and peroxisome proliferator-activated receptor alpha (*Ppara*) were up regulated 1.25, 1.57 and 1.62 respectively in *Phospho1*$^{-/-}$ hepatic tissue compared to controls (Fig. 6.2C). Furthermore, both adipose and quadriceps femoris tissue had a significant increase in *Slc2a1* in the *Phospho1*$^{-/-}$ mice (Fig. 6.2D-E) however no such change was observed in hepatic tissue (Fig. 6.2F). These subtle changes were seen on both the CD and HFD fed mice (data not shown). Results of this phenotypic analysis established that

Phospho1 function is required for the development of obesity and glucose intolerance in mice.

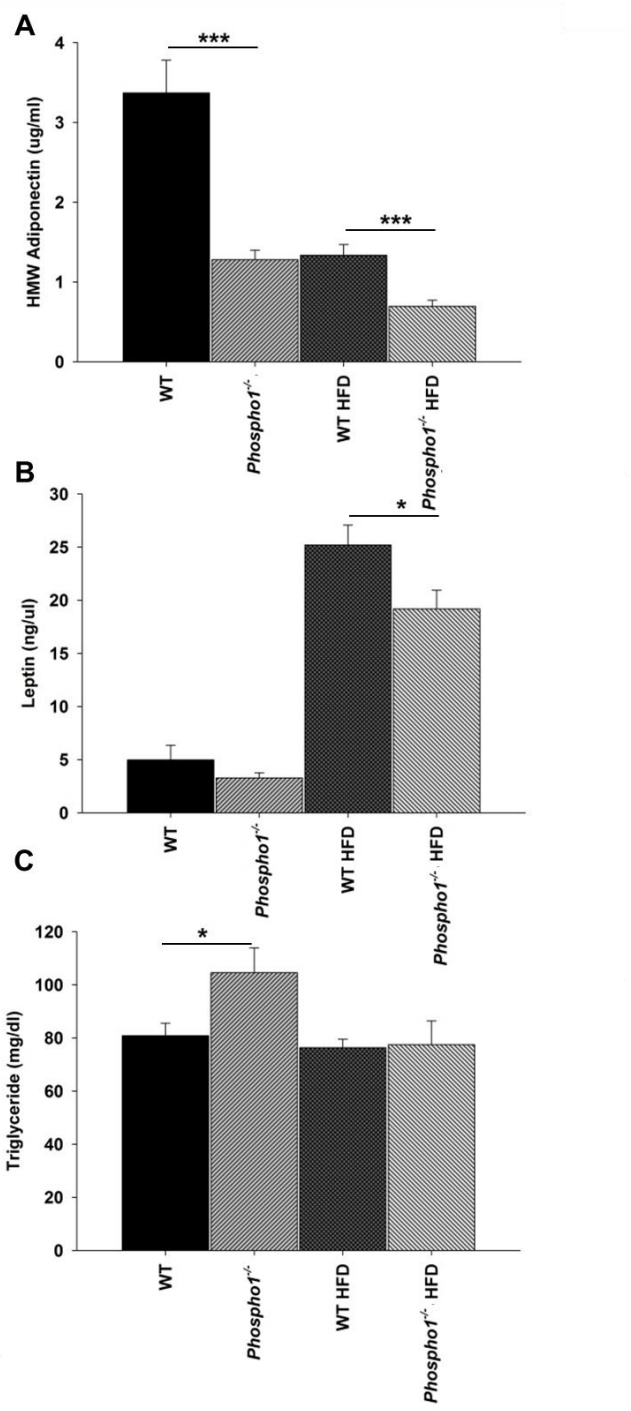

Figure 6.1 *Phospho1*$^{-/-}$ mice are insulin sensitive despite decreased adiponectin
Serum levels of adipokines and triglycerides were measured in serum from 120 day old CD and HFD male mice by ELISA **(A)** adiponectin and **(B)** leptin **(C)** triglyceride. n ≥ 8, two way repeated measures ANOVA. Data are represented as mean ±S.E.M. * *P < 0.5*, ** *P < 0.01*, ****P < 0.001*.

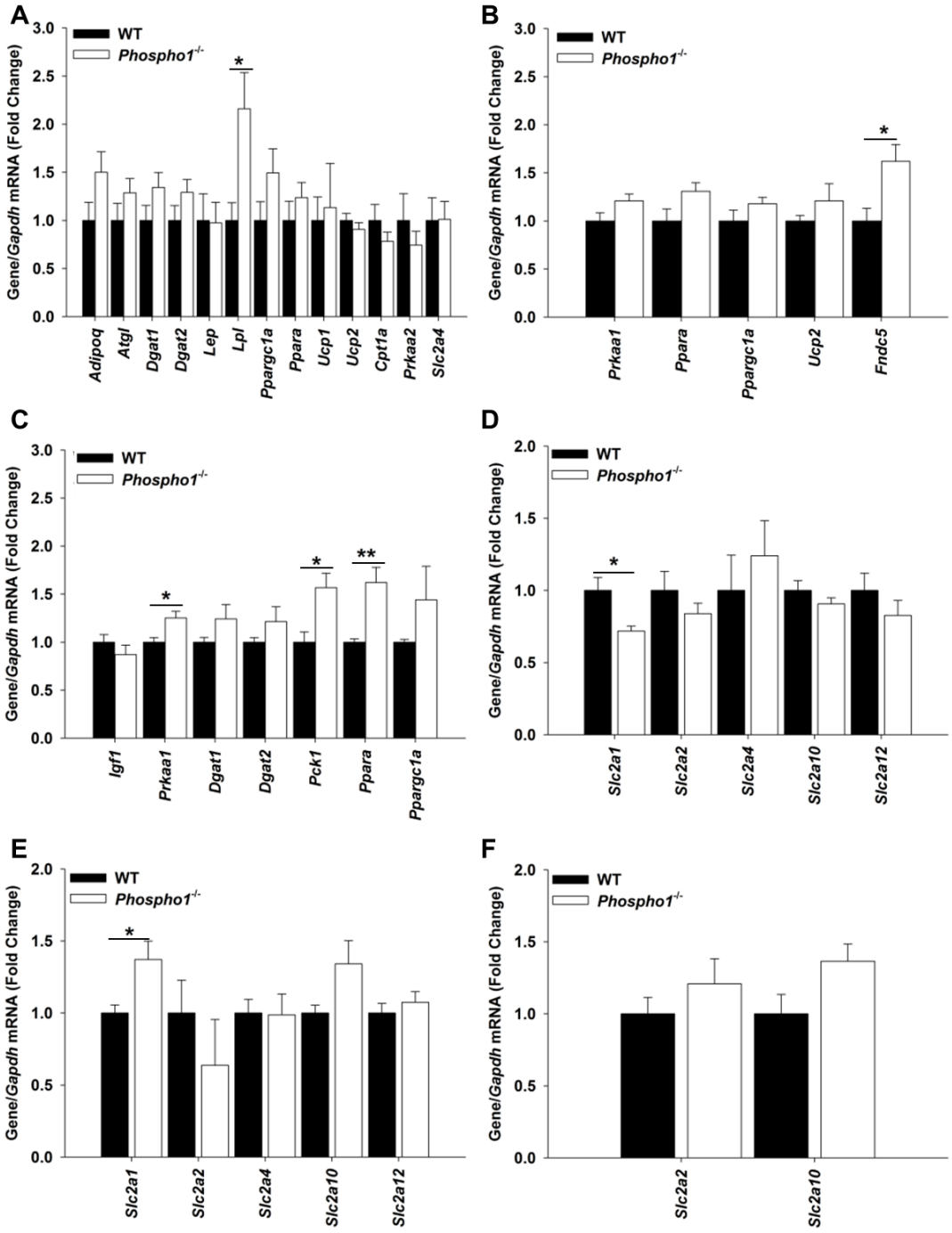

Figure 6.2 Selected metabolic target genes were largely unaltered in subcutaneous adipose quadriceps femoris and liver tissue of *Phospho1*$^{-/-}$ mice

RT-qPCR analysis of tissue extracted from 120 day old WT and *Phospho1*$^{-/-}$ mice **(A)** adipose tissue **(B)** quadriceps femoris and **(C)** liver. RT-qPCR analysis of GLUT receptors from **(D)** Adipose tissue **(E)** quadriceps femoris and **(F)** liver. mRNA values generated were normalised to *Gapdh* housekeeping gene. n = 3, t-test and Mann–Whitney rank sum test. Data are represented as mean ±S.E.M. * $P < 0.5$, ** $P < 0.01$, ***$P < 0.001$.

6.5.3 Examination of *in vitro* and *in vivo* glucose metabolism in WT and *Phospho1*$^{-/-}$ mice

Glucose metabolism and insulin responses were initially assessed *in vitro*. In brief, primary osteoblasts extracted from WT and *Phospho1*$^{-/-}$ mice were stimulated with [^{3}H]2-deoxyglucose and the incorporation of radioactive tritium (as a surrogate of glucose uptake) was measured. Surprisingly *Phospho1*$^{-/-}$ osteoblasts incorporated less glucose than WT osteoblasts, suggestive that they are less metabolically active (Fig. 6.3).

Furthermore, *Phospho1*$^{-/-}$ mice subjected to a sub-maximal *in vivo* administration of insulin (1mU/g) displayed a significant increase in the key markers of insulin sensitivity in bone (Akt phosphorylation) ($P < 0.05$) and decreases in phosphorylated-p44/42, total p44/42 and GLUT4 ($P < 0.05$). These changes were absent in WT bone and no such changes were noted in liver, muscle and fat (data not shown) suggestive of a *Phospho1*$^{-/-}$ bone driven regulation of whole body metabolism (Fig. 6.4A-B).

The differences in metabolism observed between WT and *Phospho1*$^{-/-}$ mice prompted me to compare the metabolic profile of WT and *Phospho1*$^{-/-}$ calvarial osteoblasts. The XF-24 extracellular flux analyser was used to measure oxygen consumption rate (OCR) and then a Mito Stress test was performed by using inhibitors of the mitochondrial electron transport chain in a sequence (Guntur *et al.*, 2014). Oligomycin was first injected to inhibit oxygen consumption; FCCP was injected which uncouples the electron transport chain thus increasing OCR and finally respiration was completely inhibited using a combination of complex I and complex III inhibitors, rotenone and antimycin A. It was observed that *Phospho1*$^{-/-}$ calvarial osteoblasts had higher OCRs than WT osteoblasts. Suggestive that *Phospho1*$^{-/-}$ calvarial osteoblasts may be cells less glycolytic than WT osteoblasts, however this may be due to the inability of *Phospho1*$^{-/-}$ calvarial osteoblasts to mineralise *in vitro* (6.4C).

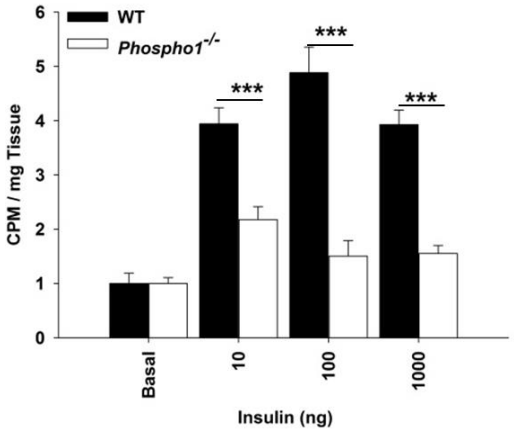

Figure 6.3 *Phospho1*$^{-/-}$ osteoblasts show decreased 2-deoxyglucose [3H] uptake upon insulin stimulation

2-deoxyglucose [3H] incorporation into insulin stimulated primary osteoblasts extracted from WT *and Phospho1*$^{-/-}$ mice. . n = 3, t-test. Data are represented as mean ±S.E.M. * $P < 0.5$, ** $P < 0.01$, ***$P < 0.001$.

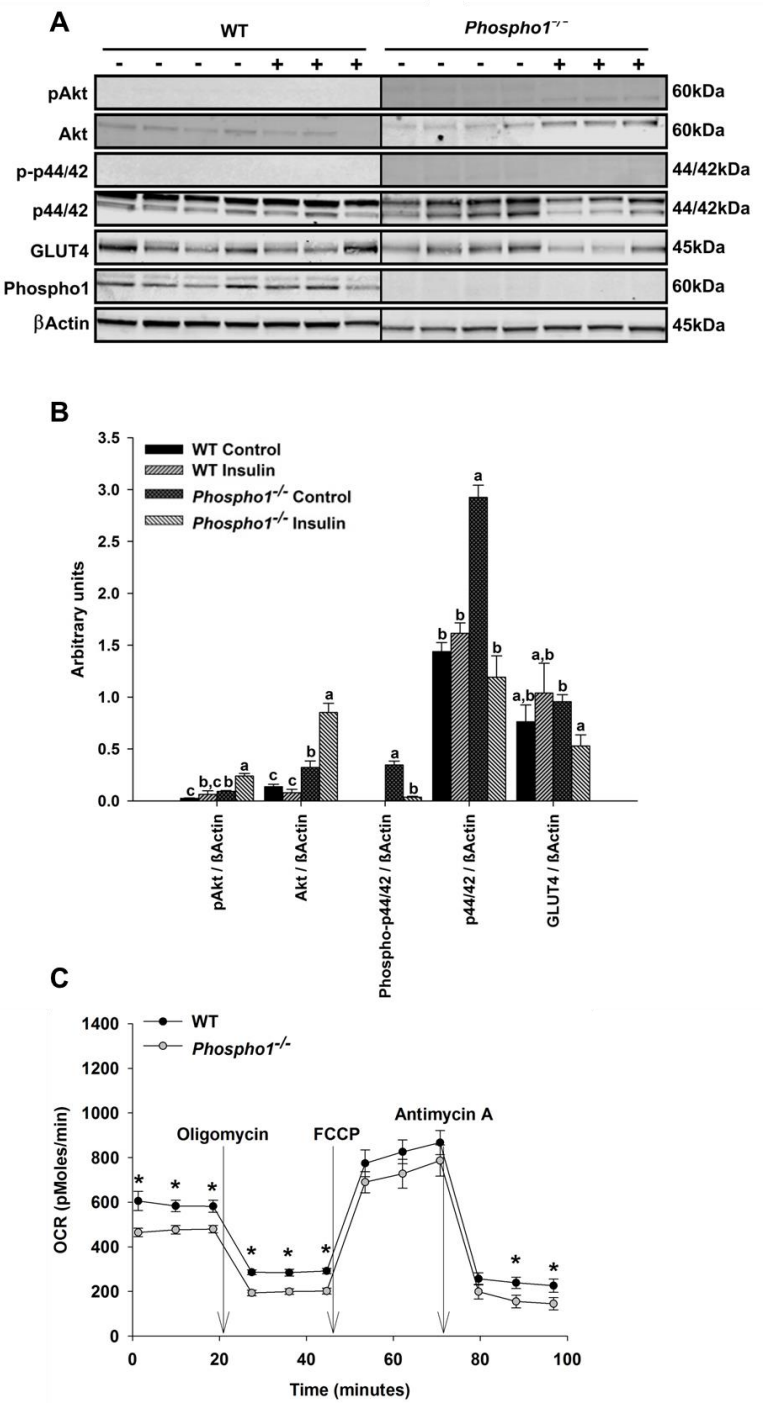

Figure 6.4 *Phospho1*$^{-/-}$ mice show increased insulin sensitivity in bone

(A) Immunoblot of WT and *Phospho1*$^{-/-}$ mice subjected to *in vivo* insulin administration 20 minutes prior to cull. **(B)** Densitometric analysis of proteins shows a significant increase in pAKT and decrease in p-p44/42 and GLUT4 was observed in insulin stimulated *Phospho1*$^{-/-}$ bone. **(C)** Seahorse X-24 analysis of OCR (an indication of oxidative phosphorylation) in WT and *Phospho1*$^{-/-}$ primary calvarial osteoblasts under basal conditions or following the addition of oligomycin, the uncoupler FCCP or the electron transport inhibitor antimycin A. *Phospho1*$^{-/-}$ primary calvarial osteoblasts had decreased OCR. . n ≥ 3, one way ANOVA (B) and t-test (C). Data are represented as mean ±S.E.M. Values assigned the same letter show no significant difference from one another ($P < 0.05$). * $P < 0.05$.

6.5.4 The effect of β3-adrenergic receptor agonist on WT and *Phospho1*$^{-/-}$ mice

The increased mitochondrial mass of *Phospho1*$^{-/-}$ BAT noted in Chapter 4 implied that the ablation of *Phospho1* may improve the metabolic phenotype by impacting non-shivering thermogenesis mechanisms. Therefore to test if the improved metabolic phenotype of *Phospho1*$^{-/-}$ mice was a consequence of enhanced sensitivity of BAT thermogenesis, 35 day old WT and *Phospho1*$^{-/-}$ mice were challenged 3 hours prior to cull with BRL-37344, a preferential β3-adrenergic receptor agonist that activates SNS signalling (Doucette and Rosen, 2014). This approach is an alternative to acute cold exposure and was used to test the immediate effects of environmental stress. Few metabolically significant changes were observed between WT and *Phospho1*$^{-/-}$ mice challenged with BRL (Fig. 6.5). However of importance, transcript levels of β3-adrenergic receptor (*Adrb3*) were increased in *Phospho1*$^{-/-}$ BAT following BRL administration. No such change was seen in WT mice (Fig. 6.5A). This suggested that there was an increase in intracellular lipolysis of triglycerides from lipid droplets, resulting in release of fatty acids into the cytoplasm. Furthermore, in *Phospho1*$^{-/-}$ mice, *Pparγ* transcript levels were increased in BAT but decreased in GF following BRL administration. No change in transcript *Pparγ* was seen in BAT or GF from WT mice. This suggests that PPARγ is involved in the physiological recruitment process in BAT but not WAT (Fig. 6.5A&B). Interestingly the expression of thermogenic associated genes in GF were differentially expressed between WT and *Phospho1*$^{-/-}$ mice in response to BRL treatment, these changes were seen at a lesser extent in SB fat. These results reveal that mimicking acute cold exposure using β3-adrenergic receptor may indicate that GF contributes to the insulin sensitive phenotype in the *Phospho1*$^{-/-}$ mice.

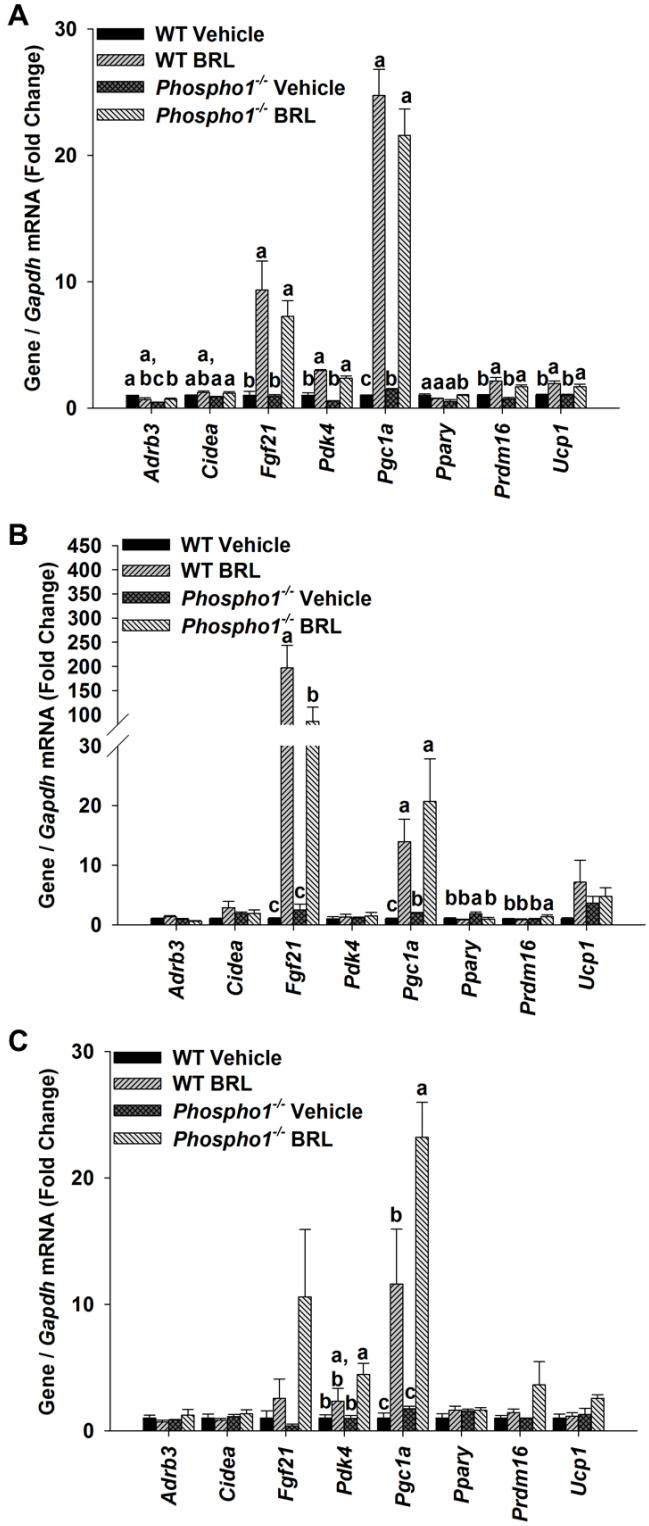

Figure 6.5 Effect of β3-adrenergic receptor agonist on WT and *Phospho1*$^{-/-}$ mice
RT-qPCR analysis of tissue extracted from 35 day old WT and *Phospho1*$^{-/-}$ mice challenged with β3-adrenergic receptor agonist **(A)** iBF **(B)** GF and **(C)** SB adipose tissue. mRNA values generated were normalised to the *Gapdh* housekeeping gene. n = 6, one way ANOVA. Values assigned the same letter show no significant difference from one another ($P < 0.05$).

6.5.5 *Phospho1*$^{-/-}$ osteoblasts secrete a factor which regulates insulin signalling, independent of OCN

The low blood glucose levels and enhanced insulin sensitivity observed in the *Phospho1*$^{-/-}$ transgenic mice is opposite to the expected similarity to the OST-PTP overexpression-like phenotype. This was therefore suggestive that there may be an increase in circulating GLU13-OCN rather than a decrease as inferred by the 60-fold up-regulation of *Esp* in *Phospho1*$^{-/-}$ osteoblasts. Indeed, I saw an increase in total OCN (GLA13-OCN) which was expected as *Phospho1*$^{-/-}$ mice display increased bone turnover (Huesa *et al.*, 2011). However, no change in GLU13-OCN in both juvenile and adult *Phospho1*$^{-/-}$ mice was observed indicating that lowered GLU13-OCN may not underlie the improved metabolic phenotype observed in *Phospho1*$^{-/-}$ mice (Fig. 6.6A-B).

Therefore, to establish if PHOSPHO1 truly regulates glucose metabolism via its osteoblastic expression, conditioned medium from WT and *Phospho1*$^{-/-}$ primary calvarial osteoblasts was collected and tested on various cell lines. This approach indicated that *Phospho1*$^{-/-}$ osteoblasts secreted factors that increased basal insulin sensitivity in primary calvarial osteoblasts (Fig. 6.7A-B), decreased insulin stimulated sensitivity in INS1e cells (Fig. 6.7C-D) and increased insulin stimulated sensitivity in 3T3-L1 cells (Fig. 6.7E-F) compared to WT conditioned medium. No effect was seen in FAZA and C2C12 cells (data not shown). These results provide evidence that in addition to GLU13-OCN other osteoblast-derived factors contribute to the global regulation of energy metabolism.

6.5.6 Investigation of ceramide and choline as regulators of insulin signalling

Having established that GLU13-OCN is not responsible for the metabolic phenotype of the *Phospho1*$^{-/-}$ mice, it is likely that other osteoblast secreted molecules contribute to global energy regulation. Neutral sphingomyelinase catalyses the hydrolysis of sphingomyelin to form ceramide and P-Cho (Stoffel *et al.*, 2005). Phosphocholine is subsequently hydrolysed into choline and P_i by PHOSPHO1 (Fig. 6.8A). Elevated

levels of both ceramide and choline result in insulin resistance in mice (Yang *et al.*, 2009; Wu *et al.*, 2013). This led to the hypothesis that *Phospho1*$^{-/-}$ mice may have reduced ceramide or choline levels resulting in increased insulin sensitivity. Analysis indicated however that there was no significant difference between various ceramide species in the two genotypes highlighting that ceramide was unlikely to underlie the insulin sensitive phenotype observed in the *Phospho1*$^{-/-}$ mice (Fig. 6.8B). Unfortunately we were unable to measure serum choline due to the lack of a mass spectrometry assay, therefore we next supplemented WT and *Phospho1*$^{-/-}$ mice with a 2% choline diet. Choline supplementation normalised the insulin sensitivity measured in *Phospho1*$^{-/-}$, measured by GTT however (Fig. 6.9A), unlike WT mice which when fed a 2% choline diet took longer to recover from the insulin challenge, *Phospho1*$^{-/-}$ showed no metabolic change in response to insulin between the diets (Fig. 6.9B). Furthermore, choline supplementation had no effect on mass, but normalised the lean phenotype observed in *Phospho1*$^{-/-}$ mice to the level seen in basal WT mice ($P < 0.05$)(Fig. 6.9C-D). This result suggested that PHOSPHO1-deficiency improves the metabolic profile of mice *in vivo* and confers resistance to obesity and diabetes possibly via the alteration of bone choline levels.

6.5.7 Identification of novel regulators of insulin signalling

The regulation of bone is a complex, multifactorial process; therefore it is possible that bone derived choline may not be the only skeletal regulator in mice and further, undefined bone secreted factors may play an important role in global energy regulation. To identify secreted proteins or lipids that may also be involved in the energy regulation via the skeleton, quantitative proteomics and lipidomics were conducted in serum from WT and *Phospho1*$^{-/-}$ CD and HFD mice. Proteomic analysis identified > 100 differentially expressed proteins in *Phospho1*$^{-/-}$ serum. These unique proteins were highly associated with glycolysis, gluconeogenesis and 'metabolic pathways' (Fig. 6.10A-B) and showed enrichment for miR-34a; a microRNAs (miRNAs) that affects diverse parts of insulin signalling in the pancreas, liver, muscle and adipose tissue (Rottiers and Naar, 2012). Furthermore, lumican, a

proteoglycan secreted by differentiating and mature osteoblasts, a constituent of the bone matrix and is observed in the decidua of the diabetic patients was found to be enriched in serum of *Phospho1*$^{-/-}$ mice by both proteomic and microarray analysis (section 6.5.7) (Raouf *et al.*, 2002; Favaro *et al.*, 2013). The key finding of preliminary lipid analysis was that cholesteryl esters (CE), were not detected in WT HFD serum (Fig. 6.11). Cholesteryl esters are molecular species that are important in the intracellular storage and intravascular transport of cholesterol and integral to membrane function (Ginsburg *et al.*, 1984; Bowden *et al.*, 2011). Conditions that effect cholesterol metabolism e.g. tumour promotion, alter tissue CE levels. Furthermore, over-nutrition which is characteristic of the HFD mouse model results in elevated tissue CE levels in the form of CE-enriched lipid droplets in tissues (Mahlberg *et al.*, 1990). As tissue levels of CE were not measured it can only by hypothesised that the lack of CE in serum may be due to the accumulation of CE in WT HFD tissue, which *Phospho1*$^{-/-}$ mice are protected from. However this must be investigated further.

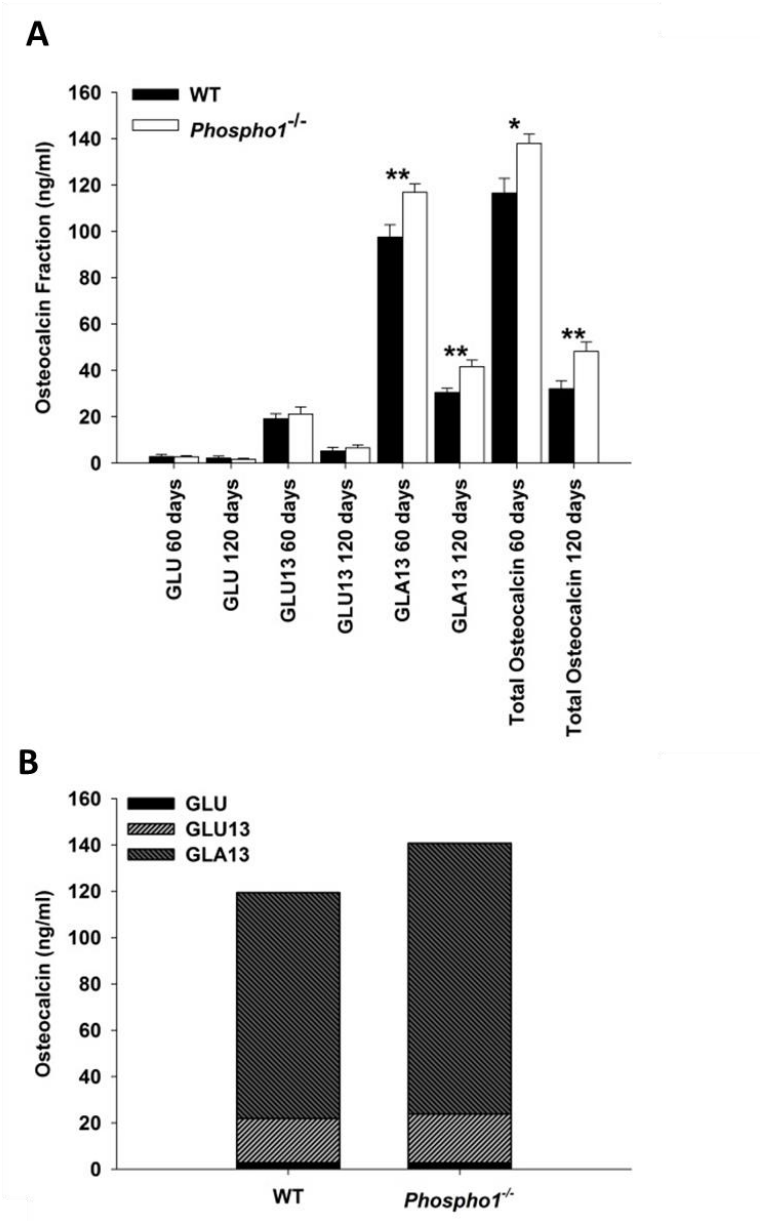

Figure 6.6 No difference in GLU13-OCN serum levels between WT and *Phospho1*$^{-/-}$ mice

(A)(B) Osteocalcin analysis in WT and *Phospho1*$^{-/-}$ mice serum from 60 and 120 days of age. . n ≥ 6, t-test. Data are represented as mean ±S.E.M. * $P < 0.05$, ** $P < 0.01$, ***$P < 0.01$.

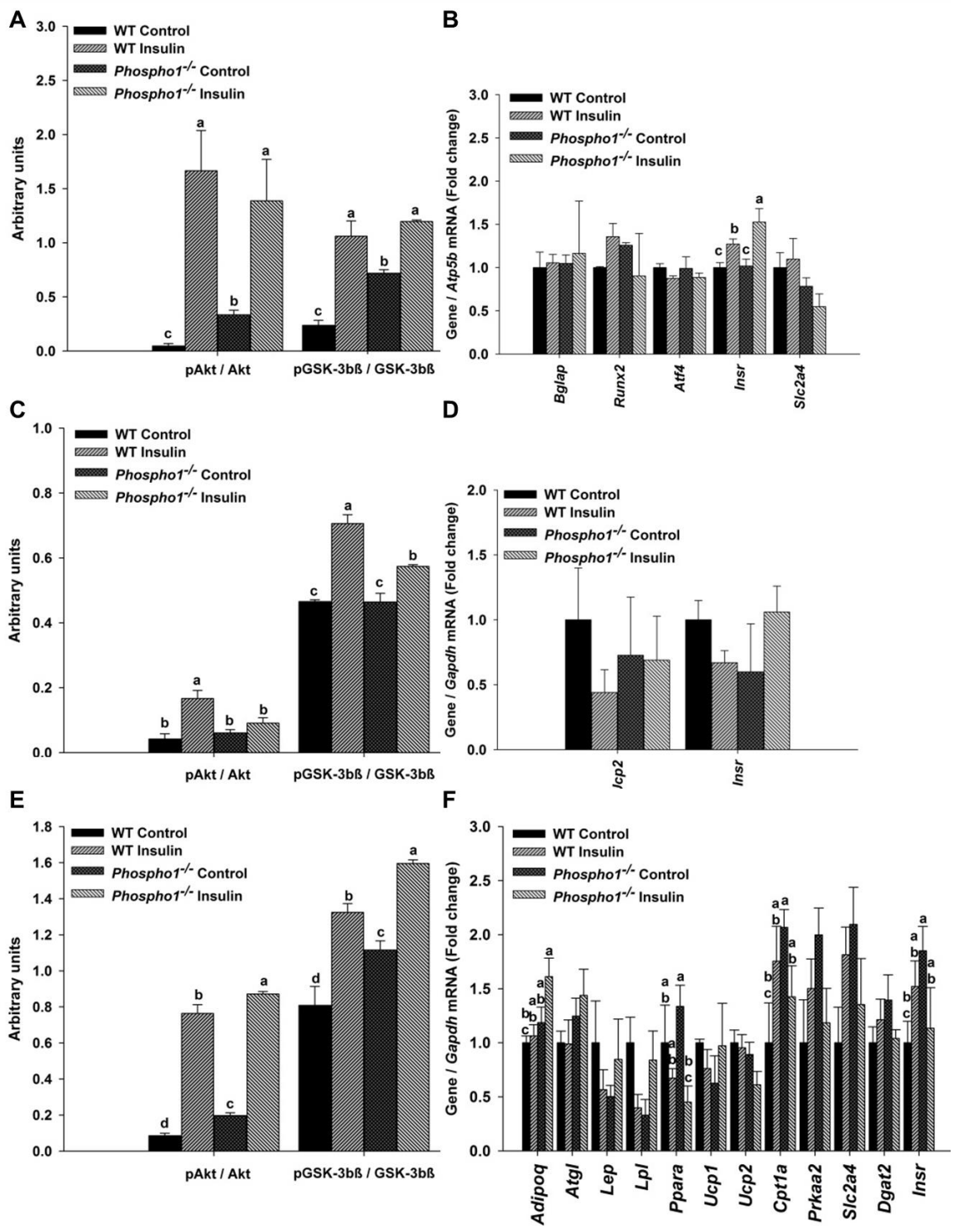

Figure 6.7 *Phospho1*$^{-/-}$ osteoblast secreted factors increased basal insulin sensitivity in primary calvarial osteoblasts

Effect of a 1 hour pre-treatment with osteoblast conditioned medium prior to 10nm insulin stimulation (15 minutes) on primary cells and cell lines. WT Primary osteoblast **(A)** Densitometry analysis **(B)** RT-qPCR analysis. Insulinoma cell line - INS-1E **(C)** Densitometry analysis**(D)** RT-qPCR analysis. Differentiated adipocytes (3T3-L1) **(E)** Protein densitometry analysis **(F)** RT-qPCR analysis. n ≥ 3, one way ANOVA. Data are represented as mean

±S.E.M. Values assigned the same letter show no significant difference from one another ($P < 0.05$).

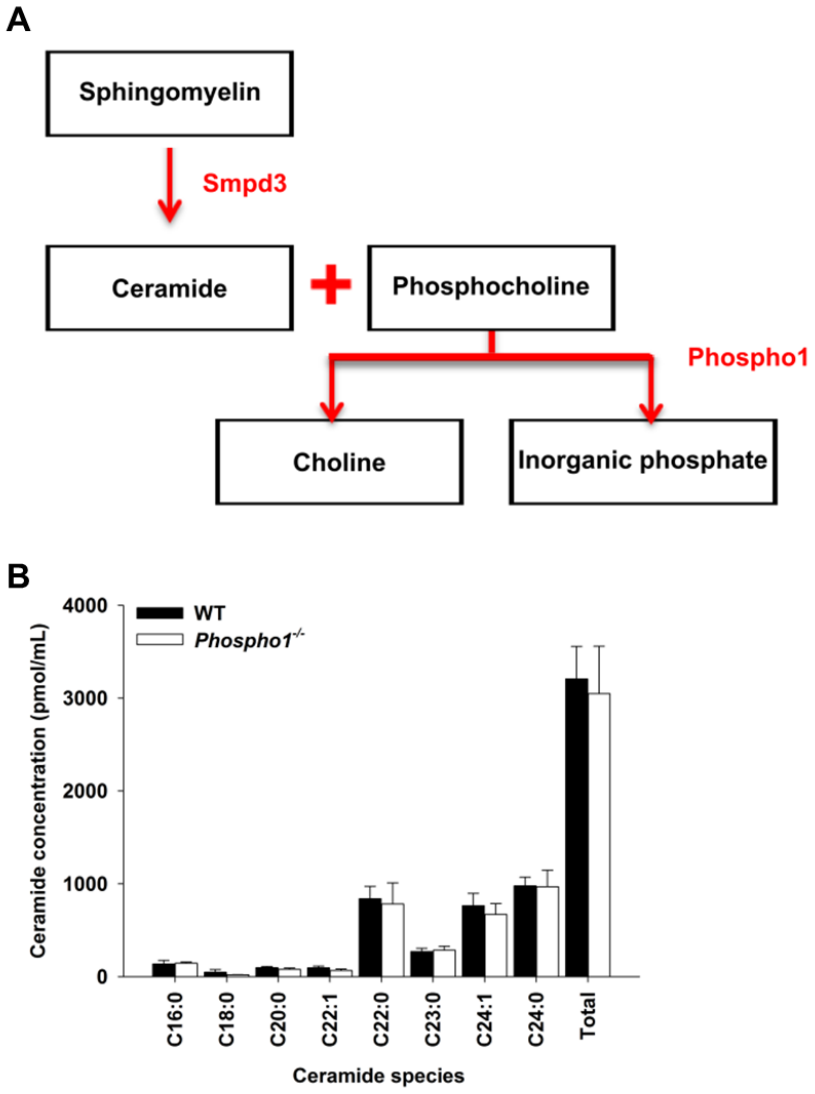

Figure 6.8 No difference in Ceramide between WT and *Phospho1*$^{-/-}$ mice
(A) Schematic diagram outlining the mechanisms by which ceramide and choline and linked. **(B)** Mouse serum ceramide analysis by LC-MS/MS. n = 5, t-test. Data are represented as mean ±S.E.M.

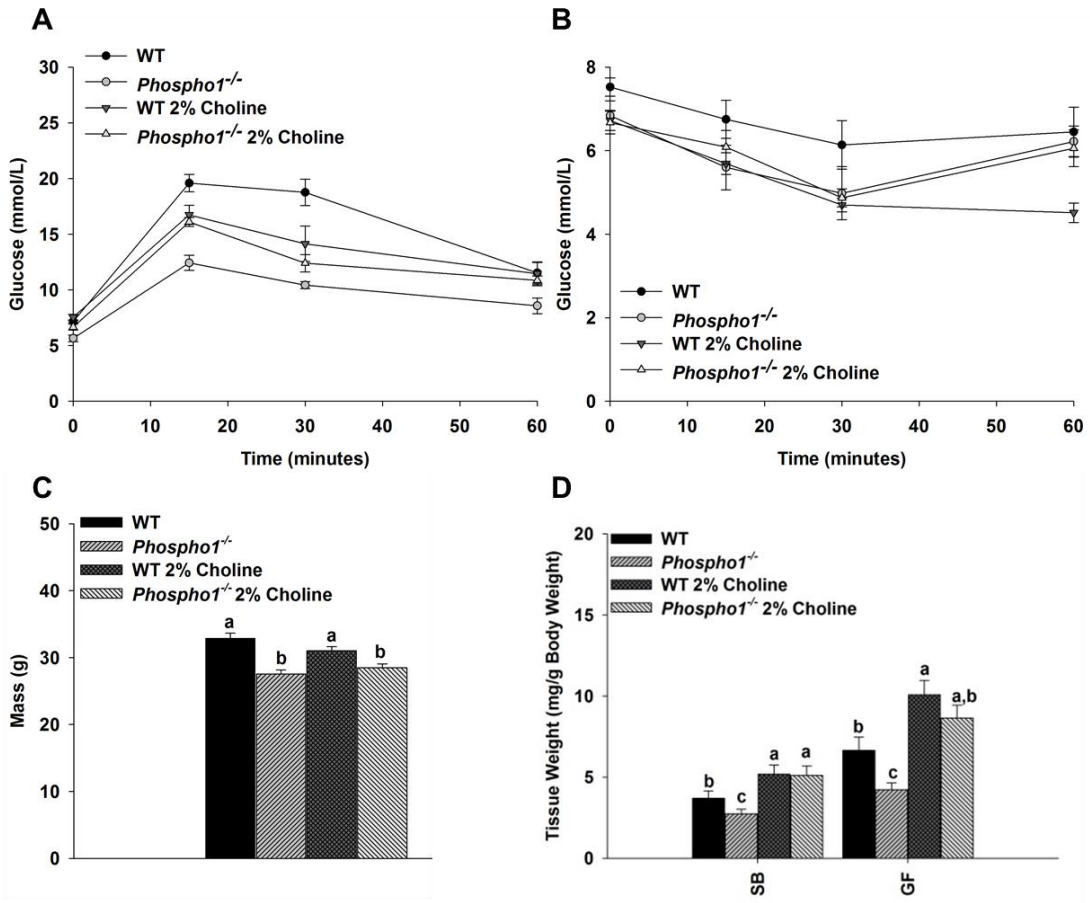

Figure 6.9 Bone derived choline regulates insulin sensitivity

(A) GTT and ITT **(B)** of 120 CD and 2% supplemented choline WT and *Phospho1*$^{-/-}$ mice **(C)** Simple weighing of 120 CD 2% choline mice revealed choline did not alter body mass. **(D)** Dissected fat depot weights, a 2% choline diet increased both SB, GF in *Phospho1*$^{-/-}$ mice however did not increased fat GF in WT mice. n ≥ 9, two way repeated measures ANOVA (A&B), one way ANOVA (C&D). Data are represented as mean ±S.E.M. Values assigned the same letter show no significant difference from one another ($P < 0.05$).

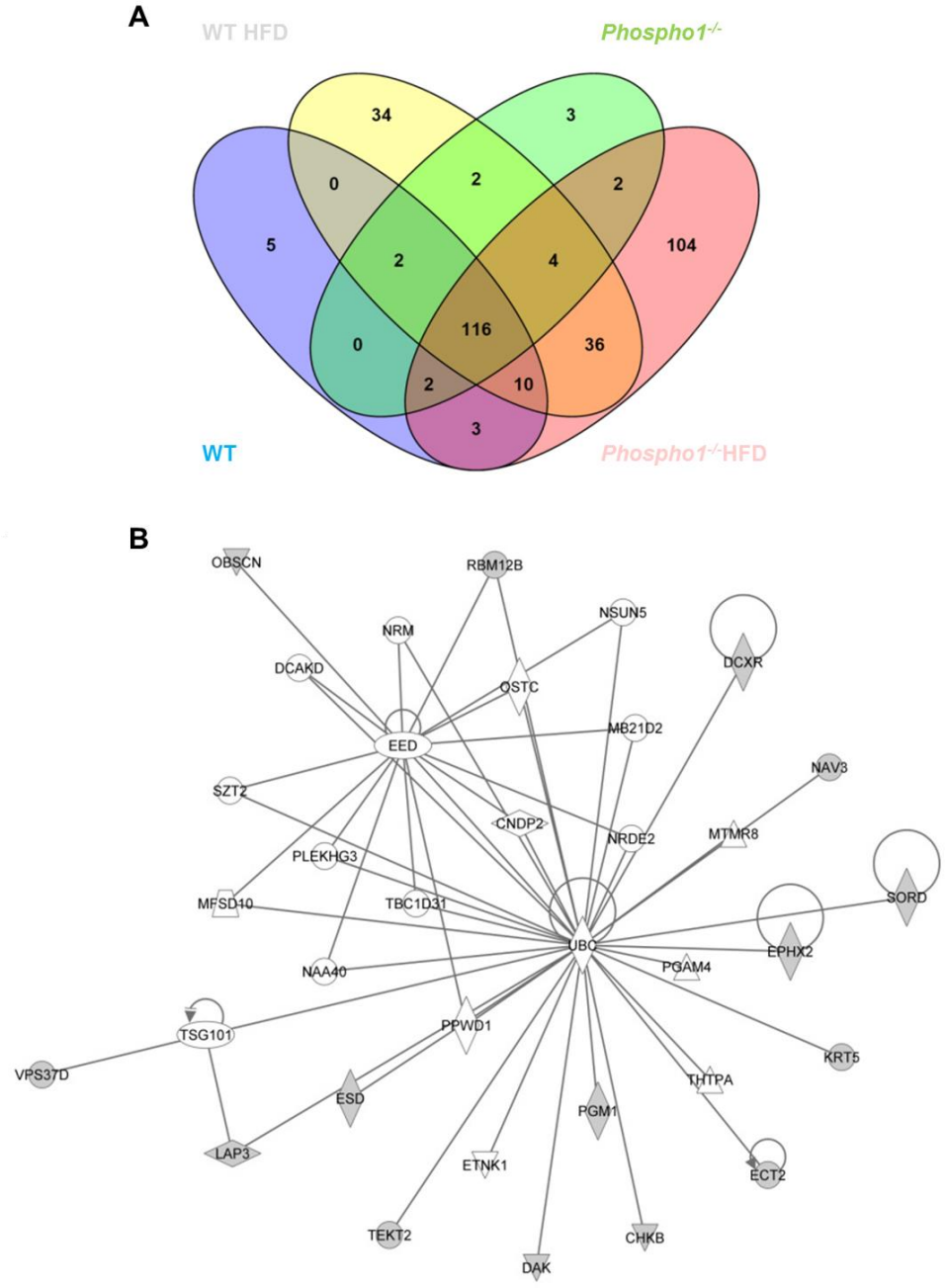

Figure 6.10 Proteomic analysis of serum from WT and *Phospho1*$^{-/-}$ mice
(A) Ven diagram representing number of unique proteins from proteomics **(B)** *Phospho1*$^{-/-}$ HFD unique network of carbohydrate, lipid metabolism (grey proteins in data set). (n = 3).

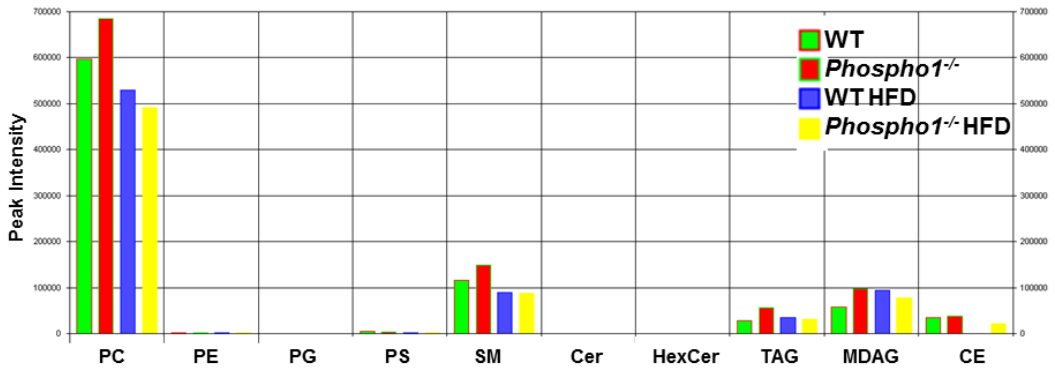

Figure 6.11 Lipidomic analysis of serum from WT and *Phospho1*$^{-/-}$ mice
All Lipid species present in serum from 120 day old male WT and *Phospho1*$^{-/-}$ CD and high fat diet mice. (Glycerophospholipid - PC, PE, PG, PS; Sphingolipids - SM, Cer, HexCer, Glycerolipids - TAG, MADAG; Sterol Lipids – CE) (n = 3). Graph kindly provided by Dr. Cal Vary, MMCRI.

6.6 Discussion

In the last decade, many reports have begun to unravel the precise mechanisms and address the aetiology, genetic and molecular aspects and the pathophysiology whereby the skeleton regulates energy metabolism. Moreover, as obesity plays a central role in the pathophysiology of diabetes mellitus, insulin resistance, dyslipidaemia, hypertension and atherosclerosis (constituting the metabolic syndrome) (Redinger, 2007); understanding the relationship between bone and energy metabolism may be helpful for the development and identification of new preventative, therapeutic and genetic strategies to combat obesity and the metabolic syndrome.

The results presented in this chapter uncover a novel role for PHOSPHO1 and bone derived choline in the regulation of energy metabolism, expanding the notion that the skeleton regulates global energy metabolism inclusive of insulin sensitivity, glucose tolerance and fat metabolism via both OCN-dependent and independent mechanisms. The data presented also suggests that *Esp* may act as a fine controller of insulin sensitivity, offering protection from severe hypoglycemia and dyslipidaemia without affecting OCN. Therefore these data add to the emerging notion of the complex skeletal regulation of energy metabolism.

6.6.1 *Esp* - a fine controller of insulin sensitivity in mice

As *Esp* offers protection against excessive insulin signalling the key finding that *Esp* was up regulated 60-fold in *Phospho1*$^{-/-}$ osteoblasts suggested the existence of an insulin resistant phenotype (Lee *et al.*, 2007). This was not found however and *Phospho1*-deficiency resulted in decreased blood glucose levels, improved insulin sensitivity and glucose tolerance and conferred protection from diet induced obesity and diabetes in mice. Furthermore, the increased insulin sensitivity was not associated with an expected rise in serum GLU13-OCN levels suggesting that PHOSPHO1-regulated energy metabolism is via OCN-independent mechanisms. This notion has previously been observed when partial genetic ablation of osteoblasts profoundly affected energy expenditure, GF weight and insulin sensitivity which were not restored by the administration of OCN (Yoshikawa *et al.*, 2011). Nevertheless, it cannot be discounted that the increased insulin sensitivity noted in the *Phospho1*$^{-/-}$ mice may be primed by an initial rise in GLU13-OCN levels, which is eventually normalised in a compensatory manner by the observed increase in *Esp* and OST-PTP expression. This being the case it would be predicted that the loss of *Esp* on a *Phospho1*$^{-/-}$ background would exacerbate the insulin sensitivity due to increased GLU13-OCN serum levels. Such experiments would be informative but were not possible due the time and budget restraints of this studentship. These data strengthen the concept that a novel pathway exists between osteoblasts and glucose homeostasis, however, it does highlight the potential cross-talk between OCN-dependent and OCN-independent mechanisms of glucose metabolism.

6.6.2 Mechanism of osteoblasts metabolic functions

The role of PHOSPHO1 in controlling bone mineralisation has been extensively investigated through the use of both *in vitro* and *in vivo* mouse models. Crucial in the initiation of mineralisation within the MV, PHOSPHO1 hydrolyses membrane lipids, primarily P-Cho to produce P_i (utilised in HA formation) and choline (Roberts *et al.*, 2004). P-Cho is generated from the hydrolysis of sphingomyelin to form P-Cho and ceramide. Mindful of this, it has been reported that elevated levels

of both ceramide and choline result in insulin resistance in mice (Yang *et al.*, 2009; Wu *et al.*, 2013). No change in ceramide species in *Phospho1*$^{-/-}$ mice were noted, whereas *Phospho1*$^{-/-}$ mice fed 2% choline rich diet displayed a normalisation in insulin sensitivity and fat mass. Choline induces hyperglycemia and insulin intolerance in mice via the modulation of plasma glucagon (Nakatani *et al.*, 2004). This chapter highlights for the first time the importance of bone derived choline in the regulation of energy metabolism, however, the precise mechanism(s) still remains unclear. It is possible that lack of choline in *Phospho1*$^{-/-}$ medium leads to the altered insulin stimulated sensitivity observed *in vitro* in INS1e and 3T3-L1 cells. However, it is also possible that alterations in bone choline influence other osteoblasts secreted factors that may regulate energy metabolism.

I have recently reviewed the literature on other osteoblast candidates beyond OCN that may be involved in bones ability to regulate glucose homeostasis (Oldknow *et al.*, 2015). These include AMP-activated protein kinase (AMPK), BMP's, GSK, FGF23, 'osteokines', sphingolipids and NPP1. Proteomic and lipidomic analysis of *Phospho1*$^{-/-}$ serum identified over 100 differentially expressed proteins and lipids in *Phospho1*$^{-/-}$ serum associated with the regulation of glycolysis and gluconeogenesis and these candidates included miR-34a which is known to affect diverse parts of insulin signalling in the pancreas, liver, muscle and adipose tissue (Kim *et al.*, 2013a). Further investigate of these candidates may uncover new skeletal regulators of energy metabolism. To add credence to our findings, a large independent prospective, nested case-control study found that DNA methylation markers that regulate gene expression and mediates the biological response to environmental exposures at the PHOSPHO1 loci were associated with BMI, waist: hip ratio, glucose concentrations, HOMA-IR, and future type 2 diabetes incidence among Indians, Asians and Europeans (Chambers *et al.*).

6.6.3 Skeletal regulation - beyond osteocalcin

Collectively, the results of this chapter add further credibility to the concept that OCN is not the sole mediator of the endocrine function of the skeleton (Yoshikawa *et al.*, 2011). The umbrella term 'glucose metabolism' encompasses insulin secretion and sensitivity, energy expenditure and lipid accumulation, which are precisely regulated by the function of the liver, pancreas, adipose tissue and muscle. Therefore, the notion that only one osteoblast/bone-derived factor (osteocalcin), contributes to the regulation of whole body glucose metabolism by regulating these diverse functions is highly unlikely. We therefore suggest, as have others have done, that further bone derived proteins/lipids work in collaboration with OCN to regulate the metabolic function of the skeleton. Indeed, this chapter has raised the possibility that bone derived choline may contribute to the regulation of the development of the metabolic syndrome, since *Phospho1*$^{-/-}$ mice who lack the ability to hydrolyse P-Cho in bone (Roberts *et al.*, 2004), do not develop obesity or diabetes. Finally the results presented in the chapter suggest that *Esp* may act as a fine controller of insulin sensitivity in mice, offering protection from severe hypoglycemia and dyslipidaemia.

Chapter 7

Final discussion and future research possibilities

7.1 General discussion

Recent developments in endocrinology, made possible by the combination of mouse genetics, integrative physiology and clinical observations have resulted in rapid and unanticipated advances in the field of skeletal biology. Indeed, the skeleton, classically viewed as a structural scaffold necessary for mobility, and regulator of calcium–phosphorus homoeostasis and maintenance of the haematopoietic niche has now been identified as a more complex organ, involved in the regulation of male fertility and whole-body glucose metabolism, in addition to the classical insulin target tissues. These seminal data have established the skeleton as a *bona fide* endocrine organ, challenging and fascinating researchers, resulting in an increased number of laboratories working in this field.

In the last decade, many laboratories have begun to unravel the precise mechanisms and address the aetiology, genetic and molecular aspects and the pathophysiology whereby the skeleton regulates energy metabolism. Obesity plays a central role in the pathophysiology of T2DM, insulin resistance, dyslipidaemia, hypertension and atherosclerosis (constituting the metabolic syndrome) (Redinger, 2007). Understanding the relationship between bone and energy metabolism may therefore be helpful for the development and identification of new preventative, therapeutic and genetic strategies to combat obesity and the metabolic syndrome. This would be both invaluable and timely as the current obesity global epidemic, presently the fifth leading risk of death worldwide costs approximately $147 billion annually (Finkelstein *et al.*, 2009; Stevens *et al.*, 2009; Grube *et al.*, 2013).

There are currently many efforts to reduce obesity, encompassing the promotion of a healthy diet and increasing physical activity in the entire population. In addition, the lipase inhibitor, Orlistat is a clinically approved anti-obesity medication that is offered to UK patients with a body mass index (BMI) of > 28 coupled with related obesity conditions including high blood pressure. In more severe cases, bariatric surgery is offered to patients whereby dietary efforts have not been successful,

therefore they continue to have a BMI of > 40 or > 35 coupled with obesity related comorbidity's such as type 2 diabetes mellitus (T2DM), obstructive sleep apnoea or high blood pressure. The two most common types of bariatric surgery are the fitting of a gastric band, reducing the volume of the stomach, or a gastric bypass whereby the 'pouch' created in the upper stomach then bypasses the remaining stomach, resulting in dramatically decreased digestion thus less calorie intake (NHS, 2014).

Obesity is clearly preventable; however, if steps are not taken to tackle obesity, the current statistic of one in four adults in the UK whom are affected could rapidly increase, constituting a huge burden to the NHS. Furthermore, obesity is associated with a multitude of chronic diseases including stroke, coronary heart disease, cancer of the breast, endometrium and colon.

This thesis focused on the bone specific phosphatase PHOSPHO1 which is indispensable for bone mineralisation and the prevention of soft tissue ossification abnormalities. Here I show that the ablation of *Phospho1* confers a remarkable degree of protection against NAFLD, insulin resistance and T2DM in mice (Chapter 4 & 5). These data support the notion that further, yet undefined osteoblast derived factors contribute to whole body energy metabolism

Non-alcoholic fatty liver disease is the most common cause of chronic liver disease in Western countries, commencing with hepatic lipid accumulation and primarily affecting the hepatic structure and function resulting in both morbidity and mortality from cirrhosis, liver failure and hepatocellular carcinoma (Table 7.1). It is now accepted that NAFLD is a multisystem disease affecting non-hepatic organs, leading to increased risk of cardiovascular and cardiac diseases, chronic kidney disease and T2DM (Anstee *et al.*, 2013)(reviewed (Byrne and Targher, 2015)). The current major risk factors for NAFLD are well established, in addition to obesity, insulin resistance and T2DM, increased ferritin and the patatin-like phospholipase

domain-containing 3 (*Pnpla3*) I148M polymorphism (prevalence of this risk allele is in 40 to 50% of Europeans) are known to result in NAFLD. However the mechanisms underlying disease progression are less well understood (particularly *Pnpla3* genotype) (Romeo *et al.*, 2008; Wang *et al.*, 2011). Alarmingly, there are currently no approved drugs for the treatment of non-alcoholic steatohepatits (NASH) (stage 2 of NAFLD -2-5% UK population), with current clinical trials focusing on insulin sensitisers (e.g. glitazones) and hepatoprotective agents (e.g. vitamin E). However it is predicted none of the molecules under investigation are likely to improve NAFLD, thus new targets must be identified (Soden *et al.*, 2007; Gastaldelli *et al.*, 2009) (reviewed in (Ratziu *et al.*, 2015). The data presented in this thesis (Chapter 5) certainly indicates that the genetic ablation of *Phospho1* offers a remarkable protection against NAFLD when mice are fed a chronic high fat diet. It is therefore plausible to suggest that the administration of PHOSPHO1 inhibitors or PHOSPHO1 neutralising antibodies may provide a therapeutic intervention in patients with NAFLD, potentially preventing the onset of fibrosis, cirrhosis and possibly reducing the risk of developing cardiovascular and cardiac diseases. Certainly this seems viable, as juvenile *Phospho1* heterozygous mice display an intermediate insulin sensitive phenotype suggestive that PHOSPHO1 may represent a druggable target (Chapter 4). Furthermore, administration of the a highly selective PHOSPHO1 inhibitor MLS-0263839 (with no detectable cross-inhibition of TNAP or NPP1) was shown to inhibit vascular calcification in mineralising murine WT vascular smooth muscle cells to 41.8% ± 2.0% of control (Kiffer-Moreira *et al.*, 2013). Additionally, inhibition of PHOSPHO1 by lansoprazole, ebselen and SCH-202676 disrupts MV mediated mineralisation in *Akp2*$^{-/-}$ osteoblasts and impairs the skeletal development chick long bones (Roberts *et al.*, 2007; MacRae *et al.*, 2010).

Stage	Nomenclature	Pathology	Symptoms	Severity
1	Simple fatty liver (steatosis)	Excess lipid accumulates in hepatocytes.	No symptoms (identified via blood test)	Mild
2	Non-alcoholic steatohepatitis (NASH)	Inflammation of the liver.	No symptoms (identified via blood test) or dull or aching pain in the top right of their abdomen	Moderate
3	Fibrosis	Persistent inflammation of the liver resulting in results in the generation of fibrous scar tissue around the hepatocytes and blood vessels.	Dull or aching pain in the top right of their abdomen	Moderate – Severe.
4	Cirrhosis	Liver shrinkage leading to liver failure / hepatocellular carcinoma.	Tiredness, loss of appetite, weight loss, nausea, pain around the liver area, itchy skin, jaundice, hair loss and oedema.	Severe

Table 7.1 Non-alcoholic fatty liver disease (NAFLD) pathology, symptoms and severity

Insulin resistance, often termed pre-diabetes, occurs when insulin is produced at a high level, over a prolonged period of time, reducing insulin tissue sensitivity, occurring years prior to the development of glucose intolerance, β cell failure and T2DM (Tabak *et al.*, 2009). Upon the onset of T2DM, patients may present with insulin resistance in muscle, adipose tissue, and liver, impaired insulin secretion, impaired incretin (hormone secreted from enteroendocrine cells, incretin functions to regulate insulin following eating) secretion and action, and altered balance of central nervous system (CNS) pathways controlling food intake and energy expenditure (Kim and Egan, 2008). Both genetic and environmental factors contribute to the onset of T2DM, with risk factors including obesity, inactivity and aging. Furthermore, mitochondrial oxidative dysfunction, endoplasmic reticulum stress, oxidative stress, and alterations in insulin signalling have all been linked to insulin resistance as reviewed in (Doria *et al.*, 2008; Sales and Patti, 2013). The recommended strategy for achieving glucose control in insulin resistance or T2DM patients is to establish a metabolic target and to adjust treatment to achieve reduced glucose levels, via lifestyle changes (controlled and healthy diet, weight loss and increase of physical activity) and medication (including but not restricted to metformin, sulphonylureas, glitazones, gliptins, GLP-1 agonists, acarbose, acarbose, nateglinide and repaglinide). Comorbidity is common in patients with T2DM taking glucose lowering drugs resulting in further chronic disease, such as joint disorders, respiratory disease, anaemia, malignancy, depression, thus further research into new drug targets must be undertaken to reduce comorbidities, reducing chronic diseases (Wami *et al.*, 2013). Since the realisation that the skeleton is an important regulator of whole-body glucose metabolism via the hormonally active OCN, which stimulates insulin secretion and β cell proliferation in the pancreas and promotes insulin sensitivity in peripheral organs in mice, many clinical studies have been conducted to deduce whether this mechanism is present in humans. One of the earliest studies to show an association between OCN and glucose metabolism was published over a decade ago. Osteocalcin levels were significantly lower in diabetic

patients, although OCN levels increased with improved glycaemic control (Rosato *et al.*, 1998). In many human studies only total OCN levels were quantified; however, the effects on glucose metabolism via bone are attributed to GLU13-OCN. These studies yielded mixed results with several of them indicating a positive correlation between serum GLU13-OCN levels and enhanced β-cell function (Hwang *et al.*, 2009; Prats-Puig *et al.*, 2010; Pollock *et al.*, 2011). However, results from other studies indicate no association between lower circulating GLU13-OCN levels and higher HOMA-IR (Shea *et al.*, 2009). Results from one recent study have indicated that there is a sex-specific action of the bone–energy homoeostasis axis with OCN being associated with improved metabolic state via adiponectin in females, and via testosterone in males (Buday *et al.*, 2013). Direct clinical evidence has been reported for the role of OCN in energy metabolism, via the removal of an OCN-producing osteoid osteoma, which resulted in elevated serum glucose, potentially associated with decreased levels of GLU13-OCN (Confavreux *et al.*, 2012). These conflicting results may be attributable to the lack of a commercially available GLU13-OCN ELISA, or differing methodologies (Ducy, 2011). The potential therapeutic implications of these recent findings have however not yet been fully exploited. Whether the use of OC is efficacious in the treatment of T2DM remains to be determined.

As highlighted in Chapter 4 & 5, the ablation of *Phospho1* offers protection against obesity and T2DM in mice, however in *Phospho1*$^{-/-}$ mice the serum levels of GLU13-OCN were normal, suggesting an OCN-independent mechanism of PHOSPHO1 regulated energy metabolism (Chapter 3 & 6). Therefore as described previously, PHOSPHO1 inhibitors or PHOSPHO1 neutralising antibodies may provide a therapeutic intervention in patients with insulin resistance and T2DM. However, it is important to note that as in addition to the skeletal pathologies such as, spontaneous fractures, bowed long bones, osteomalacia, and scoliosis in early life observed in the *Phospho1*$^{-/-}$ mice (Chapter 1)(Huesa *et al.*, 2011; Yadav *et al.*, 2011), recent data obtained from our lab suggests that *Phospho1*$^{-/-}$ mice show subchondral

bone thickening, a hallmark of osteoarthritis (OA) and unquestionably contribute to OA pathogenesis, in addition to severe articular cartilage degeneration and osteophyte formation (unpublished data). As T2DM is associated with various skeletal comorbidities such as joint disorders, PHOSPHO1 may be a challenging drug target resulting in undesirable side effects and therefore any therapeutic approaches using inhibitors will need to be managed very carefully and further research will be required

Nevertheless, in addition to PHOSPHO1, it seems plausible that other proteins expressed in bone may affect energy metabolism via OCN independent mechanisms, providing further novel drug candidates including AMPK (Jeyabalan *et al.*, 2012), BMPs, GSK3, osteokines (osteocyte-derived factors), sphingolipids and NPP1 (Fig. 7.1) reviewed in (Schulz and Tseng, 2009; Jeyabalan *et al.*, 2012; Oldknow *et al.*, 2015).

In conclusion, this thesis identifies for the first time that *Phospho1* deficiency improves the metabolic profile of mice via an OCN-independent mechanism, supporting the notion that further, yet undefined osteoblasts derived hormones contribute to whole body energy regulation via the skeleton. However many questions still remain: does OCN regulate insulin secretion over the short/long term? How does the osteoblast or osteocyte sense and use glucose or other fuels? Do bone cells utilise glucose or amino acids? Does bone fracture increase whole-body energy expenditure? Do osteocytes truly have an effect on energy metabolism? (Fulzele *et al.*, 2007; Fulzele and Clemens, 2012). The complex OCN- dependent and independent mechanisms discussed here are still somewhat in their infancy; therefore it is vital that the research community endeavour to fully establish the mechanisms undelaying these endocrine interactions resulting in the better diagnosis, clinical management and treatment of patients with metabolic diseases.

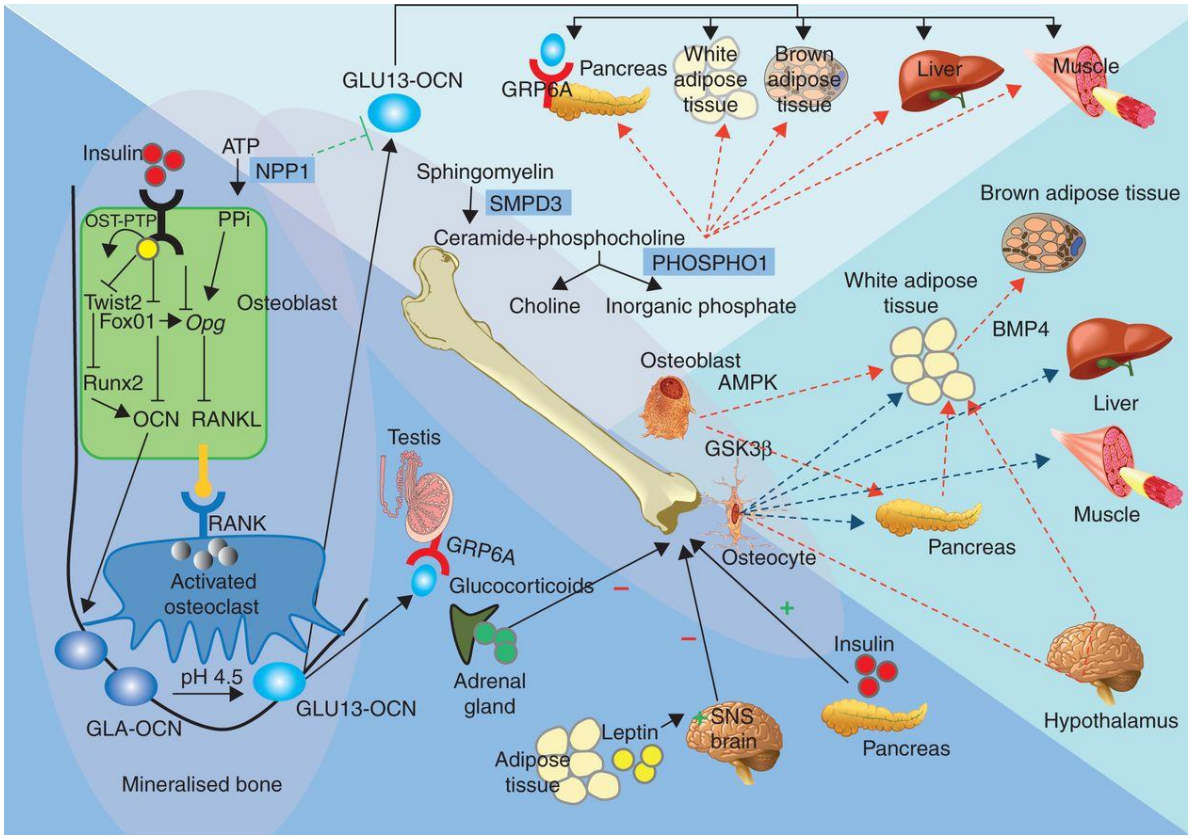

Figure 7.1 The endocrine role of bone: Osteocalcin and beyond
(Arrow key: Solid – accepted; dashed – speculative. Black = known interactions, green = indirect interactions, red = direct interactions, blue = osteokines). A feed forward loop links insulin, bone resorption and OCN activity. Insulin signalling in osteoblasts decreases the expression of *Opg* via decreasing the ratio of *Opg* (a RANKL decoy receptor) to RANKL thus increasing bone resorption by osteoclasts. This osteoclastic bone resorption generates an acidic pH in the resorption lacunae necessary to decarboxylate OCN stored in the bone extracellular matrix. GLU13-OCN is released into the blood stream, affecting glucose metabolism by binding to the OCN receptor (GPRC6A) thus stimulating insulin secretion and β cell proliferation in the pancreas and promoting insulin sensitivity in peripheral organs. In addition, GLU13-OCN promotes male fertility by stimulating testosterone synthesis in leydig cells of the testis through GPRC6A activation. *Esp* acts as an inhibitor, dephosphorylating the insulin receptor, supressing the levels of GLU13-OCN. To complete this feed forward loop, peripheral / central tissues (adrenal gland, adipose tissue, pancreas) can further indirectly regulate the release of GLU13-OCN into the peripheral circulation. New emerging evidence suggests in addition, NPP1 can indirectly inhibit GLU-13 OCN release via OPG. Independently of OCN, osteoblast specific proteins (PHOSPHO1, AMPK and GSK3β) can influence insulin secretion from β cell functions and adiposity. Osteocyte derived factors - Osteokines, may also be implicated in the endocrine regulation of glucose metabolism (Figure adapted from (Rosen and Motyl, 2010; Ferron and Lacombe, 2014) Published: (Oldknow *et al.*, 2015)

7.2 Direction for future research

The results presented in this thesis have identified that the genetic ablation of *Phospho1* results in hypoglycemia, improved glucose and insulin tolerance and offers protection from diet induced fatty liver and obesity in mice. However, further work is necessary to fully elucidate the mechanism underlying this protection in PHOSPHO1 deficiency (Chapter 6) and indeed if this mechanism is truly GLU13-OCN independent. Mouse genetic technology would offer a gateway to the exploration of these questions.

PHOSPHO1 is preferentially expressed by bone, however low protein expression is observed in non-bone organs (e.g. brain and muscle) (Chapter 3), which in its absence could possibly contribute to the insulin sensitive phenotype of *Phospho1*$^{-/-}$ mice. It would therefore be beneficial to generate a *Phospho1*$^{-/-}$*Col1a1-Phospho1* mouse model, in which *Phospho1* expression is restored in bone (using the Col1a1 promoter – Appendix VII) in a *Phospho1*$^{-/-}$ global mouse to firmly confirm that the *Phospho1*$^{-/-}$ insulin sensitive phenotype is osteoblast driven. If this were the case, metabolic normalisation would be observed in this model. Alternatively, it may be found that the insulin sensitivity is not normalised, suggestive that PHOSPHO1 has a new, non-redundant role in non-bone organs. Furthermore, it is unclear if the ablation of *Phospho1* expression in the developing embryo can have long lasting effects, effectively "priming" the mice for an insulin sensitive phenotype in later life. To discern if aged *Phospho1*$^{-/-}$ mice are protected from obesity the study of a tamoxifen inducible *Phospho1* knockout model could be of enormous value. Phosphatase, Orphan 1, conditionally ready mice (Tm1a) using 'knockout-first' (*Phospho1* embryonic stem cell clones are available from the EUCOMM consortium). Mice (Tm1a) could be bred with a FLPE line reverting to the Tm1c allele which is effectively a WT mouse but with a floxed critical exon. Finally, Tm1c mice could be bred with tamoxifen (TM) inducible germ line-Cre-driver mice to permit temporally knock-out *Phospho1* expression in all tissues (Hayashi and McMahon, 2002). Both germ line Cre-ER^{Tm} and FLPE mice are available at The Edinburgh University

however were unattainable during this PhD and the costs of these experiments would have been prohibitive. It would be beneficial to characterise insulin sensitivity in 35, 120 and 220 day old mice following intraperitoneal injection of TM to ascertain when PHOSPHO1 deficiency is most influential in age related metabolic disease.

Certainly, it would be of benefit to establish the functional role of *Esp* in *Phospho1*$^{-/-}$ mice. As described, *Esp* was more highly expressed in *Phospho1*$^{-/-}$ osteoblasts (60-fold, $P < 0.01$) indicative of decreased of GLU13-OCN secretion and insulin resistance, however this was not the case in the *Phospho1*$^{-/-}$ mice (Chapter 3). The generation of *Phospho1*;*Esp* double knockout mice would clarify if *Esp* offers protection against excessive insulin signalling due to increased GLU13-OCN serum levels. Once the role of *Esp* in mice is established, it would be essential to generate *Phospho1;Ocn* double knockout mice and conduct metabolic analysis to address if either the increased insulin sensitivity in *Phospho1*$^{-/-}$ mice is:

I. Truly OCN independent.
II. Due to an initial rise in GLU13-OCN levels which effectively "primes" the *Phospho1*$^{-/-}$ mice for an insulin sensitive phenotype throughout life. This insulin sensitivity is eventually normalised due to the compensatory increase in *Esp* expression (Fig. 7.2).

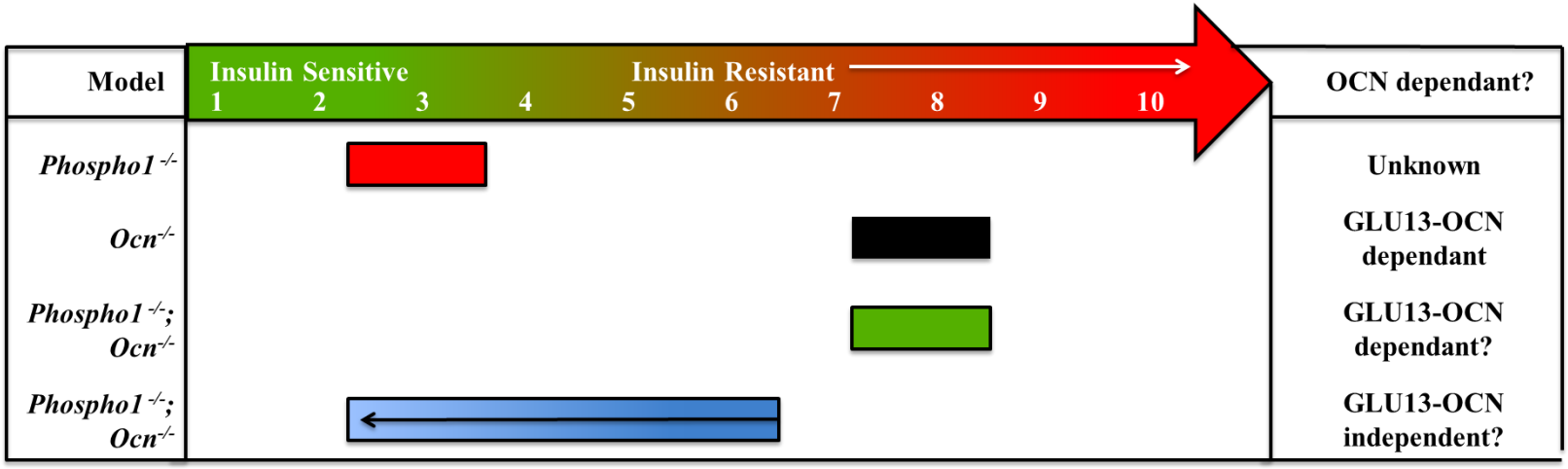

Figure 7.2 *Phospho1;Ocn* knockout mice phonotype's
If *Phospho1* ablation (on an *Ocn*$^{-/-}$ background) fails to correct the insulin resistance of *Ocn*$^{-/-}$ mice (line 2) this would suggest that PHOSPHO1's actions are GLU13-OCN dependent (line 3). Alternatively, if *Ocn*$^{-/-}$ insulin resistance is normalised in *Phospho1*/*Ocn* double knockout mice this would imply that the increased insulin sensitivity is GLU13-OCN independent (line 4).

It has been hypothesised that PHOSPHO1, together with SMPD3, through the generation and processing of P-Cho (Chapter 6), respectively, network to regulate glucose homeostasis and insulin sensitivity (Stoffel *et al.*, 2005; Oldknow *et al.*, 2015). Indeed SMPD3 may act upstream of PHOSPHO1 within the same metabolic pathway to regulate glucose homeostasis and insulin sensitivity. To investigate this two mice could be generated:

I. *Smpd3*/*Phospho1* double knockout and *Smpd3*$^{-/-}$ mice.
II. *Phospho1*$^{-/-}$ and *Phospho1*$^{-/-}$*Col1a1-Smpd3 mice (Smpd3* is overexpressed in the osteoblasts of *Phospho1*$^{-/-}$ mice).

If SMPD3 acts upstream of PHOSPHO1 the degree of insulin sensitivity in *Smpd3*/*Phospho1* double knockout and *Smpd3*$^{-/-}$ mice would be similar, and no correction of insulin sensitivity would be observed in the *Phospho1*$^{-/-}$*Col1a1-Smpd3* mice. Moreover, ceramide and choline, products of SMPD3 and PHOSPHO1 activity respectively, in excess can cause insulin resistance. Consequently, lower levels of either ceramide or choline due to *Smpd3* or *Phospho1* ablation may explain the resultant insulin sensitivity (Chapter 6) (Yang *et al.*, 2009; Wu *et al.*, 2013). However, as outlined in this thesis, normal levels of ceramide species were observed in *Phospho1*$^{-/-}$ mice, however administration of a 2% choline rich normalised the insulin sensitive phenotype in *Phospho1*$^{-/-}$ mice suggesting that decreased choline may be responsible for the insulin sensitivity observed in *Phospho1*$^{-/-}$ mice. It is therefore important to quantify total bone and serum choline by mass spectroscopy to ascertain if indeed bone derived choline is indispensable for whole body metabolism.

I have shown that osteoblast secreted candidate(s) regulate energy metabolism in *Phospho1*$^{-/-}$ mice, however these candidates remain undetected. I have conducted proteomic, lipidomic and *in silico* analysis with the aim to identify secreted candidates in serum and osteoblast conditioned medium, and for lipids principle

component multivariate data analysis was conducted to establish preliminary lipid classes and their contribution to sample differences (Chapter 6). However it was not possible to fully verify this data by western blotting, siRNA knockdown or microRNA screening. Furthermore, it would also be advantageous to obtain samples from alkaline phosphatase null mice (*Alpl*$^{-/-}$; hypomineralised, normoglycaemic), that would act as a control to help eliminate proteins whose expression is altered solely as a result of impaired matrix mineralisation.

Finally, in the thesis, I reported that BAT of *Phospho1*$^{-/-}$ mice had markedly reduced fat content and increased nuclei number ($P < 0.05$). Indeed if the elevated nuclei number translated to increased mitochondria number, the metabolic phenotype observed in *Phospho1*$^{-/-}$ mice may be due to alterations in non-shivering thermogenesis. If this is the case, *Phospho1* ablation is less likely to have persisting anti-obesity effects at thermoneutrality. Therefore it would be essential to determine if the reduced fat mass and improved metabolic phenotype of *Phospho1*$^{-/-}$ mice is a consequence of BAT thermogenesis by comparing energy expenditure in mice maintained at thermoneutrality (30°C) and ambient temperatures (23°C). As I observed no differences in the expression of BAT enriched genes (e.g. *Ucp1*), this is suggestive that canonical thermogenesis through *Ucp1* does not underlie the metabolic protection seen in *Phospho1*$^{-/-}$ mice. However, as these experiments were conducted at ambient temperatures (23°C – mice are considered mildly cold-stressed, hyper-metabolic, hypertensive and obesity-resistant). Studying WT and *Phospho1*$^{-/-}$ mice at thermoneutrality may lead to the identification of novel genes underlying increased mitochondrial number and improved metabolism with *Phospho1* deficiency directly relevant to humans (who spend most of their time at thermoneutrality) (Hayashi and McMahon, 2002). To test if the reduced fat mass and improved metabolic phenotype of *Phospho1*$^{-/-}$ mice is a consequence of enhanced sensitivity of the BAT thermogenesis system, mice could be challenged with low temperatures stimulating *Ucp1* and engendering an insulin sensitive phenotype. Mice could be exposed to chronic cold exposure from ambient (23°C) to 8°C for 98

hours, then to 4°C for up to 5 weeks. Additionally, acute cold exposure could be used to test the immediate effects of environmental stress, whereby mice could be subject to a 6-hour cold exposure (*4*°C*).* Body weight, fat and lean mass (using time domain nuclear magnetic resonance) glucose homeostasis and energy expenditure and BAT mitochondrial activity could also be determined. Specifically, mitochondrial activity in BAT could be assessed through (i) the expression of biomarkers of mitochondrial biogenesis (e.g. PGC-1α & β) and metabolic pathways linked to BAT fat oxidation (e.g. *Ucp3*, *Cpt1b* and *Pdk4*) by RT-qPCR, (ii) the expression of mitochondrial respiratory proteins (e.g. ND6, COX, CII, CIII-CORE2 and CVα) by immunoblotting and (iii) BAT mitochondrial activity (oxidative phosphorylation) and glycolysis by the 24 extracellular Flux Analyzer (Seahorse Bioscience). Furthermore, mitochondrial respiration and glycolysis of primary BAT adipocytes could be assessed using Seahorse technology (Chapter 6).

These proposed experiments would methodically illustrate the complex role of PHOSPHO1 in glycaemic control and energy metabolism. Uncovering the mechanisms whereby PHOSPHO1 impacts energy metabolism is vital, to provide impetus for the development of novel therapeutic and intervention strategies again obesity, T2DM and NAFLD.

Reference list

Abbracchio MP, Burnstock G (1994). Purinoceptors: Are there families of P2X and P2Y purinoceptors? *Pharmacology and Therapeutics* 64(3):445-475.

Alam I, Sun Q, Koller DL, Liu L, Liu Y, Edenberg HJ, Li J, Foroud T, Turner CH (2009). Differentially expressed genes strongly correlated with femur strength in rats. *Genomics* 94(4):257-262.

Alebrahim S, Khavandgar Z, Marulanda J, Murshed M (2014). Inducible transient expression of Smpd3 prevents early lethality in fro/fro mice. *Genesis* 52(5):408-416.

Alford AI, Hankenson KD (2006). Matricellular proteins: Extracellular modulators of bone development, remodeling, and regeneration. *Bone* 38(6):749-757.

Alonso A, Sasin J, Bottini N, Friedberg I, Osterman A, Godzik A, Hunter T, Dixon J, Mustelin T (2004). Protein tyrosine phosphatases in the human genome. *Cell* 117(6):699-711.

Aerni-Flessner L, Abi-Jaoude M, Koenig A, Payne M, Hruz PW (2012). GLUT4, GLUT1, and GLUT8 are the dominant GLUT transcripts expressed in the murine left ventricle. *Cardiovascular Diabetology* 11(63).

Anderson HC (1995). Molecular biology of matrix vesicles. *Clinical Orthopaedics and Related Research* (314):266-280.

Anderson HC, Garimella R, Tague SE (2005). The role of matrix vesicles in growth plate development and biomineralization. *Frontiers in Bioscience* 10:822-837.

Andrades JA, Nimni ME, Becerra J, Eisenstein R, Davis M, Sorgente N (1996). Complement proteins are present in developing endochondral bone and may mediate cartilage cell death and vascularization. *Experimental Cell Research* 227(2):208-213.

Anstee QM, Targher G, Day CP (2013). Progression of NAFLD to diabetes mellitus, cardiovascular disease or cirrhosis. *Nature Reviews Gastroenterology and Hepatology* 10(6):330-344.

Argiro L, Desbarats M, Glorieux FH, Ecarot B (2001). MEPE, the gene encoding a tumor-secreted protein in oncogenic hypophosphatemic osteomalacia, is expressed in bone. *Genomics* 74(3):342-351.

Ashley JW, Shi Z, Zhao H, Li X, Kesterson RA, Feng X (2011). Genetic ablation of CD68 results in mice with increased bone and dysfunctional osteoclasts. *PLoS One* 6(10):e25838.

Aspden RM (2003). Mechanical testing of bone ex vivo. *Methods* in *Molecular Medicine* 80:369-379.

Aubin I, Adams CP, Opsahl S, Septier D, Bishop CE, Auge N, Salvayre R, Negre-Salvayre A, Goldberg M, Guenet JL, Poirier C (2005). A deletion in the gene encoding sphingomyelin phosphodiesterase 3 (Smpd3) results in osteogenesis and dentinogenesis imperfecta in the mouse. *Nature Genetics* 37(8):803-805.

Bao J, Cui X, Cai S, Zhong J, Cai C, Chen Z (2013). Brown adipose tissue mapping in rats with combined intermolecular double-quantum coherence and Dixon water-fat MRI. *NMR Biomedicine* 26(12):1663-1671.

Barr AJ, Ugochukwu E, Lee WH, King ON, Filippakopoulos P, Alfano I, Savitsky P, Burgess-Brown NA, Muller S, Knapp S (2009). Large-scale structural analysis of the classical human protein tyrosine phosphatome. *Cell* 136(2):352-363.

Basit S (2013). Vitamin D in health and disease: a literature review. *British Journal* of *Biomedical Science* 70(4):161-172.

Bell GI, Kayano T, Buse JB, Burant CF, Takeda J, Lin D, Fukumoto H, Seino S (1990). Molecular biology of mammalian glucose transporters. *Diabetes Care* 13(3):198-208.

Berger A (2002). Magnetic resonance imaging. *British Medical Journal* 324(7328):35.

Berglund ED, Li CL, Poffenberger G, Ayala JE, Fueger PT, Willis SE, Jewell MM, Power AC, Wasserman DH (2008). Glucose metabolism *in vivo* in four commonly used inbred mouse strains. *Diabetes* 57(7):1790–1799.

Bligh EG, Dyer WJ (1959). A rapid method of total lipid extraction and purification. *Canadian Journal* of *Physiology and Pharmacology* 37(8):911-917.

Bollen M, Gijsbers R, Ceulemans H, Stalmans W, Stefan C (2000). Nucleotide pyrophosphatases/phosphodiesterases on the move. *Critical Reviews in Biochemistry and Molecular Biology* 35(6):393-432.

Bonewald LF, Wacker MJ (2013). FGF23 production by osteocytes. *Pediatr Nephrol* 28(4):563-568.

Bonucci E (2012). Bone mineralization *The Frontiers in Bioscience (Landmark Edition)* 17:100-128.

Boskey AL, Spevak L, Paschalis E, Doty SB, McKee MD (2002). Osteopontin deficiency increases mineral content and mineral crystallinity in mouse bone. *Calcified Tissue International* 71(2):145-154.

Bowden JA, Albert CJ, Barnaby OS, Ford DA (2011). Analysis of cholesteryl esters and diacylglycerols using lithiated adducts and electrospray ionization-tandem mass spectrometry. *Analytical Biochemistry* 417(2):202-210.

Brakspear KS, Mason DJ (2012). Glutamate signalling in bone. *Frontiers in Endocrinol* 3(97).

Brekken RA, Sage EH (2000). SPARC, a matricellular protein: at the crossroads of cell–matrix. *Matrix Biology* 19(7):569-580.

Bronckers AL, Lyaruu DM, Bervoets TJ, Medina JF, DenBesten P, Richter J, Everts V (2012). Murine ameloblasts are immunonegative for Tcirg1, the v-H-ATPase subunit essential for the osteoclast plasma proton pump. *Bone* 50(4):901-908.

Brown JP, Delmas PD, Malaval L, Edouard C, Chapuy MC, Meunier PJ (1984). Serum bone Gla-protein: a specific marker for bone formation in postmenopausal osteoporosis. *Lancet* 1(8386):1091-1093.

Buday B, Pach FP, Literati-Nagy B, Vitai M, Vecsei Z, Koranyi L (2013). Serum osteocalcin is associated with improved metabolic state via adiponectin in females versus testosterone in males. Gender specific nature of the bone-energy homeostasis axis. *Bone* 57(1):98-104.

Bunger L, Hill WG (1997). Effects of leptin administration on long-term selected fat mice. *Genetic Research* 69(3):215-225.

Bunger L, Macfarlane JM, Lambe NR, Conington J, McLean KA, Moore K, Glasbey CA, Simm G (2011). Use of X-ray computed tomography (CT) in UK sheep production and breeding. In: CT Scanning - Techniques and Applications. S Karuppasamy editor: INTECH Open access Publisher: 329-348.

Burcelin R, Crivelli V, Dacosta A, Roy-Tirelli A, Thorens B (2002). Heterogeneous metabolic adaptation of C57BL/6J mice to high-fat diet. *American Journal of Physiology Endocrinology and Metabolism* 282(4):E834-842.

Burnstock G, Kennedy C (1985). Is there a basis for distinguishing two types of P2-purinoceptor? *General Pharmacology* 16(5):433-440.

Burnstock G (2007). Purine and pyrimidine receptors. *Cellular and Molecular Life Sciences* 64(12):1471-1483.

Byrne CD, Targher G (2015). NAFLD: A multisystem disease. *Journal of Hepatology* 62(1S):S47-S64.

Cairns JR, Price PA (1994). Direct demonstration that the vitamin K-dependent bone Gla protein is incompletely γ-carboxylated in humans. *Journal of Bone and Mineral Research* 9(12):1989-1997.

Cancela L, Hsieh CL, Francke U, Price PA (1990). Molecular structure, chromosome assignment, and promoter organization of the human matrix Gla protein gene. *Journal of Biological Chemistry* 265(25):15040-15048.

Cancela ML, Laize V, Conceicao N (2014). Matrix Gla protein and osteocalcin: from gene duplication to neofunctionalization. *Archives of Biochemistry and Biophysics* 561:56-63.

Cao JJ, Sun L, Gao H (2010). Diet-induced obesity alters bone remodeling leading to decreased femoral trabecular bone mass in mice. *Annals of the New York Academy of Sciences* 1192(1):292-297.

Carruthers A (1990). Facilitated diffusion of glucose. *Physiolgy Reviews* 70(4):1135-1176.

Casey PA, Casey G, Fleisch H, Fussel RG (1972). The effect of polyphloretin phosphate, polyoestradiol phosphate, a diphosphonate and a polyphosphate on calcification induced by dihydrotachysterol in skin, aorta and kidney of rats. *Experientia* 28(2):137-138.

Chambers JC, Loh M, Lehne B, Drong A, Kriebel J, Motta V, Wahl S, Elliott HR, Rota F, Scott WR, Zhang W, Tan S-T, Campanella G, Chadeau-Hyam M, Yengo L, Richmond RC, Adamowicz-Brice M, Afzal U, Bozaoglu K, Mok ZY, Ng HK, Pattou F, Prokisch H, Rozario MA, Tarantini L, Abbott J, Ala-Korpela M, Albetti B, Ammerpohl O, Bertazzi PA, Blancher C, Caiazzo R, Danesh J, Gaunt TR, de Lusignan S, Gieger C, Illig T, Jha S, Jones S, Jowett J, Kangas AJ, Kasturiratne A, Kato N, Kotea N, Kowlessur S, Pitkäniemi J, Punjabi P, Saleheen D, Schafmayer C, Soininen P, Tai ES, Thorand B, Tuomilehto J, Wickremasinghe AR, Kyrtopoulos SA, Aitman TJ, Herder C, Hampe J, Cauchi S, Relton CL, Froguel P, Soong R, Vineis P, Jarvelin M-R, Scott J, Grallert H, Bollati V, Elliott P, McCarthy MI, Kooner JS (2015). Epigenome-wide association of DNA methylation markers in peripheral blood from Indian Asians and Europeans with incident type 2 diabetes: a nested case-control study. *The Lancet Diabetes & Endocrinology* 3(7):526-534.

Chandran M, Phillips SA, Ciaraldi T, Henry RR (2003). Adiponectin: more than just another fat cell hormone? *Diabetes Care* 26(8):2442-2450.

Chapman S.E. ODV, Mclaughlin W., Proctor S., Leevy M (2011). Dual energy X-ray method for direct visualization and quantitative measurement of peripheral adipose in small animals, Application Note, BRUKER.

Chengalvala MV, Bapat AR, Hurlburt WW, Kostek B, Gonder DS, Mastroeni RA, Frail DE (2001). Biochemical characterization of osteo-testicular protein tyrosine phosphatase and its functional significance in rat primary osteoblasts. *Biochemistry* 40(3):814-821.

Chenu C, Colucci S, Grano M, Zigrino P, Barattolo R, Zambonin G, Baldini N, Vergnaud P, Delmas PD, Zallone AZ (1994). Osteocalcin induces chemotaxis, secretion of matrix proteins, and calcium-mediated intracellular signaling in human osteoclast-like cells. *Journal of Cell Biology* 127(4):1149-1158.

Clelland N. BL, McLean K.A., Knott S., Lambe N.R., (2013). Prediction of intramuscular fat in Texel lamb loins using spiral x-ray computed tomography (CT) scanning. Proceedings of the Farm Animal Imaging Conference (29-30 October 2013, Kaposvár, Hungary).

Clemens TL, Karsenty G (2011). The osteoblast: an insulin target cell controlling glucose homeostasis. *Journal of Bone and Mineral Research* 26(4):677-680.

Confavreux C, Borel O, Lee F, Vaz G, Guyard M, Fadat C, Carlier M-C, Chapurlat R, Karsenty G (2012). Osteoid osteoma is an osteocalcinoma affecting glucose metabolism. *Osteoporosis International* 23(5):1645-1650.

Confavreux CB, Levine RL, Karsenty G (2009). A paradigm of integrative physiology, the crosstalk between bone and energy metabolisms. *Molecular and Cellular Endocrinology* 310(1-2):21-29.

Covey SD, Wideman RD, McDonald C, Unniappan S, Huynh F, Asadi A, Speck M, Webber T, Chua SC, Kieffer TJ (2006). The pancreatic beta cell is a key site for mediating the effects of leptin on glucose homeostasis. *Cell Metabolism* 4(4):291-302.

Cramer CL, Davis RH (1984). Polyphosphate-cation interaction in the amino acid-containing vacuole of Neurospora crassa. *Journal of Cell Biology* 259(8):5152-5157.

Dacquin R, Mee PJ, Kawaguchi J, Olmsted-Davis EA, Gallagher JA, Nichols J, Lee K, Karsenty G, Smith A (2004). Knock-in of nuclear localised beta-galactosidase reveals that the tyrosine phosphatase Ptprv is specifically expressed in cells of the bone collar. *Developmental Dynamic* 229(4):826-834.

Dallas SL, Bonewald LF (2010). Dynamics of the transition from osteoblast to osteocyte. *Annals of the New York Academy of Sciences* 1192:437-443.

David V, Martin A, Hedge AM, Rowe PS (2009a). Matrix extracellular phosphoglycoprotein (MEPE) is a new bone renal hormone and vascularization modulator. *Endocrinology* 150(9):4012-4023.

David V, Martin A, Hedge AM, Rowe PS (2009b). PHEX & MEPE ASARM motif regulate a novel bone–renal and fat-mass pathway. *Journal of Bone and Mineral Research* 24 (Suppl) Abstract MO0094.

David V, Martin AC, Hedge AM, Drezner MK, Rowe PS (2011). ASARM peptides: PHEX-dependent and independent regulation of serum phosphate. *American Journal of Physiology* 300(3):783-791.

Delany AM, Amling M, Priemel M, Howe C, Baron R, Canalis E (2000). Osteopenia and decreased bone formation in osteonectin-deficient mice. *Journal of Clinical Investigation* 105(9):1325.

Delany AM, Kalajzic I, Bradshaw AD, Sage EH, Canalis E (2003). Osteonectin-null mutation compromises osteoblast formation, maturation, and survival. *Endocrinology* 144(6):2588-2596.

Deschaseaux F, Sensebe L, Heymann D (2009). Mechanisms of bone repair and regeneration. *Trends in Molecular Medicine* 15(9):417-429.

Di Gregorio GB, Yao-Borengasser A, Rasouli N, Varma V, Lu T, Miles LM, Ranganathan G, Peterson CA, McGehee RE, Kern PA (2005). Expression of CD68 and macrophage chemoattractant protein-1 genes in human adipose and muscle tissues: association with cytokine expression, insulin resistance, and reduction by pioglitazone. *Diabetes* 54(8):2305-2313.

Doria A, Patti ME, Kahn CR (2008). The emerging genetic architecture of type 2 diabetes. *Cell Metabolism* 8(3):186-200.

Doucette CR, Rosen CJ (2014). Current protocols in mouse biology. *Current Protocols in Mouse Biology.*

Doucette CR, Horowitz MC, Berry R, MacDougald OA, Anunciado-Koza R, Koza RA, Rosen CJ (2015). A High Fat Diet Increases Bone Marrow Adipose Tissue (MAT) But Does Not Alter Trabecular or Cortical Bone Mass in C57BL/6J Mice. *Journal of Cellular Physiology* 230(9):2032-2037.

Ducy P, Desbois C, Boyce B, Pinero G, Story B, Dunstan C, Smith E, Bonadio J, Goldstein S, Gundberg C, Bradley A, Karsenty G (1996). Increased bone formation in osteocalcin-deficient mice. *Nature* 382(6590):448-452.

Ducy P, Amling M, Takeda S, Priemel M, Schilling AF, Beil FT, Shen J, Vinson C, Rueger JM, Karsenty G (2000a). Leptin inhibits bone formation through a hypothalamic relay: a central control of bone mass. *Cell* 100(2):197-207.

Ducy P, Schinke T, Karsenty G (2000b). The osteoblast: a sophisticated fibroblast under central surveillance. *Science* 289(5484):1501-1504.

Ducy P (2011). The role of osteocalcin in the endocrine cross-talk between bone remodelling and energy metabolism. *Diabetologia* 54(6):1291-1297.

Dudley HR, Spiro D (1961). The fine structure of bone. *Journal of Biophysical and Biochemical Cytology* 11(3):627-649.

Dunn T, Gable K, Beeler T (1994). Regulation of cellular Ca2+ by yeast vacuoles. *Journal of Cell Biology* 269(10):7273-7278.

Eaton SL, Roche SL, Llavero Hurtado M, Oldknow KJ, Farquharson C, Gillingwater TH, Wishart TM (2013). Total protein analysis as a reliable loading control for quantitative fluorescent Western blotting. *PLoS One* 8(8):e72457.

Elefteriou F, Ahn JD, Takeda S, Starbuck M, Yang X, Liu X, Kondo H, Richards WG, Bannon TW, Noda M, Clement K, Vaisse C, Karsenty G (2005). Leptin regulation of bone resorption by the sympathetic nervous system and CART. *Nature* 434(7032):514-520.

Engelke JA, Hale JE, Suttie JW, Price PA (1991). Vitamin K-dependent carboxylase: utilization of decarboxylated bone Gla protein and matrix Gla protein as substrates. *Biochimica et Biophysica Acta* 1078(1):31-34.

Farquharson C (2008). Bone growth. In: Biology of Growth of Domestic Animals. USA: 170-185.

Favaro RR, Salgado RM, Covarrubias AC, Bruni F, Lima C, Fortes ZB, Zorn TM (2013). Long-term type 1 diabetes impairs decidualization and extracellular matrix remodeling during early embryonic development in mice. *Placenta* 34(12):1128-1135.

Feng JQ, Zhang J, Dallas SL, Lu Y, Chen S, Tan X, Owen M, Harris SE, Macdougall M (2002). Dentin matrix protein 1, a target molecule for Cbfa1 in bone, Is a Unique Bone Marker Gene. *Journal of Bone and Mineral Research* 17(10):1822-1831.

Feng JQ, Ward LM, Liu SG, Lu YB, Xie YX, Yuan BZ, Yu XJ, Rauch F, Davis SI, Zhang SB, Rios H, Drezner MK, Quarles LD, Bonewald LF, White KE (2006). Loss of DMP1 causes rickets and osteomalacia and identifies a role for osteocytes in mineral metabolism. *Nature Genetics* 38(11):1310-1315.

Ferron M, Hinoi E, Karsenty G, Ducy P (2008). Osteocalcin differentially regulates beta cell and adipocyte gene expression and affects the development of metabolic diseases in wild-type mice. *Proc Natl Acad Sci USA* 105(13):5266-5270.

Ferron M, Wei J, Yoshizawa T, Del Fattore A, DePinho RA, Teti A, Ducy P, Karsenty G (2010a). Insulin signaling in osteoblasts integrates bone remodeling and energy metabolism. *Cell* 142(2):296-308.

Ferron M, Wei J, Yoshizawa T, Ducy P, Karsenty G (2010b). An ELISA-based method to quantify osteocalcin carboxylation in mice. *Biochemical and Biophysical Research Communications* 397(4):691-696.

Ferron M, Lacombe J (2014). Regulation of energy metabolism by the skeleton: osteocalcin and beyond. *Archives of Biochemistry and Biophysics* 561:137-146

Finkelstein EA, Trogdon JG, Cohen JW, Dietz W (2009). Annual medical spending attributable to obesity: payer-and service-specific estimates. *Health Affairs (Millwood)* 28(5):w822-831.

Fleisch H, Schibler D, Maerki J, Frossard I (1965). Inhibition of aortic calcification by means of pyrophosphate and polyphosphates. *Nature* 207(5003):1300-1301.

Fleish H, Neuman WF (1961). Mechanisms of calcification: role of collagen, polyphosphates, and phosphatase. *The American Journal of Physiology* 200:1296-1300.

Flier JS, Elmquist JK (1997). Energetic pursuit of leptin function. *Nature Biotechnology* 15(1):20-21.

Folch J, Lees M, Sloane Stanley GH (1957). A simple method for the isolation and purification of total lipides from animal tissues. *Journal of Cell Biology* 226(1):497-509.

Francis MD (1969). The inhibition of calcium hydroxypatite crystal growth by polyphosphonates and polyphosphates. *Calcified Tissue Research* 3(2):151-162.

Friedman JM, Halaas JL (1998). Leptin and the regulation of body weight in mammals. *Nature* 395(6704):763-770.

Frost HM (1990). Skeletal structural adaptations to mechanical usage (SATMU): 1. Redefining Wolff's law: the bone modeling problem. *The Anatomical Record* 226(4):403-413.

Fulzele K, DiGirolamo DJ, Liu Z, Xu J, Messina JL, Clemens TL (2007). Disruption of the insulin-like growth factor type 1 receptor in osteoblasts enhances insulin signaling and action. *Journal of Cell Biology* 282(35):25649-25658.

Fulzele K, Riddle RC, DiGirolamo DJ, Cao X, Wan C, Chen D, Faugere MC, Aja S, Hussain MA, Bruning JC, Clemens TL (2010). Insulin receptor signaling in osteoblasts regulates postnatal bone acquisition and body composition. *Cell* 142(2):309-319.

Fulzele K, Clemens TL (2012). Novel functions for insulin in bone. *Bone* 50(2):452-456.

Ganss B, Kim RH, Sodek J (1999). Bone sialoprotein. *Critical Reviews* in *Oral Biology* & *Medicine* 10(1):79-98.

Gastaldelli A, Harrison SA, Belfort-Aguilar R, Hardies LJ, Balas B, Schenker S, Cusi K (2009). Importance of changes in adipose tissue insulin resistance to histological response during thiazolidinedione treatment of patients with nonalcoholic steatohepatitis. *Hepatology* 50(4):1087-1093.
Gentili C, Cancedda R (2009). Cartilage and bone extracellular matrix. *Current Pharmaceutical Design* 15(12):1334-1348.

Gilbert SF, Developmental Biology (2006). Developmental Biology 8th Edition.

Ginsburg GS, Atkinson D, Small DM (1984). Physical properties of cholesteryl esters. *Progress in Lipid Research* 23(3):135-167.

Girgis CM, Mokbel N, Minn Cha K, Houweling PJ, Abboud M, Fraser DR, Mason RS, Clifton-Bligh RJ, Gunton JE (2014). The vitamin D receptor (VDR) is expressed in skeletal muscle of male mice and modulates 25-hydroxyvitamin D (25OHD) Uptake in Myofibers. *Endocrinology* 155(9):3227-37.

Glasbey CA, Robinson CD (2002). Estimators of tissue proportions from X-ray CT images. *Biometrics* 58(4):928-936.

Gould GW, Holman GD (1993). The glucose transporter family: structure, function and tissue-specific expression. *The Biochemical Journal* 295(2): 329-341.

Gowen LC, Petersen DN, Mansolf AL, Qi H, Stock JL, Tkalcevic GT, Simmons HA, Crawford DT, Chidsey-Frink KL, Ke HZ, McNeish JD, Brown TA (2003). Targeted disruption of the osteoblast/osteocyte factor 45 gene (OF45) results in increased bone formation and bone mass. *Journal of Cell Biology* 278(3):1998-2007.

Grube B, Chong PW, Lau KZ, Orzechowski HD (2013). A natural fiber complex reduces body weight in the overweight and obese: a double-blind, randomized, placebo-controlled study. *Obesity (Silver Spring)* 21(1):58-64.

Guntur AR, Le PT, Farber CR, Rosen CJ (2014). Bioenergetics during calvarial osteoblast differentiation reflect strain differences in bone mass. *Endocrinology* 155(5):1589-1595.

Hakim FT, Cranley R, Brown KS, Eanes ED, Harne L, Oppenheim JJ (1984). Hereditary joint disorder in progressive ankylosis (ank/ank) mice. I. Association of calcium hydroxyapatite deposition with inflammatory arthropathy. *Arthritis and Rheumatism* 27(12):1411-1420.

Hale JE, Fraser JD, Price PA (1988). The identification of matrix Gla protein in cartilage. *Journal of Cell Biology* 263(12):5820-5824.

Hamilton G, Smith DL, Jr., Bydder M, Nayak KS, Hu HH (2011). MR properties of brown and white adipose tissues. *Journal of Magnetic Resonance Imaging* 34(2):468-473.

Hannemann A, Breer S, Wallaschofski H, Nauck M, Baumeister SE, Barvencik F, Amling M, Schinke T, Haring R, Keller J (2013). Osteocalcin is associated with testosterone in the general population and selected patients with bone disorders. *Andrology* 1(3):469-474.

Harada S, Rodan GA (2003). Control of osteoblast function and regulation of bone mass. *Nature* 423(6937):349-355.

Harder KW, Owen P, Wong LK, Aebersold R, Clark-Lewis I, Jirik FR (1994). Characterization and kinetic analysis of the intracellular domain of human protein tyrosine phosphatase beta (HPTP beta) using synthetic phosphopeptides. *The Biochemical Journal* 298(2):395-401.

Harold FM (1966). Inorganic polyphosphates in biology: structure, metabolism, and function. *Bacteriological Reviews* 30(4):772-794.

Hastings IM, Hill WG (1989). A note on the effect of different selection criteria on carcass composition in mice. *Animal Production* 48:229-233.

Hauschka PV, Lian JB, Gallop PM (1975). Direct identification of the calcium-binding amino acid, gamma-carboxyglutamate, in mineralized tissue. *Proc Natl Acad Sci USA* 72(10):3925-3929.

Hauschka PV, Lian JB, Cole D, Gundberg CM (1989a). Osteocalcin and matrix Gla protein: vitamin K-dependent proteins in bone. *Physiol Reviews* 69(3):990-1047.

Hauschka PV, Lian JB, Cole DE, Gundberg CM (1989b). Osteocalcin and matrix Gla protein: vitamin K-dependent proteins in bone. *Physiol Rev* 69(3):990-1047.

Hayashi S, McMahon AP (2002). Efficient recombination in diverse tissues by a tamoxifen-inducible form of Cre: a tool for temporally regulated gene activation/inactivation in the mouse. *Devlopmental Biolology* 244(2):305-318.

Heinegard D (2009). Proteoglycans and more - from molecules to biology. *International Journal of Clinical and Experimental* Pathology 90(6):575-586.

Hinoi E, Gao N, Jung DY, Yadav V, Yoshizawa T, Myers MG, Jr., Chua SC, Jr., Kim JK, Kaestner KH, Karsenty G (2008). The sympathetic tone mediates leptin's inhibition of insulin secretion by modulating osteocalcin bioactivity. *Journal of Cell Biology* 183(7):1235-1242.

Hoac B, Kiffer-Moreira T, Millán JL, McKee MD (2013). Polyphosphates inhibit extracellular matrix mineralization in MC3T3-E1 osteoblast cultures. *Bone* 53(2):478-486.

Hoebertz A, Mahendran S, Burnstock G, Arnett TR (2002). ATP and UTP at low concentrations strongly inhibit bone formation by osteoblasts: a novel role for the P2Y2 receptor in bone remodeling. *Journal of Cellular Biochemistry* 86(3):413-419.

Holloway WR, Collier FM, Aitken CJ, Myers DE, Hodge JM, Malakellis M, Gough TJ, Collier GR, Nicholson GC (2002). Leptin inhibits osteoclast generation. *Journal of Bone and Mineral Research* 17(2):200-209.

Houston B, Seawright E, Jefferies D, Hoogland E, Lester D, Whitehead C, Farquharson C. (1999). Identification and cloning of a novel phosphatase expressed at high levels in differentiating growth plate chondrocytes. *Biochimica et Biophysica Acta* 1448(3):500-506.

Houston B, Stewart A, CFarquharson (2004). PHOSPHO1-A novel phosphatase specifically expressed at sites of mineralisation in bone and cartilage. *Bone* 34(4):629-637.

Huesa C, Yadav MC, Finnila MA, Goodyear SR, Robins SP, Tanner KE, Aspden RM, Millan JL, Farquharson C (2011). PHOSPHO1 is essential for mechanically competent mineralization and the avoidance of spontaneous fractures. *Bone* 48(5):1066-1074.

Huesa C, Zhu Z, Glover J, Ferron M, Karsenty G, Milne E, Millan J, Ahmed F, Farquharson C, Morton N, MacRae V (2014). Deficiency of the bone mineralization inhibitor NPP1 protects against obesity and diabetes. *Disease Models & Mechanisms* 7(12):1341-1350.

Huh JY, Dincer F, Mesfum E, Mantzoros CS (2014). Irisin stimulates muscle growth-related genes and regulates adipocyte differentiation and metabolism in humans. *International Journal of Obesity (Lond)* 38(12):1538-1544.

Hull P (1960). Genetic relations between carcass fat and body weight in mice. *The Journal of Agricultural Science* 55:317-321.

Hunter GK, Kyle CL, Goldberg HA (1994). Modulation of crystal formation by bone phosphoproteins: structural specificity of the osteopontin-mediated inhibition of hydroxyapatite formation. *The Biochemical Journal* 300(3):723-728.

Hunter T (1995). Protein kinases and phosphatases: the yin and yang of protein phosphorylation and signaling. *Cell* 80(2):225-236.

Hunziker EB, Schenk RK, Cruz-Orive LM (1987). Quantitation of chondrocyte performance in growth-plate cartilage during longitudinal bone growth. *The Journal of Bone and Joint Surgery American Volume* 69(2):162-173.

Hwang YC, Jeong IK, Ahn KJ, Chung HY (2009). The uncarboxylated form of osteocalcin is associated with improved glucose tolerance and enhanced β-cell function in middle-aged male subjects. *Diabetes/Metabolism Research and Reviews* 25(8):768-772.

Javaheri B, Carriero A, Staines KA, Chang YM, Houston DA, Oldknow KJ, Millan JL, Kazeruni BN, Salmon P, Shefelbine S, Farquharson C, Pitsillides AA (2015). Phospho1 deficiency transiently modifies bone architecture yet produces consistent modification in osteocyte differentiation and vascular porosity with ageing. *Bone*. In press.

Jeansson M, Granqvist AB, Nystrom JS, Haraldsson B (2006). Functional and molecular alterations of the glomerular barrier in long-term diabetes in mice. *Diabetologia* 49(9):2200-2209.

Jeyabalan J, Shah M, Viollet B, Chenu C (2012). AMP-activated protein kinase pathway and bone metabolism. *Journal of Endocrinology* 212(3):277-290.

Johnson K, Moffa A, Chen Y, Pritzker K, Goding J, Terkeltaub R (1999). Matrix vesicle plasma cell membrane glycoprotein-1 regulates mineralization by murine osteoblastic MC3T3 cells. *Journal of Bone and Mineral Research* 14(6):883-892.

Johnston SL, Peacock WL, Bell LM, Lonchampt M, Speakman JR (2005). PIXImus DXA with different software needs individual calibration to accurately predict fat mass. *Obesity Research* 13(9):1558-1565.

Joost HG, Thorens B (2001). The extended GLUT-family of sugar/polyol transport facilitators: nomenclature, sequence characteristics, and potential function of its novel members (review). *Molecular Membrane Biology* 18(4):247-256.

Kanasaki K, Koya D (2011). Biology of obesity: lessons from animal models of obesity. *Journal of Biomedicine Biotechnolgy* 197636(10):5.

Kanatani Y, Usui I, Ishizuka K, Bukhari A, Fujisaka S, Urakaze M, Haruta T, Kishimoto T, Naka T, Kobayashi M (2007). Effects of pioglitazone on suppressor of cytokine signaling 3 expression: potential mechanisms for its effects on insulin sensitivity and adiponectin expression. *Diabetes* 56(3):795-803.

Kanazawa I, Tanaka K, Ogawa N, Yamauchi M, Yamaguchi T, Sugimoto T (2013). Undercarboxylated osteocalcin is positively associated with free testosterone in male patients with type 2 diabetes mellitus. *Osteoporosis International* 24(3):1115-1119.

Kang HS, Okamoto K, Takeda Y, Beak JY, Gerrish K, Bortner CD, DeGraff LM, Wada T, Xie W, Jetten AM (2011). Transcriptional profiling reveals a role for RORalpha in regulating gene expression in obesity-associated inflammation and hepatic steatosis. *Physiogical Genomics* 43(13):818-828.

Karsenty G (2006). Convergence between bone and energy homeostases: leptin regulation of bone mass. *Cell Metabolism* 4(5):341-348.

Karsenty G (2012). The mutual dependence between bone and gonads. *Journal of Endocrinology* 213(2):107-114.

Karsenty G, Ferron M (2012). The contribution of bone to whole-organism physiology. *Nature* 481(7381):314-320.

Karsenty G, Oury F (2014). Regulation of male fertility by the bone-derived hormone osteocalcin. *Molecular and Cellular Endocrinology* 382(1):521–526.

Khavandgar Z, Poirier C, Clarke CJ, Li J, Wang N, McKee MD, Hannun YA, Murshed M (2011). A cell-autonomous requirement for neutral sphingomyelinase 2 in bone mineralization. *Journal of Cell Biology* 194(2):277-289.

Khavandgar Z, Alebrahim S, Eimar H, Tamimi F, McKee MD, Murshed M (2013). Local regulation of tooth mineralization by sphingomyelin phosphodiesterase 3. *Journal of Dental Research* 92(4):358-364.

Khavandgar Z, Murshed M (2015). Sphingolipid metabolism and its role in the skeletal tissues. *Cellular and Molecular Life Sciences* 72(5):959-969.

Kiffer-Moreira T, Yadav MC, Zhu D, Narisawa S, Sheen C, Stec B, Cosford ND, Dahl R, Farquharson C, Hoylaerts MF, MacRae VE, Millan JL (2013). Pharmacological inhibition of PHOSPHO1 suppresses vascular smooth muscle cell calcification. *Journal of Bone and Mineral Research* 28(1):81-91.

Kim HR, Roe JS, Lee JE, Cho EJ, Youn HD (2013a). p53 regulates glucose metabolism by miR-34a. *Biochemical and Biophysical Research Communications* 437(2):225-231.

Kim W, Egan JM (2008). The role of incretins in glucose homeostasis and diabetes treatment. *Pharmacological Reviews* 60(4):470-512.

Kim YE, Hipp MS, Bracher A, Hayer-Hartl M, Hartl FU (2013b). Molecular chaperone functions in protein folding and proteostasis. *Annual Review of Biochemistry* 82:323-355.

King MJ, Sale GJ (1990). Dephosphorylation of insulin-receptor autophosphorylation sites by particulate and soluble phosphotyrosyl-protein phosphatases. *The Biochemical Journal* 266(1):251-259.

Kode A, Mosialou I, Silva BC, Joshi S, Ferron M, Rached MT, Kousteni S (2012). FoxO1 protein cooperates with ATF4 protein in osteoblasts to control glucose homeostasis. *Journal of Cell Biology* 287(12):8757-8768.

Kornberg A (1995). Inorganic polyphosphate: toward making a forgotten polymer unforgettable. *Journal Bacteriolgy* 177(3):491-496.

Kornberg A (1999). Inorganic polyphosphate: a molecule of many functions. *Progress in Molecular and Subcellular Biology* 23: 1-18.

Kousteni S (2011). FoxO1: A Molecule for All Seasons. *Journal of Bone and Mineral Research* 26(5):912-917.

Kousteni S (2012). FoxO1, the transcriptional chief of staff of energy metabolism. *Bone* 50(2):437-443.

Kozawa O, Hatakeyama D, Uematsu T (2002). Divergent regulation by p44/p42 MAP kinase and p38 MAP kinase of bone morphogenetic protein-4-stimulated osteocalcin synthesis in osteoblasts. *Journal of Cellular Biochemistry* 84(3):583-589.

Kulaev IS (1975). Biochemistry of inorganic polyphosphates. *Reviews of Physiology, Biochemistry and Pharmacology* 73:131-158.

Kumagai H, Sakamoto H, Guggino S, Filburn CR, Sacktor B (1989). Neurotransmitter regulation of cytosolic calcium in osteoblast-like bone cells. *Calcified Tissue International* 45(4):251-254.

Kumagai H, Sacktor B, Filburn CR (1991). Purinergic regulation of cytosolic calcium and phosphoinositide metabolism in rat osteoblast-like osteosarcoma cells. *Journal of Bone and Mineral Research* 6(7):697-708.

Laakso K, Kinnunen H, Huttunen S (2001). The glutathione status of mature Scots pines during the third season of UV-B radiation exposure. *Environmental Pollution* 111(2):349-354.

Lanyon LE (1993). Osteocytes, strain detection, bone modelling and remodelling. *Calcified Tissue International* 53: S102-106.

Lebrun P, Van Obberghen E (2008). SOCS proteins causing trouble in insulin action. *Acta Physiol (Oxf)* 192(1):29-36.

Lee K, Nichols J, Smith A (1996). Identification of a developmentally regulated protein tyrosine phosphatase in embryonic stem cells that is a marker of pluripotential epiblast and early mesoderm. *Mechanisms of Development* 59(2):153-164.

Lee NK, Sowa H, Hinoi E, Ferron M, Ahn JD, Confavreux C, Dacquin R, Mee PJ, McKee MD, Jung DY, Zhang Z, Kim JK, Mauvais-Jarvis F, Ducy P, Karsenty G (2007). Endocrine regulation of energy metabolism by the skeleton. *Cell* 130(3):456-469.

Leyhausen G, Lorenz B, Zhu H, Geurtsen W, Bohnensack R, Muller WE, Schroder HC (1998). Inorganic polyphosphate in human osteoblast-like cells. *Journal of Bone and Mineral Research* 13(5):803-812.

Ling Y, Rios HF, Myers ER, Lu Y, Feng JQ, Boskey AL (2005). DMP1 depletion decreases bone mineralization *in vivo*: An FTIR imaging analysis. *Journal of Bone and Mineral Research* 20(12):2169-2177.

Liu S, Rowe PS, Vierthaler L, Zhou J, Quarles LD (2007). Phosphorylated acidic serine-aspartate-rich MEPE-associated motif peptide from matrix extracellular phosphoglycoprotein inhibits phosphate regulating gene with homologies to endopeptidases on the X-chromosome enzyme activity. *Journal of Endocrinology* 192(1):261-267.

Ljunggren Ö, Bolinder J, Johansson L, Wilding J, Langkilde AM, Sjöström CD, Sugg J, Parikh S (2012). Dapagliflozin has no effect on markers of bone formation and resorption or bone mineral density in patients with inadequately controlled type 2 diabetes mellitus on metformin. *Diabetes, Obesity and Metabolism* 14(11):990-999.

Lorenz B, Batel R, Bachinski N, Muller WE, Schroder HC (1995). Purification and characterization of two exopolyphosphatases from the marine sponge Tethya lyncurium. *Biochimica et biophysica acta* 1245(1):17-28.

Lorenz B, Munkner J, Oliveira MP, Kuusksalu A, Leitao JM, Muller WE, Schroder HC (1997). Changes in metabolism of inorganic polyphosphate in rat tissues and human cells during development and apoptosis. *Biochimica et biophysica acta* 1335(1-2):51-60.

Luo G, Ducy P, McKee MD, Pinero GJ, Loyer E, Behringer RR, Karsenty G (1997). Spontaneous calcification of arteries and cartilage in mice lacking matrix GLA protein. *Nature* 386(6620):78-81.

Luu YK, Lublinsky S, Ozcivici E, Capilla E, Pessin JE, Rubin CT, Judex S (2009). In vivo quantification of subcutaneous and visceral adiposity by micro-computed tomography in a small animal model. *Medical Engineering & Physics* 31(1):34-41.

Lyons MK (2013). Molecular, cellular, and genetic determinants of bone structure and formation. In: Primer on the Metabolic Bone Diseases and Disorders of Mineral Metabolism: John Wiley & Sons, Inc 1-2.

MacDougall M, Simmons D, Luan X, Nydegger J, Feng J, Gu TT (1997). Dentin phosphoprotein and dentin sialoprotein are cleavage products expressed from a single transcript coded by a gene on human chromosome 4. Dentin phosphoprotein DNA sequence determination. *Journal of Cell Biology* 272(2):835-842.

Mackenzie NC, Zhu D, Milne EM, van 't Hof R, Martin A, Darryl Quarles L, Millan JL, Farquharson C, MacRae VE (2012a). Altered bone development and an increase in FGF-23 expression in Enpp1(-/-) mice. *PLoS One* 7(2):e32177.

Mackenzie NCW, Huesa C, Rutsch F, MacRae VE (2012b). New insights into NPP1 function: Lessons from clinical and animal studies. *Bone* 51(5):961-968.

MacRae VE, Burdon T, Ahmed SF, Farquharson C (2006). Ceramide inhibition of chondrocyte proliferation and bone growth is IGF-I independent. *Journal of Endocrinology* 191(2):369-377.

MacRae VE DM, McTeir L, Narisawa S, Yadav MC, Millan JL, Farquharson C. (2010). Inhibition of PHOSPHO1 activity results in impaired skeletal mineralization during limb development of the chick. *Bone* 46(4):1146-1155.

Mahlberg FH, Glick JM, Jerome WG, Rothblat GH (1990). Metabolism of cholesteryl ester lipid droplets in a J774 macrophage foam cell model. *Biochimica et Biophysica acta* 1045(3):291-298.

Malaval L, Wade-Guéye NM, Boudiffa M, Fei J, Zirngibl R, Chen F, Laroche N, Roux J-P, Burt-Pichat B, Duboeuf F, Boivin G, Jurdic P, Lafage-Proust M-H, Amédée J, Vico L, Rossant J, Aubin JE (2008). Bone sialoprotein plays a functional role in bone formation and osteoclastogenesis. *The Journal of Experimental Medicine* 205(5):1145-1153.

Maloney SK, Fuller A, Mitchell D, Gordon C, Overton JM (2014). Translating animal model research: does it matter that our rodents are cold? *Physiology* 29(6):413-420.

Manolagas SC (2000). Birth and death of bone cells: basic regulatory mechanisms and implications for the pathogenesis and treatment of osteoporosis. *Endocrine Reviews* 21(2):115-137.

Martin A, David V, Laurence JS, Schwarz PM, Lafer EM, Hedge AM, Rowe PS (2008). Degradation of MEPE, DMP1, and release of SIBLING ASARM-peptides (minhibins): ASARM-peptide(s) are directly responsible for defective mineralization in HYP. *Endocrinology* 149(4):1757-1772.

Martin B, Pallen CJ, Wang JH, Graves DJ (1985). Use of fluorinated tyrosine phosphates to probe the substrate specificity of the low molecular weight phosphatase activity of calcineurin. *Journal of Cell Biology* 260(28):14932-14937.

Mauro LJ, Olmsted EA, Skrobacz BM, Mourey RJ, Davis AR, Dixon JE (1994). Identification of a hormonally regulated protein tyrosine phosphatase associated with bone and testicular differentiation. *Journal of Cell Biology* 269(48):30659-30667.

McKee MD, Yadav MC, Foster BL, Somerman MJ, Farquharson C, Millan JL (2013). Compounded PHOSPHO1/ALPL deficiencies reduce dentin mineralization. *Journal of Dental Research* 92(8):721-727.

Medicherla B, Goldberg AL (2008). Heat shock and oxygen radicals stimulate ubiquitin-dependent degradation mainly of newly synthesized proteins. *Journal of Cell Biology* 182(4):663-673.

Millan JL (2006). Alkaline Phosphatases: Structure, substrate specificity and functional relatedness to other members of a large superfamily of enzymes. *Purinergic Signal* 2(2):335-341.

Millan JL (2013). The role of phosphatases in the initiation of skeletal mineralization. *Calcified Tissue International* 93(4):299-306.

Mishima S, Nagai A, Abdullah S, Matsuda C, Taketani T, Kumakura S, Shibata H, Ishikura H, Kim SU, Masuda J (2010). Effective ex vivo expansion of hematopoietic stem cells using osteoblast-differentiated mesenchymal stem cells is CXCL12 dependent. *European Journal of Haematology* 84(6):538-546.

Mohammad Hafiz U, Takuya M, Masayuki O, Atsushi N, Taiji S (2010). Biomimetic fabrication of apatite related biomaterials. *ISBN 978-953-307-025-4.*

Morris DC, Masuhara K, Takaoka K, Ono K, Anderson HC (1992). Immunolocalization of alkaline phosphatase in osteoblasts and matrix vesicles of human fetal bone. *Bone and Mineral* 19(3):287-298.

Morrison MS, Turin L, King BF, Burnstock G, Arnett TR (1998). ATP is a potent stimulator of the activation and formation of rodent osteoclasts. *The Journal of Physiology* 511 (Pt 2):495-500.

Mueckler M, Thorens B (2013). The SLC2 (GLUT) family of membrane transporters. *Molecular Aspects* of *Medicine* 34(2-3):121-138.

Munroe PB, Olgunturk RO, Fryns JP, Van Maldergem L, Ziereisen F, Yuksel B, Gardiner RM, Chung E (1999). Mutations in the gene encoding the human matrix Gla protein cause Keutel syndrome. *Nature Genetics* 21(1):142-144.

Murshed M, Schinke T, McKee MD, Karsenty G (2004). Extracellular matrix mineralization is regulated locally; different roles of two gla-containing proteins. *Journal of Cell Biology* 165(5):625-630.

Myers MG, Backer JM, Siddle K, White MF (1991). The InsR functions normally in Chinese hamster ovary cells after truncation of the C terminus. *Journal of Cell Biology* 266(16):10616-10623.

Nakashima T, Hayashi M, Fukunaga T, Kurata K, Oh-Hora M, Feng JQ, Bonewald LF, Kodama T, Wutz A, Wagner EF, Penninger JM, Takayanagi H (2011). Evidence for osteocyte regulation of bone homeostasis through RANKL expression. *Nature Medicine* 17(10):1231-1234.

Nakatani Y, Kaneto H, Kawamori D, Hatazaki M, Miyatsuka T, Matsuoka TA, Kajimoto Y, Matsuhisa M, Yamasaki Y, Hori M (2004). Modulation of the JNK pathway in liver affects insulin resistance status. *Journal of Cell Biology* 279(44):45803-45809.

Nampei A, Hashimoto J, Hayashida K, Tsuboi H, Shi K, Tsuji I, Miyashita H, Yamada T, Matsukawa N, Matsumoto M, Morimoto S, Ogihara T, Ochi T, Yoshikawa H (2004). Matrix extracellular phosphoglycoprotein (MEPE) is highly expressed in osteocytes in human bone. *Journal of Bone and Mineral Metabolism* 22(3):176-184.

Newman B, Gigout LI, Sudre L, Grant ME, Wallis GA (2001). Coordinated expression of matrix Gla protein is required during endochondral ossification for chondrocyte survival. *Journal of Cell Biology* 154(3):659-666.

Ng KW (2011). Regulation of glucose metabolism and the skeleton. *Clinical Endocrinology (Oxf)* 75(2):147-155.

NHS (2014). Obesity – Treatment: http://www.nhs.uk/Conditions/Obesity/Pages/Treatment.aspx. Accessed 04/08/2015

Oldknow K, Morton N, Yadav M, Rajoanah S, Huesa C, Bunger L, Ball D, Ferron M, Karsenty G, MacRae V, Millán J, C Farquharson. (2013). PHOSPHO1: Recognition of roles beyond skeletal mineralization. *Journal of Bone and Mineral* 28 (Meeting Abstract: 1041).

Oldknow KJ, MacRae VE, Farquharson C (2015). The endocrine role of bone: recent and emerging perspectives beyond osteocalcin. *Journal of Endocrinology* 225(1):R1-19.

Orriss IR, Utting JC, Brandao-Burch A, Colston K, Grubb BR, Burnstock G, Arnett TR (2007). Extracellular nucleotides block bone mineralization in vitro: evidence for dual inhibitory mechanisms involving both P2Y2 receptors and pyrophosphate. *Endocrinology* 148(9):4208-4216.

Orriss IR, Burnstock G, Arnett TR (2010). Purinergic signalling and bone remodelling. *Current Opinion in Pharmacology* 10(3):322-330.

Orriss IR, Key ML, Brandao-Burch A, Patel JJ, Burnstock G, Arnett TR (2012). The regulation of osteoblast function and bone mineralisation by extracellular nucleotides: The role of p2x receptors. *Bone* 51(3):389-400.

Oury F, Karsenty G (2011). Towards a serotonin-dependent leptin roadmap in the brain. *Trends in Endocrinology & Metabolism* 22(9):382-387.

Oury F, Sumara G, Sumara O, Ferron M, Chang H, Smith CE, Hermo L, Suarez S, Roth BL, Ducy P, Karsenty G (2011). Endocrine regulation of male fertility by the skeleton. *Cell* 144(5):796-809.

Oury F, Ferron M, Wang HZ, Confavreux C, Xu L, Lacombe J, Srinivas P, Chamouni A, Lugani F, Lejeune H, Kumar TR, Plotton I, Karsenty G (2013). Osteocalcin regulates murine and human fertility through a pancreas-bone-testis axis. *Journal of Clinical Investigation* 123(6):2421-2433.

Patsch JM, Kiefer FW, Varga P, Pail P, Rauner M, Stupphann D, Resch H, Moser D, Zysset PK, Stulnig TM, Pietschmann P (2011). Increased bone resorption and impaired bone microarchitecture in short-term and extended high-fat diet-induced obesity. *Metabolism* 60(2):243-249.

Peng XG, Ju S, Fang F, Wang Y, Fang K, Cui X, Liu G, Li P, Mao H, Teng GJ (2013). Comparison of brown and white adipose tissue fat fractions in ob, seipin, and Fsp27 gene knockout mice by chemical shift-selective imaging and (1)H-MR spectroscopy. *American Journal of Physiology Endocrinology and Metabolism* 304(2):13.

Petersen DN, Tkalcevic GT, Mansolf AL, Rivera-Gonzalez R, Brown TA (2000). Identification of osteoblast/osteocyte factor 45 (OF45), a bone-specific cDNA encoding an RGD-containing protein that is highly expressed in osteoblasts and osteocytes. *Journal of Cell Biology* 275(46):36172-36180.

Pi M, Chen L, Huang MZ, Zhu W, Ringhofer B, Luo J, Christenson L, Li B, Zhang J, Jackson PD, Faber P, Brunden KR, Harrington JJ, Quarles LD (2008). GPRC6A null mice exhibit osteopenia, feminization and metabolic syndrome. *PLoS One* 3(12):e3858.

Pi M, Zhang L, Lei SF, Huang MZ, Zhu W, Zhang J, Shen H, Deng HW, Quarles LD (2010). Impaired osteoblast function in GPRC6A null mice. *Journal of Bone and Mineral Research* 25(5):1092-1102.

Pi M, Wu Y, Quarles LD (2011). GPRC6A mediates responses to osteocalcin in beta-cells in vitro and pancreas in vivo. *Journal of Bone and Mineral Research* 26(7):1680-1683.

Plantalech L, Guillaumont M, Vergnaud P, Leclercq M, Delmas PD (1991). Impairment of gamma carboxylation of circulating osteocalcin (bone gla protein) in elderly women. *Journal of Bone and Mineral Research* 6(11):1211-1216.

Pollock NK, Bernard PJ, Gower BA, Gundberg CM, Wenger K, Misra S, Bassali RW, Davis CL (2011). Lower Uncarboxylated Osteocalcin Concentrations in Children with Prediabetes Is Associated with β-Cell Function. *The Journal of Clinical Endocrinology & Metabolism* 96(7):E1092-E1099.

Prats-Puig A, Mas-Parareda M, Riera-Perez E, Gonzalez-Forcadell D, Mier C, Mallol-Guisset M, Diaz M, Bassols J, de Zegher F, Ibanez L, Lopez-Bermejo A (2010). Carboxylation of osteocalcin affects its association with metabolic parameters in healthy children. *Diabetes Care* 33(3):661-663.

Price PA, Otsuka AA, Poser JW, Kristaponis J, Raman N (1976). Characterization of a gamma-carboxyglutamic acid-containing protein from bone. *Proc Natl Acad Sci USA* 73(5):1447-1451.

Price PA, Williamson MK (1985). Primary structure of bovine matrix Gla protein, a new vitamin K-dependent bone protein. *Journal of Cell Biology* 260(28):14971-14975.

Rached MT, Kode A, Silva BC, Jung DY, Gray S, Ong H, Paik JH, DePinho RA, Kim JK, Karsenty G, Kousteni S (2010). FoxO1 expression in osteoblasts regulates glucose homeostasis through regulation of osteocalcin in mice. *Journal of Clinical Investigation* 120(1):357-368.

Rampersad M., Bünger L (2005). Developing a method to predict body composition in mice using computerised tomography. Proceedings of the Annual BSAS Meeting (4-6 April 2005, York, UK).

Raouf A, Ganss B, McMahon C, Vary C, Roughley PJ, Seth A (2002). Lumican is a major proteoglycan component of the bone matrix. *Matrix Biology* 21(4):361-367.

Rasch D HG, Bock J and Busch K (1978a). Verfahrensbibliothek versuchsplanung und -auswertung - Band 1. Berlin.: VEB Deutscher Landwirtschaftsverlag.

Rasch D HG, Bock J and Busch K (1978b). Verfahrensbibliothek versuchsplanung und -auswertung - Band 2. Berlin: VEB Deutscher Landwirtschaftsverlag.

Ratziu V, Goodman Z, Sanyal A (2015). Current efforts and trends in the treatment of NASH. *Journal of Hepatology* 62(1S):S65-S75.

Raynal C, Delmas PD, Chenu C (1996). Bone sialoprotein stimulates in vitro bone resorption. *Endocrinology* 137(6):2347-2354.

Redinger RN (2007). The pathophysiology of obesity and its clinical manifestations. *Journal of Gastroenterology and Hepatology* 3(11):856-863.

Reimer WJ, Dixon SJ (1992). Extracellular nucleotides elevate [Ca2+]i in rat osteoblastic cells by interaction with two receptor subtypes. *The American Journal of Physiology* 263(1):C1040-1048.

Reynolds D.S. KTH (2001). Body Composition Analysis of Animals A Handbook of Non-Destructive Methods. Cambrdge: Cambridge University Press.

Richard D, Picard F (2011). Brown fat biology and thermogenesis. *Frontiers in Bioscience (Landmark Ed)* 16:1233-1260.

Ridgman WJ (1988). Animal and human calorimetry. *The Journal of Agricultural Science* 111(01):204-204.

Riggs BL, Wahner HW, Seeman E, Offord KP, Dunn WL, Mazess RB, Johnson KA, Melton LJ, 3rd (1982). Changes in bone mineral density of the proximal femur and spine with aging. Differences between the postmenopausal and senile osteoporosis syndromes. *Journal of Clinical Investigation* 70(4):716-723.

Riggs BL, Khosla S, Melton LJ, 3rd (1998). A unitary model for involutional osteoporosis: estrogen deficiency causes both type I and type II osteoporosis in postmenopausal women and contributes to bone loss in aging men. *Journal of Bone and Mineral Research* 13(5):763-773.

Roberts SJ, Stewart AJ, Sadler PJ, Farquharson C. (2004). Human PHOSPHO1 exhibits high specific phosphoethanolamine and P-Cho phosphatase activities. *The Biochemical journal* 382(Pt 1):59-65.

Roberts SJ, Narisawa S, Harmey D, Millan J, Farquharson C (2007). Functional involvement of PHOSPHO1 in matrix vesicle-mediated skeletal mineralization. *Journal of Bone and Mineral Research* 22(4):617-627.

Roberts SJ, Farquharson C. (2008). Identification of a novel splice variant of the haloacid dehalogenase: PHOSPHO1. *Biochemical and Biophysical Research Communications* 371(4):872-876.

Rodan GA, Martin TJ (2000). Therapeutic approaches to bone diseases. *Science* 289(5484):1508-1514.

Rodriguez-Florez N, Garcia-Tunon E, Mukadam Q, Saiz E, Oldknow KJ, Farquharson C, Millán JL, Boyde A, Shefelbine SJ (2015). An investigation of the mineral in ductile and brittle cortical mouse bone. *Journal of Bone and Mineral Research* 30(5):786-795.

Rogers P, Webb GP (1980). Estimation of body fat in normal and obese mice. *British Journal of Nutrition* 43(1):83-86.

Romeo S, Kozlitina J, Xing C, Pertsemlidis A, Cox D, Pennacchio LA, Boerwinkle E, Cohen JC, Hobbs HH (2008). Genetic variation in PNPLA3 confers susceptibility to nonalcoholic fatty liver disease. *Nature Genetics* 40(12):1461-1465.

Romero D, O'Neill C, Terzic A, Contois L, Young K, Conley BA, Bergan RC, Brooks PC, Vary CP (2011). Endoglin regulates cancer-stromal cell interactions in prostate tumors. *Cancer Research* 71(10):3482-3493.

Rosato MT, Schneider SH, Shapses SA (1998). Bone turnover and insulin-like growth factor I levels increase after improved glycemic control in noninsulin-dependent diabetes mellitus. *Calcified Tissue International* 63(2):107-111.

Rosen C, Motyl K (2010). No bones about it: insulin modulates skeletal remodeling. *Cell* 142(2).

Rottiers V, Naar AM (2012). MicroRNAs in metabolism and metabolic disorders. *Nature Reviews Molecular Cell Biology* 13(4):239-250.

Rowe PSN, Goulding JN, Francis F, Oudet C, Econs MJ, Hanauer A, Lehrach H, Read AP, Mountford RC, Summerfield, Weissenbach J, Fraser W, Drenzer MK, Davies KE, O'Riordan JL (1996). The gene for X-linked hypophosphataemic rickets maps to a 200–300 kb region in Xp22.1, and is located on a single YAC containing a putative vitamin D response element (VDRE). *Human Genetics* 97(3):345-352.

Sales V, Patti M-E (2013). The Ups and Downs of Insulin Resistance and Type 2 Diabetes: Lessons from Genomic Analyses in Humans. *Current Cardiovascular Risk Reports* 7(1):46-59.

Samuelson DA (2007). Textbook of Veterinary Histology: Saunders-Elsevier.

Schilling AF, Schinke T, Munch C, Gebauer M, Niemeier A, Priemel M, Streichert T, Rueger JM, Amling M (2005). Increased bone formation in mice lacking apolipoprotein E. *Journal of Bone and Mineral Research* 20(2):274-282.

Schlessinger J (2000). Cell signaling by receptor tyrosine kinases. *Cell* 103(2):211-225.

Schroder HC, Kurz L, Muller WE, Lorenz B (2000). Polyphosphate in bone. *Biochemistry (Mosc)* 65(3):296-303.

Schubert U, Anton LC, Gibbs J, Norbury CC, Yewdell JW, Bennink JR (2000). Rapid degradation of a large fraction of newly synthesized proteins by proteasomes. *Nature* 404(6779):770-774.

Schulz TJ, Tseng YH (2009). Emerging role of bone morphogenetic proteins in adipogenesis and energy metabolism. *Cytokine Growth Factor Reviews* 20(5-6):523-531.

Seeman E (2009). Bone modelling and remodelling. *Critical Reviews in Eukaryotic Gene Expression* 19(3):219-233.

Sharp GL, Hill WG, Robertson A (1984). Effects of selection on growth, body composition and food intake in mice. *Genetics Research* 43(1): 75-92.

Shea MK, Gundberg CM, Meigs JB, Dallal GE, Saltzman E, Yoshida M, Jacques PF, Booth SL (2009). Gamma-carboxylation of osteocalcin and insulin resistance in older men and women. *American Journal of Clinical Nutrition* 90(5):1230-1235.

Shirley DG, Faria NJ, Unwin RJ, Dobbie H (2010). Direct micropuncture evidence that matrix extracellular phosphoglycoprotein inhibits proximal tubular phosphate reabsorption. *Nephrology Dialysis Transplantation* 25(10):3191-3195.

Shum L, Nuckolls G (2002). The life cycle of chondrocytes in the developing skeleton. *Arthritis Research* 4(2):94-106.

Simons B, Kauhanen D, Sylvanne T, Tarasov K, Duchoslav E, Ekroos K (2012). Shotgun lipidomics by sequential precursor ion fragmentation on a hybrid quadrupole time-of-flight mass spectrometer. *Metabolites* 2(1):195-213.

Skurk T, Alberti-Huber C, Herder C, Hauner H (2007). Relationship between Adipocyte Size and Adipokine Expression and Secretion. *The Journal of Clinical Endocrinology & Metabolism* 92(3):1023-1033.

Soden JS, Devereaux MW, Haas JE, Gumpricht E, Dahl R, Gralla J, Traber MG, Sokol RJ (2007). Subcutaneous vitamin E ameliorates liver injury in an in vivo model of steatocholestasis. *Hepatology* 46(2):485-495.

Somani R, Richardson VR, Standeven KF, Grant PJ, Carter AM (2012). Elevated properdin and enhanced complement activation in first-degree relatives of South Asian subjects with type 2 diabetes. *Diabetes Care* 35(4):894-899.

Sommerfeldt DW, Rubin CT (2001). Biology of bone and how it orchestrates the form and function of the skeleton. *European Spine Journal* 10(S2):86-95.

Staines KA, MacRae VE, Farquharson C (2012). The importance of the SIBLING family of proteins on skeletal mineralisation and bone remodelling. *Journal of Endocrinology* 214(3):241-255.

Stefan C, Jansen S, Bollen M (2005). NPP-type ectophosphodiesterases: unity in diversity. *Trends in Biochemical Sciences* 30(10):542-550.

Stevens G, Mascarenhas M, Mathers C (2009). Global health risks: progress and challenges. *Bulletin of the World Health Organization* 87(9):646-646.

Stevenson KT, van Tets IG (2008). Dual-energy X-ray absorptiometry (DXA) can accurately and nondestructively measure the body composition of small, free-living rodents. *Physiological and Biochemical Zoology* 81(3):373-382.

Stewart AJ, Roberts S, Blindauer CA, Paisey SJ, Farquharson C. (2003). Comparative modelling of human PHOSPHO1 reveals a new group of phosphatases within the haloacid dehalogenase superfamily. *Protein Engineering* 16(12):889-895.

Stewart AJ, Roberts S, Seawright E, Davey M, Fleming R, Farquharson C (2006). The presence of PHOSPHO1 in matrix vesicles and its developmental expression prior to skeletal mineralization. *Bone* 39(5):1000-1007.

Stoffel W, Jenke B, Block B, Zumbansen M, Koebke J (2005). Neutral sphingomyelinase 2 (smpd3) in the control of postnatal growth and development. *Proc Natl Acad Sci USA* 102(12):4554-4559.

Stohn JP, Wang Q, Siviski ME, Kennedy K, Jin Y-R, Kacer D, DeMambro V, Liaw L, Vary CP, Rosen CJ, Prudovsky I, Lindner V (2015). Cthrc1 controls adipose tissue formation, body composition, and physical activity. *Obesity* 23(8):1633-1642.

Tabak AG, Jokela M, Akbaraly TN, Brunner EJ, Kivimaki M, Witte DR (2009). Trajectories of glycaemia, insulin sensitivity, and insulin secretion before diagnosis of type 2 diabetes: an analysis from the Whitehall II study. *Lancet* 373(9682):2215-2221.

Takahashi M, Takahashi Y, Takahashi K, Zolotaryov FN, Hong KS, Iida K, Okimura Y, Kaji H, Chihara K (2007). CXCL14 enhances insulin-dependent glucose uptake in adipocytes and is related to high-fat diet-induced obesity. *Biochemical and Biophysical Research Communications* 364(4):1037-1042.

Takeda H, Ozaki K, Yasuda H, Ishida M, Kitano S, Hanazawa S (1998). Sphingomyelinase and ceramide inhibit formation of F-actin ring in and bone resorption by rabbit mature osteoclasts. *FEBS Letters* 422(2):255-258.

Takata Y, Webster NJ, Olefsky JM (1991). Mutation of the two carboxyl-terminal tyrosines results in an insulin receptor with normal metabolic signaling but enhanced mitogenic signaling properties. *Journal of Cell Biology* 266(14):9135-9139.

Tang S, Zhang R, Yu W, Jiang F, Wang J, Chen M, Peng D, Yan J, Bao Y, Jia W (2013). Association of genetic variants of BMP4 with type 2 diabetes mellitus and clinical traits in a Chinese Han population. *BioMed Research International* 238150.

Teitelbaum SL (2000). Osteoclasts, integrins, and osteoporosis. *Journal of Bone and Mineral Metabolism* 18(6):344-349.

Terkeltaub RA (2001). Inorganic pyrophosphate generation and disposition in pathophysiology. *American journal of cell physiology* 281(1):C1-C11

Teitelbaum SL, Ross FP (2003). Genetic regulation of osteoclast development and function. *Nature Reviews Genetics* 4(8):638-649.

Terkeltaub R (2006). Physiologic and pathologic functions of the NPP nucleotide pyrophosphatase/phosphodiesterase family focusing on NPP1 in calcification. *Purinergic Signal* 2(2):371-377.

Termine JD, Kleinman HK, Whitson SW, Conn KM, McGarvey ML, Martin GR (1981). Osteonectin, a bone-specific protein linking mineral to collagen. *Cell* 26(1):99-105.

Thrailkill KM, Jo CH, Cockrell GE, Moreau CS, Lumpkin CK, Jr., Fowlkes JL (2012). Determinants of undercarboxylated and carboxylated osteocalcin concentrations in type 1 diabetes. *Osteoporosis International* 23(6):1799-1806.

Tonks NK (2006). Protein tyrosine phosphatases: from genes, to function, to disease. *Nature Reviews Molecular Cell Biology* 7(11):833-846.

Toyosawa S, Shintani S, Fujiwara T, Ooshima T, Sato A, Ijuhin N, Komori T (2001). Dentin matrix protein 1 is predominantly expressed in chicken and rat osteocytes but not in osteoblasts. *Journal of Bone and Mineral Research* 16(11):2017-2026.

Ueki K, Kondo T, Tseng YH, Kahn CR (2004). Central role of suppressors of cytokine signaling proteins in hepatic steatosis, insulin resistance, and the metabolic syndrome in the mouse. *Proc Natl Acad Sci U S A* 101(28):10422-10427.

Vabulas RM, Hartl FU (2005). Protein synthesis upon acute nutrient restriction relies on proteasome function. *Science* 310(5756):1960-1963.

Vaingankar SM, Fitzpatrick TA, Johnson K, Goding JW, Maurice M, Terkeltaub R (2004). Subcellular targeting and function of osteoblast nucleotide pyrophosphatase phosphodiesterase 1. *American Journal of Cell Physiology* 286(5):C1177-1187.

Verdelis K, Ling Y, Sreenath T, Haruyama N, MacDougall M, van der Meulen MC, Lukashova L, Spevak L, Kulkarni AB, Boskey AL (2008). DSPP effects on in vivo bone mineralization. *Bone* 43(6):983-990.

Vergnaud P, Garnero P, Meunier PJ, Breart G, Kamihagi K, Delmas PD (1997). Undercarboxylated osteocalcin measured with a specific immunoassay predicts hip fracture in elderly women: the EPIDOS Study. *Journal of Clinical Endocrinology and Metabolism* 82(3):719-724.

Wainwright SD, Bondeson J, Caterson B, Hughes CE (2013). ADAMTS-4_v1 is a splice variant of ADAMTS-4 that is expressed as a protein in human synovium and cleaves aggrecan at the interglobular domain. *Arthritis & Rheumatology* 65(11):2866-2875.

Wami WM, Buntinx F, Bartholomeeusen S, Goderis G, Mathieu C, Aerts M (2013). Influence of chronic comorbidity and medication on the efficacy of treatment in patients with diabetes in general practice. *The British Journal of General Practice* 63(609):e267-e273.

Wang CW, Lin HY, Shin SJ, Yu ML, Lin ZY, Dai CY, Huang JF, Chen SC, Li SS, Chuang WL (2011). The PNPLA3 I148M polymorphism is associated with insulin resistance and nonalcoholic fatty liver disease in a normoglycaemic population. *Liver International* 31(9):1326-1331.

Wang F, Canadeo LA, Huibregtse JM (2015). Ubiquitination of newly synthesized proteins at the ribosome. *Biochimie* 114:127-133.

Wang L, Foster BL, Kram V, Nociti FH, Jr., Zerfas PM, Tran AB, Young MF, Somerman MJ (2014). Fibromodulin and Biglycan Modulate Periodontium through TGFbeta/BMP Signaling. *Journal of Dental Research* 93(8):780-787.

Ward MM, Jobling AI, Kalloniatis M, Fletcher EL (2005). Glutamate uptake in retinal glial cells during diabetes. *Diabetologia* 48(2):351-360.

Wei J, Ferron M, Clarke CJ, Hannun YA, Jiang H, Blaner WS, Karsenty G (2014a). Bone-specific insulin resistance disrupts whole-body glucose homeostasis via decreased osteocalcin activation. *Journal of Clinical Investigation* 124(4):1-13.

Wei J, Hanna T, Suda N, Karsenty G, Ducy P (2014b). Osteocalcin promotes beta-cell proliferation during development and adulthood through Gprc6a. *Diabetes* 63(3):1021-1031.

Wei J SJKG (2014). Glut1-dependent glucose uptake in osteoblasts is necessary for bone formation before and after birth and whole-body glucose homeostasis. *Journal of Bone and Mineral Research* 29(1): Abstract 1090.

Weisberg SP, McCann D, Desai M, Rosenbaum M, Leibel RL, Ferrante AW, Jr. (2003). Obesity is associated with macrophage accumulation in adipose tissue. *Journal of Clinical Investigation* 112(12):1796-1808.

Welchman RL, Gordon C, Mayer RJ (2005). Ubiquitin and ubiquitin-like proteins as multifunctional signals. *Nature Reviews Molecular Cell Biology* 6(8):599-609.

White MF, Kahn CR (1994). The insulin signaling system. *Journal of Cell Biology* 269(1):1-4.

Whitfield PD, Nelson P, Sharp PC, Bindloss CA, Dean C, Ravenscroft EM, Fong BA, Fietz MJ, Hopwood JJ, Meikle PJ (2002). Correlation among genotype, phenotype,

and biochemical markers in Gaucher disease: implications for the prediction of disease severity. *Molecular Genetics and Metabolism* 75(1):46-55.

Winther K, Nybo M, Vind B, Pedersen SM, Hojlund K, Rasmussen LM (2011). Acute hyperinsulinemia is followed by increased serum concentrations of fibroblast growth factor 23 in type 2 diabetes patients. *Scandinavian Journal of Clinical and Laboratory Investigation* 72(2):108-113.

Wishart JM, Need AG, Horowitz M, Morris HA, Nordin BE (1995). Effect of age on bone density and bone turnover in men. *Clinical Endocrinology (Oxf)* 42(2):141-146.

Wolf G (1996). Function of the bone protein osteocalcin: definitive evidence. *Nutrition Reviews* 54(10):332-333.

Worley JR, Baugh MD, Hughes DA, Edwards DR, Hogan A, Sampson MJ, Gavrilovic J (2003). Metalloproteinase expression in PMA-stimulated THP-1 cells. Effects of peroxisome proliferator-activated receptor-gamma (PPAR gamma) agonists and 9-cis-retinoic acid. *Journal of Cell Biology* 278(51):51340-51346.

Wright EM, Turk E (2004). The sodium/glucose cotransport family SLC5. *Pflugers Arch* 447(5):510-518.

Wu G, Zhang L, Li T, Zuniga A, Lopaschuk GD, Li L, Jacobs RL, Vance DE (2013). Choline supplementation promotes hepatic insulin resistance in phosphatidylethanolamine N-methyltransferase-deficient mice via increased glucagon action. *Journal of Cell Biology* 288(2):837-847.

Wysolmerski JJ (2012). Osteocytic osteolysis: time for a second look? *Bonekey Reports* 229 (1):1-10.

Xiao S, Yu C, Chou X, Yuan W, Wang Y, Bu L, Fu G, Qian M, Yang J, Shi Y, Hu L, Han B, Wang Z, Huang W, Liu J, Chen Z, Zhao G, Kong X (2001). Dentinogenesis imperfecta 1 with or without progressive hearing loss is associated with distinct mutations in DSPP. *Nature Genetics* 27(2):201-204.

Xiong J, Onal M, Jilka RL, Weinstein RS, Manolagas SC, O'Brien CA (2011). Matrix-embedded cells control osteoclast formation. *Nature Medicine* 17(10):1235-1241.

Xu H, Barnes GT, Yang Q, Tan G, Yang D, Chou CJ, Sole J, Nichols A, Ross JS, Tartaglia LA, Chen H (2003). Chronic inflammation in fat plays a crucial role in the development of obesity-related insulin resistance. *Journal of Clinical Investigation* 112(12):1821-1830.

Yadav MC, Simao AM, Narisawa S, Huesa C, McKee MD, Farquharson C, Millan JL (2011). Loss of skeletal mineralization by the simultaneous ablation of PHOSPHO1 and alkaline phosphatase function: a unified model of the mechanisms of initiation of skeletal calcification. *Journal of Bone and Mineral Research* 26(2):286-297.

Yang G, Badeanlou L, Bielawski J, Roberts AJ, Hannun YA, Samad F (2009a). Central role of ceramide biosynthesis in body weight regulation, energy metabolism, and the metabolic syndrome. *American Journal of Physiology - Endocrinology and Metabolism* 297(1):E211-E224.

Yang X, Karsenty G (2004). ATF4, the osteoblast accumulation of which is determined post-translationally, can induce osteoblast-specific gene expression in non-osteoblastic cells. *Journal of Cell Biology* 279(45):47109-47114.

Yoshizawa T, Hinoi E, Jung DY, Kajimura D, Ferron M, Seo J, Graff JM, Kim JK, Karsenty G (2009). The transcription factor ATF4 regulates glucose metabolism in mice through its expression in osteoblasts. *Journal of Clinical Investigation* 119(9):2807-2817.

Yoshikawa Y, Kode A, Xu L, Mosialou I, Silva BC, Ferron M, Clemens TL, Economides AN, Kousteni S (2011). Genetic evidence points to an osteocalcin-independent influence of osteoblasts on energy metabolism. *Journal of Bone and Mineral Research* 26(9):2012-2025.

Yu H, Ferrier J (1993). ATP induces an intracellular calcium pulse in osteoclasts. *Biochemical and Biophysical Research Communications* 191(2):357-363.

Yunker LA, Undersander A, Lian JB, Stein GS, Carlson CS, Mauro LJ (2004). The tyrosine phosphatase, OST-PTP, is expressed in mesenchymal progenitor cells early during skeletogenesis in the mouse. *Journal of Cellular Biochemistry* 93(4):761-773.

Zee T, Settembre C, Levine RL, Karsenty G (2012). T-cell protein tyrosine phosphatase regulates bone resorption and whole-body insulin sensitivity through its expression in osteoblasts. *Molecular Cell Biology* 32(6):1080-1088.

Zhang X, Zhao J, Li C, Gao S, Qiu C, Liu P, Wu G, Qiang B, Lo WH, Shen Y (2001). DSPP mutation in dentinogenesis imperfecta Shields type II. *Nature Genetics* 27(2):151-152.

Zhou X, Cui Y, Zhou X, Han J (2012). Phosphate/pyrophosphate and MV-related proteins in mineralisation: discoveries from mouse models. *International Journal of Biological Sciences* 8(6):778-790.

Zhu D, Mackenzie NC, Millan JL, Farquharson C, MacRae VE (2011). The appearance and modulation of osteocyte marker expression during calcification of vascular smooth muscle cells. *PLoS One* 6(5):e19595.

Zhu L LL, Wong GW, Kahn B, Riddle R, Clemens T. (2013). Expression of Glucose Transporter-4 by the osteoblast is required for global glucose metabolism (Meeting Abstract). *Journal of Bone and Mineral Research* 28:1.

Zimmermann H, Zebisch M, Strater N (2012). Cellular function and molecular structure of ecto-nucleotidases. *Purinergic Signal* 8(3):437-502.

Appendix

Appendix I – Buffers and solutions

Cell culture buffers

Primary osteoblast medium

αMEM with 10% FBS and 0.05mg/ml gentamicin.

FAZA maintenance medium

McCoy's 5a (1:1), supplemented with 10% FBS, 2mM L-Glutamine and 0.05mg/ml gentamicin.

INS1e maintenance medium

RPMI (1640) (1:1), supplemented with 5% FBS, 2mM Hepes, 50μM β-mercaptoethanol, 1mM pyruvate and 0.05mg/ml gentamicin.

C2C12 maintenance medium

DMEM (d5796 high glucose 4500 mg/L glucose), supplemented with 10% FBS, 2mM L-Glutamine and 0.05mg/ml gentamicin.

C2C12 Differentiation medium

DMEM (d5796) (1:1), supplemented with 1% FBS, 2mM L-Glutamine and 0.05mg/ml gentamicin.

3T3 maintenance medium

DMEM (d5546 low glucose 1000 mg/L glucose), supplemented with 10% foetal bovine serum (FBS), 2mM L-Glutamine and 0.05mg/ml gentamicin.

3T3 Differentiation medium

DMEM (d5796 high glucose 4500 mg/L glucose), supplemented with 10% FBS, 2mM L-Glutamine, 100nM dexamethasone and 0.05mg/ml gentamicin (1st 2-3 days additional IBMX supplementation).

Freezing mix 1

60% DMEM/F-12; 20% FBS; 20% DMSO (suitable for standard cell lines)

Freezing mix 2

70% αMEM; 20% FBS; 20% DMSO (suitable for primary calvarial osteoblasts)

Gel Electrophoresis

Tris-Acteric Acid-EDTA (TAE)

40mM Tris, 1mM EDTA, 0.1 % Acetic Acid

Tris-Boric Acid-EDTA (TBE)

(90mM Tris, 2mM EDTA, 90mM boric acid

Western Blotting

RIPA buffer

20mM Tris-HCl (pH8), 135mM NaCl, 10% Glycerol, 1% IGEPAL, 0.1% SDS, 0.5% Na Deoxycholate, 2mM EDTA

LDS Sample Buffer

10% Glycerol, 141 mM Tris Base, 106 mM Tris HCl, 2% LDS, 0.51 mM EDTA, 0.22 mM SERVA® Blue G250, 0.175 mM Phenol Red, pH 8.5

MOPS running buffer

50 mM MOPS pH 7.7, 50 mM Tris, 0.1% SDS, 1mM EDTA

1X Transfer buffer

100ml 10X transfer buffer, 200ml 98% Ethanol, 700ml dH2O

10X Transfer buffer

29.3mg/ml glycine, 58mg/ml Tris Base (trismethylamine), 18.8µl/ml 20% SDS in dH2O

Tris-Bufferd Saline with Tween 20 (TBST)

10mM Tris HCl pH8.0, 150mM NaCl, 0.1% Tween-20

Blocking Solution ECL

5% (w/v) dried milk protein (Marvel) / BSA Faction V in TBST

Pancreas Lysis

Lysis buffer

50mmol/l Tris, pH 7.4, 0.27 mol/l sucrose, 1mmol/l sodium orthovanadate, pH 10, 1mmol/l EDTA, 1mmol/l EGTA, 10mmol/l sodium β-glycerophosphate, 50mmol/l NaF, 5mmol/l sodium pyrophosphate, 1%[wt/vol] Triton X-100, 0.1% [vol/vol] 2-mercaptoethanol, and protease inhibitors—EDTA free tablets (Roche)

Fixatives and histological stains

10% Neutral Buffered Formalin (NBF)

100ml strong formalin, 900ml tap water, 4.0g sodium dihydrogen phosphate, monohydrate ($NaH_2PO_4.H_2O$) and 6.5g Disodium hydrogen phosphate, anhydrous (Na_2HPO_4)

4% Paraformaldehyde (PFA)

800ml 1x PBS 60°C, 40g paraformaldehyde powder, 1N NaOH added dropwise until the solution cleared, adjust volume to 1L with 1x PBS

Oil-Red-O stock stain

0.5g Oil-Red-O (CI 26125, Merc Millipore) dissolve in 100ml isopropanol with gentle heat

Oil-Red-O working solution

Dilute 30ml stock stain in 20 ml of dH_20, stand and filter

General buffer recipes

Phosphate Buffered Saline (PBS)

140mM NaCl, 2.5mM KCl, 10mM Na_2HPO_4, 1.8mM KH_2PO_4

Hanks Buffered Saline Solution (HBSS)

1.26 mM $CaCl_2$, 0.493 mM $MgCl_2$, 0.407 mM $MgSO_4$, 5.33 mM KCl, 0.441 mM KH_2PO_4, 4.17 mM $NaHCO_3$, 137.93 mM NaCl, 0.338 mM Na_2HPO_4, 5.56 mM D-Glucose

Appendix II - Antibodies

Primary antibodies

Antibody	Species	Source	Use	Dilution
AKT	Rabbit	Cell Signaling Technology	Western Blotting	1:1000
ERK	Rabbit	Cell Signaling Technology	Western Blotting	1:1000
GLUT4	(1F8) Mouse	Cell Signaling Technology	Western Blotting	1:1000
GSK3β	Rabbit	Cell Signaling Technology	Western Blotting	1:1000
InsR	Rabbit	Cell Signaling Technology	Immunocytochemistry	1:200
pAKT	Rabbit	Cell Signaling Technology	Western Blotting	1:1000
pERK	Rabbit	Cell Signaling Technology	Western Blotting	1:1000
pGSK3β	Rabbit	Cell Signaling Technology	Western Blotting	1:1000
PHOSPHO1	Human	AbD Serotec, Bio-rad	Immunohistochemistry Western Blotting	1:200 / 1:1000
SMPD3	Rabbit	Santa Cruz	Western Blotting	1:1000
UCP1	Rabbit	Cell Signaling	Western Blotting	1:1000
β-actin (HRP-linked)	Mouse	Sigma	Western Blotting	1:50000

Secondary antibodies

Antibody	Source	Use	Dilution
Alexa Fluor@488 goatanti mouse	Life Technologies	Immunocytochemistry	1:500
Alexa Fluor@594 goatanti rabbit	Life Technologies	Immunocytochemistry	1:500
Goat anti-mouse	Dako	Western Blotting	1:5000
Goat anti-rabbit	Dako	Western Blotting	1:5000
Goat anti-human	Dako	Western Blotting	1:5000

Appendix III - Seahorse XF24 Analyzer protocol

Command	Time (min)	Parameter	Port
Calibrate	0.00		
Equilibrate			
Loop Start	3.00		
Mix	3.00		
Wait	2.00		
Measure	3.00		
Loop End			
Inject		A	OLIGO
Loop Start	3.00		
Mix	3.00		
Wait	2.00		
Measure	3.00		
Loop End			
Inject		B	FCCP
Loop Start	3.00		
Mix	3.00		
Wait	2.00		
Measure	3.00		
Loop End			
Inject		C	ROT/ANTI
Loop Start	3.00		
Mix	3.00		
Wait	2.00		
Measure	3.00		
Loop End			

Appendix IV - Genotyping

DNA extraction solutions

Solution 1

100ml dH_2O, 40ul of 0.5M EDTA, 0.1g NaOH

Solution 2

96ml dH_2O, 4ml 1M TRIS, Adjust to pH 5.5

Genotyping primers and mutation detail

Genotyping Assay	Source		Sequence (5'-3')
Genotyping Assay Phospho1_R74X	INGENOtyping	F	TCCTCCTCACCTTCGACTTC
		R	ATGCGGCGGAATAAACTGT

Mutation position

5'-GTACATGCAAC/TGAGTCTTTAA-3'

WT: C

Phospho1$^{-/-}$: T

PCR fragment (355 bp):

TCCTCCTCACCTTCGACTTCGATGAGACCATCGTGGACGAGAACAGCGACG
ACTCGATCGTGCGTGCCGCGCCAGGCCAGCAACTGCCCGAGAGCCTGCGTG
CCACCTATCGCGAGGGCTACTACAATGAGTACATGCAA**C/T**GAGTCTTTAAG
TACCTGGGTGAGCAGGGTGTACGGCCCCGGGACCTGCGCGCTGTCTACGAG
ACCATCCCCCTGTCGCCAGGCATGGGCGATTTGTTGCAGTTCATAGCCAAAC
AGGGCTCCTGCTTCGAGGTTATTCTCATTTCGGATGCCAACACCTTCGGTGTG
GAGAGTGCCCTGCGTGCCGCTGGCCACCACAGTTTATTCCGCCGCAT

Phospho1 genotyping mix

1µl 10x Buffer, 0.5µl 10mM DNTPs, 0.75 µl 50mM $MgCl_2$, 1µl forward primer, 1µl reverse primer, 1.25µl 1%W, 0.25µl Taq DNA Polymerase and 4.25 µl extracted DNA per reaction.

Phospho1 genotyping programme

(94.0°C 30 sec, 61.0°C 30 sec, 72.0°C 90 sec) x 2

(94.0°C 30 sec, 59.0°C 30 sec, 72.0°C 90 sec) x 2

(94.0°C 30 sec, 57.0°C 30 sec, 72.0°C 90 sec) x 2

(94.0°C 30 sec, 55.0°C 30 sec, 72.0°C 90 sec) x 28

(94.0°C 30 sec, 61.0°C 30 sec, 72.0°C 10 min) End

Phospho1 Restriction mix

0.15µl BSA Faction V, 0.5µl Bsrd1 restriction enzyme, 1.5µl NEB buffer and 2.85µl dH_20. Heat together with PCR product at 65.0°C for 1 hour. Run product on 1.5% agarose gel.

Appendix V – PCR primers

Gene	Source		Sequence (5'-3')
Acadm	PrimerBank	F	AACACAACACTCGAAAGCGG
		R	TTCTGCTGTTCCGTCAACTCA
Adamts4	PrimerBank	F	ATGGCCTCAATCCATCCCAG
		R	GCAAGCAGGGTTGGAATCTTTG
Adipoq	PrimerBank	F	GGCCGTTCTCTTCACCTACG
		R	TGGAGGAGCACAGAGCCAG
Adipor1	PrimerBank	F	AACGGGCCATCCATTTTTG
		R	TTAGCCGGGCTACATCAAGG
Ang	PrimerBank	F	TCAAAAGTGTTAAGGGACATGGG
		R	GGCAGCTATTGTTCTTGACAGT
Atf4	PrimerBank	F	CCTGAACAGCGAAGTGTTGG
		R	TGGAGAACCCATGAGGTTTCAA
Atgl	PrimerBank	F	GGCCATGATGGTGCCCTAT
		R	CACTCCAACAAGCGGATGGT
b3ar	PrimerBank	F	GGCACAGGAATGCCACTCCAAT
		R	AGGAGGGGAAGGTAGAAGGAGAC
Bglap	Dr. Dongxing Zhu	F	CCGGGAGCAGTGTGAGCTTA
		R	TAGATGCGTTTGTAGGCGGTC
Bmp4	PrimerBank	F	ATTCCTGGTAACCGAATGCTG
		R	CCGGTCTCAGGTATCAAACTAGC
Cd68	PrimerBank	F	CCATCCTTCACGATGACACCT
		R	GGCAGGGTTATGAGTGACAGTT
Cebpa	PrimerBank	F	AACAGCAACGAGTACCGGGT
		R	CACCTTCTGTTGCGTCTCCAC
Cfp	PrimerBank	F	CTGCTACTGGTTATCCTGCCA
		R	TCTACCCTGATGTCTCTCCCA

Gene	Source		Sequence (5'-3')
Cidea	PrimerBank	F	TGACATTCATGGGATTGCAGAC
		R	GGCCAGTTGTGATGACTAAGAC
Clec4d	PrimerBank	F	ACCCGACATCCCCAACTGAT
		R	CTCTCGTCCAGCGTAAAAAGT
Col1a1	Qiagen	F	Not disclosed
		R	Not disclosed
Ifi202b	PrimerBank	F	GTGGCATTGAAAGCAACAAAACT
		R	GCCAGAGACCCATACATACCA
Il1rn	PrimerBank	F	GCTCATTGCTGGGTACTTACAA
		R	CCAGACTTGGCACAAGACAGG
Insr	PrimerBank	F	CCTGGTTATCTTCGAGATGGTCC
		R	CCCCACATTCCTCGTTGTCA
Lep	PrimerBank	F	ATTTCACACACGCAGTCGGTAT
		R	GGTGGAGCCCAGGAATGAAG
Lpl	PrimerBank	F	TCTGTACGGCACAGTGG
		R	CCTCTCGATGACGAAGC
Lum	PrimerBank	F	CTCTTGCCTTGGCATTAGTCG
		R	GGTCATCACAGTACATGGCAGT
Mpeg1	PrimerBank	F	CTGGATGATAATAGCGTGTGCT
		R	AAGACAGGTAGTTTCAGGGCA
Nco6	PrimerBank	F	CTCGCAAGAGCATAAAGGCG
		R	CAAGGAAGAGGCAGAGGAGG
Pck1	PrimerBank	F	CATATGCTGATCCTGGGCATAAC
		R	CAAACTTCATCCAGGCAATGTC
Pdk4	PrimerBank	*F*	AGGATTACTGACCGCCTCTT
		R	CGTCTGTCCCATAACCTGAC

Gene	Source		Sequence (5'-3')
Phospho1	Primer Design	F	TTCTCATTTCGGATGCCAACA
		R	TGAGGATGCGGCGGAATAA
Ppara	PrimerBank	F	CCCTGAACATCGAGTGTCGA
		R	AATAGTTCGCCGAAAGAAGCC
Pparg	Primer Design	F	CTGCCTATGAGCACTTCACAAG
		R	CTCTTGTGAATGGAATGTCTTCA
Ppargc1a	PrimerBank	*F*	CCCTGCCATTGTTAAGACC
		R	TGCTGCTGTTCCTGTTTTC
Ppargc1b	PrimerBank	*F*	TCCTGTAAAAGCCCGGAGTAT
		R	GCTCTGGTAGGGGCAGTGA
Prdm16	PrimerBank	F	CCTAACTTTCCCCACTCCCTTA
		R	GCTCAGCCTTGACCAGCAA
Prdx	PrimerBank	F	GCTGCAAAGCCAGTTCTGTG
		R	CCACTGAGGGAATGGCATCTC
Prkaa2	PrimerBank	F	GTCAAAGCCGACCCAATGATA
		R	CGTACACGCAAATAATAGGGGTT
Ptpn1	PrimerBank	*F*	ACGGCGTACCTGGTCATCTA
		R	CTATGGTAGCTCCCCTTAGCC
Runx2	Dr. Dongxing Zhu	F	ACCATAACAGTCTTCACAAATCCT
		R	ACCATAACAGTCTTCACAAATCCT
Slc1a3	PrimerBank	F	ACCAAAAGCAACGGAGAAGAG
		R	GGCATTCCGAAACAGGTAACTC
Slc2a1	(Flessner *et al.*, 2012)	F	TCAACACGGCCTTCACTG
		R	CACGATGCTCAGATAGGACATC
Slc2a2	(Flessner *et al.*, 2012)	F	TGTGCTGCTGGATAAATTCGCCTG
		R	AACCATGAACCAAGGGATTGGACC

Gene	Source		Sequence (5'-3')
Slc2a3	(Flessner *et al.*, 2012)	F	TTCTGGTCGGAATGCTCTTC
		R	AATGTCCTCGAAAGTCCTGC
Slc2a4	Primer Design	F	CCAGTATGTTGCGGATGCTAT
		R	TTTTAGGAAGGTGAAGATGAAGAAG
Slc2a5	((Flessner *et al.*, 2012)	F	GGCTCATCTTCCCCTTCATTC
		R	ATGAATGTCCTGCCCTTGG
Slc2a6	(Flessner *et al.*, 2012)	F	TTGGTGCTGTGAGGCT
		R	TGGCACAAACTGGACGTA
Slc2a8	(Flessner *et al.*, 2012)	F	TTCATGGCCTTTCTAGTGACC
		R	GAGTCCTGCCTTTAGTCTCAG
Slc2a9	(Flessner *et al.*, 2012)	F	TGCTTCCTCGTCTTCGCCACAATA
		R	CTCTTGGCAAATGCCTGGCTGATT
Slc2a10	(Flessner *et al.*, 2012)	F	ACCAAAGGACAGTCTTTAGCTG
		R	ATCTTCCAAGCAGACGGATG
Slc2a12	(Flessner *et al.*, 2012)	F	GGGTGTCAACCTTCTCATCTC
		R	CCAAAGAGCATCCCTTAGTCTC
Sp7	PrimerBank	F	ATGGCGTCCTCTCTGCTTGA
		R	GAAGGGTGGGTAGTCATTTG
Tcirg1	PrimerBank	F	CTCCTACTTGCGTCTCTGGG
		R	GAGCCCCTCCATCACTAACA
Ucp1	PrimerBank	F	GGATGGTGAACCCGACAACT
		R	AACTCCGGCTGAGAAGATCTTG
Ucp2	PrimerBank	F	AATCTCGGGAGGCACCTTTC
		R	GAGAATGGGACTGGGCAGAG
Vdr	PrimerBank	F	GAATGTGCCTCGGATCTGTGG
		R	ATGCGGCAATCTCCATTGAAG

Appendix VI – Ceramide species

Ceramide species	Parent Mass
C14	510.7
C16	538.5
C17	552.5
C18:1	564.5
C18:0	566.5
C20:1	592.6
C20:0	594.6
C22:1	620.6
C22:0	622.6
C23:0	636.6
C24:1	648.6
C24:0	650.6
C25:1	662.6
C25:0	664.6

Appendix VII – *Phospho1*$^{-/-}$*Col1a1*-Phospho1 mice

Generation of *Phospho1*$^{-/-}$*Col1a1*-Phospho1

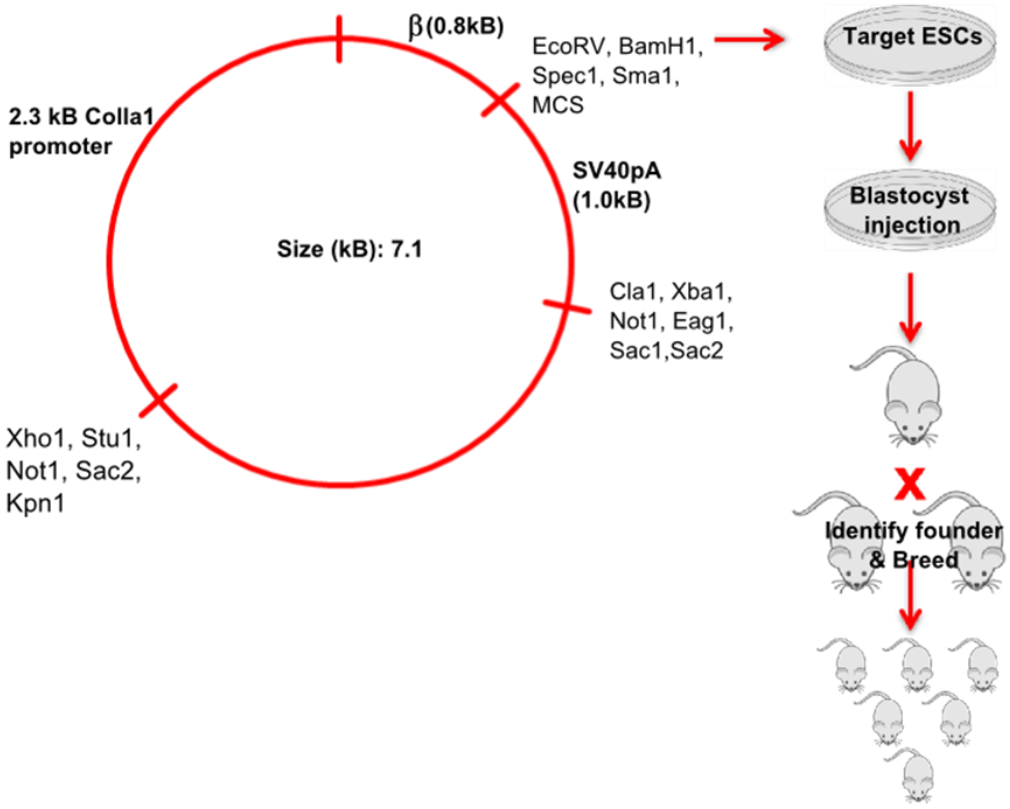

Genotyping primers

Primer	Source	Sequence (5'-3')
Col1a1/F	Dr. Monzur Murshed	CAGCTCTCCATCAAGATGGT
Beta-g-intron	Dr. Monzur Murshed	CCGGTTTGGACTCAGAGTAT